

Department of Physics

PhD program in **Physics and Astronomy**

Cycle XXXV - Curriculum in **Astrophysics**

The Polarized Emission from our Galaxy: Forecasts, Measurements, Analysis, and Characterization as a Foreground in the context of Current and Next-generation Cosmic Microwave Background Experiments

Surname **Fanfani** Name **Valentina**

Registration number **854373**

Tutor: **Prof. Federico Nati**

Coordinator: **Prof. Stefano Ragazzi**

ACADEMIC YEAR 2021/2022

Alla mia *Stella Tonina*, la tua *Ninin*.

Alla luce dell'*Aurora*, magico dono.

Alla mia *famiglia*, con amore infinito.

May God bless and keep you always
May your wishes all come true
May you always do for others
And let others do for you
May you build a ladder to the stars
And climb on every rung

May you grow up to be righteous
May you grow up to be true
May you always know the truth
And see the light surrounding you
May you always be courageous
Stand upright and be strong

May your hands always be busy
May your feet always be swift
May you have a strong foundation
When the winds of changes shift
May your heart always be joyful
May your song always be sung

Bob Dylan

Acknowledgments

I thank my loved family, who have always been there, taught me to be courageous and to always have hope. Thank you granpa Neno for the help.

I thank Federico for the immense opportunity he gave me by believing in me.

I thank all my collaborators from the Simons Observatory, BLAST, and ACT groups, in particular: Brandon and Susan, who have guided me and teaching me what I know today; Laura and Nicoletta, for being precious with their inputs.

I am thankful for the opportunity to work with people from these international collaborations who welcomed, inspired and taught me with the example of passionate and authentic dedication.

I thank those I have met on my journey, and who left an indelible mark on me: hi Oscar, Irene, Simran, Eirik.

I thank all the true friends who supported me.

I am grateful to have had the opportunity to see special places, such as Princeton, thus realizing my ancient dream; and Oslo, San Diego, Tenerife and Ferrara.

I thank those who respected me, who were patient and valued me, without ever judging me.

I apologize for the mistakes I made, I will try every day to be better.

Per aspera ad astra

Contents

| | | |
|----------|---|-----------|
| 1 | Introduction | 1 |
| 1.1 | Scientific and experimental context | 1 |
| 1.2 | Polarized Galactic emissions | 5 |
| 1.2.1 | Synchrotron emission | 8 |
| 1.2.2 | Emission from interstellar dust | 11 |
| 1.2.3 | Open questions | 17 |
| 1.2.4 | Polarized Galactic emissions as CMB foreground | 20 |
| 1.3 | Main contributions of my PhD thesis work and its structure | 22 |
| 2 | Power spectrum forecast of multi-frequency polarized Galactic emissions with the SO experiment | 26 |
| 2.1 | Introduction | 26 |
| 2.2 | The Simons Observatory experiment | 28 |
| 2.3 | Survey description and noise models | 32 |
| 2.3.1 | SO noise model | 32 |
| 2.3.2 | Noise models for ancillary data | 34 |
| 2.3.3 | Sky coverage | 36 |
| 2.4 | Power spectrum forecasting framework | 37 |
| 2.4.1 | Galactic emission model | 37 |
| 2.4.2 | Simulated power spectra | 39 |
| 2.4.3 | Model fitting | 41 |
| 2.5 | The Galactic synchrotron SED | 43 |
| 2.5.1 | Motivation | 43 |
| 2.5.2 | Forecasting framework | 43 |
| 2.6 | The composition of interstellar dust | 45 |
| 2.6.1 | Motivation | 45 |
| 2.6.2 | Forecasting framework | 46 |
| 2.7 | Results | 47 |
| 2.7.1 | The Galactic synchrotron SED results | 47 |
| 2.7.2 | The Galactic synchrotron and dust SEDs results | 49 |
| 2.7.3 | The correlation between synchrotron and dust emission | 52 |
| 2.8 | Conclusions | 54 |

| | | |
|----------|--|-----------|
| 3 | New starlight polarization analysis with Planck data | 57 |
| 3.1 | Introduction | 57 |
| 3.2 | The emission-to-extinction polarization ratio | 60 |
| 3.3 | Starlight polarization data | 64 |
| 3.3.1 | The preliminary sample | 64 |
| 3.3.2 | Distances estimates | 69 |
| 3.3.3 | Estimates for starlight reddening | 70 |
| 3.3.4 | Estimates for optical degree of polarization | 73 |
| 3.3.5 | Stokes parameters in extinction | 76 |
| 3.3.6 | Selection of the lines of sight | 76 |
| 3.4 | Polarized emission data | 77 |
| 3.4.1 | Planck data | 81 |
| 3.5 | Results | 82 |
| 3.6 | Conclusions | 84 |
| 4 | Observational strategy simulations to map polarized Galactic dust emission as CMB foregrounds with the BLAST experiment | 89 |
| 4.1 | Introduction | 89 |
| 4.2 | The Balloon-borne Large-Aperture Submillimeter Telescope experiments | 92 |
| 4.2.1 | The BLAST-TNG experiment | 94 |
| 4.2.2 | The BLAST Observatory experiment | 96 |
| 4.3 | Target field visibility | 100 |
| 4.3.1 | The BLAST-TNG target field visibility | 101 |
| 4.3.2 | The BLAST Observatory target field visibility | 101 |
| 4.4 | Observational strategy | 105 |
| 4.4.1 | The BLAST-TNG observational strategy | 106 |
| 4.4.2 | The BLAST Observatory observational strategy | 106 |
| 4.5 | Sensitivity | 107 |
| 4.5.1 | The BLAST-TNG sensitivity | 108 |
| 4.5.2 | The BLAST Observatory sensitivity | 109 |
| 4.6 | Foreground simulations | 111 |
| 4.7 | Quality factors | 113 |
| 4.8 | Constraints on the polarized SED | 116 |
| 4.9 | HI column density maps | 118 |
| 4.9.1 | The BLAST-TNG selection strategy | 119 |
| 4.9.2 | The BLAST Observatory selection strategy | 121 |
| 4.10 | Results | 122 |
| 4.10.1 | The BLAST-TNG diffuse ISM field selection | 122 |
| 4.10.2 | The BLAST Observatory diffuse ISM fields selection | 126 |
| 4.11 | Conclusions | 136 |

| | | |
|----------|---|------------|
| 5 | Post-flight performance analysis of the BLAST-TNG star cameras pointing system | 138 |
| 5.1 | Introduction | 138 |
| 5.2 | The pointing system | 139 |
| 5.2.1 | The pointing motors | 140 |
| 5.2.2 | The pointing sensors | 140 |
| 5.3 | In-flight star cameras performance | 145 |
| 5.3.1 | Polar mesospheric clouds | 146 |
| 5.4 | Post-flight star cameras analysis | 148 |
| 5.4.1 | Astrometry.net: an astrometric calibration service | 149 |
| 5.4.2 | Filtering techniques | 155 |
| 5.4.3 | Estimation of stars number in anti-sun images | 158 |
| 5.4.4 | Results | 158 |
| 5.5 | Conclusions | 161 |
| 6 | Conclusions | 164 |
| | Bibliography | 170 |

Chapter 1

Introduction

The topic of my PhD thesis is mainly related to the theme of polarized emissions of Galactic origin, i.e. synchrotron and dust, which will be described in Section 1.2, and which I have tried to explore from as many perspectives as possible. I have concentrated my efforts on their characterization, especially from the modeling point of view, trying both to bring further experimental confirmations to the current knowledge, and to demonstrate that it will be possible to narrow the field of uncertainties in the very near future.

Understanding these emissions is important not only for their characterization per se, which is in turn connected to a series of topics such as Galactic magnetic fields, but also for the role of contaminant foregrounds that these emissions play (see Subsection 1.2.4), when it is about observing the Cosmic Microwave Background radiation (CMB): a snapshot of the oldest light in our Universe, imprinted on the sky when it was just 380,000 years old.

The current and next-generation CMB experiments have moved and are moving around this goal, as it is described in Section 1.1, since by now it is clear that to advance in knowledge we cannot ignore the knowledge of Galactic emissions, even polarized.

1.1 Scientific and experimental context

During last years, that defined the era of “precision cosmology”, CMB observations yielded very tight constraints on a number of cosmological parameters (e.g.: [BICEP2 Collaboration et al., 2018](#); [Adachi et al., 2020](#); [Aiola et al., 2020](#); [Choi et al., 2020](#); [Planck Collaboration VI, 2020](#); [Balkenhol et al., 2021](#); [BICEP/Keck Collaboration et al., 2021](#); [Dutcher et al., 2021](#)); furthermore, current and next-generation CMB experiments are also particularly focused on measuring the polarized light from the CMB. One of the main cosmological efforts is the search for primordial B -mode polarization¹ from inflationary gravitational waves, to provide information about Inflation ([Hensley et al., 2022](#)).

¹A polarization pattern on the sky can be characterized in terms of a scalar field, E , and a pseudo-scalar field, B ([Kamionkowski et al., 1997](#); [Zaldarriaga et al., 1997](#)). A deeper description will be given in Section 1.2.

If we assume the Big Bang model, the only way proposed to explain what we observe today (in terms of its flat geometry) is the inflationary model. It consists of a period of expansion that happened just after the Universe began. Considering standard models of inflation, perturbations deriving from initial quantum fluctuations, give rise to an almost scale invariant spectrum of primordial gravitational waves, directly related to the energy scale of inflation (Clarke et al., 2020). A gravitational wave is a perturbation of space-time that propagates with an undulatory character, causing a rhythmic contraction and dilation of the distances between the points of space-time. Primordial gravitational waves imprinted characteristic polarization signals on the CMB: the E -mode pattern, much weaker than other sources of E -modes (e.g. Thomson scattering); and the faint B -mode pattern, which is the direct signature of the presence of a stochastic background of gravitational waves, as is schematized in Figure 1.1.

The CMB B -mode detection has become a major goal in the field, prompting many groups to build experiments to reach the required unprecedented sensitivity on scales $\gtrsim 1^\circ$ (Kamionkowski & Kovetz, 2016), and to start thinking about future satellite missions dedicated to polarization.

To bring back to the importance of my PhD thesis topic, since we live in a galaxy and we are surrounded by very diffuse matter that emits microwaves, the CMB B -modes detection depend on the capability to measure the polarized Galactic foregrounds, i.e. late-time, low-redshift components diffused throughout all the sky, and to thoroughly understand and characterize their distinct emission mechanisms: mainly in the form of diffuse synchrotron and thermal dust emissions, which will be described in detail in Section 1.2.

While CMB experiments in the past have been optimized primarily for cosmology, they have also made important contributions to the field of polarized foregrounds, and have the potential to make even greater contributions.

Moreover, current and next-generation CMB experiments, thanks to their combination of frequency coverage from about ~ 30 GHz up to ~ 300 GHz, with higher and lower frequencies than the peak of the CMB emission at ~ 160 GHz, large sky area, high angular resolution and sensitivity, also offer significant additional science returns (Abazajian et al., 2019; Simons Observatory Collaboration, 2019), and can provide new probes of the structure and physics of the magnetic interstellar medium (ISM) of our Galaxy (Hensley et al., 2022).

First of all, in the past a very important role has been played by the CMB satellite missions, which have a long legacy of expanding the knowledge and understanding of our Galaxy through all-sky observations.

One of the most important was the COsmic Background Explorer (COBE) satellite which has provided different information, as Hensley et al. (2022) mentions: all-sky maps of interstellar [CII] and [NII] emission at an angular resolution of 7° (Fixsen et al.,

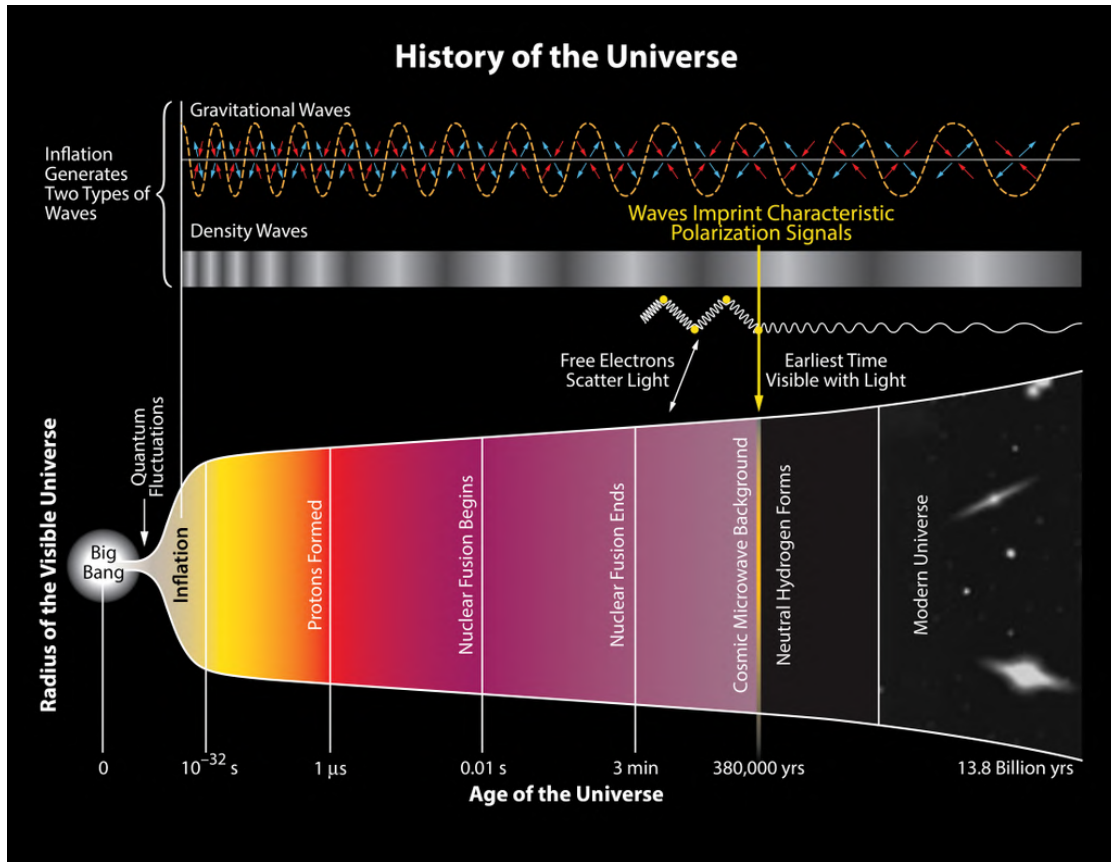


Figure 1.1: *The evolution of the Universe: a schematic representation of the expansion history. The bottom part of this illustration shows the scale of the Universe versus time. Peculiar epochs are indicated, such as the last scattering surface where the CMB was emitted at 380,000 years after the Big Bang. This relic radiation carries the imprints of the fluctuations in the matter distribution as measurable anisotropies, as well as polarization signals divided into E- and B-modes. The density waves appear as temperature and E-mode polarization, while the gravitational waves left a characteristic signature in the CMB polarization, producing the B-modes. Both density and gravitational waves derive from initial quantum fluctuations which have been magnified by Cosmic Inflation, producing effects in the CMB photons at the time they were emitted. Credit to: National Science Foundation (NASA, JPL, Keck Foundation, Moore Foundation, related) - Funded BICEP2 Program.*

1999); a detailed measurement of the frequency dependence of Galactic dust emission² (Finkbeiner et al., 1999); the first full-sky measurement of 3.5 – 12 μm emission from Polycyclic Aromatic Hydrocarbons (PAHs), at an angular resolution of 0.7°³, attesting their ubiquity in the Galactic ISM (Dwek et al., 1997); finally the initial evidence for the existence of the Anomalous Microwave Emission⁴ (AME⁵; Kogut et al., 1996).

²Both measurements through the Far-Infrared Absolute Spectrophotometer (FIRAS).

³Using the Diffuse InfraRed Background Explorer (DIRBE).

⁴Using the Differential Microwave Radiometer (DMR).

⁵AME (Anomalous Microwave Emission) is an electric dipole emission from rapidly spinning small

Another crucial satellite was the Wilkinson Microwave Anisotropy Probe (WMAP), which serve as a primary input to 3D models of the Galactic magnetic field (Jansson & Farrar, 2012; Unger & Farrar, 2017) through observations of polarized synchrotron emission at 1° angular resolution (Gold et al., 2011; Hensley et al., 2022). The latest and most important experiment in this kind of tradition is the *Planck* satellite. It mapped the full sky in nine frequency channels, of which seven were sensitive to polarization, with an angular resolution $< 10'$ (Planck Collaboration I, 2011). These data have had a huge impact on understanding a number of topics, as Hensley et al. (2022) mentions: the composition of the interstellar dust in our Galaxy (Planck Collaboration Int. XXII, 2015) and in the Magellanic Clouds (Planck Collaboration XVII, 2011); the grain alignment (Planck Collaboration et al., 2020a); the interstellar turbulence (Planck Collaboration Int. XX, 2015); the role of magnetic fields in governing the structure of molecular clouds (Planck Collaboration Int. XXXV, 2016); the ubiquity of high density “cold clumps” (Planck Collaboration XXVIII, 2016); the geometry of the Galactic magnetic field (Planck Collaboration Int. XLII, 2016); the geometry of synchrotron-bright radio loops (Planck Collaboration XXV, 2016); the spectral energy distribution (SED) of synchrotron emission (Planck Collaboration X, 2016; Planck Collaboration XXV, 2016); finally the nature of AME and its spectral variations in the Galaxy (Planck Collaboration Int. XV, 2014).

In addition to satellites, also ground-based CMB experiments have made important discoveries in Galactic astrophysics (observing up to 280 GHz), as Hensley et al. (2022) mentions: the Owens Valley Radio Observatory which, as part of the RING5M experiment, with observations at 14.5 and 32 GHz, was the key for establishing the existence of AME (Leitch et al., 1997); the Background Imaging of Cosmic Extragalactic Polarization (BICEP; Ade et al., 2014a; BICEP2 Collaboration et al., 2018; BICEP/Keck Collaboration et al., 2021); the South Pole Telescope (SPT; Crawford et al., 2016), which mapped in total intensity the Magellanic Clouds; the Atacama Cosmology Telescope (ACT), which has furnished a multi-frequency view of magnetic fields in the Galactic center at an angular resolution of the order of arcminute (Guan et al., 2021).

There is also a next-generation of ground-based CMB experiments that promise a great expansion on this kind of studies as a result of enhanced frequency coverage, sky area, angular resolution and sensitivity, such as: the Prime-Cam receiver on the Fred Young Submillimeter Telescope (FYST), which has five frequency bands spanning from 220 up to 850 GHz (Choi et al., 2020; Prime Collaboration et al., 2021); the Simons Observatory (SO) experiment, which will be described in Section 2.2; and CMB-S4 (“Stage 4”), which will survey the sky with over 500,000 detectors and 21 telescopes at the South Pole and the Chilean Atacama desert, for a total of 7 years (Abazajian et al., 2022).

In addition to satellites and ground-based telescopes, there are also another kind of

dust grains at frequencies of ~ 30 GHz (Draine & Lazarian, 1998). It remains unknown whether AME is polarized (Dickinson et al., 2018).

experiments, the balloon-borne experiments, which have the potential to make significant contributions. These telescopes are required since they can observe at higher frequencies and with greater sensitivity than ground-based telescopes; moreover, they are particularly suitable for studying thermal dust emission because they operate closer to the peak of the dust spectral emission curve. Following [Hensley et al. \(2022\)](#), I can mention: the SPIDER experiment, which observed up to 280 GHz ([Crill et al., 2008](#); [Shaw et al., 2020](#)); the PIPER experiment, which has a frequency coverage up to 600 GHz ([Essinger-Hileman et al., 2020](#)); the OLIMPO experiment, which observes up to 460 GHz ([Presta et al., 2020](#)); the PILOT experiment, which extends up to 1.2 THz ([Bernard et al., 2016](#)); finally the Balloon-Borne Large Aperture Submillimeter Telescope (BLAST) experiment, described in [Section 4.2](#), and in particular the proposal BLAST Observatory ([Lowe et al., 2020](#)), which would have the capability to observe at frequencies between 850 GHz and 1.7 THz and survey hundreds of square degrees, providing a strong lever arm to distinguish between proposed dust models.

Looking at the future, also a number of CMB satellites have been proposed, such as the PIXIE experiment ([Kogut et al., 2016](#)) and the Probe of Inflation and Cosmic Origins (PICO) experiment ([Sutin et al., 2018](#); [Hanany et al., 2019](#)), with polarization sensitivity at frequencies above 300 GHz ([Hensley et al., 2022](#)). Currently, the only funded satellite is the LiteBIRD CMB mission, which covers frequencies up to 448 GHz ([Hazumi et al., 2020](#); [Montier et al., 2020](#)), and this means that, over the next decade, wide sky-area high-frequency measurements at higher resolutions have been left to ground-based and balloon-borne observatories ([Hensley et al., 2022](#)).

During my PhD I worked in close collaboration with some of this current and future experiments as a member of their Galactic Science Working Groups, in particular with ACT, SO and the BLAST experiments, and my PhD project developed around the subject of polarized Galactic foregrounds. I will describe my thesis work, with its structure, its common thread and all main contributions in [Section 1.3](#).

1.2 Polarized Galactic emissions

Polarized Galactic emissions are late-time, low-redshift components diffuse throughout all the sky, and the main ones are synchrotron and dust emissions (see [Subsections 1.2.1](#) and [1.2.2](#)). There are also other microwave foregrounds, but they are not polarized, e.g.: the free-free emission and maybe the Anomalous Microwave Emission (AME; already mentioned in [Section 1.1](#)), which at most provides an additional subdominant contribution, as will be described in [Subsection 1.2.4](#).

Before going into details, it should be emphasized that, when we talk about polarized emission, we mean linearly polarized, a particular kind of emission: waves in which oscillations preferentially⁶ take place in a single direction.

⁶Unless the signal is 100% polarized, the light waves can have a variety of orientations.

Moreover, these emissions are intrinsically polarized, to be distinguished with emissions that originate as unpolarized and become polarized due to external mechanisms, as we will see in Sections 1.2.2 and 3.1 talking about the selective extinction of starlight by dust grains.

Polarization can be described through the semi-minor and semi-major axes of the polarization ellipse, i.e. an instantaneous representation of polarized light in the most general state, its orientation, and the direction of rotation. The most familiar polarization states, linear and circular, are degenerate cases of this ellipse, and they are particularly important for two main reasons: polarization measurements, as well as many polarization calculations, are greatly simplified using these specific polarization states; and they are relatively easy to create in a laboratory using linear and circular polarizers.

In the context of Galactic emission, the polarization is described in terms of Q and U Stokes parameters. Stokes parameters are a set of four values that, from a physical point of view, describe the polarization state of electromagnetic radiation: I describes the total (polarized and unpolarized) intensity; Q describes the linear polarization in the direction parallel or perpendicular to the reference plane; U describes the linear polarization in the directions 45° to the reference plane; finally V describes the circular polarization. Since each parameter corresponds to a difference or to a sum of real and measurable quantities, with same units, this method is advantageous from an experimental point of view. An example of different forms of 100% linear polarization and 100% circular polarization is shown in Figure 1.2.

Two derivative quantities, often studied in the topic of polarized Galactic emissions, are the linear polarized total intensity and the polarization fraction, i.e. the degree of linear polarization, respectively defined as:

$$P = \sqrt{Q^2 + U^2} \quad , \quad (1.1)$$

$$p = \frac{P}{I} \quad . \quad (1.2)$$

In general, the polarization pattern has two geometrical components. Instead of describing it by the Stokes parameters, which depend on an arbitrary choice of coordinates, we can describe it by its orientation relative to itself.

In Section 1.1, talking about CMB B -modes, I already introduced that a polarization pattern on the sky can be also characterized in terms of a scalar field, E , and a pseudo-scalar field, B (Kamionkowski et al., 1997; Zaldarriaga et al., 1997), and so the CMB polarization pattern is geometrically decomposed into a curl-free component (E -mode) and curl component (B -mode). In detail, if the polarization is parallel or perpendicular to the plane wave direction, it is called an E -mode polarization while, if it is crossed at 45° angles, it is called a B -mode polarization.

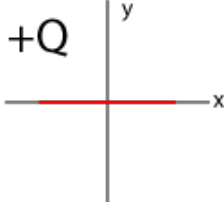
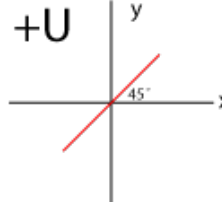
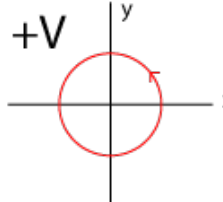
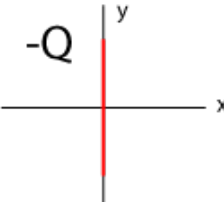
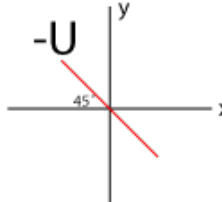
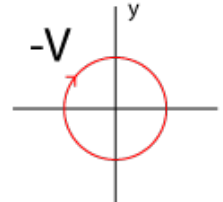
| 100% Q | 100% U | 100% V |
|---|---|--|
| <p>+Q</p>  <p>$Q > 0; U = 0; V = 0$ (a)</p> | <p>+U</p>  <p>$Q = 0; U > 0; V = 0$ (c)</p> | <p>+V</p>  <p>$Q = 0; U = 0; V > 0$ (e)</p> |
| <p>-Q</p>  <p>$Q < 0; U = 0; V = 0$ (b)</p> | <p>-U</p>  <p>$Q = 0; U < 0; V = 0$ (d)</p> | <p>-V</p>  <p>$Q = 0; U = 0; V < 0$ (f)</p> |

Figure 1.2: Stokes parameters in some degenerate cases: (a) represents linearly horizontal polarized light; (b) represents linearly vertical polarized light; (c) represents linear $+45^\circ$ polarized light; (d) represents linear -45° polarized light; (e) represents left circularly polarized light, and rotates counter-clockwise when propagating toward the observer; finally (f) represents right circularly polarized light, and rotates clockwise when propagating toward the observer. The signs of the Stokes parameters are determined by the helicity and the orientation of the semi-major axis of the polarization ellipse. Source: <https://en.wikipedia.org/wiki/File:StokesParameters.png>.

An example of E - and B -mode patterns of polarization is shown in Figure 1.3. The full polarization pattern is a random superposition of these plane-wave modulated patterns.

For completeness, being the E - B decomposition a linear transformation of the Q - U field on the sky, and being this transformation invertible, it is always possible to transform Q and U polarized emission maps in E -mode and B -mode maps, and vice-versa, through position dependent rotations in Fourier space⁷. Introducing the angle $\Psi = \arctan \frac{k_x}{k_y}$, where k_x and k_y are the wave numbers, the relations between E - B and Q - U are given by:

$$\begin{cases} \tilde{Q} = \tilde{E} \cos 2\Psi - \tilde{B} \sin 2\Psi \\ \tilde{U} = \tilde{E} \sin 2\Psi + \tilde{B} \cos 2\Psi \end{cases} \quad (1.3)$$

⁷The Fourier space (or frequency domain) is a space into which the Fourier transform maps a function, consisting of the amplitude and phase of the sine function at various frequencies that sum to produce the same shape. The Fourier space is a domain where it is easier to understand concepts and make calculations, since it offers more means of manipulation and analysis. For example, in this E - B and Q - U transformation, the convolution operation becomes a multiplication (Zaldarriaga, 2001)

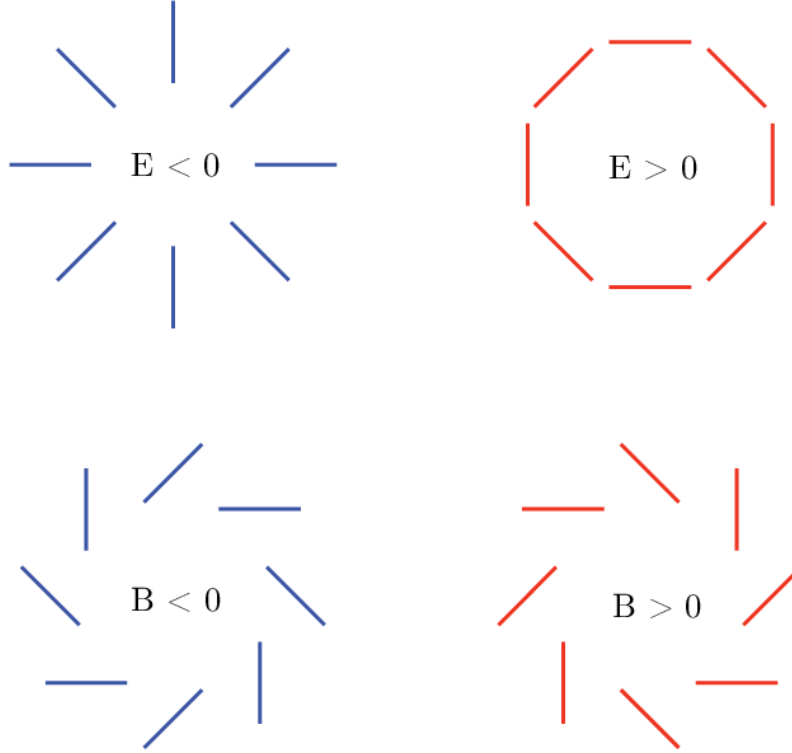


Figure 1.3: An example of E and B -mode patterns of polarization (Baumann et al., 2009).

$$\begin{cases} \tilde{E} = \tilde{Q}\cos 2\Psi + \tilde{U}\sin 2\Psi \\ \tilde{B} = -\tilde{Q}\sin 2\Psi + \tilde{U}\cos 2\Psi \end{cases}, \quad (1.4)$$

where \tilde{Q} , \tilde{U} , \tilde{E} and \tilde{B} are quantities in Fourier space. The sign convention is chosen so that positive values of E generate a tangential pattern of polarization (Zaldarriaga, 2001).

1.2.1 Synchrotron emission

Accelerated charged particles always emit electromagnetic radiation, as a direct consequence of Maxwell's laws.

Considering charged particles moving at relativistic speeds in a magnetic field, they undergo an acceleration perpendicular to their direction of motion, and the radiation they emit is known as synchrotron radiation. The force due to the field is always perpendicular to both the direction of the field and to the direction of the motion, as expressed by the Lorenz's law. When the radiation is emitted by a particle moving in a plane, when observed in that plane, the emitted radiation is linearly polarized, as is shown in Figure 1.4.

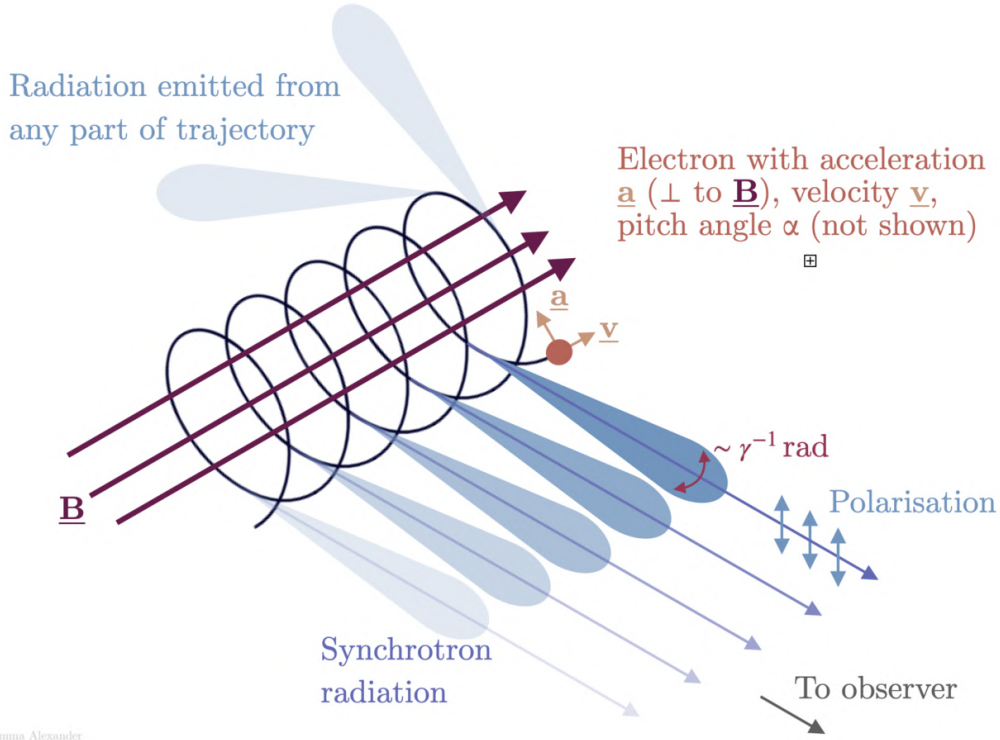


Figure 1.4: Representation of the synchrotron emission mechanism, originating by an electron moving around an ordered magnetic field, following a helical path. The acceleration \underline{a} is perpendicular to the magnetic field vector \underline{B} , and both are perpendicular to the circular component of the electron's velocity \underline{v} , as consequence of the Lorentz's law. The radiation is concentrated in a beam width of $\sim 1/\gamma$ radians, where γ is the Lorentz factor. The Lorentz factor is defined as $\gamma = 1/\sqrt{1 - \frac{v^2}{c^2}}$, where v is the relative velocity between inertial reference frames, and c is the speed of light in vacuum. Source: <https://emmaalexander.github.io/resources.html>.

The synchrotron emission arises primarily from cosmic-rays electrons accelerated by the Galactic magnetic field and spiraling around its lines. This radiation dominates the radio sky in polarization at frequencies below ~ 70 GHz, and it is linearly polarized when observed in the plane in which the particle moves, with a microwave polarization fraction observed to be of a few percent in the Galactic plane and typically up to 15% or greater at intermediate and high Galactic latitudes (Planck Collaboration XXV, 2016; Page et al., 2007), since the distribution of cosmic-rays electrons may extend to large Galactic scale heights (Hensley et al., 2022).

A power-law Spectral Energy Distribution (SED) of the cosmic-ray electrons produces a synchrotron SED that is also a power law, brighter at low frequencies and faint at higher frequencies, in this thesis described in one of Stokes Q and U parameter in brightness temperature units.

The polarized synchrotron SED in each pixel is described by this parametric form:

$$S_{\nu,s}^{[QU]} = A_s^{[QU]} \left(\frac{\nu}{\nu_{0,s}} \right)^{\beta_s}, \quad (1.5)$$

where $S_{\nu,s}^{[QU]}$ is one of Stokes Q or U in brightness temperature units (e.g., μK_{RJ}); A_s is the amplitude parameter; β_s is the emission spectral index; and $\nu_{0,s}$ is an arbitrary reference frequency.

In general, the arbitrary reference frequency is chosen in correspondence with a frequency range where the emission is dominant, typically is taken to be equal to 23 GHz.

Radio observations of Galactic synchrotron emission over large sky areas have provided evidence for a spectral index non-constant throughout the Galaxy, and a trend has been observed: regions in the Galactic plane show a shallower spectrum than those located at higher latitudes (e.g., [Lawson et al., 1987](#)). However, in the GHz frequency range, the presence of other emission mechanisms complicates the analysis of total intensity data, making interpretation difficult ([Hensley et al., 2022](#)).

In last years, constraints on synchrotron spectral parameters have been obtained in polarized intensity as well, thanks to the availability of ground-based surveys of synchrotron polarization, such as: the S-band Polarization All-Sky Survey (S-PASS) experiment, a 2.3 GHz survey of the Southern Sky (Dec. $< -1^\circ$) in polarization ([Carretti et al., 2019](#)); the C-band All-Sky Survey (C-BASS) experiment, an on-going full sky polarimetric survey at 5 GHz ([Jones et al., 2018](#)), and the Q, U, I Joint Experiment in Tenerife (QUI-JOTE; [Cepeda-Arroita et al., 2021](#)), in addition to full-sky measurements from *Planck* and WMAP ([Hensley et al., 2022](#)).

These analyses have suggested that the power-law index of polarized synchrotron emission, though a certain level of variation has been observed ([Planck Collaboration XXV, 2016](#); [Krachmalnicoff et al., 2018](#); [Fuskeland et al., 2021](#)), it is fairly uniform over a large part of the sky ([Dunkley et al., 2009](#); [Svalheim et al., 2020](#)). For example, [Krachmalnicoff et al. \(2018\)](#), by combining S-PASS with WMAP and *Planck* data, reported a mean value of synchrotron spectral index equal to $\beta_s \sim -3.2$, with spatial variability of the order of a few percent in the frequency range 2.3 and 33 GHz ([Hensley et al., 2022](#)).

Therefore, at current sensitivities, the simple parametrization referring to Equation 1.5, with a constant spectral index β_s , provide a good description at both map level and power spectrum level, and it has proven effective at modeling synchrotron emission also in CMB analyses, even when utilizing data with as low frequency as the 408 MHz Haslam map ([Planck Collaboration X, 2016](#)).

The synchrotron emission is important since it contain information about the underlying emission physics, such as the properties of Galactic cosmic-rays electrons, and more in general, where there are relativistic electrons, allowing a probing of the structure and physics of the magnetic interstellar medium (ISM) of our Galaxy.

Since the direction of linear polarization of the synchrotron emission is set by the orientation of the local magnetic field, its measurements can be used to infer the Galactic magnetic field.

A visualization of Galactic magnetic field lines traced by synchrotron radiation at 30 GHz, as detected by ESA’s *Planck* satellite over the entire sky, is shown in Figure 1.5.

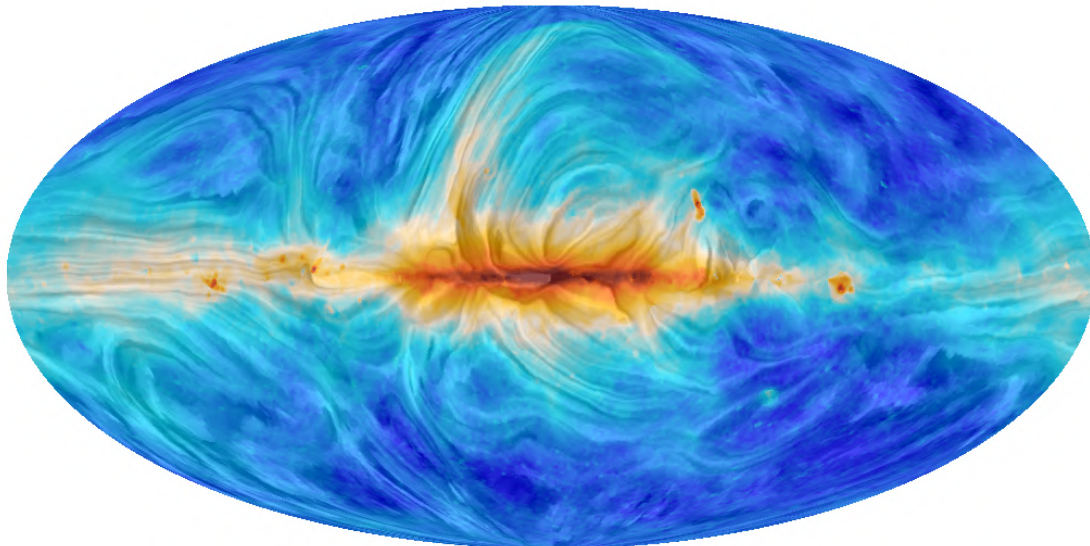


Figure 1.5: All-sky view of the polarization angle at 30 GHz, rotated by 90 deg to indicate the direction of the Galactic magnetic field projected on the plane of the sky. The colour scale represents the total intensity, dominated at this frequency by synchrotron emission. The “drapery” pattern was obtained by applying the line integral convolution (LIC; Cabral & Leedom, 1993) procedure using an IDL implementation provided by Diego Falceta-Gonçalves (<http://each.uspnet.usp.br/fgoncalves/pros/lic.pro>). This gives an effective way of visualizing regions where the field is coherent, but where the field varies significantly along the line of sight, the orientation pattern is irregular and difficult to interpret (Planck Collaboration X, 2016).

1.2.2 Emission from interstellar dust

Dust is an ubiquitous feature of the Cosmos, a minor but crucial component of the interstellar medium (ISM), about 1% of its mass, that pervades space in the Milky Way and other galaxies, playing a central role in the astrophysics of the ISM: from the star formation dynamics to the chemistry and thermodynamics of the gas (Draine, 2003). Interstellar dust grains are heated by the absorption of the interstellar radiation field (ISRF), the near-infrared radiation, visible and the ambient ultraviolet (UV) produced by stars in the Galaxy (Planck Collaboration et al., 2020a). The grains cool via thermal emission, which is in the far-infrared/sub-millimetre, as determined by the equilibrium temperature corresponding to a balance between absorbed and emitted power, observed to be of order of $T_d \sim 20$ K (Planck Collaboration XI, 2014; Planck Collaboration Int. XXII, 2015) for the ISRF found in the bulk of the ISM (Planck Collaboration et al., 2020a).

It was estimated that about 30%, or more, of the energy emitted as starlight in the Universe is re-radiated by dust in the infrared (Bernstein et al., 2002; Draine, 2003). While energy is radiated in the infrared, there is a wavelength-dependence of its attenuation, often referred to as “reddening”, because of the tendency for the extinction to be greater in the blue than in the red wavelengths (Draine, 2003). Therefore, dust shapes the galaxies spectra, determining what galaxies look like.

Dust is a general name for microscopic bits of matter (“grains”), solid particles with a sub-micron size that are irregularly-shaped, with porosity ranging from fluffy to compact (Mathis et al., 1977). However, there is no discontinuity in the physics as the particle size decreases from microns to Angstroms, and the term “dust grain” could be understood to extend down to molecules containing tens of atoms (Draine, 2003). Dust it is made of thin, highly flattened flakes of graphite (carbon) and/or silicates (rock-like minerals), often coated with water ice, especially in dense clouds (Draine, 2003). The meaning of this ambiguous conjunction (and/or) will be clarified in Subsection 1.2.3, but it is well-established that interstellar dust is composed of both carbonaceous and silicate materials on account of spectroscopic features in extinction, scattering, or emission associated with these materials, which provide direct information on the composition of interstellar dust (Draine, 2003).

Strong extinction features at 9.7 and 18 μm attest to the abundance of amorphous silicates, while extinction features at 2175 \AA , the center of the the broad “bump” in the extinction curve, 3.4 μm , 6.85 μm , and 7.25 μm , as well as a number of mid-infrared emission features, require a substantial amount of carbonaceous dust in both aromatic and aliphatic forms (Hensley & Draine, 2020; Hensley & Draine, 2021).

Depending on the grain populations, dust comes in a whole range of sizes, whose distributions peak around $\sim 0.1 \mu\text{m}$, with limits up to an order of magnitude more or two orders of magnitude less (Draine, 2003). For illustrative purpose, without claiming to consider it representative of interstellar grains, in Figure 1.6 is shown an interplanetary dust particle, as example of fluffy dust aggregates, with a size of about $\sim 10 \mu\text{m}$.

The polarized emission from interstellar dust grains originates mainly in the Galactic disk while, at high latitudes, from gas within a few hundred parsecs of the solar neighborhood (e.g., Alves et al., 2018; Skalidis & Pelgrims, 2019).

Interstellar clouds of gas and dust are also threaded by the Galactic magnetic field, and dust grains tend to align their longest axis perpendicular to the direction of the field (Ferrière, K., 2009; Ferrière, 2015; Planck Collaboration X, 2016), as it is schematized in Figure 1.7.

This mechanism is well explained by the Radiative Alignment Torque (RAT) theory, which provides a powerful paradigm for grain alignment. Whether the grain alignment happens in respect to the magnetic field (B -RATs) or in respect to radiation (k -RATs) depends mostly on the radiation intensity, the Galactic magnetic field strength and the grain magnetic properties (Lazarian & Hoang, 2019).

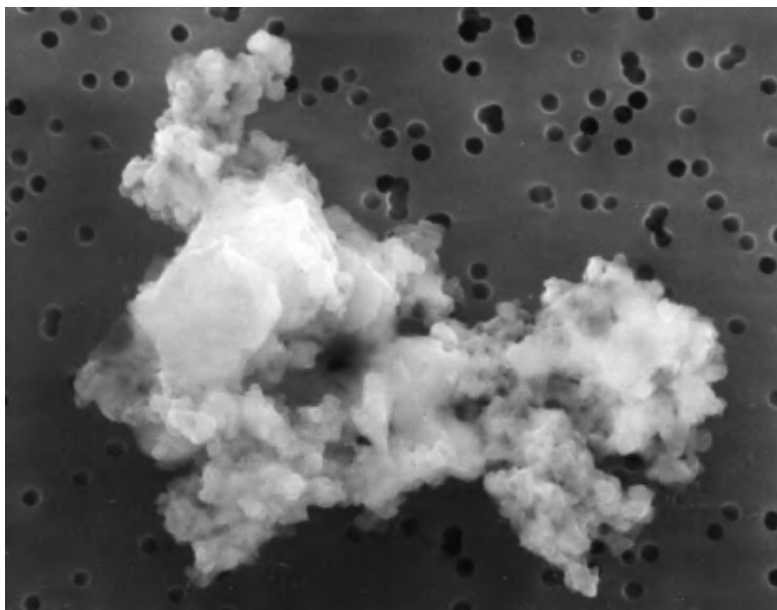


Figure 1.6: *Scanning electron microscope image of an interplanetary dust particle, with a size of about $\sim 10 \mu\text{m}$ (in its largest dimension). It represents an example of fluffy dust aggregates: large conglomerates of small dust grains, with lots of empty space in the structure. It was collected with an airborne experiment in the Earth’s stratosphere. Credit to: NASA/JPL.*

However, under this paradigm, the linearly polarized light emitted by dust grains can be used to probe both the Galactic magnetic fields, the ISM environments and the dust grain characteristics (Andersson et al., 2015; Lazarian & Hoang, 2019).

Initially, an external radiation field, with wavelength λ , impart torques to irregular grains, with diameter d , when $\lambda < d$, triggering them and make them spin around a random axis. Then, individual grains which align their rotation with one of their “principal axes”, gain an angular momentum \vec{L} (Andersson et al., 2015; Lazarian & Hoang, 2019). If grains are paramagnetic, they tend also to gain a magnetic momentum \vec{M} , parallel to the axis of spin. This is because of the so-called “Barnett Effect”, which says that an uncharged body rotating with angular velocity $\vec{\omega}$ on its axis, tends to spontaneously magnetize while conserving angular momentum⁸. Then, these grains aligns their magnetic moment with the external magnetic field (\vec{B}) and so, at the end, $\vec{\omega} \parallel \vec{L} \parallel \vec{M} \parallel \vec{B}$ (Dolginov, 1990; Andersson et al., 2015; Lazarian & Hoang, 2019).

If grains are diamagnetic, do not magnetize, and so are not susceptible to the alignment with the Galactic magnetic field, but they can align along the radiation direction (Andersson et al., 2015; Lazarian & Hoang, 2019). Also if the radiation field is strong and anisotropic, the alignment is along the radiation, and this mechanism is more efficient for larger grains (Andersson et al., 2015; Lazarian & Hoang, 2019).

⁸If a grain rotates around a non-symmetry axis and nutates, thus changing the direction of rotation, it happens that nutation is often faster than the equilibrium time for the Barnett effect.

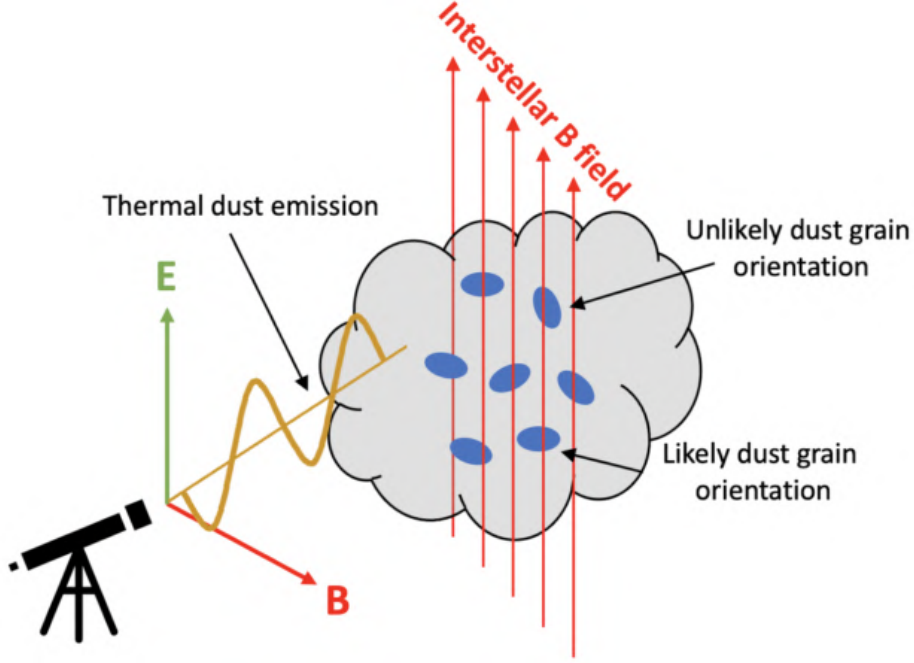


Figure 1.7: A schematic representation which demonstrates how a local magnetic field influences the likely orientation of dust grains, which emit a linearly polarized emission. Source: <https://astrobites.org/2021/08/07/magnetic-menagerie/>.

Recent analyses of polarized dust emission have found that the frequency dependence of polarized dust emission at millimeter wavelengths is well-fit by a modified blackbody (MBB), having an opacity law scaling as ν^{β_d} , with a spectral index $\beta_d \simeq 1.5$ (Planck Collaboration X, 2016; Planck Collaboration et al., 2020b). Therefore, dust emission peak at higher frequencies than the CMB, thus becoming dominant at frequencies higher than ~ 70 GHz.

The polarized dust SED is described by this parametric form:

$$S_{\nu,d}^{[QU]} = A_d^{[QU]} \left(\frac{\nu}{\nu_{0,d}} \right)^{\beta_d-2} \frac{B_\nu(T_d)}{B_{\nu_{0,d}}(T_d)}, \quad (1.6)$$

where $S_{\nu,d}$ is one of Stokes Q or U in brightness temperature units (e.g., μK_{RJ}); A_d is the amplitude parameter; $B_\nu(T)$ is the Planck function; T_d is the dust temperature; and $\nu_{0,d}$ is an arbitrary reference frequency.

At current sensitivities, this simple parametrization provides a good description at both map level and power spectrum level, and it has proven effective at modeling dust emission also in CMB analyses (Hensley et al., 2022).

In general, the arbitrary reference frequency is chosen in correspondence with a frequency range where the emission is dominant, typically is taken to be equal to 353 GHz.

The same values of T_d and β_d are found for both temperature and polarization to within measurement uncertainties (Planck Collaboration et al., 2020b), but as far as the spectral index is concerned, all related scientific questions still open will be dealt with in Subsection 1.2.3.

The dust emission is important since it contains astrophysical information, revealing information about the underlying emission physics, such as tests of single vs multi-component dust models, which will be detailed in Subsection 1.2.3. More in general, its observations allow a probing of the structure and physics of the magnetic interstellar medium (ISM) of our Galaxy, as: the Galactic magnetic field, star formation, and the chemical composition of our Galaxy.

Regarding the Galactic magnetic field, since the direction of linear polarization of dust emission is set by the orientation of the local magnetic field, the same as for the synchrotron (suggesting that synchrotron and dust emissions have to be correlated to some extent), also dust measurements can be used to infer the Galactic magnetic field. About this topic, the difference in the ISM phases that can be traced by dust emission vs synchrotron emission will be discussed in Section 1.2.3.

The *Planck* collaboration used the polarised emission of interstellar dust to reconstruct the Galaxy’s magnetic field and study its role in the build-up of structure in the Milky Way, leading to star formation (Planck Collaboration X, 2016). A visualization of Galactic magnetic field lines traced by dust radiation at 353 GHz, as detected by ESA’s *Planck* satellite over the entire sky, is shown in Figure 1.8.

The role of dust in star formation is related to the fact that it is an important tracer of star formation. In fact, star formation takes place in molecular clouds, which are cold and giant condensations of dust and molecular gas, threaded by magnetic fields inherited from the ISM out of which they condensed, and which influence cloud’s morphology and evolution. Since dust grains increase the molecular formation rate by two orders of magnitude compared to the case without dust (e.g., Hollenbach & McKee, 1979), the ISM is cooled efficiently by molecules and dust (Asano et al., 2012).

Considering the role played by dust in allowing a probing of the structure and physics of the magnetic interstellar medium (ISM) of our Galaxy, we have to talk about the chemical composition of our Galaxy.

Dust grains provide a “catalytic” surface for the formation of molecules, where simple molecules can react to form bigger more complex molecules: the surfaces of dust grains operate as tiny chemical factories, as they manage to bring together atoms catalyzing their reactions which, otherwise, could only rarely meet (Potapov et al., 2019). This happens also because the presence of the external ice layer, since it is full of chemical diversity, and photons and cosmic-rays help drive ice chemistry (Meinert et al., 2011). For example, considering the conditions present in molecular clouds, it is quite rare that a H_2 molecule is formed through the collision of two hydrogen atoms.

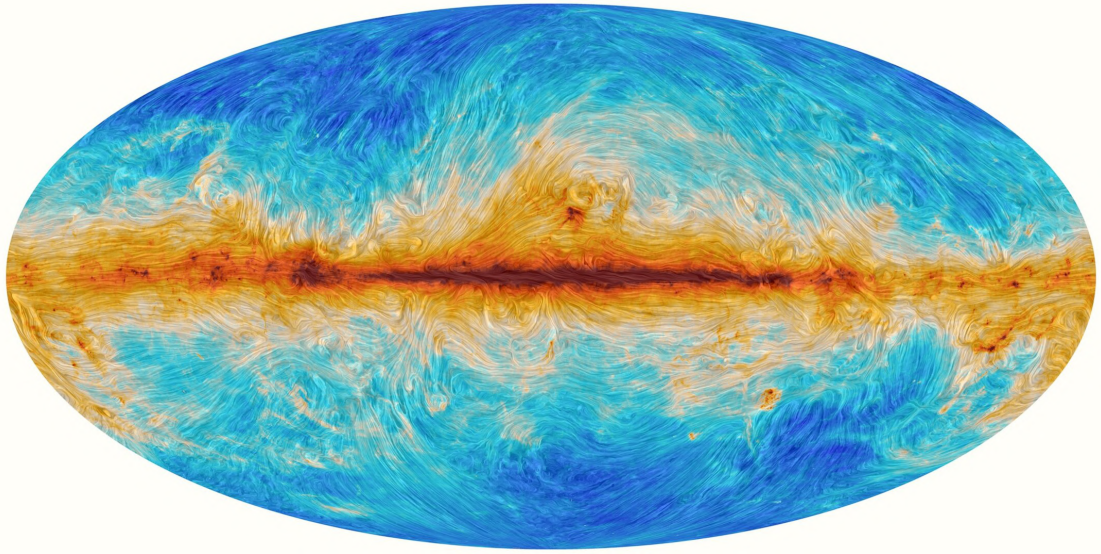


Figure 1.8: All-sky view of the angle of polarization at 353 GHz, rotated by 90 deg to indicate the direction of the Galactic magnetic field projected on the plane of the sky. The colour scale represents the total intensity, dominated at this frequency by thermal dust emission. The “drapery” pattern was obtained by applying the line integral convolution (LIC; Cabral & Leedom, 1993) using an IDL implementation provided by Diego Falceta-Goncalves (<http://each.uspnet.usp.br/fgoncalves/pros/lic.pro>). Where the field varies significantly along the line of sight, the orientation pattern is irregular and difficult to interpret (Planck Collaboration X, 2016).

However, if atoms are attached to the surface of a dust grain, which is able to absorb the collision excess energy, H_2 molecules are able to form (Gavilan et al., 2012; Wakelam et al., 2017). An illustration is shown in Figure 1.9.

Moreover, dust act as a shield: blocking the interstellar radiation field from heating the gas within molecular clouds, it protect molecules that have already formed from being destroyed, so having an important role for molecule formation.

To conclude, it is important to highlight that dust emission, as well as synchrotron emission, is intrinsically polarized. In addition, it is possible to transform unpolarized light ($Q = U = V = 0$) into polarized light through a variety of methods, such as by reflection, by refraction, by scattering and by transmission. The latter method, for example, can be induced through the use of a polarizing filter, as shown schematically in Figure 1.10.

A typical example is provided by the unpolarized light of stars which transforms into polarized light. In fact, dust grains in the ISM, which in themselves emit a polarized emission, act as polarizing filters for the optical emission, as will be better described in Section 3.1, being this effect the basis of the analysis I carried out described in Chapter 3.

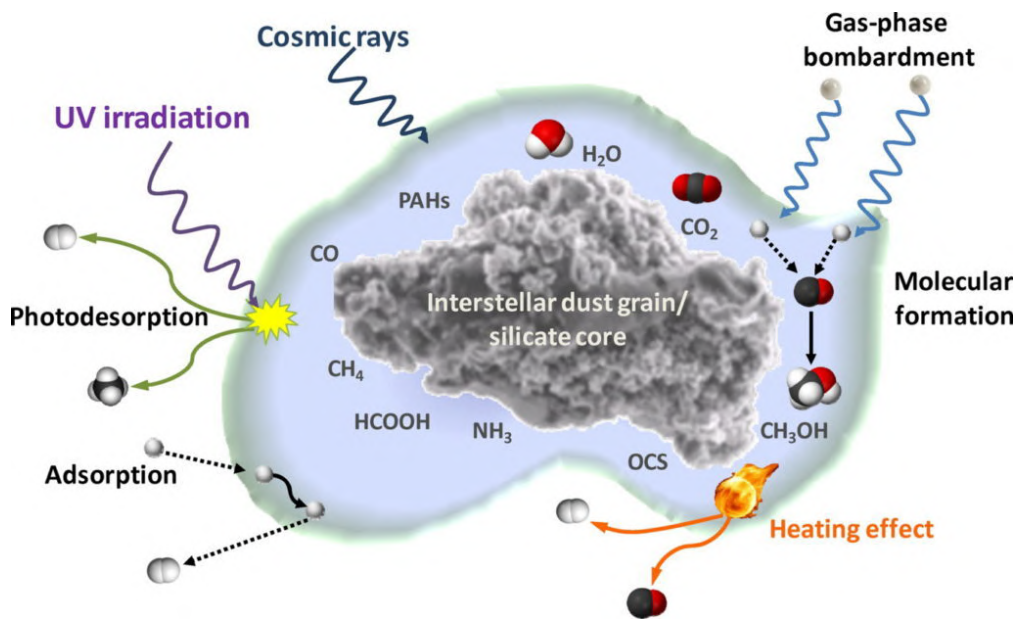


Figure 1.9: An interstellar dust grain is a chemical factory, where simple molecules can react to form bigger more complex molecules. Note that the ice layer is full of chemical diversity, and photons and cosmic rays help drive ice chemistry (Meinert et al., 2011).

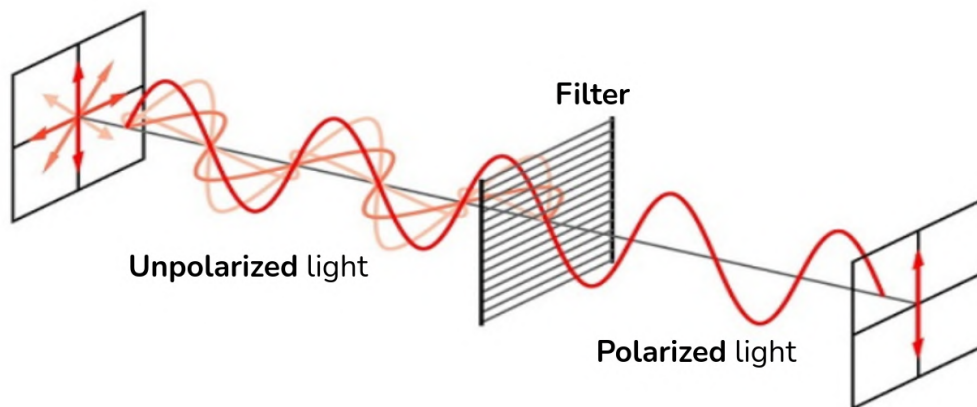


Figure 1.10: A wire-grid polarizer converts an unpolarized incident beam, with oscillations along all directions, into one with oscillations only along one direction, so a single linear polarization. Coloured arrows depict the electric field vector. Only the vertical components of the diagonally polarized waves are transmitted and contribute to the transmitted polarization. The horizontal components, instead, are absorbed and reflected (not shown in the drawing). Source: en.wikipedia.org/wiki/Polarizer.

1.2.3 Open questions

Regarding the polarized Galactic emissions, there are three main open questions. The first is referred to the fact that the idealization of the synchrotron SED as a power law is expected to break down in detail.

The cosmic-rays electron energy distribution is likely to have a high energy cut-off resulting, at sufficiently high frequency, in an exponential fall-off in the synchrotron spectrum (Hensley et al., 2022). The spectrum steepens as the electrons lose energy via radiation, thus making the synchrotron spectral index a probe of the time since injection (e.g., Lisenfeld & Voelk, 1999).

A further complexity is that multiple synchrotron emitting regions along the line of sight may have different slopes of the energy distribution. The integrated emission will not be a power law, although the SED of each emitting region may be (Hensley et al., 2022). These effects motivate a search for curvature of the spectral index in the synchrotron spectrum, and some suggestions of curvature in the synchrotron spectrum have been reported in total intensity analyses of radio data combined with WMAP (Dickinson et al., 2009; Kogut, 2012). The forecast analysis I did and presented in Chapter 2, concerns new constraints I found on the curvature parameter, using SO simulated observations. With the addition of a curvature parameter, the polarized synchrotron SED is described by the parametric form:

$$S_{\nu,s} = A_s \left(\frac{\nu}{\nu_{0,s}} \right)^{\beta_s + s_{run} \log(\nu/\nu_{0,s})}, \quad (1.7)$$

where s_{run} is the curvature parameter.

The second open question presented here concerns the dust modeling. Historically, as Hensley et al. (2022) mentions, most physical dust models have posited separate populations of carbonaceous and silicate grains (e.g., Mathis et al., 1977; Draine & Lee, 1984; Zubko et al., 2004; Siebenmorgen et al., 2014; Jones et al., 2017; Guillet et al., 2018). After understanding through spectral features that both materials are dust constituents, a natural explanation for the different polarization properties observed in carbonaceous and silicate materials, was that the carbonaceous and silicate materials reside on separate grains⁹. In this picture, the silicate grains are able to achieve rapid alignment with the interstellar magnetic field, perhaps on account of enhanced paramagnetic character (e.g., Hoang & Lazarian, 2016), while the carbonaceous grains are not. And so, basically, being made of different materials, the grains have distinct opacity laws (i.e., different β_d) and come to different temperatures, even when exposed to the same radiation field (Hensley et al., 2022).

Therefore, even if pre-*Planck* models anticipated significant differences in the dust SED in polarization vs total intensity (Draine & Fraisse, 2009), these have not been observed. For example, balloon-borne observations from BLASTPol extending to submillimeter wavelengths (see Section 4.2), likewise found consistency between the dust SED in total intensity and polarization, with deviations not exceeding $\sim 10\%$ (Ashton et al., 2018; Planck Collaboration et al., 2020b).

⁹The origin of distinct populations can potentially be traced to the stellar outflows in which the grains condense—oxygen-rich outflows yield CO with the leftover O forming silicate grains whereas carbon-rich outflows yield CO with the leftover C forming carbonaceous grains.

Only in the last few years, some dust models consistent with *Planck* and BLASTPol observations have been proposed.

Concerning models based on separate dust populations, [Guillet et al. \(2018\)](#) presented a series of four models with both highly elongated (3 : 1) silicates and carbonaceous grains. These models are consistent with the observed frequency independence of the dust polarization fraction at the $\sim 10\%$ level, but with distinct variations at the few percent level ([Hensley et al., 2022](#)).

In contrast, a single-component model named “astrodust”, based on a single homogeneous grain type, has been proposed by [Draine & Hensley \(2021\)](#). This model predicts an approximately polarization fraction across microwave and submillimeter frequencies, deviating from this behavior only at THz frequencies ([Hensley et al., 2022](#)).

The models of [Guillet et al. \(2018\)](#) and [Draine & Hensley \(2021\)](#), as well as two-versus one-component models more broadly, can be tested through differences in the dust frequency spectrum in total intensity vis-a-vis polarization, through the parameter $\Delta\beta = \beta_P - \beta_I$ ([Hensley et al., 2022](#)). In fact, single-component models predict small but nonzero $\Delta\beta$, with $\beta_I \simeq \beta_P$, while two-components models typically predict large $\Delta\beta$ ([Draine & Hensley, 2021](#)).

The question is still open although, according to the latest results of [Planck Collaboration et al. \(2020b\)](#), which found $\beta_I = 1.48$ in total intensity and $\beta_P = 1.53 \pm 0.03$ in polarized intensity, with a $\Delta\beta = 0.05 \pm 0.03$, it would seem that single-component models remain viable and perhaps favored. This open question is taken into consideration in the forecast analysis I did and presented in Chapter 2, where I demonstrated how the Simons Observatory experiment will be able to improve the current constraints on the spectral index of polarized dust emission.

Finally, the third open question refers to the difference in the ISM phases probed by polarized dust and synchrotron emissions.

Considering that the distribution of cosmic-rays electrons may extend to large Galactic scale heights, while in contrast the distribution of dust grains arises largely from the Galactic disk and, at high latitudes, from gas within a few hundred parsecs of the Solar neighborhood, it remains unclear to what extent the synchrotron and dust polarizations signals probe different phases of the ISM and different regions of the Galaxy ([Hensley et al., 2022](#)).

Therefore, even if we expect the polarized synchrotron and dust emission to be correlated to some extent because the direction of linear polarization for both emission mechanisms is set by the orientation of the local magnetic field, this correlation may change qualitatively depending upon region of the sky and angular scale probed. Also this kind of open question is taken into consideration in the forecast analysis I did and presented in Chapter 2, since I used SO simulated data to obtain improved constraints on the parameter governing the synchrotron and dust correlation.

1.2.4 Polarized Galactic emissions as CMB foreground

When we talk about foregrounds, we mean the diffuse late-time, low-redshift components throughout the sky. We need a deep understanding of their distinct emission mechanisms to measure the CMB, both in intensity and polarization, since we live in a galaxy and we are surrounded by very diffuse matter that emits microwaves.

This is the territory of components separation, which aims to remove diffuse Galactic foreground contamination.

In case of total intensity signal, there are a number of components of great relevance in addition to dust and synchrotron emissions, such as the Cosmic Infrared Background (CIB) emission, the free-free emission from accelerated electrons in the ionized gas, the Anomalous Microwave Emission (AME), and the CO emission, which have not yet been detected in polarization, and they are believed to be largely unpolarized (e.g., [Planck Collaboration IV, 2020](#), and references therein). Therefore, the component separation problem is greatly simplified in polarization relative to total intensity, since the polarized foregrounds consist only of dust and synchrotron emissions.

However, a major challenge for all experiments dedicated to the polarized CMB study, which aim to observe the signal produced by the weak primordial B -modes, is that there is no frequency or region in the sky where polarized foregrounds are proved to be subdominant with respect to CMB B -modes, as was shown by the sky reconstruction of the synchrotron component obtained from WMAP and *Planck* data, explicitly targeting angular scales of $\sim 1^\circ$ ([Planck Collaboration Int. XXX, 2016](#); [Krachmalnicoff et al., 2016](#)). The Galactic foregrounds SEDs in intensity and polarization are shown in [Figure 1.11](#).

Since the detection of CMB polarization anisotropies has become a major goal in cosmology, many groups of scientists are involved in the effort to build experiments to perform high-sensitivity observations in polarization, including future dedicated satellite missions.

For achieving the promise of the next generation of CMB polarization experiments, which constitute the next frontier of experimental cosmology, even if the actual SEDs parametrization has proven effective at modeling these emission also in CMB analyses, i.e. power-law for the synchrotron and modified blackbody for the dust, it remains critical to characterize the polarized Galactic foregrounds. For example, the introduction of curvature in the synchrotron SED, as described in [Subsection 1.2.3](#), can complicate removal of polarized synchrotron emission as a CMB foreground.

To conclude, it is necessary to have a deep knowledge of the properties of foreground emissions and to understand the underlying emission physics. My PhD thesis work fits exactly into this context, as it is described in [Section 1.3](#).

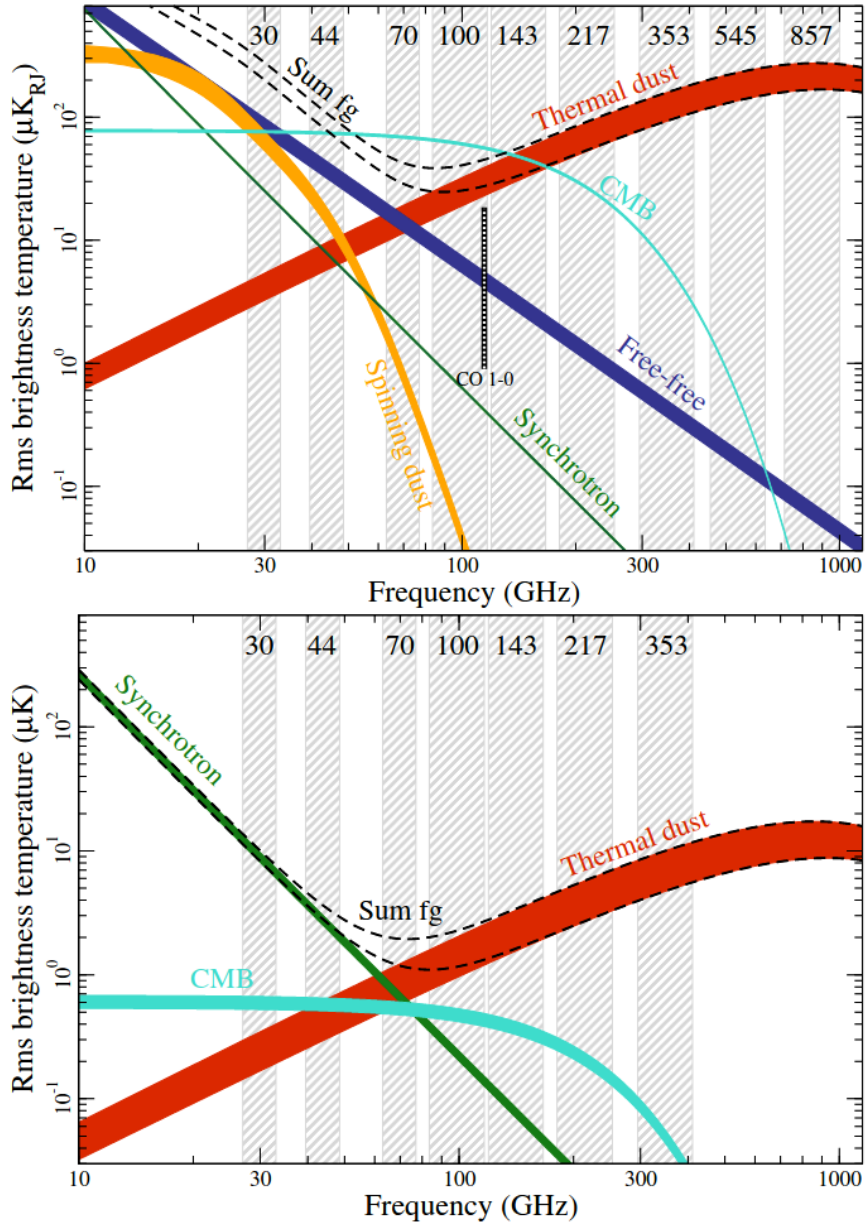


Figure 1.11: *Brightness temperature rms as a function of frequency and astrophysical component for temperature (top) and polarization (bottom), evaluated with COMMANDER software. For temperature, each component is smoothed to an angular resolution of 1 deg FWHM, and the lower and upper edges of each line are defined by masks covering 81 and 93% of the sky, respectively. For polarization, the corresponding smoothing scale is 40', and the sky fractions are 73 and 93%. We note that foreground rms values decrease nearly monotonically with sky fraction, whereas the CMB rms is independent of sky fraction, up to random variations. For reference, zodiacal light emission is roughly two orders of magnitude weaker than thermal dust emission in temperature (Planck Collaboration X, 2016).*

1.3 Main contributions of my PhD thesis work and its structure

My PhD project developed around the subject of Galactic polarized foregrounds. These diffuse components across the whole sky, are synchrotron and dust thermal emission, which dominate at different and complementary frequencies. My intent was to characterize them at several levels, also focusing on their role of contaminant for CMB B -modes measurements. In fact, in order to obtain pure CMB measurements, we need a deep understanding of their distinct emission mechanisms.

An overview of what I did can be summarized in these points:

- In the context of modeling of polarized Galactic foregrounds, I contributed to the research topic by forecasting new constraints on the spectral models parameters for current and upcoming polarized microwave experiments, among which the Simons Observatory (SO) experiment. SO is ground-based telescope under construction in the Chilean Desert, which will carry out its first observations between the end of this year and the beginning of next year. As junior member of the collaboration, I collaborated with the Galactic Science working group.

I am the recognized leader¹⁰ of the power spectrum analysis of multi-frequency Galactic emission, published in the SO Galactic Science paper (Hensley et al., 2022). I forecasted the ability of SO to improve constraints of synchrotron and dust spectral parameters in the harmonic domain, using a set of frequencies from various experiments, i.e. S-PASS, C-BASS, WMAP and *Planck*, with channels from 2.3 up to 353 GHz. I made a fitting of the SED models, using an MCMC method, to simulated auto- and cross-angular power spectra at different frequency channels and angular scales, including the relative noise figures, for E - and B -modes separately, starting from map-level simulations.

I quantified the effect of the addition of SO data to existing measurements in test models of Galactic emission finding new improved constraints on all spectral parameters, in particular including: the energetics of synchrotron emission, constraining the curvature of the synchrotron spectral index with an improvement of a factor of two level relative to current constraints; the composition of interstellar dust, constraining the frequency spectral index of polarized dust, β_d , with an improvement of a factor of two level relative to current constraints, achieving $\sigma(\beta_d) < 0.01$, and so enabling detailed tests of one- versus two-component dust models; finally, the nature of the observed spatial correlation between dust and synchrotron emission, constraining the correlation parameter with an improvement of a factor of two greater precision than is possible with current data.

This analysis is presented in Chapter 2.

¹⁰A supplement describing author contributions to this paper can be found at https://simonsobservatory.org/wp-content/uploads/2022/02/SO_GS_Contributions.pdf

- In the context of polarized dust characterization, I contributed to the research topic by presenting an updated quantitative validation of the correlation between starlight polarization and polarized dust emission in the diffuse ISM at high-Galactic latitude, being a powerful probe to disentangle several effects measurable at both frequency ranges, since both dust emission and extinction are affected by the grain shape, the grain alignment efficiency and the magnetic field orientation. I performed a novel analysis to extend existing results of [Planck Collaboration et al. \(2020b\)](#) based on the PR3 *Planck* 353 GHz emission channel, using the last data release (PR4, [Planck Collaboration Int. LVII, 2020](#)) and going to smaller frequencies down to 143 GHz.

Even if the SNR is lower for dust polarized emission at smaller frequencies, I wanted to explore the robustness of the theoretical predictions on the comparison between polarized emission and starlight polarization data even at lower frequencies, where dust is still dominant. I obtained new original experimental estimates of the emission-to-extinction polarization ratio, a diagnostic involving dust emission and extinction for the aligned grains population, consistent with those predicted by dust models.

Using existing stellar catalogues of Berdyugin series ([Berdyugin et al., 2001](#); [Berdyugin & Teerikorpi, 2001](#); [Berdyugin, A. & Teerikorpi, P., 2002](#); [Berdyugin et al., 2004](#); [Berdyugin, A. et al., 2014](#)), [Green et al. \(2018\)](#) reddening estimates, and Gaia DR2 distances ([Bailer-Jones et al., 2018](#)), I built a stellar sample of 1693 stars. To handle with emission data, I implemented the photometric aperture method, which allowed me to explore the polarization ratio behavior using different radius choices centered on each star. In correspondence with minima of residuals with respect to the expected values, obtained in the function describing the trend of the polarization ratios with respect to the aperture radii, I found the optimal aperture radius at which compute the polarization ratios estimates for all three frequency channels considered: 353 GHz, 217 GHz and 143 GHz. Then, I found new estimates of the emission-to-extinction polarization ratios through a joint correlation of the Stokes parameters pair in emission, (Q, U) , with the Stokes parameters pair in extinction, (q_V, u_V) , at the three frequency channels.

This project was designed in collaboration with the Galactic Science working group of the Atacama Cosmology Telescope (ACT) collaboration, of which I am a junior member. ACT is a high-resolution ground-based telescope in the Chilean Desert, already active since 2007 and arrived at its latest data collection. My intention is to exploit the higher resolution of new ACT data to inspect the robustness of the emission-to-extinction polarization ratio, observing dust behavior at smaller scales. I will publish all these results as first author in a paper in preparation titled “New starlight polarization analysis with ACT and *Planck* data”.

This analysis is presented in Chapter 3.

- In the context of the observational strategy definition for an IR polarimetry balloon experiment, I contributed to the topic by planning the diffuse ISM polarization observation strategy for the Balloon-borne Large Aperture Submillimeter Telescope

(BLAST) experiment. BLAST boasts a long series of experiments starting since 2003, and as junior member of the collaboration, I collaborated with the Science team of both BLAST-TNG (The Next Generation), launched from Antarctica during last campaign in January 2020, and the NASA proposal BLAST Observatory, its successor, which is expected to launch in 2028 from New Zealand.

I developed and implemented an algorithm to identify some ISM fields to be observed in order to characterize the diffuse dust emission and suitable for study the dust as a CMB foreground: I look for regions of the sky (“patches”) with features similar to the ones of diffuse, low-intensity and highly-polarized dust regions. I took into account different possible launch dates and the instrument sensitivity and resolution, trying a range of patch sizes and required observational time to find the optimal combination. I developed a series of selection criteria, among which one based on three parameters called “Quality Factors”, which are scalar values defined as the average values of the polarization fraction, the signal-to-noise ratio (SNR) of the polarization fraction, and the SNR of the polarization power contrast of all the pixels within a certain patch. I considered also HI column density maps from HI4PI survey to be able to consider a patch “diffuse” in the CNM, in the sense of having little to no molecular hydrogen and, finally, I found constraints on the polarized dust SED inside selected ISM fields.

The best diffuse dust patch I identified for the BLAST-TNG experiment has been selected as target to be observed in the flight plan of the BLAST-TNG 2019/2020 campaign. For the BLAST Observatory, I identified two best ISM fields to be observed, suitable for two different performance scenarios (both the one based on current telescope design and the one based on the mission top level requirements to meet all science objectives): one which overlaps with the Simons Observatory SAT field, and one which also overlaps with the BICEP/Keck experiment.

Both have been used to make theoretical predictions by the Science team presented in the NASA proposal, including the demonstration that, thanks to the observation of one of these patches, it will be possible to distinguish one- versus two-component dust model.

This analysis is presented in Chapter 4.

- In the context of the attitude control system of an IR polarimetry balloon experiment, I contributed to the topic by analyzing attitude data related to the star cameras pointing system from the ~ 15 hours 2020 science flight of the BLAST-TNG experiment.

I analyzed 5,161 star camera images, searching for images astrometric calibration, that is pointing, scale, and orientation, but being the most part of images contaminated by the presence of Polar Mesospheric Clouds (PMCs), which lead to the inability to solve most images, I implemented a custom algorithm based on advanced filtering techniques to clean all the PMCs-contaminated images. I was able to obtain a total of 1,983 new post-flight star camera solutions, $\sim 38\%$ of the total star camera images analyzed post-flight, recovering 1,650 solutions compared to only 333 found without the use of filtering techniques, and so increasing

the number of original post-flight star camera solutions by a factor larger than 4. This results I found is mentioned in [Coppi et al. \(2020\)](#), and this work was crucial both for testing the accuracy of the pointing system and understanding the performance of the instrument, and for reconstructing the post-flight pointing solution with the required accuracy to make maps from BLAST-TNG raw data that over-sample the angular resolution of the telescope.

This analysis is presented in [Chapter 5](#).

In general, to carry out the various works I have dealt with, I worked with data, both collected and simulated, belonging to a broad range of wavelengths: from optical, going through infrared, microwaves, up to radio data. This allowed me to fully understand how the sky appears in a wide range of frequencies, and what are the various types of experiments that can exist to observe them, with their various strengths and weaknesses: satellites, ground-experiments, and stratospheric balloons.

I had the opportunity to work with data, both collected and simulated, characterized by a wide range of resolutions, which allowed me to understand how the emissions appear on various angular scales, from large up to small.

Many of my efforts have focused on the dust foreground, on the characterization of its model and properties: in general, to achieve these objectives, I approached the topic from different perspectives, dealing both with data analysis and with simulations, both at maps level and power spectra level.

The analysis I carried out on pointing system data, allowed me to get in touch with more instrumental aspects, which have given me a broader and more multi-faceted overview of cosmology, even from a more experimental point of view.

For each project, I developed codes written in Python language, contained in the github repositories of the various experiments.

In conclusion, this PhD gave me the possibility to work with international working groups specialized in Galactic Science, and I can say that my PhD thesis work is broad, aware and robust, and has allowed me to add a small brick on the knowledge of the research topic of Galactic polarized foregrounds.

In [Chapter 6](#) the main results I found are summarized.

Chapter 2

Power spectrum forecast of multi-frequency polarized Galactic emissions with the SO experiment

2.1 Introduction

Within the last decade, CMB polarization experiments have reached a sensitivity such that polarized emission from the Galaxy, rather than detector noise, has become the dominant systematic in many cosmological analyses, including the search for B -mode polarization from primordial gravitational waves. All significant science returns that current and next-generation CMB instruments offer, depend on the capability to measure and extract the foregrounds emissions from our Galaxy in order to separate them, pushing to both higher and lower frequencies to observe the dust and the synchrotron emission, respectively. In addition to their principal cosmological goals, these efforts are also aimed to furnish sensitive new probes of the structure and physics of the Milky Way's magnetic ISM.

Among these experiments, one of the most important is the Simons Observatory (SO), a set of telescopes under construction optimized for CMB survey observations. It will enable myriad new investigations into the multi-scale physics of Galactic structure and the physics and frequency dependence of Galactic emission, providing a robust component separation, thanks to its combination of extended frequency coverage, large sky area, high angular resolution, and exquisite sensitivity.

I am a junior member of the SO collaboration, and during my PhD I collaborated with the Galactic Science working group lead by Susan E. Clark¹ and Brandon S. Hensley².

¹Assistant Professor at Department of Physics, Stanford University, CA, USA.

²Lyman Spitzer, Jr. Postdoctoral Fellow at Department of Astrophysical Sciences, Princeton University, NJ, USA.

To highlight the potential of the Simons Observatory experiment for Galactic astrophysics, with the SO Galactic Science team we published a paper: [Hensley et al. \(2022\)](#). It provided quantitative forecasts on astrophysical parameters of interest for a range of Galactic science cases.

My original contribution to the research field of polarized Galactic foregrounds, which will be described in this Chapter, concerns the evaluation and demonstration of how the capabilities of the SO instruments translate into constraints on the models of polarized Galactic emission. I am the recognized leader³ of the power spectrum analysis of multi-frequency polarized Galactic emissions with the SO experiment, described in Chapter 3 in [Hensley et al. \(2022\)](#).

In this work I quantified the relative improvement of constraints on polarized Galactic emission models using also SO data compared to those obtained with an existing data set. For this reason, in addition to SO polarized data, this forecasts considered joint analysis with observations from the *Planck* and WMAP satellites, as well as low-frequency ground-based data from the C-band All-Sky Survey (C-BASS) experiment, an on-going full sky polarimetric survey at 5 GHz ([Jones et al., 2018](#)), and the S-band Polarization All-Sky Survey (S-PASS) experiment, a 2.3 GHz survey of the Southern Sky (Dec. $< -1^\circ$) in polarization ([Carretti et al., 2019](#)).

Going a little more into detail, the analysis I did is composed by two different forecasts, one with the focus on forecasting the ability of SO to constrain just the synchrotron SED at low frequencies, and the other one to constrain both the synchrotron and dust SEDs together. All the codes I developed for this purpose can be found in the Simons Observatory github repository available to the collaboration members.

I took in consideration exclusively the polarized emission for two main reasons.

The first is that high sensitivity SO observations of polarized dust and synchrotron emission will probe their emission physics in unprecedented detail, not possible with previous experiments, also near the Galactic Plane.

The second reason is that it is not possible to deeply test the physical models of the diffuse emission mechanisms with intensity-only observations. In fact, for example, variations in the dust spectral indices in polarization can reveal physical and chemical processing of interstellar grains ([Planck Collaboration et al., 2020b](#)), while the corresponding variations in synchrotron emission probe the energy distribution of cosmic-rays electrons ([Planck Collaboration X, 2016](#)), and understanding the magnitude of these variations is also critical for foreground mitigation ([Krachmalnicoff et al., 2016](#)). Therefore, it is very important to characterize models of polarized Galactic emission, including the energetic of synchrotron emission, the composition of interstellar dust, and the nature of the observed spatial correlation of dust and synchrotron emission, and highlight what can be learned about the underlying emission physics ([Hensley et al., 2022](#)).

³A supplement describing author contributions to the [Hensley et al. \(2022\)](#) paper can be found at https://simonsobservatory.org/wp-content/uploads/2022/02/SO_GS_Contributions.pdf.

This includes properties of Galactic cosmic-ray electrons, tests of single versus multi-component dust models, and the difference in ISM phases probed by polarized dust and synchrotron emission, respectively (Hensley et al., 2022).

2.2 The Simons Observatory experiment

The Simons Observatory (SO) is a set of new telescopes optimized for CMB survey observations, now under construction in the Chilean Atacama Desert, one of the driest places on Earth, at an altitude of 5,200 meters (17,000 ft). The SO location and its site are shown in Figure 2.1.

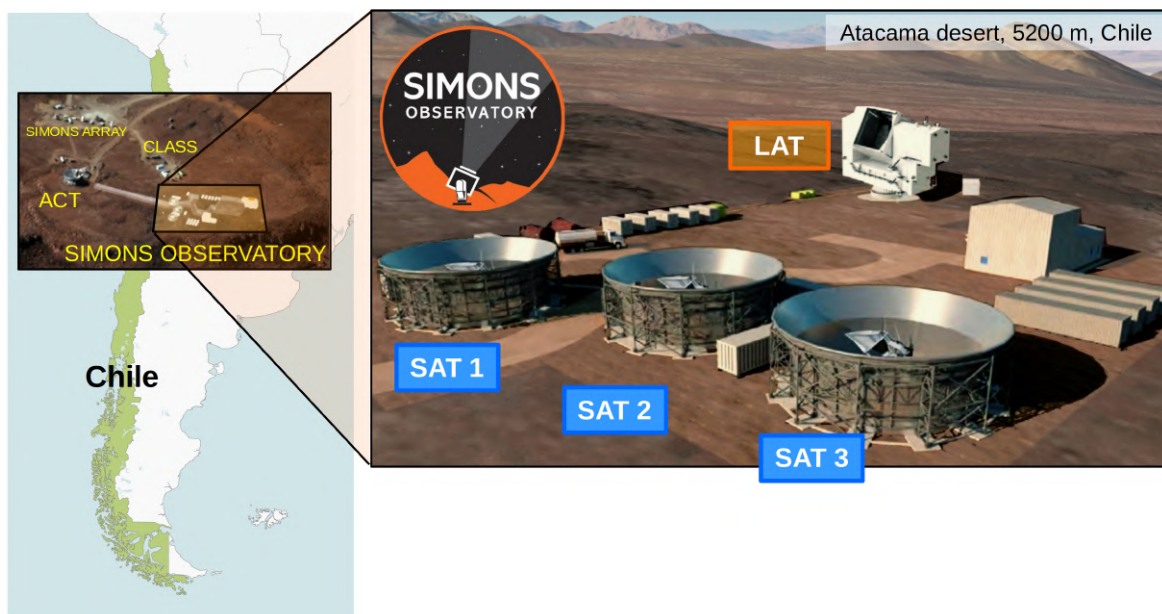


Figure 2.1: On the left, the location of the Simons Observatory in Northern Chile. On the right, a drawing of the site of the Simons Observatory, currently under construction, with three Small-Aperture Telescopes (SATs) and one Large-Aperture Telescope (LAT), in the Atacama Desert, on Cerro Toco, at an altitude of 5,200 meters (17,000 ft). Credit: SO collaboration.

This observatory is formed out of an international collaboration between the Simons Foundation and the Heising-Simons Foundation, the founding US Universities (University of Pennsylvania; Princeton University; the University of California, San Diego; the University of California, Berkeley; and the Lawrence Berkeley National Laboratory) and over 40 collaborating institutions across the globe, including the University of Milano-Bicocca where I did my PhD, with the participation of more than 350 scientists.

SO will see its first light in the middle/second half of this year, up to become fully operational at the beginning of 2024, as it is summarized in Table 2.1.

| Mid 2023 | Early 2024 |
|-----------------------------------|----------------------------------|
| First science operations expected | Full science operations expected |

Table 2.1: *SO timeline.*

Being a next-generation CMB experiment, it will observe both the CMB, just under its peak at 160.3 GHz since below the atmospheric opacity is low, and also higher and lower frequencies to measure and extract the foregrounds emissions from our Galaxy in order to remove them. Therefore, SO will map the sky in six frequency bands, with the following exact band centers: two low frequencies, 27 and 39 GHz; two medium frequencies, 93 and 145 GHz, and two high frequencies, 225 and 280 GHz.

In the original configuration, SO was designed to have three 0.5 m Small Aperture Telescopes (SATs), and one 6 m Large Aperture Telescope (LAT), with different characteristics linked to specific scientific objectives, whose renderings are shown in Figures 2.2 and 2.3, respectively.

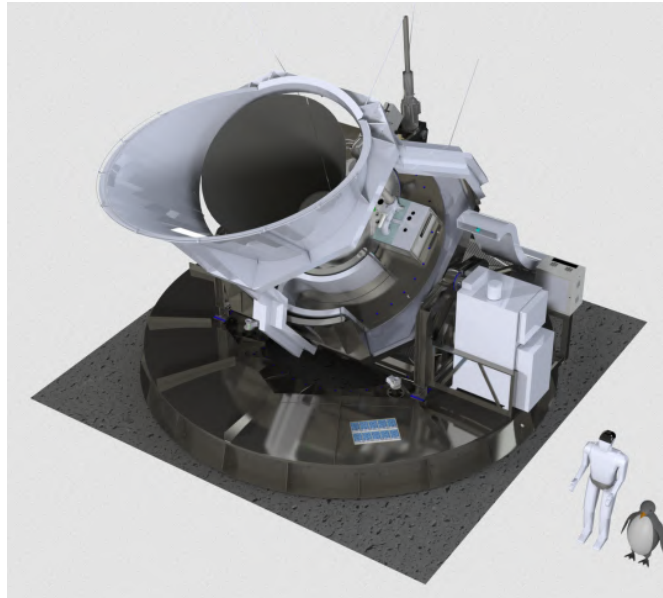


Figure 2.2: A rendering of one of the Small Aperture Telescopes (SATs) on its mount. The co-moving ground screens can be seen along with the electronics and detector readout systems. Source: <https://simonsobservatory.org/small-aperture-telescope-gallery/>.

The SATs (Ali et al., 2020) were designed to measure a fraction of the sky of about $f_{sky} \sim 10\%$ at angular resolutions ranging from $\sim 91'$ up to $\sim 9'$, with very low noise on large angular scales. Considering two scenarios, the expected scenario (the “goal” one), and the “baseline” scenario, i.e. the minimum value reached, in both cases SATs were designed to achieve more than an order of magnitude higher polarization sensitivity

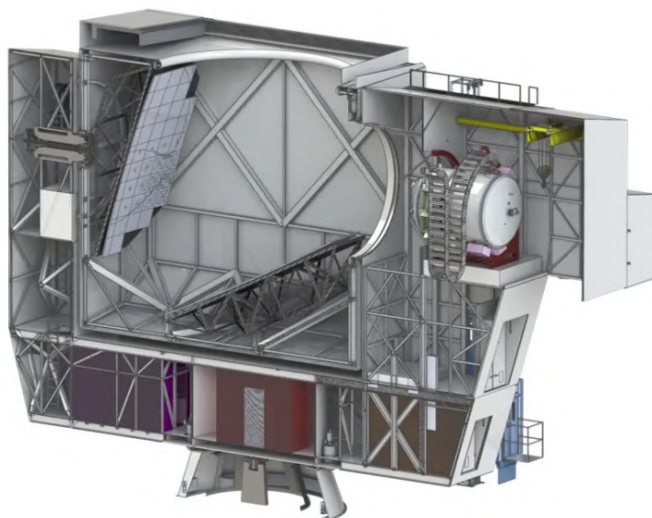


Figure 2.3: A cross section through the SO-LAT showing the mirrors housed in the elevation structure. The Primary mirror is 6 m in diameter and in the center and the secondary is to its left. The receiver sits to the right of the elevation bearing and is over 2.4 m in diameter. Source: <https://simonsobservatory.org/large-aperture-telescope-gallery/>.

than the *Planck* satellite, up to $\sim 2 \mu\text{K-arcmin}$ ⁴.

The LAT (Gudmundsson et al., 2021; Xu et al., 2021) were designed to map a fraction of the sky of about $f_{\text{sky}} \sim 40\%$ with an high angular resolution, ranging from $\sim 7'.4$ up to $\sim 0'.9$. The LAT 225 GHz band has a projected sensitivity improvement of over three in temperature and over four in polarization when compared to the *Planck* 217 GHz band (Simons Observatory Collaboration, 2019; Planck Collaboration I et al., 2020). A description of the SATs and LAT sky coverages will be given in Subsection 2.3.3.

All these properties are summarized in Table 2.2, published in Simons Observatory Collaboration (2019), and compared to which there has been a small improvement for the 93 and 145 GHz channels. The technical groups have managed to achieve a noise level in the “baseline” scenario equal to $\sim 2 \mu\text{K-arcmin}$ for both channels with the SAT telescope (instead of 2.6 and $3.3 \mu\text{K-arcmin}$, respectively), and equal to $\sim 6 \mu\text{K-arcmin}$ for both channels with the LAT (instead of 8.0 and $10.0 \mu\text{K-arcmin}$, respectively).

⁴The integrated sensitivity of an experiment is given by the map noise achieved at the end of observations. The polarization map depth at a single frequency band ν can be expressed in unit of $\mu\text{K-arcmin}$, given by the equation which highlight the combination of all the main dependencies: $\sigma_\nu [\mu\text{K-arcmin}] \sim \sqrt{\frac{f_{\text{sky}}}{T_{\text{obs}}[\text{yr}] \times \epsilon}} \times \frac{\beta \times NET_{\text{det},\nu} [\mu\text{K} \cdot \sqrt{\text{s}}]}{\sqrt{N_{\text{det},\nu} \times Y}}$, where f_{sky} is the fraction of the sky observed; T_{obs} is the length of observations for the total survey; $NET_{\text{det},\nu}$ is the sensitivity of the detector array for the frequency ν ; finally, $N_{\text{det},\nu}$ is the detectors number for the frequency ν . The scalars ϵ , β and Y , which are the overall observing efficiency, the degradation to N_{det} and the detector yield, respectively, were introduced to accurately predict the sensitivity of a potential instrument. For a more detailed description, see Subsection 4.5 of Barron et al. (2018).

| Frequency [GHz] | FWHM ['] | Noise (baseline) [μk -arcmin] | Noise (goal) [μk -arcmin] |
|--------------------------|-------------|--|------------------------------------|
| SATs ($f_{sky} = 0.1$) | | | |
| 27 | 91 | 35 | 25 |
| 39 | 63 | 21 | 17 |
| 93 | 30 | 2.0 | 1.9 |
| 145 | 17 | 2.0 | 2.1 |
| 225 | 11 | 6.3 | 4.2 |
| 280 | 9 | 16 | 10 |
| LAT ($f_{sky} = 0.4$) | | | |
| 27 | 7.4 | 71 | 52 |
| 39 | 5.1 | 36 | 27 |
| 93 | 2.2 | 6.0 | 5.8 |
| 145 | 1.4 | 6.0 | 6.3 |
| 225 | 1.0 | 22 | 15 |
| 280 | 0.9 | 54 | 37 |

Table 2.2: *Properties of the planned SO surveys. “Noise” columns give anticipated white noise levels for temperature, with polarization noise $\sqrt{2}$ higher as both Q and U Stokes parameters are measured. Noise levels are quoted as appropriate for a homogeneous hits map (Simons Observatory Collaboration, 2019).*

However, in the last 2022 year, the project has even expanded: a consortium of UK Universities, and a consortium of Japanese Universities, have managed to get a major upgrade with a total of three additional SAT telescopes, which will provide a major increase in the sensitivity of the facility. There is also the possibility of further future expansion with other LATs telescopes.

An overview of the major science goals that these telescopes will pursue, using data collected by its CMB surveys, was presented by [Simons Observatory Collaboration \(2019\)](#) and by [Hensley et al. \(2022\)](#), to which this work also belongs. For completeness, I will mention a few: in star-forming regions, the scales probed by SO will bridge the high-resolution measurements from the Atacama Large Millimeter/sub-millimeter Array (ALMA) and the large-scale measurements from *Planck*, connecting collapsing cold core regions to the larger environment [Hensley et al. \(2022\)](#); SO will also have the polarization sensitivity to map magnetic fields in a statistical sample of molecular clouds, allowing analyses to marginalize over effects like inclination angle in assessing the dynamical importance of magnetic fields [Hensley et al. \(2022\)](#); on larger scales, SO observations will test the connection of the gas and dust to the Galactic magnetic field, illuminating mechanisms of magnetic hydrodynamic turbulence as they operate in the ISM, such as the dissipation scale [Hensley et al. \(2022\)](#); on even larger scales, both the polarized dust and synchrotron emission measured by SO will contribute to the ongoing, multi-probe effort to map the global magnetic field of the Galaxy [Hensley et al. \(2022\)](#);

finally, with its frequency coverage extending from 27 to 280 GHz, SO will also enable detailed tests of physical models of the frequency dependence of Galactic emission mechanisms in both total and polarized intensity [Hensley et al. \(2022\)](#).

In the work I’ve done, described here, I have actually quantified how SO data will test models of polarized Galactic emission.

2.3 Survey description and noise models

Throughout this work, I adopted the noise models of the SO SAT and LAT instruments for polarized observations, which are publicly available⁵, and the respective sky survey footprints presented in [Simons Observatory Collaboration \(2019\)](#), and which I will describe in this Section. I also adopted the noise models for other experiments used in joint forecasts on which this work is based, and which I will also describe.

2.3.1 SO noise model

Regarding the SO polarization noise models, I adopted the SO noise power spectrum described in [Simons Observatory Collaboration \(2019\)](#), which takes into account both the instrumental and atmospheric noise, since at high frequencies and large angular scales the atmospheric $1/f$ noise⁶ becomes dominant. The noise model used has the following parametric form, for both the SAT and the LAT instruments, in the multipole space, where ℓ is the dimensionless angular wavenumber, the multipole of the power spectrum, and it is related to the inverse of the angular scale⁷:

$$N_\ell = N_{\text{red}} \left(\frac{\ell}{\ell_{\text{knee}}} \right)^{\alpha_{\text{knee}}} + N_{\text{white}} \quad . \quad (2.1)$$

The white noise component of the instrument’s detectors is described by the term N_{white} . The correlated atmospheric noise (i.e., “red noise”), which describes the contribution from $1/f$ noise, can be parameterized as a power-law in multipole space.

It is described by an effective amplitude N_{red} , a pivot scale ℓ_{knee} indicating the angular scale where the atmospheric and instrumental noise have the same power, and a spectral index $\alpha_{\text{knee}} < 0$ that describes how rapidly the noise increases at large angular scales. The noise model is normalized such that the amplitude of the red noise is equal to the amplitude of the white noise, $N_{\text{red}} = N_{\text{white}}$.

I assumed nominal SO mission parameters for a 5-year survey, listed in [Tables 2.3 and 2.4](#) for SAT and LAT, respectively, using the parameter values corresponding to the “baseline” model for all forecasts presented here, i.e, the minimum value reached, and adopting the “pessimistic” value of the pivot scale ℓ_{knee} .

⁵https://github.com/simonsobs/so_noise_models.

⁶The so-called $1/f$ noise is a particular type of stationary random signal, ie its average characteristics remain constant over time. Its noise spectrum is a function that decreases as the frequency increases: in this case the power carried by a certain Fourier component at frequency f is inversely proportional to f .

⁷If θ is the angular scale, in degrees, $l = 180^\circ/\theta$ represents the multipole order, dimensionless.

I have decided to choose the least favorable condition, the “pessimistic” one, in order to have even more confidence in the final results, eliminating the possibility that the success of the forecast was due to overly optimistic assumptions.

| Frequency (GHz) | Noise (μk -arcmin) | α_{knee} | ℓ_{knee} |
|-----------------|--------------------------|------------------------|----------------------|
| 27 | 49.5 | -2.4 | 30 |
| 39 | 29.7 | -2.4 | 30 |
| 93 | 3.7 | -2.5 | 50 |
| 145 | 4.7 | -3.0 | 50 |
| 225 | 8.9 | -3.0 | 70 |
| 280 | 22.6 | -3.0 | 100 |

Table 2.3: *The SO polarization noise model parameters for the SAT instrument. The noise model is normalized such that $N_{\text{red}} = N_{\text{white}}$, and this is the value reported in the “Noise” column. All values are quoted for Q and U maps.*

| Frequency (GHz) | Noise (μk -arcmin) | α_{knee} | ℓ_{knee} |
|-----------------|--------------------------|------------------------|----------------------|
| 27 | 100.4 | -1.4 | 700 |
| 39 | 50.9 | -1.4 | 700 |
| 93 | 11.3 | -1.4 | 700 |
| 145 | 14.1 | -1.4 | 700 |
| 225 | 31.1 | -1.4 | 700 |
| 280 | 76.4 | -1.4 | 700 |

Table 2.4: *The SO polarization noise model parameters for the LAT instrument. The noise model is normalized such that $N_{\text{red}} = N_{\text{white}}$, and this is the value reported in the “Noise” column. All values are quoted for Q and U maps.*

The parameters adopted for each band, listed in Table 2.3 for the SAT instrument, derived from values calculated for other experiments: QUIET (Collaboration et al., 2011, 2012) and ABS (Kusaka et al., 2018), both near the SO site in Chile, assuming a scan speed twice as fast as that adopted by ABS and QUIET; and BICEP2 and Keck Array (Ade et al., 2016), at the South Pole (Simons Observatory Collaboration, 2019). These values account for both the $1/f$ noise and the loss of modes due to filtering, and are also consistent with data taken by Polarbear in Chile with a continuously rotating half-wave plate (Takakura et al., 2017; Simons Observatory Collaboration, 2019). The $1/f$ noise was scaled to each of the SO bands by evaluating the deviation of the brightness temperature due to expected changes in Precipitable Water Vapor (PWV) level using the AM model (Paine, 2018) and the Atmospheric Transmission at Microwaves (ATM) code (Pardo et al., 2001; Simons Observatory Collaboration, 2019).

The parameters adopted for each band, listed in Table 2.4 for the LAT instrument, derived from values calculated for ACTPol (Louis et al., 2017) near the SO site in Chile, and they are consistent with data taken by Polarbear in Chile with a continuously ro-

tating half-wave plate (Ade et al., 2014b; Collaboration et al., 2017; Simons Observatory Collaboration, 2019).

For simplicity, I had also assumed a delta function bandpasses, i.e. considering that the detectors were sensitive to emission only at the nominal frequency. This is because, accounting for bandpass uncertainties would have slightly increased the forecasted uncertainties on parameter constraints presented here, but I expected the assessments of the relative improvements afforded by SO compared to existing data to be robust to this assumption, as it is also applied to all other data sets considered, and I was more focused on relative improvements over existing data than in absolute improvements.

In Figure 2.4, you can see how the SO noise power spectra in polarization, \mathcal{N}_ℓ , look like considering the six frequency channels, for both SAT and LAT instruments, and you can note how the sensitivity of the SATs telescopes is better by about an order of magnitude compared to the LAT one. In this Figure, the beam transfer functions are not deconvolved for illustrative purpose; but, in my analysis, the noise power spectra were calculated with the deconvolution of the Gaussian beam transfer functions.

2.3.2 Noise models for ancillary data

This forecast considered joint analysis of SO polarized data with observations from the *Planck* and WMAP satellites, the C-band All-Sky Survey (C-BASS) experiment, and the S-band Polarization All-Sky Survey (S-PASS) experiment.

For *Planck* frequency channels, I used noise values calculated by another member of the SO Galactic Science team, Nicoletta Krachmanilkoff⁸, who used the same noise power spectrum model adopted for SO, with the form reported in Equation (2.1). The four noise model parameters (N_{white} , N_{red} , ℓ_{knee} and α_{knee}) were retrieved by her for each *Planck* frequency by fitting the model to the *EE* and *BB* angular power spectra of the noise simulated maps publicly available on the *Planck* Legacy Archive⁹, which also include the contribution of instrumental systematic effects. All fits were performed on full-sky data, but were found no qualitative differences in the noise power spectra when restricting to the LAT or SAT footprints.

The noise model for WMAP were calculated by another member of the SO Galactic Science team, Steve Choi¹⁰, who first computed the *EE* and *BB* noise power spectra of the K- and Ka-band maps in the LAT and SAT observing regions after masking the Galactic plane (Galactic latitudes $|b| < 10^\circ$ deg), and then fitted the same four-parameter model to these noise power spectra.

When simulating C-BASS observations, I assumed a uniform noise rms of 4.5 mK-arcmin and a resolution of 45', following Jones et al. (2018).

⁸Assistant Professor at International School for Advanced Studies (SISSA), Trieste, Italy.

⁹<http://pla.esac.esa.int/pla>.

¹⁰NSF Postdoctoral Fellow at Department of Astronomy, Cornell University, Ithaca, NY, USA.

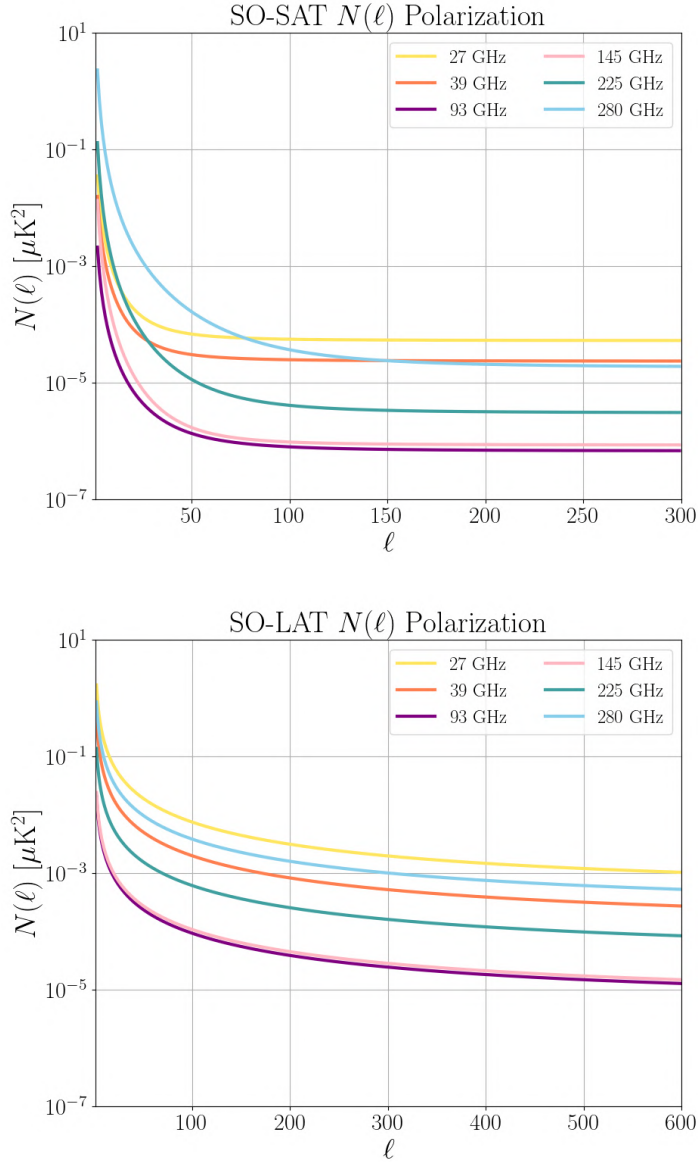


Figure 2.4: Noise power spectra in polarization of SO channels (27, 39, 93, 145, 225 and 280 GHz), for the SAT instrument up to $\ell = 300$ (top), and for the LAT instrument up to $\ell = 600$ (bottom), with the same y-axis. In all cases, the beam transfer functions are not deconvolved for illustrative purpose. Source: https://github.com/simonsobs/so_noise_models.

Finally, regarding the S-PASS experiment, as the survey was conducted with the 64 m Parkes radio telescope, these maps have a resolution of $8.9'$ (FWHM). When simulating S-PASS observations, I assumed a uniform noise rms of 8 mK-arcmin following [Kraichmalnicoff et al. \(2018\)](#) (see also [Carretti et al. 2019](#)).

In Figure 2.5, you can see a comparison between all the noise power spectra in polarization referred to the low frequencies set I used for the synchrotron forecast, which will be described in the Section 2.5, i.e. S-PASS (2.3 GHz), C-BASS (5 GHz), WMAP (23 and 33 GHz), Planck (28.4 GHz) and SO-SAT (27 and 39 GHz). You can note how the sensitivity of the SATs telescopes is better of more than two order of magnitude compared to the best of the others.

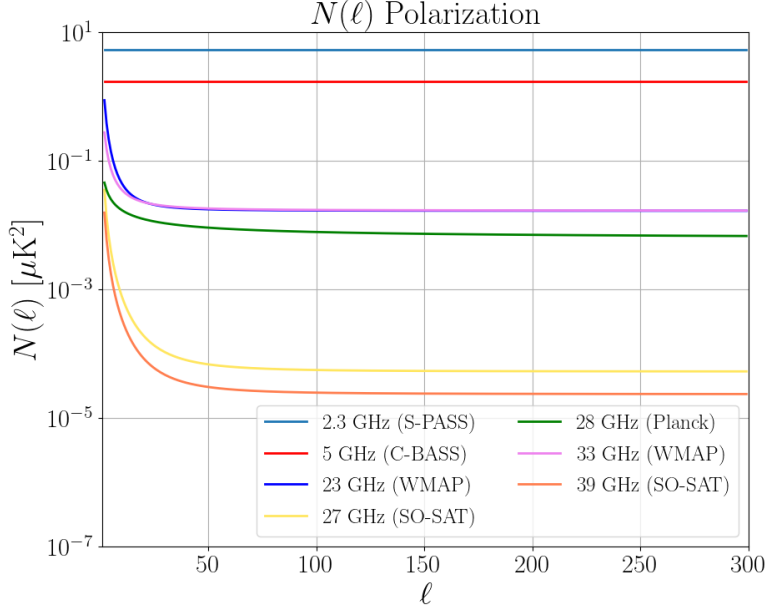


Figure 2.5: Noise power spectra in polarization of S-PASS (2.3 GHz), C-BASS (5 GHz), WMAP (23 and 33 GHz), Planck (28.4 GHz) and SO-SAT (27 and 39 GHz) channels, up to $\ell = 300$. In all cases, the beam transfer functions are not deconvolved for illustrative purpose.

2.3.3 Sky coverage

In all forecasts I employed the masks corresponding to the nominal SO survey regions for the LAT and SAT surveys, presented in Stevens et al. (2018), with a nominal total sky fractions, f_{sky} , equal to 57.5% and 34.4%, respectively. These masks are pixellated to an HEALPix¹¹ grid (Gorski et al., 2005). They have $N_{\text{side}} = 512$, a parameter relative to the pixelization of the sphere which corresponds to a pixel resolution of about 6'.9 arcminutes.

These footprints were computed by SO technical working groups, which consider the ensemble of the observing strategies, the telescope hardware and the science goals of SO.

¹¹See <http://healpix.jpl.nasa.gov> and <http://healpix.sourceforge.net>.

Therefore, they have been apodized and counts-weighted, and these effects lead to smaller effective sky fractions equal to 14.1% and 8.2% for the LAT and SAT surveys, respectively, as it is summarized in Table 2.5.

| f_{sky} | SAT | LAT |
|------------------|-------|-------|
| Nominal | 34.4% | 57.5% |
| Effective | 8.2% | 14.1% |

Table 2.5: *Nominal and effective (already count-weighted and apodized) sky fractions, f_{sky} , for the SAT and LAT surveys, respectively.*

The apodization is an effect in which the signal is concentrated at the center of the map, approaching to zero at the edges, trying to mediate the loss of sensitivity. This is necessary for the power spectra analysis, to avoid the generation of spurious signals because of edge effects, that can be generated in the power spectra calculation. These masks are presented in Figure 2.6.

2.4 Power spectrum forecasting framework

To forecast the ability of SO to constrain the component SEDs in polarization, both just the synchrotron SED at low frequencies, and the synchrotron and dust SEDs, I implemented a power spectrum-based forecasting framework. All the codes I developed for this purpose can be found in the Simons Observatory github repository available to the collaboration members.

First of all, I simulated the polarized Galactic emissions at each frequency channels of the considered set in the SO footprint (see Subsection 2.4.1); then I calculated the full set of auto- and cross-spectra, adding noise at power-spectra level using the model and values described in Subsection 2.3 (see Subsection 2.4.2); finally, I fitted these spectra with various parametric models to derive constraints on the foreground model parameters of interest (see Subsection 2.4.3). I discuss each step of this process in greater detail below.

2.4.1 Galactic emission model

The forecast begins with map-domain simulations of polarized Galactic emission at the relevant frequencies, made with a public software based on true data (*Haslam*, WMAP and ARCADE data for synchrotron model, at 408 MHz and 23 GHz in polarization and scaling to different frequencies; and *Planck* data for dust model, at 353 GHz in polarization and scaling to different frequencies), named Python Sky Model (PySM; [Thorne et al., 2017](#); [Zonca et al., 2021](#)).

As Galactic emission has the most power on large scales (e.g. [Dunkley et al., 2013](#); [Planck Collaboration et al., 2020b](#)), I performed this analysis on multipoles $\ell < 1000$.

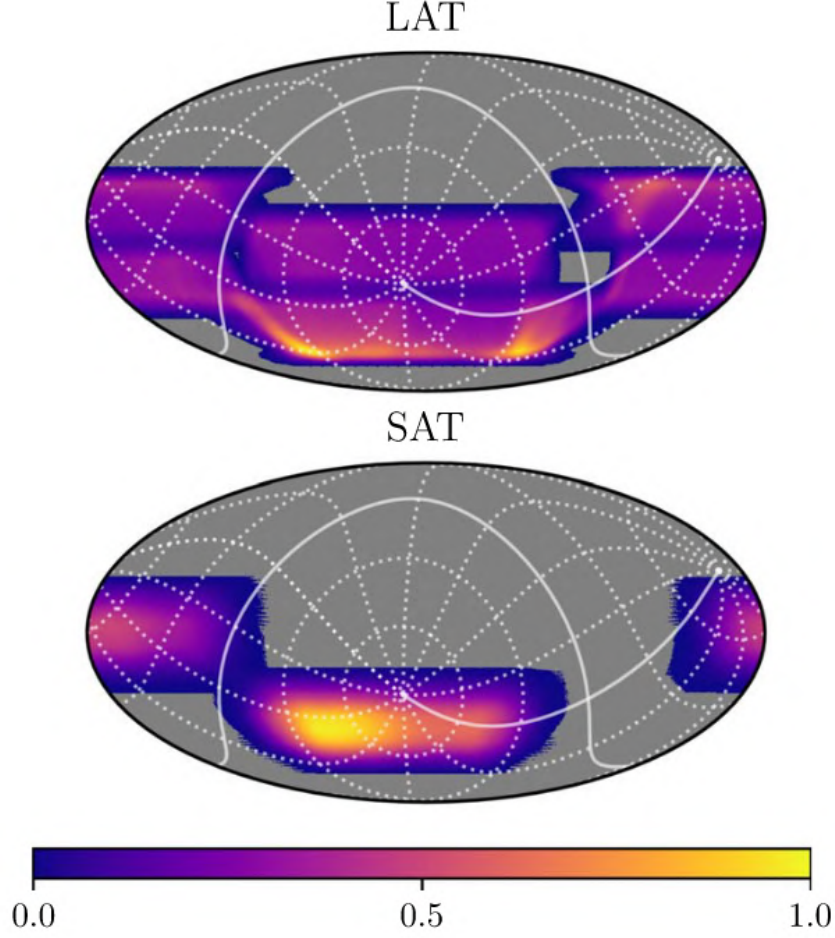


Figure 2.6: Counts-weighted and apodized masks for the LAT (top) and SAT (bottom) surveys used in the forecasts presented here. Both masks are shown in Equatorial projection with gridlines corresponding to Galactic coordinates (Hensley et al., 2022).

Therefore, I generated and analyzed maps with the HEALPix parameter $N_{\text{side}} = 512$, corresponding to a resolution of $6.9'$.

I simulated the dust emission with the PySM “d0” model¹², based on the COMMANDER dust parameter maps (Planck Collaboration X, 2016). The dust SED in each pixel, one of Stokes Q or U in brightness temperature units (e.g., μK_{RJ}), is described by a single-component modified blackbody:

$$S_{\nu,d}^{[QU]} = A_d^{[QU]} \left(\frac{\nu}{\nu_{0,d}} \right)^{\beta_d-2} \frac{B_\nu(T_d)}{B_{\nu_{0,d}}(T_d)} \quad , \quad (2.2)$$

¹²Each model is identified with a letter and a number: the letter indicates the kind of emission and the number the type of model, generally in order of complexity.

where A_d is an amplitude parameter in each of Stokes Q and U in brightness temperature units; $\nu_{0,d}$ is an arbitrary reference frequency, taken to be $\nu_{0,d} = 353$ GHz for convenience (usually where the emission is well dominant); $B_\nu(T)$ is the Planck function; T_d is the dust temperature equal to $T_d = 20$ K in all pixels (typical reference value, or something less); and β_d is the spectral index equal to $\beta_d = 1.54$, assuming the same spectral index for polarization as for intensity, fixed in all pixels which means that the dust spectrum is not spatially variable¹³.

The emission templates are smoothed to a resolution of 2.6° ($\ell = 70$) to which small-scale Gaussian fluctuations are added as described in [Thorne et al. \(2017\)](#).

I simulated the synchrotron emission with the PySM “s0” model, based on the WMAP 9 year Q and U maps ([Bennett et al., 2013](#)).

The synchrotron SED in each pixel is described by a power law scaling in one of Stokes Q and U in brightness temperature units:

$$S_{\nu,s}^{[QU]} = A_s^{[QU]} \left(\frac{\nu}{\nu_{0,s}} \right)^{\beta_s}, \quad (2.3)$$

where A_s is the amplitude parameter in Q and U in brightness temperature units; $\nu_{0,s}$ is an arbitrary reference frequency, taken to be $\nu_{0,s} = 23$ GHz (usually where the emission is well dominant); and β_s is a fixed spectral index, taken to be -3 over the full sky, without spatial variability also in this case.

The synchrotron polarization templates are smoothed to a scale of 5° and then smaller scales are added assuming Gaussian fluctuations following [Thorne et al. \(2017\)](#).

For completeness, I also tried different values for pivot frequency ($\nu_{0,s} = 5, 27$ or 30 GHz), finding that the forecast was robust respect to this arbitrary choice.

Both of these simple parametrizations provides a good description at both the map level and the power spectrum level at current sensitivities.

Finally, to the Galactic emission I added a realization of the CMB signal using the PySM “c1” model. This model draws a Gaussian CMB realization from a primordial unlensed CMB power spectrum computed with the software `CAMB`¹⁴ ([Lewis et al., 2000](#)), and then apply lensing in pixel space with the `Taylens` code¹⁵ ([Næss & Louis, 2013](#)).

2.4.2 Simulated power spectra

Following the framework already employed for cosmological analyses both in [Simons Observatory Collaboration \(2019\)](#) and in other experiments ([Choi & Page, 2015](#); [BICEP2 Collaboration et al., 2018](#); [Planck Collaboration et al., 2020b](#); [Abazajian et al., 2022](#)), I

¹³The spatial variability property has not been taken into consideration in this work, but it is the purpose of a possible future extension.

¹⁴<https://github.com/cmbant/CAMB>.

¹⁵<https://github.com/amaurea/taylens>

constrained the frequency dependence of each emission mechanism using the combination of all auto- and cross-power spectra that can be constructed from the set of observed frequencies.

The effective frequencies to calculate the cross-spectra are defined as the geometrical mean of each couple of frequencies, as:

$$\nu_{ij} = \sqrt{\nu_i \cdot \nu_j} . \quad (2.4)$$

In this formulation, the cross-spectrum $\mathcal{C}_\ell^{XX}(\nu_1 \times \nu_2)$, which takes into consideration both the CMB, the synchrotron (spectral parameters are indicated with the letter “s”), and the dust (spectral parameters are indicated with the letter “d”), where the power-law angular dependence of these foregrounds emissions is also explicit, has the following parametric form:

$$\begin{aligned} \mathcal{C}_\ell^{XX}(\nu_1 \times \nu_2) = & \mathcal{C}_{\ell, \text{CMB}}^{XX}(\nu_1 \times \nu_2) + \\ & A_d^{XX} S_{\nu_1, d} S_{\nu_2, d} \left(\frac{\ell}{\ell_0}\right)^{\alpha_d} + A_s^{XX} S_{\nu_1, s} S_{\nu_2, s} \left(\frac{\ell}{\ell_0}\right)^{\alpha_s} + \\ & \rho^{XX} \sqrt{A_d A_s} [S_{\nu_1, d} S_{\nu_2, s} + S_{\nu_1, s} S_{\nu_2, d}] \left(\frac{\ell}{\ell_0}\right)^{(\alpha_d + \alpha_s)/2} , \end{aligned} \quad (2.5)$$

where X is one of E or B polarization mode; $\mathcal{C}_{\ell, \text{CMB}}^{XX}$ is the CMB power spectrum; A_d^{XX} and A_s^{XX} are the amplitudes of the XX (EE or BB) dust and synchrotron auto-spectra at 353 and 23 GHz, respectively; and ρ^{XX} is the correlation coefficient between dust and synchrotron emission, taken here to be independent of ℓ . The amplitude parameters are normalized at a multipole $\ell_0 = 84$ (and so at an angular scale $\theta \sim 2.2^\circ$).

The parameter ρ is very important also to understand the relation between synchrotron and dust emissions and Galactic magnetic field, as will be explained in the Subsection 2.7.3.

In this formulation, there is the implied assumption that both dust and synchrotron emission are perfectly correlated across frequencies. While such “frequency decorrelation” has yet to be observed in the dust BB spectrum (Planck Collaboration et al., 2020b), variations in dust spectral parameters are well-attested (Planck Collaboration IV, 2020; Pelgrims et al., 2021), and even small levels of frequency decorrelation can influence constraints on the tensor-to-scalar ratio r (BICEP2 Collaboration et al., 2018; Abazajian et al., 2022).

Nevertheless, for forecasting purposes, I did not include frequency decorrelation in both simulated maps and parametric fits, even if searching for frequency decorrelation in dust and synchrotron emission is a potential Galactic science objective using SO data, and could be a possible future extension for this kind of work.

Using the sky simulations presented in the Subsection 2.4.1, the cross-spectra $\mathcal{C}_\ell^{XX}(\nu_1 \times \nu_2)$ for all combinations of ν_1 and ν_2 are computed using the `NaMaster` software¹⁶ (Alonso et al., 2019).

The power spectra were calculated in the SO masks, already described in the Subsection 2.3.3, with a further apodization using the ‘‘C1’’ method in `NaMaster`, in which pixels are multiplied by a factor f (with $0 \leq f \leq 1$) based on their distance to the nearest fully masked pixel, with an apodization scale of 3° (all pixels separated from any masked pixel by more than the apodization scale are left untouched).

This additional apodization caused no difference in the LAT mask, and slightly modified the SAT mask.

Moreover, E - and B -mode purification is used when computing EE and BB spectra, respectively. In fact, for a map with incomplete sky coverage, the E - and B -mode separation is necessarily hampered by the presence of ‘‘ambiguous’’ modes which could be either E or B modes. With a specific approach, already implemented in `NaMaster`, it is possible to remove the ambiguous modes and separating the map into ‘‘pure’’ E - and B components. Note that, generally, it’s not a good idea to purify both, since you’ll lose sensitivity on E . For this reason I applied this purification separately when computing EE and BB spectra.

I employed a constant bandpower binning width equal to $\Delta\ell = 15$, finding in this constant value the best compromise after trying a number of different binning widths, also considering variable values depending on the multipole range.

Finally, I added to the computed spectra the noise $\sigma(\mathcal{C}_\ell^{XX})$ following the formula of Knox (1995):

$$\sigma(\mathcal{C}_\ell^{XX}) = \sqrt{\frac{2}{(2\ell + 1)f_{sky}\Delta\ell}[(\mathcal{C}_\ell^{XX})^2 + \mathcal{N}_\ell^2]} \quad , \quad (2.6)$$

where the noise power spectra \mathcal{N}_ℓ were the same already presented in Section 2.3, with the deconvolution of the Gaussian beam transfer functions. These noise power spectra were combined for auto- and cross-spectra, respectively, following this formula:

$$\mathcal{N}_\ell^2 = \mathcal{N}_\ell(\nu_1)^2, \nu_1 = \nu_2 \quad , \quad (2.7)$$

$$\mathcal{N}_\ell^2 = \frac{1}{2}\mathcal{N}_\ell(\nu_1)\mathcal{N}_\ell(\nu_2), \nu_1 \neq \nu_2 \quad . \quad (2.8)$$

2.4.3 Model fitting

As described in Subsection 2.4.1, the dust SED in each pixel of simulated sky maps is a modified blackbody, and the synchrotron emission in each pixel is a power law. Thus, it was most natural to model the $S_{\nu,d}$ and $S_{\nu,s}$ terms in the cross-spectra Equation

¹⁶<https://github.com/LSSTDESC/NaMaster>.

(2.5) using the parametric forms corresponding to a modified blackbody and a power-law emissions (Equations (2.2) and (2.3), respectively). And since I had adopted input simulations that have spatially uniform frequency spectra for dust and synchrotron, I expected my fits to the cross-spectra to reproduce these values.

It is important to note that the Equation (2.5) is not an exact description of the input, since the ℓ -dependence of the simulated emission at large angular scales is based on observational data, and thus does not conform precisely to the power-laws which appear in this Equation. However, this parameterization is considered adequate for all the forecasting presented here, and sufficient for assessing the constraining power of the SO observations. This limitation should only be kept in mind when interpreting the results.

I made two additional approximations to simplify the model fitting, reducing the size of parameters space.

First, given the lack of constraining power on the dust temperature at low frequencies, where dust emission is in the Rayleigh-Jeans limit, I fix T_d to its input value of 20 K in all analysis, without leaving it as a free parameter, also “authorized” by what [Planck Collaboration et al. \(2020b\)](#) has already done also fixing the dust temperature value in its analysis.

Second, since determination of the CMB spectrum is a principal aim for cosmological analyses, I assume for my purposes that it is perfectly known and thus do not include it as a free parameter in the fit. For future analysis on SO data, the intention is to combine the framework presented here with that detailed in [Simons Observatory Collaboration \(2019\)](#), to measure jointly both cosmological and astrophysical parameters.

With these assumptions, the most general multi- ℓ parametric fit to the ensemble of auto- and cross-power spectra in EE or BB involves seven astrophysical parameters, i.e. the amplitudes in each of Stokes Q and U , the multipoles spectral indices, the frequency spectral indices, both for synchrotron and dust, and the correlation coefficient between dust and synchrotron: A_s , α_s , β_s , A_d , α_d , β_d , and ρ .

The simulated power spectra were fit using the PyMC software ([Fonnesbeck et al., 2015](#)), a Markovian Chain Monte Carlo (MCMC) algorithm implemented with the Python programming language, using a Metropolis step method and setting uniform flat distributions for the priors, with a variable number of iterations between 1,000,000 and 1,200,000 depending on the forecast. The mean values of the posterior distributions were chosen as the final best-fit values of the various spectral parameters, and the standard deviations of the relative distributions were taken as the associated error.

Finally, it is important to underline that I was interested both in how well the parameters of this model can be constrained with SO data, and also how well extensions to this model can be constrained. In fact, in the Equation. (2.5), I introduced the spatial correlation between dust and synchrotron emission, the meaning of which will be explored in more detail in the Subsection [2.7.3](#).

Moreover, I explored the sensitivity to the curvature of the spectral index in the synchrotron SED in Section 2.5.

The spatial variability property of frequency spectral indices has not been taken into consideration in this work. However, a more detailed study of spatial variability is possible both by separately analyzing different sub-regions of the sky, or by map-level modeling of the SEDs. These more sophisticated approaches are beyond the scope of the present study, but it is the purpose of a possible future extension of this work.

2.5 The Galactic synchrotron SED

2.5.1 Motivation

In this analysis I explored the SO sensitivity to constrain parameters of a standard model extension, which involves the additional curvature parameter in the synchrotron SED. As was already written in Subsection 1.2.3, the idealization of the synchrotron SED as a power law is expected to break down in detail, and there are a number of reasons and effects motivating a search for curvature in the synchrotron spectrum.

From an experimental point of view, suggestions of a curvature in the synchrotron spectrum have been reported in some analyses of WMAP combined with radio data in total intensity (Dickinson et al., 2009; Kogut, 2012), and this motivates further research also in polarization.

From a theoretical point of view, the cosmic-rays electron energy distribution is likely to have a high energy cutoff, resulting in an exponential fall-off in the synchrotron spectrum at sufficiently high frequency, and as the electrons lose energy via radiation, the spectrum steepens. Moreover, multiple synchrotron emitting regions along the line of sight may have different slopes of the energy distribution, and while the SED of each emitting region may itself be a power law, the integrated emission will not be.

In addition, curvature in the synchrotron SED complicates removal of polarized synchrotron emission as a CMB foreground.

2.5.2 Forecasting framework

As synchrotron emission dominates the low-frequency sky, I performed this analysis using only low frequency data. In this framework I have quantified the power of low frequency SO data (27 and 39 GHz) to improve upon existing and forthcoming constraints on the synchrotron spectral properties with respect to S-PASS (2.3 GHz), C-BASS (5 GHz), WMAP (23 and 33 GHz), and *Planck* (28.4 GHz).

This is because the sensitivity of low frequency observations from *Planck* and WMAP does not allow the detection of synchrotron signal at intermediate and high Galactic latitudes, where SO will observe. Moreover, S-PASS and C-BASS have a great potential in terms of studying the synchrotron component as a contaminant to CMB polarization measurements, given the fact that at these frequencies the synchrotron signal is much

stronger than at the typical low frequency channels of CMB experiments. Finally, the cross-correlation of all of these data sets will be important to gain insight into the polarized synchrotron behavior, specifically investigating a potential frequency dependence of the spectral index.

The Q and U simulated input maps in the full set of seven frequency channels yielded 28 auto- and cross-spectra for each of EE and BB , while the reduced set of five frequencies without the two SO channels yielded 15 auto- and cross-spectra for each of EE and BB . The Figure 2.7 shows an example of how the full set of 28 cross-spectra look like, for both E - and B -modes, at a specific angular scale ($\ell = 84$).

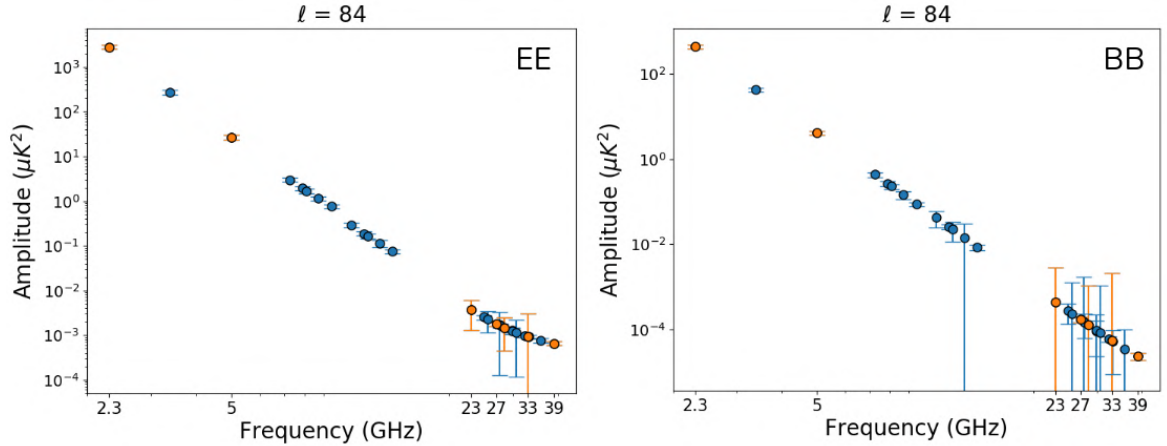


Figure 2.7: The 28 auto-spectra (orange) and cross-spectra (blue) considering the full set of frequencies (2.3 5 23, 27, 28.4, 33 and 39 GHz) for the Galactic synchrotron SED forecast, for both E -modes (left) and B -modes (right), at a specific angular scale ($\ell = 84$).

To assess sensitivity to curvature in the synchrotron SED, I added the curvature parameter s_{run} to the parametric model of synchrotron emission in Equation (2.3), obtaining a new parametric form:

$$S_{\nu,s} = A_s \left(\frac{\nu}{\nu_{0,s}} \right)^{\beta_s + s_{\text{run}} \log(\nu/\nu_{0,s})} \quad (2.9)$$

In the input sky model simulations, the synchrotron emission was modeled by the “s0” model, without any curvature term ($s_{\text{run}} = 0$)¹⁷, as described in Subsection 2.4.1. Therefore, I expect to obtain a best-fit value for this spectral parameter equal to zero, but associated with a certain error, which will be the relevant one in demonstrating the relative improvement of adding the SO data to the existing dataset.

¹⁷On the PySM software exist some curved power-law models, that take into account also the curvature term, as “s1”, “s3” and “s7”, based on ARCADE data, for example supporting a single isotropic curvature index with amplitude taken from Kogut (2012) results.

As for the sky area, I focused the synchrotron forecast on the SAT survey. In fact, although the LAT covers a greater sky area, including synchrotron-bright regions near the Galactic plane, Faraday rotation complicates analysis of the low-frequency ancillary data, particularly S-PASS (2.3 GHz). The requisite masking negates much of the LAT’s advantage over the more sensitive SAT.

Since the SAT survey footprint overlaps with some potentially problematic regions being too close to the Galactic plane, I augmented the SAT mask (Subsection 2.3.3) with an additional Galactic latitude cut of $|b| < 30^\circ$ ¹⁸ to avoid depolarization effects caused by Faraday Rotation, which reduced the SAT mask-weighted, f_{sky} , to 6.8%.

Given the limited sky area and limited resolution of the 27 and 39 GHz SAT channels, 91’ and 63’ respectively, I restricted the analysis to the range of multipoles $70 < \ell < 300$.

In this forecast, the cross-spectrum $\mathcal{C}_\ell^{XX}(\nu_1 \times \nu_2)$, takes this parametric form:

$$\mathcal{C}_\ell^{XX}(\nu_1 \times \nu_2) = \mathcal{C}_{\ell, \text{CMB}}^{XX}(\nu_1 \times \nu_2) + A_s^{XX} S_{\nu_1, s} S_{\nu_2, s} \left(\frac{\ell}{\ell_0}\right)^{\alpha_s}, \quad (2.10)$$

where, although simulated maps contain polarized emission from dust too, the latter is sufficiently subdominant at these frequencies (from 2.3 up to 39 GHz) that it can be neglected in the parametric fitting.

I focused primarily on fits to the BB spectrum, both for the importance of accurate foreground modeling for B -mode science, as well as the fact that a BB analysis is less sensitive to treatment of the CMB component itself, and this framework aims to measure astrophysical parameters only.

Therefore, since I neglected both dust and the CMB as free parameters in the fit, there are only four free parameters to be fit: A_s , α_s , β_s , and s_{run} .

2.6 The composition of interstellar dust

2.6.1 Motivation

In this analysis I explored the SO sensitivity to constrain all the parameters of the model presented in Equation (2.5).

As was already written in Subsection 1.2.3, there is a totally open debate regarding the two- versus one-component dust models: for example, the suite of four models based on separate populations of highly elongated (3:1) silicate and carbonaceous grains, presented by Guillet et al. (2018), versus the “astrodust” model produced by Draine & Hensley (2021), that posits that the submillimeter emission and polarization arises from a single homogeneous grain type.

¹⁸By analysis with less aggressive masking of the Galactic plane, I verified that masking the low Galactic latitudes did not significantly impact the derived parameter constraints.

These dust models can be tested through differences in the dust frequency spectrum in total intensity vis-a-vis polarization, in particular through the difference of dust spectral indices in polarization and intensity, $\Delta\beta = \beta_P - \beta_I$. In fact, single-component models predict small but nonzero $\Delta\beta$, with $\beta_I \simeq \beta_P$, while two-components models typically predict large $\Delta\beta$ (see discussion in [Draine & Hensley, 2021](#)).

The additional frequency coverage and the polarization sensitivity of SO will reveal the nature of the interstellar dust, thanks to the tighter constraints that will be placed on the polarized dust spectral index β_P , and that I also quantified in the work presented here.

I analyzed synchrotron spectral parameters both with SAT and LAT instruments: this analysis could seem “double” since I obtain constraints of synchrotron amplitude, synchrotron spectral index in frequency and synchrotron spectral index in ℓ , two times, but this duplicity is only apparent. I was interested in partially superimposing the analysis, with the aim of investigating the different properties of the two telescopes, and understanding how much the synchrotron parameter estimates change considering different frequency sets, a different multipole range, and different sky coverages. This attempt also belongs to the possibility of exploiting the two telescopes in a different way, even subtly, making the most of what these two different technologies allow us to understand about Galactic science.

2.6.2 Forecasting framework

I performed this analysis on data from 23 up to 353 GHz. In this framework I have quantified the power of SO data (27, 39, 93, 145, 225 and 280 GHz) to improve upon existing constraints on the synchrotron and dust spectral properties with respect to WMAP (K- and Ka-bands at 23 and 33 GHz, respectively), and *Planck* (28.4, 44.1, 70.4, 100, 143, 217 and 353 GHz).

The Q and U simulated input maps in the full set of fifteen frequency channels yielded 120 auto- and cross-spectra for each of EE and BB , while the reduced set of nine frequencies without the six SO channels yielded 45 auto- and cross-spectra for each of EE and BB . The [Figure 2.8](#) shows an example of how the full set of 120 cross-spectra look like, for both E - and B -modes, at a specific angular scale ($\ell = 84$).

As for the sky area, I focused the synchrotron and dust forecast on the LAT survey. In fact, the SO LAT survey covers a greater sky area than the SO SAT survey, and is thus better suited for this analysis. Moreover, unlike the forecast presented in [Section 2.5](#), I did not employ ancillary low-frequency radio data, and so I am not concerned about Faraday rotation on sight-lines near the Galactic plane.

Given the high angular resolution of the LAT instrument, which permits signal-dominated forecasts on Galactic emission up to high ℓ values, I analyzed a bigger range of multipoles $70 < \ell < 600$.

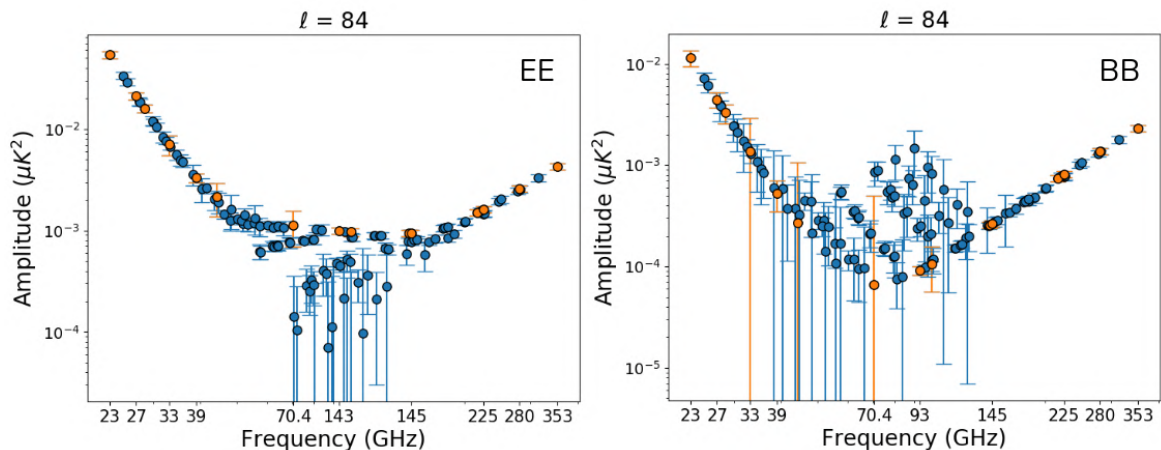


Figure 2.8: The 120 auto-spectra (orange) and cross-spectra (blue) considering the full set of frequencies (23, 27, 28.4, 33, 39, 44.1, 70.4, 93, 100, 143, 145, 217, 225, 280 and 353 GHz) for the Galactic synchrotron and dust SED forecast, for both E -modes (left) and B -modes (right), at a specific angular scale ($\ell = 84$).

I focused primarily on fits to the BB spectrum, both for the importance of accurate foreground modeling for B -mode science, as well as the fact that a BB analysis is less sensitive to treatment of the CMB component itself, and this framework aims to measure astrophysical parameters only.

Therefore, since I neglected CMB as free parameters in the fit, there are seven free parameters to be fit: A_s , α_s , β_s , A_d , α_d , β_d , and ρ .

2.7 Results

2.7.1 The Galactic synchrotron SED results

The posterior distributions of the spectral parameters I obtained from the full fit to the simulated BB cross-spectra between multipoles $70 < \ell < 300$, with and without the SO frequency bands, are presented in Figure 2.9.

I recovered the input parameters without bias in all cases. However, the posteriors on all model parameters tighten with the addition of SO data, illustrating significant improvement on all parameter constraints with the inclusion of SO observations. In particular, the constraints on the synchrotron amplitude (A_s^{BB}), on the spectral index in ℓ (α_s), on the spectral index in frequency (β_s), and on the curvature of the spectral index (s_{run}), improve by factors of 2.3, 1.2, 1.7 and 1.3, respectively.

Therefore, I found that the additional sensitivity of upcoming data from both the lowest-frequency SO bands and C-BASS will provide a stringent test of a curved power-law model of synchrotron polarization, and a significant improvement on current constraints on the Galactic synchrotron SED that employ S-PASS, WMAP, and Planck data alone (Krachmalnicoff et al., 2018).

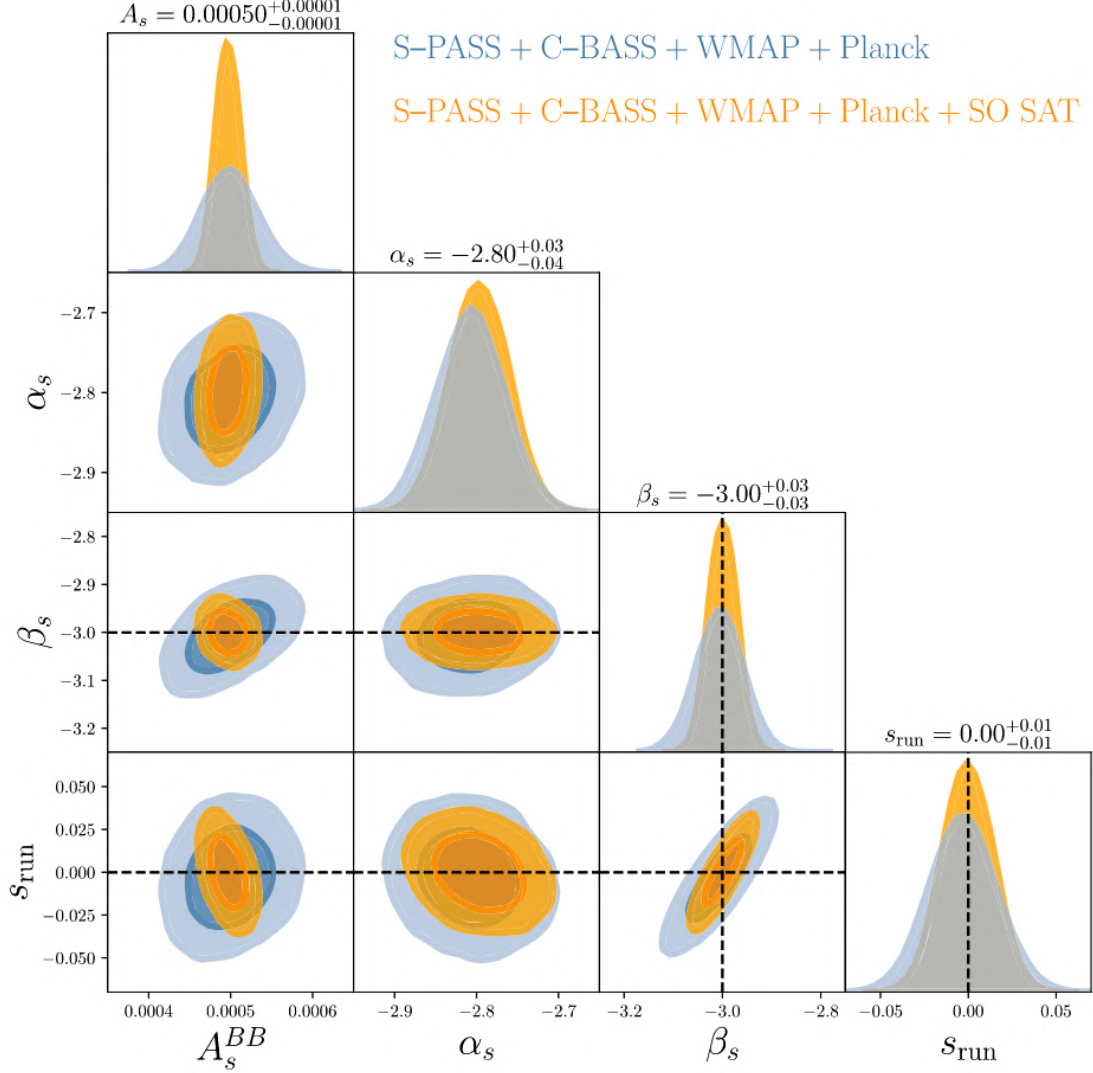


Figure 2.9: Posterior distributions of the synchrotron amplitude (A_s^{BB} , in brightness temperature unit, i.e. μK_{RJ}), spectral index in ℓ (α_s), spectral index in frequency (β_s), and curvature of the spectral index (s_{run}) I obtained from fits to the BB cross-spectra between multipoles $70 \ell < 300$. The addition of SO SAT data (27 and 39 GHz) to existing S-PASS (2.3 GHz), C-BASS (5 GHz), WMAP (23 and 33 GHz), and *Planck* data (28.4 GHz) improves parameter constraints on A_s^{BB} , α_s , β_s and s_{run} by factors of 2.3, 1.2, 1.7 and 1.3, respectively, as illustrated by the relative sizes of the orange (including SO) versus blue (without SO) contours. The values quoted atop the 1D histograms are the 1σ constraints I found on each parameter when including SO SAT data (Hensley et al., 2022).

Figure 2.9 also highlights, for instance, how the sensitivity of the SO data at comparatively high radio frequencies can break the degeneracy between the synchrotron amplitude A_s^{BB} and the spectral index β_s , sharpening constraints on the level of synchrotron emission. In addition to furnishing new constraints on the synchrotron SED, this result I found helps enable searches for other polarized emission mechanisms at these frequencies, notably the Anomalous Microwave Emission (AME).

For completeness, in Figure 2.10 I show an example of how spectral parameter chains appear, considering the full set of frequencies, with SO data too. These plots are useful to perform a visual diagnostics on chain convergence, since it is possible to observe just a roughly white noise, or random variability, around the forecasted values. For this forecast I used a number of iterations equal to 1,200,000.

2.7.2 The Galactic synchrotron and dust SEDs results

The posterior distributions of the spectral parameters I obtained from the full fit to the simulated BB spectra between multipole $70 < \ell < 600$, with and without the SO frequency bands, are presented in Figure 2.11.

I recovered the input parameters without bias in all cases. However, the posteriors on all model parameters tighten with the addition of SO data, illustrating significant improvement on all parameter constraints with the inclusion of SO observations. In particular, the constraints on the synchrotron amplitude (A_s^{BB}), on the synchrotron spectral index in ℓ (α_s), on the synchrotron spectral index in frequency (β_s), on the dust amplitude (A_d^{BB}), on the dust spectral index in ℓ (α_d), on the dust spectral index in frequency (β_d) and on the correlation between dust and synchrotron (ρ) improve by factors of 1.7, 3.1, 2.4, 1.7, 2.0, 1.8 and 2.2, respectively.

In general, I found that constraints on the synchrotron and dust amplitudes (A_s^{BB} and A_d^{BB} , respectively), the synchrotron and dust spectral indices (β_s and β_d), the scale dependence of the dust emission (α_d), and the correlation between synchrotron and dust emission (ρ) all tighten at the factor of two level. While the constraint on the scale dependence of the synchrotron emission (α_s) I found improves by more than a factor of three due to the coverage and sensitivity of the SO data at low frequencies.

First of all, the uncertainty on β_d of $\sigma(\beta_d) = 0.01$ I derived here with only WMAP and *Planck* data is only slightly more optimistic than the $\sigma(\beta_d) = 0.02$ derived from analysis of BB spectra from a much narrower ℓ range ($40 < \ell < 59$) by [Planck Collaboration et al. \(2020b\)](#), lending credence to this framework.

Moreover, I shown here that the additional frequency coverage and polarization sensitivity of SO will reveal the nature of interstellar dust: the uncertainty on β_d achievable with SO as forecasted here, $\sigma(\beta_d) = 0.004$, is more than sufficient to discern whether the $\beta_d = 1.48$ measured in total intensity, with much smaller uncertainty, < 0.01 , is indeed discrepant with the $\beta_d = 1.53 \pm 0.02$ measured in polarization ([Planck Collaboration et al., 2020b](#)), and in general to discern one-component (i.e. “astrodust”, [Draine](#)

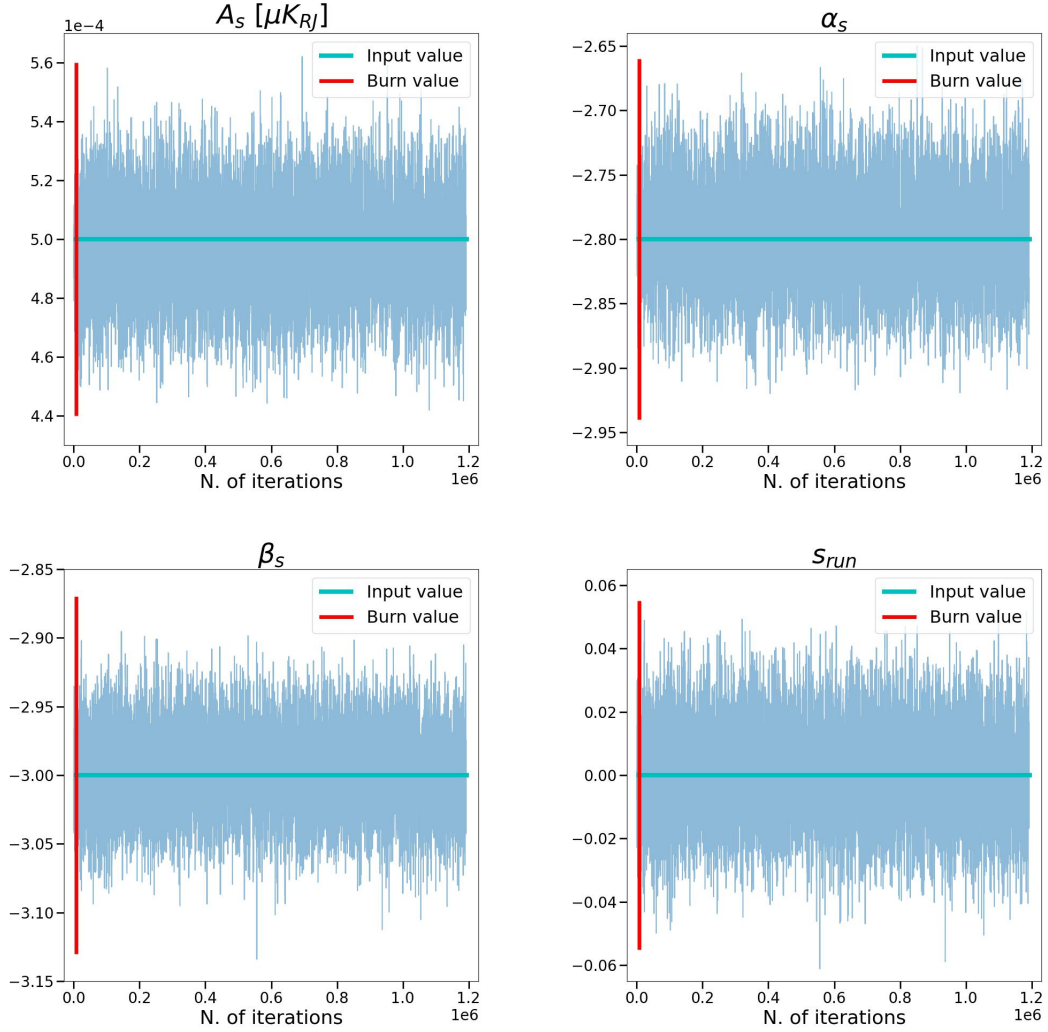


Figure 2.10: *Spectral parameters chains of the Galactic synchrotron SED forecast, considering the full set of frequencies, with SO data too: the synchrotron amplitude (A_s^{BB}) on the top left; the spectral index in ℓ (α_s) on the top right; the spectral index in frequency (β_s) on the bottom left; and the curvature of the spectral index (S_{run}) on the bottom right. All chains are convergent since it is possible to observe just a roughly white noise, or random variability, around the forecasted values. The number of iterations used is equal to 1,200,000.*

& Hensley, 2021) versus two-components (i.e. Guillet et al., 2018) dust models, and thus whether the interstellar dust responsible for the FIR emission and polarization are most consistent with dust grain models which predict a largely homogeneous dust grain population.

There are two main apparent weaknesses in these results I found: the presence of a very slightly bias ($< 1\sigma$) in the recovered model parameters β_s and β_d ; and the different

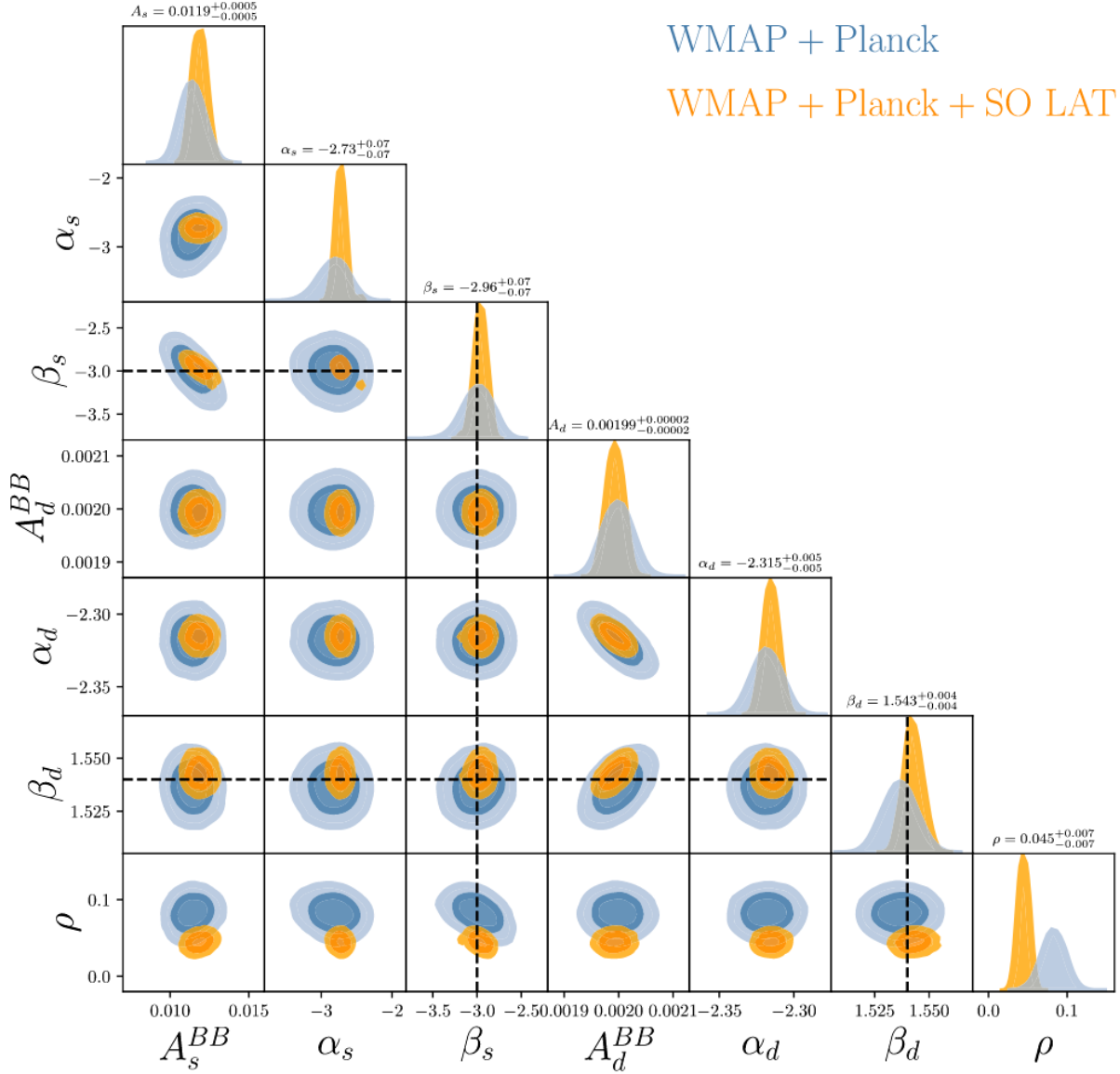


Figure 2.11: *Posterior distributions of the synchrotron amplitude (A_s^{BB} , in brightness temperature unit, i.e. μK_{RJ}), the synchrotron spectral index in ℓ (α_s), the synchrotron spectral index in frequency (β_s), the dust amplitude (A_d^{BB} , in brightness temperature unit, i.e. μK_{RJ}), the dust spectral index in ℓ (α_d), the dust spectral index in frequency (β_d) and the correlation between dust and synchrotron (ρ) I obtained from fits to the BB cross-spectra between multipoles $70 < \ell < 600$. The addition of SO LAT data (27, 39, 93, 145, 225 and 280 GHz) to existing WMAP (23 and 33 GHz), and Planck data (28.4, 44.1, 70.4, 100, 143, 217 and 353 GHz) improves parameter constraints on A_s^{BB} , α_s , β_s , A_d^{BB} , α_d , β_d and ρ by factors of 1.7, 3.1, 2.4, 1.7, 2.0, 1.8 and 2.2, respectively, as illustrated by the relative sizes of the orange (including SO) versus blue (without SO) contours. The values quoted atop the 1D histograms are the 1σ constraints I found on each parameter when including SO LAT data (Hensley et al., 2022).*

posteriors on the correlation parameter ρ , with and without the inclusion of SO data, which is quite sensitive to the inclusion of additional data, shifting from a larger degree of correlation ($\rho = 0.08$) to a lesser degree ($\rho = 0.04$) with the addition of SO data.

I believe that the source of these bias is due to the inherent limitations of the model used: even if the sky in my simulations is simplified and idealized, the parametric model of Equation (2.5) I used to fit is not an exact description of the input, and it can only approximate the input sky.

In particular, as discussed in Section 2.6, since the scale dependence of the dust and synchrotron emission I simulated is based on the observational data of the Galaxy at large angular scales, it cannot be an analytic formula, a perfect law, nor is the correlation between dust and synchrotron emission necessarily scale-independent.

Moreover, regarding the different posteriors on ρ I found, most likely they are caused by the the parameter degeneracies inherent in the model. Further arguments related to the correlation parameter ρ will be presented in the dedicated Subsection 2.7.3.

2.7.3 The correlation between synchrotron and dust emission

Analyzing the Galactic synchrotron and dust forecast constraints from the BB spectra presented in Figure 2.11, I found that the inclusion of SO data improve existing constraints on the parameter ρ governing the synchrotron-dust correlation at the factor of two level. I also found different posteriors on this parameter with and without the inclusion of SO data to the analysis, shifting from a larger degree of correlation ($\rho = 0.08 \pm 0.02$) to a lesser degree ($\rho = 0.04 \pm 0.01$) with the addition of SO data.

The imperfect correlation found is not totally unexpected. For sure, considering that the direction of linear polarization for both synchrotron radiation and thermal dust emission is set by the orientation of the local Galactic magnetic field, we expect the polarized synchrotron and dust emission to be correlated at some extent, as has been observed at the $\sim 20\%$ level at large angular scales (Choi & Page, 2015; Krachmalnicoff et al., 2018).

However, actually it remains unclear to what extent the synchrotron and dust polarizations signals probe different phases of the ISM and different regions of the Galaxy, and if they are correlated also on sub-degree scale. Therefore, the main cause of the different posteriors result on ρ I found, could be attributed to the fact that I modeled the correlation between synchrotron and dust with a scale-independent coefficient.

The synchrotron emission may extends to large Galactic scale heights, depending upon the cosmic-rays electron distribution. In contrast, the dust emission arises largely from the Galactic disk and, at high latitudes, from gas within a few hundred parsecs of the Solar neighborhood (e.g., Alves et al., 2018; Skolidis & Pelgrims, 2019), being the distributions of dust grains correlated with the atomic and molecular gas in the ISM. Therefore, the correlation between polarized synchrotron and dust emission may change qualitatively depending upon region of the sky and angular scale probed.

This means that, even if the correlation parameter ρ found in this forecast, with and without the inclusion of the SO data, are different, they are not necessarily conflicting.

This highlights that a key role for additional sensitive observations is not simply tightening constraints on ρ , but also testing the validity of the underlying model and whether the correlation between the two emission mechanisms can be adequately modeled as scale-independent, since this may not be the case for the real sky.

In the case of sky simulations employed here, I find this to be an excellent approximation, without need to resort to more sophisticated models to accommodate the additional data, finding instead that input parameters β_s and β_d were successfully recovered with even greater fidelity.

A possible modification to my analysis could have been to fit the scale dependence of ρ , for example with a step function, but the primary goal was to illustrate improved parameter constraints, limiting the number of model parameters employed, vis-a-vis to advocate for particular parametric models. Moreover, I was aware of the bias I would have obtained, and I thought it could be of scientific interest to quantify it, since it provides us with information that connects the large and small scales.

Through a small modification to the analysis I carried out, and fitting each multipole separately, I have also emphasized the ability that SO will have in solving smaller scales. In Figure 2.12 it is possible to see the constraints on the correlation parameter between synchrotron and dust emissions, ρ , for each multipole up to $\ell = 300$, with all the other characteristics of the framework already described repeated identical.

Considering the analysis done by (Planck Collaboration et al., 2020b), the spatial correlation between dust and synchrotron polarized emissions was detected with high confidence only for $\ell \leq 40$, and it seemed to decrease with increasing multipole. The correlation might extend to higher multipoles, but the decreasing SNR of the synchrotron polarized emission precludes detecting it (Planck Collaboration et al., 2020b). These results are consistent with the analysis done by Choi & Page (2015), considering the dust emission as measured by Planck at 353 GHz and the synchrotron emission as measured by WMAP at 23 GHz: they found a spatial correlation of $\rho \approx 0.4$ or greater for $\ell \leq 20$ and a fraction of the sky of $f_{sky} \geq 0.5$, dropping to smaller values going to higher multipoles.

What I found in this preliminary analysis is something of consistent too: at smaller multipoles, and so higher angular scales, it is easy to see a positive correlation very well constrained, with no significant difference in the two datasets, considering all *Planck* and WMAP simulated data, and with or without the addition of SO data. Instead, going up to bigger multipoles, it is easy to see how the addition of SO data can improve the constraints on the spatial correlation parameter up to a factor of 5. While *Planck* and WMAP simulated data alone are unable to detect a significant departure from no correlation for multipoles bigger than $\ell > 150$, on the contrary the correlation param-

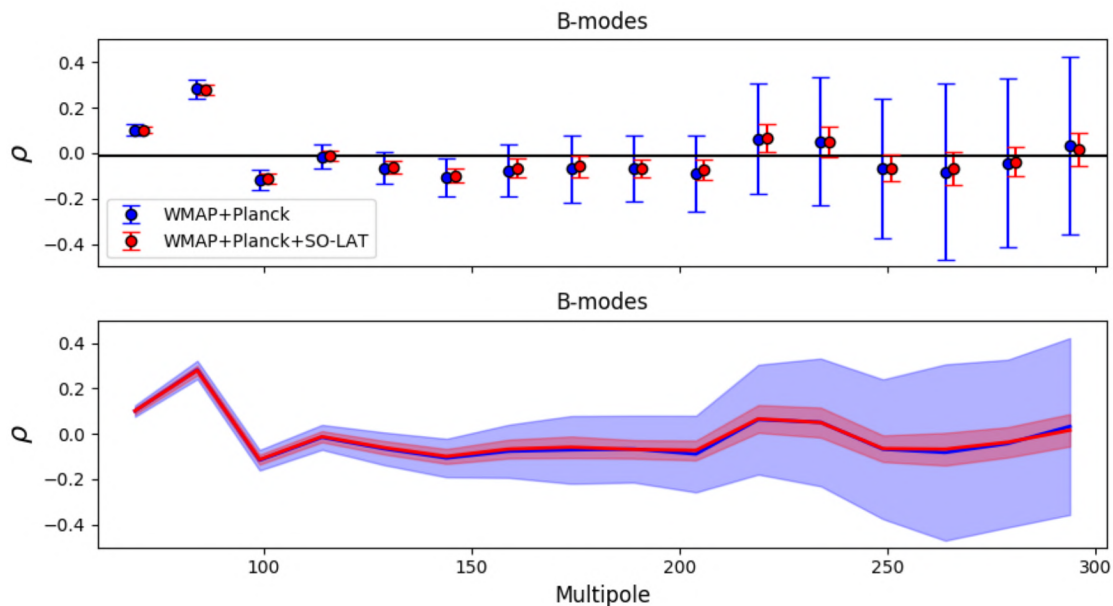


Figure 2.12: The ℓ -by- ℓ constraints on the correlation parameter between synchrotron and dust emissions, ρ , for B -mode polarization, for each multipoles up to $\ell = 300$, with all the other characteristics of the Galactic synchrotron and dust SEDs framework already described repeated identical.

eter constraints obtained with the addition of SO data show a 1σ departure from no correlation from $\ell > 120$ up to $\ell \approx 250$. I found the change from positive to negative correlations, similarly to what was found in (Planck Collaboration et al., 2020b).

To conclude, coming back to the main result I found on the parameter ρ shown in Figure 2.12, whether a scale-independent model is sufficient, and what the implications are for where the observed dust and synchrotron emission originate in the Galaxy, require new observational data to answer. Therefore, it is not possible to establish which of the two correlation parameter ρ values found in this analysis is correct.

The Simons Observatory, with its large sky area, high angular resolution, and high sensitivity polarimetry of the microwave sky, will allow us to elaborate our models beyond what has sufficed for the lower sensitivity observations of WMAP and *Planck*, and will provide means of disentangling these correlations and clarifying the interrelationships between interstellar cosmic-rays, dust, and magnetic fields.

2.8 Conclusions

The Simons Observatory (SO) is poised to address many questions in Galactic astrophysics, in addition to its principal cosmological goals, thanks to its frequency-space coverage and sensitive measurements of Galactic emission.

The analysis I carried out, described in this Chapter, made quantitative forecasts on the frequency spectra of both dust and synchrotron polarized emission, demonstrating how the capabilities of the SO instruments translate into constraints on the models of polarized Galactic emission. This constitutes my original contribution to the research field of polarized Galactic foregrounds.

This power spectrum analysis is extracted from Chapter 3 of the paper [Hensley et al. \(2022\)](#). I am recognized leader¹⁹ of this analysis. All the codes I developed for this purpose can be found in the Simons Observatory github repository available to the collaboration members.

I focused primarily on B -modes, both for the importance of accurate foreground modeling for B -mode science, as well as the fact that a BB analysis is less sensitive to treatment of the CMB component itself, and this framework aims to measure astrophysical parameters only.

I found significant improvement on all spectral parameter constraints with the inclusion of SO observations. The main results I found are summarized here:

1. Regarding the energetic of synchrotron emission, at low frequencies (up to 39 GHz), and in the multipole range $70 < \ell < 300$, the additional sensitivity of upcoming data from both the lowest-frequency SO bands and C-BASS will constrain the presence of curvature in the Galactic synchrotron SED, improving by a factor of two level compared to constraints that employ S-PASS, WMAP, and *Planck* data alone.
Furthermore, I demonstrated that the sensitivity of the SO data at comparatively high radio frequencies can break the degeneracy between the synchrotron amplitude A_s and the spectral index β_s , sharpening constraints on the level of synchrotron emission (see Subsection 2.7.1).
2. Regarding the composition of interstellar dust, at higher frequencies (up to 353 GHz), and in the multipole range $70 < \ell < 600$, the polarization sensitivity of SO will reveal the nature of interstellar dust, enabling detailed tests of one- versus two-component models by constraining the frequency spectrum of polarized dust emission, and in particular the value of the dust spectral index in polarization β_d , with an improvement of a factor of two level relative to current constraints. Achieving the forecasted sensitivity of $\sigma(\beta_d) < 0.01$ will definitively establish whether the two current, distinct, best determinations of $\beta_d = 1.48$ (measured in total intensity with much smaller uncertainty) and $\beta_d = 1.53 \pm 0.02$ (measured in polarization) published in ([Planck Collaboration et al., 2020b](#)), actually correspond to two distinct grain populations, thus testing one-component dust models, which predict nearly identical β_d for both (see Subsection 2.7.2).
3. Finally, regarding the nature of the observed spatial correlation between dust and

¹⁹A supplement describing author contributions to the [Hensley et al. \(2022\)](#) paper can be found at https://simonsobservatory.org/wp-content/uploads/2022/02/SO_GS_Contributions.pdf.

synchrotron emission, SO in combination with other microwave and radio polarimetry up to 353 GHz, and in the multipole range $70 < \ell < 600$, will measure the correlation coefficient between polarized dust and synchrotron emission with a factor of two greater precision than is possible with current data.

Therefore, SO’s multi-frequency view of Galactic magnetic fields probing both dust and synchrotron emission, will help unravel the field structure in different ISM phases and in different regions of the Galaxy, to understand how they correlate with each other as well as the distinct properties of each, as it is explained in Subsection 2.7.3.

More broadly, the quantitative forecasts on astrophysical parameters of interest I found, will serve as a roadmap for Galactic science with other microwave polarization experiments, to expand their scientific scope via Milky Way astrophysics, since analysis of the CMB is moving into “Stage 4”. In fact, the next generation of CMB survey data, in addition to probing cosmology, will provide rich information on the physics of Galactic processes and sources of emission, and will join SO in pushing the boundaries of Galactic polarization science. For example, this science case detailed here is directly applicable to the future ground-based experiment CMB-S4, or it can be extended to all-sky data with proposed satellite experiments like LiteBIRD (Montier et al., 2020) and PICO (Hanany et al., 2019).

I propose a final summary of some possible future extensions of this work:

1. For future analysis with SO data, the intention is to combine the framework presented here with that detailed in [Simons Observatory Collaboration \(2019\)](#), to measure jointly both cosmological and astrophysical parameters.
2. For future analysis with SO data, it is possible to apply a more sophisticated approach of the present study, considering a more detailed study of spatial variability property of frequency spectral indices. There are in fact two possibilities: by separately analyzing different sub-regions of the sky, or by map-level modeling of the SEDs.
3. A potential Galactic science objective using SO data is to search for frequency decorrelation in dust and synchrotron emission, including it in both simulated maps and parametric fits.

Chapter 3

New starlight polarization analysis with Planck data

3.1 Introduction

It is known that the same large aspherical dust grains around $0.1 \mu m$ in size, which dominate the mass in grain size distribution and align with the Galactic magnetic field (Draine & Li, 2007), being the small grains either spherical or not aligned (Kim & Martin, 1995)¹, emit a sub-millimetre polarized radiation and also extinguish and polarize starlight in the visible. This is also bolstered by direct observations of the strength and spectral shape of the polarized emission in the sub-millimetre (Planck Collaboration Int. XXII, 2015).

A comparison of both mechanisms in selected lines of sight provides important diagnostics of properties of dust, and therefore a deep understanding and strong constraints for the entire complexity of models of Galactic dust in the diffuse ISM (Draine & Hensley, 2021), also providing further empirical validation of many of the common underlying assumptions of the models.

Starlight polarization was discovered by Hall (1949) and by Hiltner (1949), and it was ascribed to differential extinction by aspherical dust grains with a preferential alignment related to the configuration of the interstellar Galactic magnetic field (Davis & Greenstein, 1949; Davis & Greenstein, 1951; Planck Collaboration et al., 2020a). To explain how this alignment occurs, a number of theories have been put forward (Anderson et al., 2015), but the mechanism favoured currently involves Radiative Alignment Torques (RATs) acting on grains subject to anisotropic illumination (Hoang & Lazarian, 2016; Planck Collaboration et al., 2020a), as it is explained in Subsection 1.2.2.

¹Current models of interstellar dust commonly feature multiple grain components and not all components (even those that are in thermal equilibrium with the interstellar radiation field and are the major contributors to extinction in the visible and emission in the submillimetre) might be aspherical and aligned.

Differential extinction implies differential emission for thermal processes, as Kirchhoff’s law states, and so the sub-millimetre thermal emission from dust grains is also polarized orthogonally to that of extinction, and for dust grains aligned with respect to the Galactic magnetic field, the observed emission is also partially linearly polarized (Stein, 1966; Hildebrand et al., 1999; Benoît et al., 2004; Kogut et al., 2007; Vaillancourt et al., 2008; Bierman et al., 2011; Planck Collaboration Int. XIX, 2015; Planck Collaboration et al., 2020a).

The polarization of starlight transmitted through interstellar dust reveals the average orientation of the magnetic field projected on the plane of the sky, whereas the direction of polarized emission is rotated by 90° with respect to the magnetic field (Planck Collaboration et al., 2020a). This is because the spin axis of a dust particle is perpendicular to its long axis, and the alignment statistically parallel to the local orientation of the magnetic field (Planck Collaboration et al., 2020a).

Observations of the sub-millimetre diffuse thermal emission from Galactic dust, which is also a foreground contaminant for the Cosmic Microwave Background radiation (CMB) signal, in both total intensity and linear polarization, the latter being a valuable probe for precision cosmology, have gained a strong attention thanks to the *Planck* satellite² (Planck Collaboration et al., 2014; Planck Collaboration XVI, 2014; Planck Collaboration Int. XXI, 2015; Planck Collaboration Int. XXX, 2016; Planck Collaboration et al., 2020a). This was due to its full-sky maps, the sky-coverage and sensitivity of which vastly exceed the previously-available data from ground-based, balloon-borne (e.g., Benoît et al., 2004), and space-based observations (e.g., Gold et al., 2011; Planck Collaboration et al., 2020a).

The CMB decreases toward higher frequencies, while the thermal emission by diffuse interstellar dust increases, and so dust becomes the dominant signal in the submillimetre at the high-frequency end of the spectrum (Planck Collaboration XII, 2014; Planck Collaboration Int. XXI, 2015).

The *Planck*-HFI instrument (Lamarre et al., 2010) has multi-frequency polarization sensitivity in the “dust channels”, covering the spectral range where this transition occurs and up to 353 GHz (Planck Collaboration Int. XXI, 2015), which is therefore the highest-frequency polarization-sensitive channel of *Planck* where the signal-to-noise ratio (SNR) is highest for dust polarized emission (Ade et al., 2010; Planck Collaboration et al., 2014), and where polarized thermal dust emission is about two orders of magnitude stronger than the polarized CMB (Planck Collaboration et al., 2016, 2020a).

353 GHz is the preferential channel used to study this Galactic emission, and several *Planck* papers have already provided comprehensive empirical data of earlier releases and analyses to investigate both the frequency dependence and spatial fluctuations of

²*Planck* is a project of the European Space Agency (ESA) (<http://www.esa.int/Planck>) and over four years (2009–2013) surveyed the entire sky in nine frequency bands, from 30 up to 857 GHz, with high sensitivity, and angular resolutions varying from $30'$ at 30 GHz to $4'.8$ at 857 GHz. All but the two highest-frequency channels (545 and 857 GHz) were sensitive to linear polarization of the observed radiation.

the polarized intensity from thermal dust, being also crucial in refining the separation of this CMB contamination, and were also explored aspects of dust polarization related to the link between dust polarization and physical properties of the ISM, especially the structure of the Galactic magnetic field, including the starlight polarization (Planck Collaboration Int. XXI, 2015; Planck Collaboration et al., 2020a).

In the context of polarized dust characterization, I contributed to the research topic by presenting an updated quantitative validation of the correlation between starlight polarization and polarized dust emission in the diffuse ISM at high-Galactic latitude, following analysis introduced in Planck Collaboration et al. (2020a) for the *Planck* 353 GHz channel. I performed a novel analysis extending the existing results up to smaller frequencies down to 143 GHz, and using the last *Planck* data release (PR4), obtaining new original experimental estimates of the emission-to-extinction polarization ratio $R_{P/p}$, a diagnostic involving dust emission and extinction for the aligned grains population, consistent with those predicted by dust models.

Even if the SNR is lower for dust polarized emission at smaller frequencies, I want to explore the robustness of the theoretical predictions on the comparison between polarized emission and starlight polarization data even at lower frequencies, where dust is still dominant.

I was motivated to examine the polarization ratio since many of the factors driving interstellar polarization in the visible affect also the diffuse dust polarized emission in the sub-millimetre in similar ways, and they are hard to disentangle. For example: the grains shape and the degree of asphericity, whether elongation or flattening; the dust chemical composition and corresponding optical properties at the wavelengths of observation; the 3D-orientation of the magnetic field along the line of sight; and the alignment efficiency, so the degree of alignment, with respect to magnetic field lines, of dust grain populations of different composition and size.

I concentrated the analysis on high-Galactic latitudes and diffuse ISM lines of sights since more homogeneous properties might be expected, and for which the most comprehensive observational constraints on dust models are already available and exploited (e.g., Draine & Li, 2007; Compiègne et al., 2011; Jones et al., 2013; Siebenmorgen, R. et al., 2014).

This project was designed in collaboration with the Galactic Science working group of the Atacama Cosmology Telescope (ACT) collaboration, of which I am a junior member. ACT is a high-resolution ground-based telescope in the Chilean Desert, already active since 2007 and arrived at its latest data collection.

My intention is to exploit the higher resolution and sensitivity of new ACT data to inspect the robustness of the emission-to-extinction polarization ratio, observing dust behavior at smaller scales. I will publish all these results as first author in a paper in preparation titled “New starlight polarization analysis with ACT and *Planck* data”.

3.2 The emission-to-extinction polarization ratio

Many of factors driving interstellar polarization in the visible, near the peak of the polarization curve as the grain shape and alignment efficiency, and the magnetic field orientation, affect also diffuse dust polarized emission in the sub-millimetre in similar ways (Planck Collaboration Int. XXI, 2015; Planck Collaboration et al., 2020a). Therefore, I am motivated to compare them and to correlate the polarization properties of the aligned grain population with the Galactic magnetic field through the emission-to-extinction polarization ratio, $R_{P/p}$, and so quantifying the amount of polarized sub-millimetre emission per unit of optical polarized extinction (Planck Collaboration Int. XXI, 2015; Planck Collaboration et al., 2020a). It is defined as:

$$R_{P/p} = \frac{P}{p_V} \quad , \quad (3.1)$$

where P is the polarized emission measured in the sub-millimetre (see Equation 1.1), and p_V is the optical polarization degree toward the star (in the V band). It has the units of polarized intensity, here MJy/sr.

$R_{P/p}$ is a diagnostic which measure the effects of the same grains at different wavelengths, and it focus directly on the polarization properties of the aligned grains population alone, allowing to primary characterize them, and addressing how efficient they are at producing polarized sub-millimetre emission compared to their ability at polarizing starlight (Planck Collaboration Int. XXI, 2015; Planck Collaboration et al., 2020a).

Although P and p_V both depend on the column density, $R_{P/p}$ is sensitive to two geometrical effects, which affect the comparison of polarized emission with interstellar polarization from differential extinction of a star: to estimate the emission-to-extinction polarization ratio all observations should probe the entire line of sight through the Galactic dust, and ideally they should be done in a pencil-beam. Systematic effects on the quantities appearing in the ratio are introduced due to deviations from this ideal situation (Planck Collaboration et al., 2020a).

Regarding the second geometrical effect, the visible interstellar polarization and extinction result from the dust averaged over the star's angular diameter, which is tiny compared to the sub-millimeter instrumental-beam; and systematic distortions of the sub-millimetre polarization signal occur due to the averaging of Stokes Q and U in the telescope beam (Planck Collaboration Int. XXI, 2015).

Regarding the first geometrical effect, sub-millimetre observations probe the entire line-of-sight through the Galaxy, thus including a contribution from any background ISM observations, while observations in the visible probe the ISM only up to the star's distance. As consequence, particular attention must be paid to exclude lines of sight characterized by a significant background emission (Planck Collaboration Int. XXI, 2015).

As I discussed in Subsections 3.3.3 and 3.3.6, the effect of this first geometrical effect can be mitigated and assessed, while I did not consider in my analysis the systematic beam depolarization effect.

If the dust probed is the same, the unbiased comparison between optical and sub-millimetre measurements also requires agreement on polarization angles. Since for starlight polarization the direction of the magnetic field’s projection on the sky’s plane can be inferred directly from the polarization angle, while for the polarized emission a rotation by 90° is required, the polarization orientations should be orthogonal (Planck Collaboration et al., 2020a).

This is the case for the lines of sight used in my analysis, and I found that the agreement is quite remarkable. To quantify this agreement, which is shown in Subsection 3.4.1, following Planck Collaboration Int. XXI (2015) and Planck Collaboration et al. (2020a) I defined the difference in orientation angles between the submillimetre (“S”) and optical (or visual, “V”) polarization data as $\Delta\psi_{S/V} = (\psi + 90^\circ) - \psi_V$. In terms of Stokes parameters this can be written as:

$$\Delta\psi_{S/V} = \frac{1}{2} \operatorname{atan2}[(U_{qV} - Q_{uV}), -(Q_{qV} + U_{uV})] \quad , \quad (3.2)$$

which takes into account the 90° difference, and so orthogonality corresponds to $\Delta\psi_{S/V} = 0^\circ$.

The expression for $\Delta\psi_{S/V}$ follows from the arctan addition rule, as for Equation (7) in Planck Collaboration Int. XIX (2015), with a minus sign before each argument allowing for the rotation by 90° of the polarization direction in emission as measured by ψ_S , and an additional sign change in the first argument because $\Delta\psi_{S/V}$, like ψ_S and ψ_V , follows the IAU convention for angles, increasing from north through east.

For lines of sight where $\Delta\psi_{S/V}$ is significantly different than the expected 0° , the rms scatter about the best fit correlations yielding $R_{P/p}$ is larger.

In Equation 3.2, q_V and u_V are the Stokes parameters in extinction, measurements of stellar polarization, expressed in terms of the degree of polarization, p_V , and of the position angle, ψ_V , both in the V band. In the HEALPix, or COSMO, convention are defined as:

$$\begin{cases} q_V = p_V \cos(2\psi_V) \\ u_V = -p_V \sin(2\psi_V) \end{cases} \quad , \quad (3.3)$$

while in the IAU convention the sign of u_V must be changed. These Equations change the signs of both q_V and u_V when the position angle ψ_V is changed by 90° .

In my analysis, regarding the selection of lines of sight based on the direction of polarization, I decided to use a slightly different approach than the one used in Planck Collaboration et al. (2020a): they excluded those lines of sight where the difference in orientation angles between the submillimetre and optical polarization data was significantly different than the expected 0° , for which $\Delta\psi_{S/V} > 45^\circ$, using this arbitrary

threshold to be conservative and retain enough lines of sight for the subsequent statistical analysis.

On the contrary, in my analysis I decided to not exclude lines of sight significantly far from orthogonality, and to retain all lines of sight for the polarization ratios estimations. This choice has been possible thanks to the goodness of my sample selection, since all the $\Delta\psi_{S/V}$ distributions were well peaked around the expected centring on 0° , with a small scatter. An example of this distribution is shown in Subsection 3.4.1.

For lines of sight of the diffuse high-latitude Galactic ISM, corresponding to neutral hydrogen column densities $N_H < 10^{21} \text{ cm}^{-2}$, and excluding polarization directions away from orthogonality of more than 45° , [Planck Collaboration et al. \(2020a\)](#) derived an estimate of the polarization ratio referred to a reference frequency of $\nu_0 = 353 \text{ GHz}$, using the *Planck* 2018 data release (PR3, [Planck Collaboration et al., 2020c](#)), finding:

$$R_{P/p}(\nu_0 = 353 \text{ GHz}) = [5.42 \pm 0.05] \text{ MJy/sr} \quad , \quad (3.4)$$

where the uncertainty is both statistical and systematic.

This value provided strong constraints for models of dust polarized emission, and the *DustEM* model ([Compiègne et al., 2011](#)) has been updated by [Guillet et al. \(2018\)](#) to take these constraints into account. It is important to underline that the only value published in literature refers to the 353 GHz.

Since in my analysis I derived polarization ratio estimates up to smaller *Planck* frequencies, in detail $\nu = 217 \text{ GHz}$ and $\nu = 143 \text{ GHz}$, the expected values have been extrapolated scaling with a modified black body (MBB) dust model law from the $R_{P/p}(\nu_0)$ ratio, as:

$$R_{P/p}(\nu) = S(\nu) \cdot R_{P/p}(\nu_0) \quad , \quad (3.5)$$

with the following scale factor $S(\nu)$:

$$S(\nu) = \left(\frac{\nu}{\nu_0} \right)^{\beta_d+3} \cdot \frac{e^{\frac{h \cdot \nu_0}{k \cdot T_d}} - 1}{e^{\frac{h \cdot \nu}{k \cdot T_d}} - 1} \quad , \quad (3.6)$$

where $\beta_d = 1.54$ is the assumed dust spectral index and $T = 20 \text{ K}$ is the assumed dust temperature.

The theoretical reference values for the polarization ratios estimated in correspondence of $\nu = 217 \text{ GHz}$ and $\nu = 143 \text{ GHz}$, considering the same systematic errors and statistical errors related to the star sample amplitudes which led to 3.4, are:

$$R_{P/p}(\nu = 217 \text{ GHz}) = [1.16 \pm 0.01] \text{ MJy/sr} \quad , \quad (3.7)$$

$$R_{P/p}(\nu = 143 \text{ GHz}) = [0.292 \pm 0.003] \text{ MJy/sr} \quad . \quad (3.8)$$

The emission-to-extinction polarization ratio can in principle be obtained by correlating P with p_V , two quantities derived non-linearly from the original data: the Stokes parameters in emission (Q and U) and the Stokes polarization parameters in optical extinction (q_V and u_V).

In the presence of errors, P and p_V are biased estimates of the true values (Wardle & Kronberg, 1974; Simmons & Stewart, 1985; Quinn, 2012; Plaszczyński et al., 2014; Planck Collaboration Int. XIX, 2015; Planck Collaboration et al., 2020a), and the polarization ratio would be affected by the same problem.

In the ideal case, where noise is negligible and the polarization pseudo-vectors in extinction and emission are orthogonal, holds $Q/P = -q_V/p_V$ and $U/P = -u_V/p_V$, which yields:

$$\begin{cases} Q = -R_{P/p} \cdot q_V \\ U = -R_{P/p} \cdot u_V \end{cases} . \quad (3.9)$$

Therefore, the polarization ratio $R_{P/p}$ can be operationally estimated not only by correlating P with p_V , but also from the linear relation between their projections in Q and U .

In my analysis, following the approach in both Planck Collaboration Int. XXI (2015) and Planck Collaboration et al. (2020a), I derived $R_{P/p}$ through a joint correlation of the pair (Q, U) with (q_V, u_V) , and this approach is both motivated and justified, since it has several advantages, in addition to the fact as already mentioned that, unlike the quantities P and p_V , their equivalents in Q and U are not biased (Planck Collaboration Int. XXI, 2015).

First, since the data in Q and U can be both negative and positive, each show a better dynamic range than in P ; moreover, if the position angle changes, they can vary from line of sight to line of sight, even while P and p remain fairly constant (Planck Collaboration Int. XXI, 2015). This allows for a better definition of the correlation and therefore a better constraint on the slope, which is the polarization ratio (Planck Collaboration Int. XXI, 2015).

Second, from the slope of separate correlations for Q and for U , I can get two independent estimates of the polarization ratio. These two estimates of the polarization ratio should be the same as they are measuring the same phenomenon, and the intercepts should be close to zero, assuming that for the selected stars samples the measured polarization in emission and extinction arises from the same aligned grains (Planck Collaboration Int. XXI, 2015). This is what I found for the Q and U independent correlations analyzed as reinforced of final results, and the results of these independent fits also reflected the quality of selected data (these separate fit are not shown in the final results, as I did these as a consistency check).

3.3 Starlight polarization data

3.3.1 The preliminary sample

For this analysis, I chose to employ the same preliminary stars sample adopted in the similar analysis carried out in [Planck Collaboration et al. \(2020a\)](#), using data from a series of optical polarization catalogues of high-latitude stars.

In details, these are five catalogues from 2001 up to 2014, with a total of 3,064 stars: [Berdyugin et al. \(2001\)](#)³, [Berdyugin et al. \(2004\)](#)⁴, [Berdyugin, A. et al. \(2014\)](#)⁵; [Berdyugin & Teerikorpi \(2001\)](#)⁶ and [Berdyugin, A. & Teerikorpi, P. \(2002\)](#)⁷. In the shorthand notation, I indicate these catalogues hereafter with: B01, B04, B14; BT01 and BT02, respectively. In particular, the B01 and BT02 catalogues contain stars just belonging to the North Galactic Pole Area (336 stars at $b \geq 68^\circ$ and 102 stars at $b > 55^\circ$, respectively), with associated distances values up to 1,487 pc (a single star with a distance equal to 3,051 pc) and up to 490 pc, respectively; B04 and BT01 contain stars just belonging to the South Galactic Pole Area ($b < -70^\circ$), 183 stars with expressed distances up to 608 pc and 43 stars with expressed distances up to 500 pc, respectively; finally, B14 contain a wider number of stars, equal to 2,400, covering both the North and the South Pole Areas ($b \geq 30^\circ$ and $b < -58^\circ$), with expressed parallaxes values corresponding to distances up to 848 pc, and provides a new higher resolution view around the Galactic poles than previous maps.

For each star, catalogues provide measurements of stellar polarization: the degree of polarization (p_V) with the associated error ($\sigma(p_V)$), both given in percents; and the position angle (ψ_V) with the associated error ($\sigma(\psi_V)$), both expressed in degrees between 0° and 180° , in the IAU equatorial convention.

Since in this analysis I worked with *Planck* data, which are expressed in Galactic coordinates, I also needed to transform polarization angles into the Galactic coordinate system, using the following formula ([Appenzeller, 1968](#); [Stephens et al., 2011](#)):

$$\psi_{V,Gal} = \psi_{V,eq} - \arctg\left(\frac{\sin(l - l_{NP})}{\cos(b)\operatorname{tg}(b_{NP}) - \cos(l - l_{NP})\sin(b)}\right), \quad (3.10)$$

³Table with positions and polarization results is available in electronic form at the CDS via <http://cdsarc.u-strasbg.fr/viz-bin/cat/J/A+A/372/276> ([Berdyugin A.V., 2001](#)).

⁴The data of this catalogue, which is not public and available in electronic form, had been provided to us by the author himself.

⁵Table with positions and polarization results is available in electronic form at the CDS via <http://cdsarc.u-strasbg.fr/viz-bin/qcat?J/A+A/561/A24> ([Berdyugin A., 2013](#)).

⁶The data of this catalogue, which is not available in electronic form, had been transcribed from the ones published in the article itself.

⁷Table with positions and polarization results is available in electronic form at the CDS via <http://cdsarc.u-strasbg.fr/viz-bin/qcat?J/A+A/384/1050> ([Berdyugin A., 2002](#)).

where $\psi_{V,eq}$ is the polarization angle expressed in the equatorial system and given by catalogues themselves; l and b indicate the Galactic coordinates of stars; and l_{NP} and b_{NP} indicate the North Pole (NP) Galactic coordinates, assumed equal to $l_{NP} = 122.932^\circ$ and $b_{NP} = 27.128^\circ$. As the polarization angles expressed in Galactic coordinates, $\psi_{V,Gal}$, had to be expressed in degrees between 0° and 180° , I added or subtracted 180° if the angle was less than 0° or greater than 180° , respectively.

Then, since I could ignore the propagation of the errors on the NP coordinates and on stars coordinates, being negligible, the Galactic polarization error was estimated by the following formula:

$$\sigma(\psi_{V,Gal}) = \psi_{V,Gal} \cdot \frac{\sigma(\psi_{V,eq})}{\psi_{V,eq}} \quad , \quad (3.11)$$

where $\sigma(\psi_{V,eq})$ is the polarization angle error expressed in the equatorial system and given by catalogues themselves.

Observing the behavior of three stars in the final result, I became suspicious as they appeared as outliers. Extensive research showed that for two of these three stars, updated data from new spectro-polarimetric observations had been published in [Nikolov \(2022\)](#), which I have thus replaced in my preliminary catalogue (these stars belonged to the B14 catalogue): *HD 142762* and *HD 142053*.

For the first star, the degree of polarization increased by a factor of 1.4, its error decreased by a factor of 4.1, while the position angle decreased by a factor of 1.7 and its error by a factor of 3.1. For the second star, all the values decreased: the degree of polarization slightly by a factor of 1.1, its associated error by a factor of 3.3, the position angle by a factor of 1.5 and its error by a factor of 2.

Catalogues come in different coordinate systems (B04 and BT01 use Galactic coordinates, while BT02 uses equatorial coordinates), so I wrote a Python code based on the `astropy` library ([Astropy Collaboration et al., 2022](#)) to convert and express their data in a uniform way. This process facilitated subsequent manipulations and cross-checking between catalogues.

In various catalogues, stars are characterized by different designations: the BT02 stars have just the BD (Bonner Durchmusterung) identifier; the BT01 and the B14 stars have both the BD and the HD (Henry Draper) identifiers; the B04 stars have both the BD, the HD, the CD (Cordoba Durchmusterung) and the SAO (Smithsonian Astrophysical Observatory) identifiers; finally, the B01 stars present both the BD, the HD, the Kn (Knude) and the ss2 (Sletterback & Stock) identifiers.

To facilitate the cross-match across the various catalogues, also stars names were arranged in order to have a consistent format, since even in the case of the same designation they appeared written in an incomparable way.

Considering the B01 catalogue, I realized that some of stars named with the HD number were misspelled, as the last digit appeared truncated. This did not create particular discomfort as the BD number was also present (with the exception of 12 stars), and spelled correctly. However, the HD number's truncation caused ambiguity, and I report these inconsistencies in Table 3.1, both with the HD numbers spelled incorrectly, the various associated BD numbers, and with the HD number that should be correctly associated.

| HD number (wrong) | BD number | HD number (correct) |
|-------------------|--|-------------------------------------|
| HD 10846 | BD+28 2116 BD+18 2611 BD+25 2508 | HD 108466 HD 108468 HD 108467 |
| HD 11504 | BD+31 2464 BD+12 2572 | HD 115045 HD 115046 |
| HD 11453 | BD+14 2585 BD+16 2476 | HD 114538 HD 114725 |
| HD 10951 | BD+19 2584 BD+22 2490 | HD 109511 HD 109519 |
| HD 11002 | BD+21 2439 BD+17 2511 | HD 110024 HD 110025 |
| HD 11219 | BD+22 2521 BD+22 2522 | HD 112197 HD 112196 |
| HD 11384 | BD+21 2487 BD+46 1847 | HD 113848 HD 113847 |
| HD 11432 | BD+20 2802 BD+17 2595 | HD 114325 HD 114326 |
| HD 11437 | BD+18 2697A BD+39 2611 | HD 114378 HD 114376 |
| HD 11598 | BD+20 2824 BD+18 2717 | HD 115980 HD 115981 |
| HD 11850 | BD+25 2652 BD+28 2244 | HD 118508 HD 118507 |
| HD 11730 | BD+32 2356 BD+11 2575 | HD 117301 HD 117304 |

Table 3.1: *Twelve stars in Berdyugin et al. (2001) (B01) with HD number names misspelled (first column), with the last digit truncated causing ambiguity. To the same incorrect name expressed as HD number, different BD number names are associated (second column), with the correct spelling. In the third column there are the correct HD numbers names associated with the BD stars.*

I also notice that there was an error related to a star belonging to the BT01 catalogue, whose values are published in [Berdyugin & Teerikorpi \(2001\)](#): values associated to the star *HD 2305*, such as the coordinates and the optical polarization data, they actually refer to the star *HD 2503*.

In my analysis, I investigated the cases of stars ambiguity in the same catalogue, therefore the presence of double stars with different associated polarization values. In the BT02 catalogue, I found one star appearing twice, with identical values, *BD+16 2297*, and I removed one.

In the B01 catalogue, I found one star repeated twice, *BD+22 2521*, with same name, coordinates and distance values, but with slightly different polarization values: $p_V = 0.15\%$ and $p_V = 0.13\%$; $\psi_{V,eq} = 68^\circ$ and $\psi_{V,eq} = 78^\circ$, and $\sigma(\psi_{V,eq}) = 3^\circ$ and $\sigma(\psi_{V,eq}) = 4^\circ$. Since these values were very similar, and not knowing which ones to give more credibility to, I associated the star with average values, including errors, equal to: $p_V = 0.14\%$, $\psi_{V,eq} = 73.0^\circ$ and $\sigma(\psi_{V,eq}) = 3.5^\circ$.

In the B14 catalogue, I found 19 star repeated twice, with same names and coordinates. In detail, two of these, *BD+67 750* and *HD 83872*, also showed equal distance values, but in one case they did not show the degree of polarization and the polarization angle values, and the relative errors, while in the other case they did, and I took these present values for good. The other seventeen stars showed slightly different (within 2.5σ) polarization values: *HD 139897*, *HD 143178*, *HD 145247*, *HD 149755*, *HD 148619*, *HD 93979*, *HD 67201*, *HD 84299*, *HD 87502*, *HD 120406*, *HD 139379*, *HD 9357*, *HD 8840*, *HD 9959*, *HD 10315*, *HD 9691*, *HD 12177*. Since these values were similar (within 2.5σ), with the exception of one star, *HD 87502*, which showed a discrepancy of more than 5.5σ in polarization angle values, as shown in [Figure 3.1](#), and not knowing which ones to give more credibility to, I associated average values, errors included, with the stars. Two of these, *HD 139897* and *HD 12177*, also showed slightly different parallaxes values, equal to 2.96 mas and 3.59 mas, and 4.67 mas and 4.61 mas, respectively, so I took an average value (3.28 mas and 4.64 mas, respectively); and one of them, *HD 139379*, showed missing parallax values.

My investigation also went to analyze overlapping cases, so cases of ambiguity between stars repeated in several catalogues, by cross-matching the catalogues with the identifier number as the first-order criterion: in this case, I chose to retain the data from the next catalogue, considering it more up-to-date, and to remove stars in common within previous catalogues.

I eliminated 4 stars from the B01 catalogue, as they were also present in the subsequent BT02 catalogue: *BD+16 2319*, *BD+37 2195*, *BD+44 2285* and *BD+22 2521*. These stars had equal distance values, and very similar polarization data values (degree of polarization and polarization angle, and relative errors).

I also eliminated 40 stars from the BT02 catalogue, as they were also present in the subsequent B14 catalogue. These stars had nearly identical polarization data values, but different distances values.

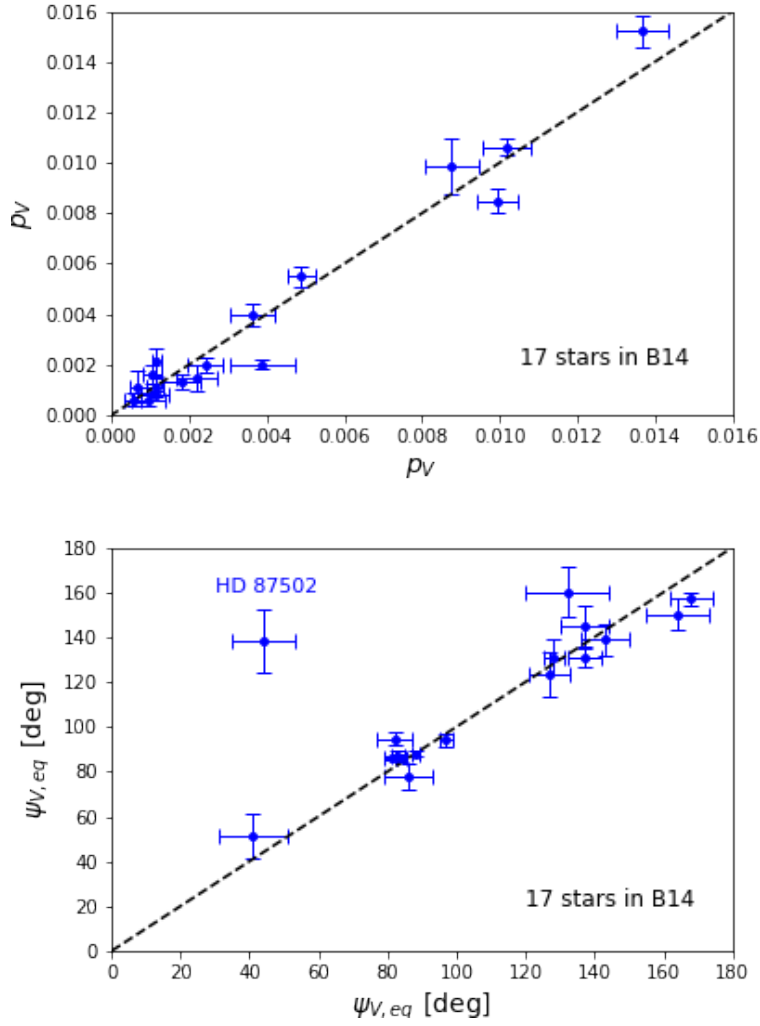


Figure 3.1: The degree of polarization (p_V), in decimals, with the relative error (top) and the polarization angle ($\psi_{V,eq}$) in equatorial coordinates and IAU convention, in degrees, with the relative error (bottom) of 17 stars belonging to the *Berdyugin, A. et al. (2014)* catalogue (B14) which doubles appear, with the same name and coordinates, but different values of the optical polarization data. The plots show that the difference is not particularly significant, within 2.5σ , and only one star, HD 87502, shows a discrepancy of more than 5.5σ in polarization angle values. Not knowing which value to give more credibility, in my sample I took an average value, including errors.

I then eliminated the star *HD 13459* from the BT01 catalogue since it was also present in the subsequent B14 catalogue.

At this point, having to clean up data of these catalogues (coordinates, polarization values, polarization angles, distances) that had null or missing values, I eliminated: 89 stars from the B01 catalog; 17 stars from the B04 catalog; 401 stars from the B14 catalog; one star from the BT01 catalogue and 2 stars from the BT02 catalogue.

To conclude, I extracted data for 2,487 lines of sight to stars with measured optical polarization data, without repeating stars or ambiguity, having constructed a single homogeneous and error-free preliminary catalogue with high-Galactic latitude stars. All the selection steps applied in sequence are summarized in Table 3.2.

| | Initial Stars Sample | After Internal Cleaning | After Cross-Cleaning | After Null+Missing values Cleaning |
|-------|----------------------|-------------------------|----------------------|------------------------------------|
| B01 | 336 | 335 | 331 | 242 |
| B04 | 183 | 183 | 183 | 166 |
| B14 | 2,400 | 2,381 | 2,381 | 1,980 |
| BT01 | 43 | 42 | 41 | 40 |
| BT02 | 102 | 101 | 61 | 59 |
| Total | 3,064 | 3,042 | 2,997 | 2,487 |

Table 3.2: *Evolution of the number of stars remaining after the preliminary selection steps applied sequentially, in total and with respect to each catalogue: Berdyugin et al. (2001) (B01); Berdyugin et al. (2004) (B04); Berdyugin, A. et al. (2014) (B14); Berdyugin & Teerikorpi (2001) (BT01); and Berdyugin, A. & Teerikorpi, P. (2002) (BT02).*

3.3.2 Distances estimates

In order to enable appropriate comparison of polarization properties in the optical and in the submillimetre on lines of sight to stars, I had to obtain an estimate of the reddening to the star.

To achieve this purpose, first of all it was necessary to obtain an estimate of the stars distance (D^*). Excluding 4 stars for which I did not obtain distance estimates, in most cases (90.1%) I obtained the distances inferred from 1.33 billion stars with parallaxes published in the second Gaia data release (DR2), with a procedure that takes into account the non-linearity of the transformation and the asymmetry of the resulting probability distribution⁸ (Bailer-Jones et al., 2018).

When Gaia data was not available (9.9% of cases), I obtained the star distances from the B01, B04, BT01 and BT02 polarization catalogues, or deduced them by inverting the parallax values in the case of the B14 catalogue.

Regarding the errors to be associated with distances, the optical catalogues did not present either errors associated with the distances (B01, B04, BT01 and BT02) or errors associated with the parallax values (B14).

⁸Table with positions and distances estimates is available in electronic form at the CDS via <https://cdsarc.cds.unistra.fr/viz-bin/cat/I/347> (Bailer-Jones C.A.L., 2018).

Therefore, for 9.9% of the stars (245 stars) at this point of the catalogue construction, there are no errors associated with distances.

Regarding the distances extrapolated from Gaia DR2, instead, I have associated as error the half width of the confidence interval of the estimated distance, defined by the difference between the upper and the lower bound, whose values were provided in the electronic catalogue.

Gaia distances were associated with the stars of the optical catalogues by equatorial coordinate-match criterion, with an acceptance radius of variable values. Taking as upper limit a value of the radius equal to $10''$, variable values were chosen depending on the catalogue, trying to obtain a compromise between the precision of the search and the statistics of stars identified.

For B01, B04 and BT01 catalogues, I used an acceptance radius equal to $10''$; for the BT02 catalogue I used a smaller acceptance radius equal to $5''$; finally, I used an even smaller radius for the B14 catalogue, equal to $2''$, being the last catalogue released of those used, and characterized by smaller errors on the coordinates.

Preliminary, I found 1,952 Gaia distances for B14 catalogue stars, discarding 6 ambiguous match cases; 133 Gaia distances for B01 catalogue stars, discarding 10 ambiguous match cases; 59 Gaia distances for BT02 catalogue stars; 18 Gaia distances for BT01 catalogue stars, discarding 1 ambiguous match case; finally, 81 Gaia distances for B04 catalogue stars, discarding 3 ambiguous match cases.

Then, I checked that there was a perfect match between stars coordinates found from Gaia and those of the optical catalogues, investigating and solving the cases of ambiguity, as: the stars *BD+10 2226* and *BD+10 2227* in the B14 catalogue, having very similar coordinates: (164.482;9.671) and (164.549;9.702) as (RA; Dec) in equatorial system, respectively.

Finally, after all controls, I found Gaia distances for about 90% of the total sample: 1,951 stars of the B14 catalogue; 130 of B01; 59 of BT02; 80 of B04 and 18 of BT01. Except in 4 cases without distance estimates, I obtained the missing values from the optical catalogues themselves: 27 stars from the B14 catalog; 110 from B01; 86 from B04 and 22 from BT01.

All these results refereeing to distances origin, are summarized in Table 3.3.

The distribution of the stars distances belonging to the sample built up to now is presented in Figure 3.2, where it is possible to see that the values extend over a wide range, from a minimum of 15 pc up to more than 3,000 pc, but most of the values ($\sim 90\%$) are concentrated in a smaller range: [150 – 550] pc.

3.3.3 Estimates for starlight reddening

Accurate extinction data were needed both for Stokes parameters in extinction, as it is show in Subsections 3.3.4 and 3.3.5, and for stars selection, as it is shown in Subsection 3.3.6.

| | D(Gaia) | D(catalog) | Total D | Missing |
|-------|---------|------------|---------|---------|
| B01 | 130 | 110 | 240 | 2 |
| B04 | 80 | 86 | 166 | |
| B14 | 1,951 | 27 | 1,978 | 2 |
| BT01 | 18 | 22 | 40 | |
| BT02 | 59 | | 59 | |
| Total | 2,238 | 245 | 2,483 | 4 |

Table 3.3: Scheme of how many stars have associated a distance value that derives from Gaia DR2 (Bailer-Jones et al., 2018), in the first column, and how many from the optical catalogs themselves, in the second column, both in total ($\sim 90.1\%$ and $\sim 9.9\%$, respectively) and relative to each catalogue: Berdyugin et al. (2001) (B01); Berdyugin et al. (2004) (B04); Berdyugin, A. et al. (2014) (B14); Berdyugin & Teerikorpi (2001) (BT01); and Berdyugin, A. & Teerikorpi, P. (2002) (BT02). The third column shows the number of stars characterized by a distance estimate, while the last column the number of stars without distance estimates, both in total and for each catalogue.

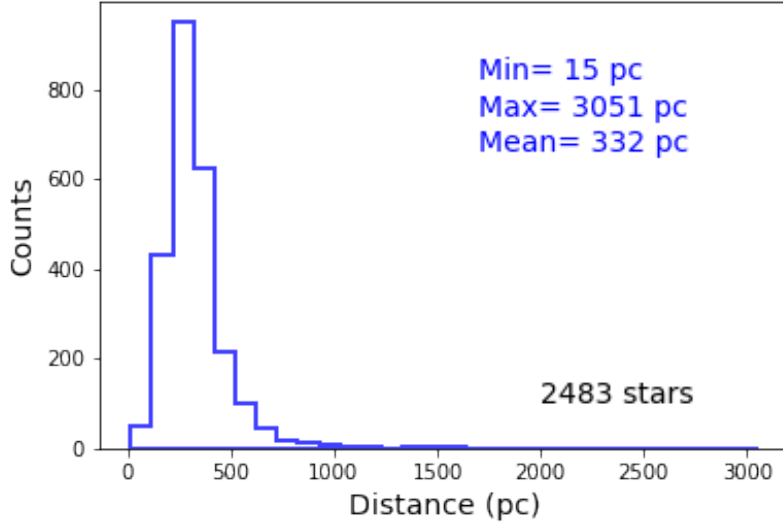


Figure 3.2: Distance distribution of 2,483 stars for which I have both distance estimates and optical polarization data, selected so far from the initial samples: Berdyugin et al. (2001) (B01); Berdyugin et al. (2004) (B04); Berdyugin, A. et al. (2014) (B14); Berdyugin & Teerikorpi (2001) (BT01); and Berdyugin, A. & Teerikorpi, P. (2002) (BT02). The distanced values extend over a wide range, from a minimum of 15 pc up to more than 3,000 pc, but most of the values ($\sim 90\%$) are concentrated in a smaller range: [150 – 550] pc.

I derived an estimate of the reddening, or colour excess, to the star, $E(B - V)^*$, by interpolating at the star distances D^* the PS1-based 3-dimensional reddening data cube composed of 31 maps, each representing a range in distance modulus.

There are three versions of the 3D dust map, and I used the one named `Bayestar17` (Green et al., 2018), which assume the reddening vectors derived by Schlafly et al. (2016). The `Bayestar17` normalization was chosen to predict the same $E(g - r)$ as a unit of the original SFD (Schlegel, Finkbeiner and Davis) reddening map (Schlegel et al., 1998), and to convert `Bayestar17` to extinction in the Pan-STARRS 1 or 2MASS passbands, I had to multiply the value reported by the map by the following coefficients:

| g | r | i | z | y | J | H | K_s |
|-------|-------|-------|-------|-------|-------|-------|-------|
| 3.384 | 2.483 | 1.838 | 1.414 | 1.126 | 0.650 | 0.327 | 0.161 |

Table 3.4: *Bayestar17* extinction coefficients, which were derived assuming zero reddening in the WISE W2 passband. Source: <http://argonaut.skymaps.info/usage>.

So to convert extinction or reddening in the Pan-STARRS 1 or 2MASS passbands in other passbands, I had to assume some relation. For example, by applying the $R_V = 3.1$ Fitzpatrick (1999) reddening law to a 7000 K source spectrum, as done in Table 6 of Schlafly & Finkbeiner (2011), I obtained the following relations to convert the PS1-based reddenings to the Johnson scale $E(B - V)_J$, which I used in my analysis without explicit subscription, as was done in Planck Collaboration et al. (2020a):

$$E(B - V)_J = 0.981 \cdot E(g - r)_{PS1} \quad , \quad (3.12)$$

$$E(B - V)_J = 0.932 \cdot E(r - z)_{PS1} \quad . \quad (3.13)$$

Since the Fitzpatrick (1999) reddening law is different from the reddening law which is assumed to produce the values reported by `Bayestar17`, to obtain the Johnson scale-based reddening $E(B - V)_J$ directly from the `Bayestar17` maps values, and assuming the 3.13 relation, I used this conversion relation:

$$E(B - V)_J = 0.996 \cdot (\text{Bayestar17}) \quad . \quad (3.14)$$

To query `Bayestar17` maps remotely, and to retrieve only the coordinates I was interested in, I used the `dustmaps` Python package (Green, 2018). Since multiple estimates of the distance versus reddening relationship are provided for each line of sight, I used the maximum-probability density estimate, the best-fitting distance-reddening curve (`mode=best`).

The uncertainties related to the reddening maps, $E(B - V)^*$, were estimated from the uncertainty on the PS1-based reddening data at stars distance, assumed as $\sigma(E(B - V)^*)/E(B - V)^* = 0.1$, and the uncertainty on stellar distance, $\sigma(D^*)$, following the procedure described in Appendix G.3 of Planck Collaboration et al. (2020a).

In fact, the distance uncertainty leads to a further uncertainty about the reddening, which can be roughly estimated by considering the variations of the reddening with the variation of the distance in its range of uncertainty, i.e. from $D^* - \sigma(D^*)$ to $D^* + \sigma(D^*)$:

$$\sigma^{D^*}(E(B - V)^*) = \frac{E(B - V)_{D^* - \sigma(D^*)}^* - E(B - V)_{D^* + \sigma(D^*)}^*}{2}, \quad (3.15)$$

where $E(B - V)_{D^* - \sigma(D^*)}^*$ and $E(B - V)_{D^* + \sigma(D^*)}^*$ are the reddening to the star obtained for the limits of distances uncertainty range.

Gathering the two sources of uncertainty, the total uncertainty on the reddening, $E(B - V)^*$, is then:

$$\sigma(E(B - V)^*) = \sqrt{[0.1 \cdot E(B - V)^*]^2 + [\sigma^{D^*}(E(B - V)^*)]^2}. \quad (3.16)$$

From the same maps I also obtained the sub-millimetre optical depth converted into the total reddening along the line of sight, $E(B - V)^\infty$, which was useful both for defining the Stokes parameters in extinction (see Subsections 3.3.4 and 3.3.5), and to apply a selection criterion to the stars sample (see Subsection 3.3.6).

The associated uncertainty was calculated as:

$$\sigma(E(B - V)^\infty) = 0.1 \cdot E(B - V)^\infty \quad (3.17)$$

After removing 50 stars falling outside the region covered by PS1, I also removed 51 stars belonging to the B14 catalog, which had ambiguous reddening values at star distances. The ambiguity was due to the fact that, considering the equatorial or Galactic coordinates, I obtained different reddening values by querying the `Bayestar17` catalogue remotely (a discrepancy up to 8σ , and between 3σ and 8σ for 21 out of 51 stars).

This discrepancy may be due to the fact that these stars are located in borderline positions in maps pixels, and the change of coordinates, calculated with the `astropy` Python package (Astropy Collaboration et al., 2022), causes different reddening values to be obtained. These ambiguous reddening values are shown in Figure 3.3.

There remain 2,382 stars for which I had both reddening estimates and optical polarization data, as is summarized in Table 3.5.

3.3.4 Estimates for optical degree of polarization

I used the MAS (Modified ASymptotic) estimator (Plaszczynski et al., 2014) to debias the degree of polarization in the optical, p_V , by the presence of noise:

$$p_V^{MAS} = p_V - \sigma^2(p_V) \frac{1 - e^{-p_V^2/\sigma^2(p_V)}}{2p_V}, \quad (3.18)$$

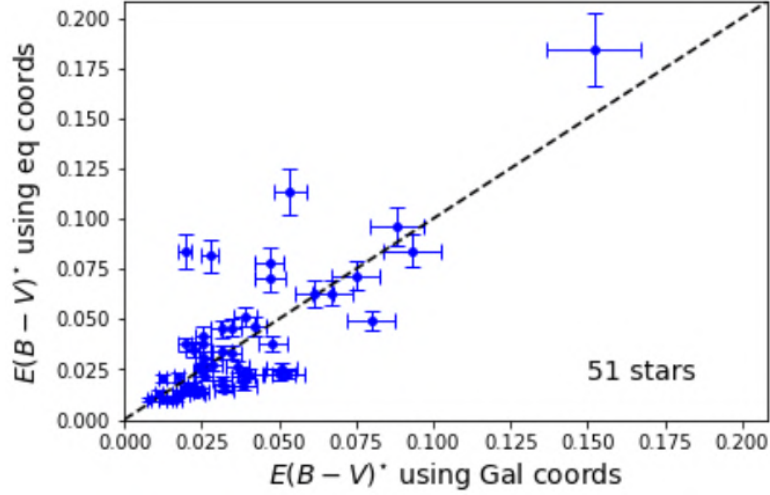


Figure 3.3: Reddening estimates at star distance ($E(B - V)^*$) derived from the *Bayestar17* catalogue, queried remotely, using the same coordinates expressed in Galactic (x axis) and equatorial (y axis) systems. These reddening estimated refer to 51 stars belonging to the *Berdyugin, A. et al. (2014)* catalogue (B14), which I discarded in my sample selection due to a discrepancy up to 8σ , and between 3σ and 8σ for 21 out of 51 stars.

| Initial Sample | After Missing $E(B - V)^*$ | After Ambiguous $E(B - V)^*$ |
|----------------|----------------------------|------------------------------|
| 2,483 | 2,433 | 2,382 |

Table 3.5: Evolution of the number of stars remaining after the selection steps related to reddening estimates at star distances applied sequentially: first, the effect of the lack of such estimates (because of stars falling outside the region covered by PS1), and then the effect of the ambiguity of some estimates. Considering the equatorial or Galactic coordinates systems, I got different reddening values by querying the *Bayestar17* catalogue remotely: a discrepancy up to 8σ , and between 3σ and 8σ for 21 out of 51 stars.

where $\sigma(p_V)$ is the error of the optical degree of polarization. The bias on the polarization angle is usually negligible.

Emission-to-extinction polarization ratios are subject to systematic errors because extinction probes the ISM in the foreground to the star, while emission probes the entire line of sight (*Planck Collaboration Int. XXI, 2015*).

Figure 3.4 presents the histogram of the ratio of the reddening to the star to the total reddening, i.e., the fraction of ISM material that is in front of each star.

For lines of sight with little background emission beyond the star, I would expect a peak near ~ 1 . However, I found a value for the median ratio of the entire sample equal to 0.85.

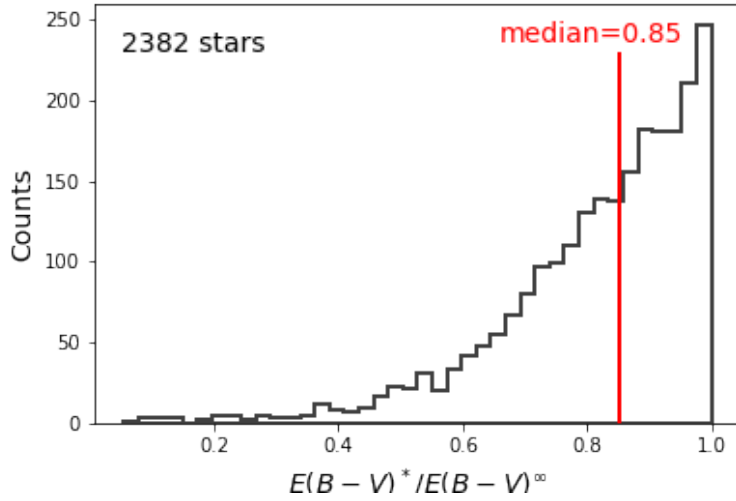


Figure 3.4: Histogram of the ratio of the reddening to the star to the total reddening on the same line of sight, $E(B-V)^*/E(B-V)^\infty$, as derived from the Pan-STARRS1 3D cube (Green et al., 2018), for stars that have passed my preliminary check, and for which both polarization data, distances and reddening estimates are available (2,382 stars). The red line indicates the median ratio.

In general, this might indicate or that for some lines of sight the dust opacity might be higher than for the diffuse ISM adopted here to derive $E(B-V)^\infty$ (see, e.g., Martin et al., 2012; Roy et al., 2013), leading to an overestimation, or the presence of a significant background beyond the star, illustrating the potential for systematic effects on the polarization ratio. In my analysis, I was more inclined to believe this second option.

If I assumed for simplicity that the ISM along the line of sight is uniform (in magnetic-field orientation, dust properties and density), then the polarization ratio would artificially increase linearly with decreasing of the reddening ratio, $E(B-V)^*/E(B-V)^\infty$ (Planck Collaboration et al., 2020a).

Given this bias due to the background, to enable appropriate comparison of polarization properties in the visible and in the sub-millimetre on lines of sight to stars, and so to debias my estimate of the polarization ratio, I corrected the optical polarization degree, p_V , and replaced it by a linear estimate of what its value would be if the star were at infinity, by multiplying the degree of polarization by the ratio of the total reddening along the line of sight on the reddening of the star at its distance:

$$p_V^\infty = p_V \frac{E(B-V)^\infty}{E(B-V)^*}, \quad (3.19)$$

with an associated uncertainty which just depends on the error of the degree of polarization of the star, under the hypothesis of uniform background, equal to:

$$\sigma(p_V^\infty) = \sigma(p_V) \frac{E(B - V)^\infty}{E(B - V)^*} , \quad (3.20)$$

following what was done in [Planck Collaboration et al. \(2020a\)](#). By neglecting the presence of background material beyond the star, and so defining the optical degree of polarization in standard way without the new definition described in Equation 3.19, I found that I would typically overestimate the polarization ratio by 11%, considering all frequency channels of my analysis (353, 217 and 143 GHz).

3.3.5 Stokes parameters in extinction

Using the new definition for the optical degree of polarization if the star were at the infinity, p_V^∞ , as described in Equation 3.19, and the polarization angles expressed in Galactic coordinates and IAU convention, ψ_V , I recovered a representation of the Stokes parameters in extinction: q_V^∞ and u_V^∞ . The Stokes parameters in extinction were expressed in the HEALPIX (COSMO) convention as *Planck* data (see Subsection 3.4.1), where there is a minus sign in front of the Stokes U parameter to switch from the IAU convention to the HEALPIX one (see [Planck Collaboration et al., 2020a](#)):

$$q_V^\infty = p_V^\infty \cos(2\psi_V) , \quad (3.21)$$

$$u_V^\infty = -p_V^\infty \sin(2\psi_V) . \quad (3.22)$$

I calculated the associated uncertainties as the propagation of both the error of the degree of polarization of the star, if the star were at the infinity, and the error of the polarization angle:

$$\sigma(q_V^\infty) = \sqrt{\cos^2(2\psi_V)\sigma^2(p_V^\infty) + 4(p_V^\infty)^2 \sin^2(2\psi_V)\sigma^2(\psi_V)} , \quad (3.23)$$

$$\sigma(u_V^\infty) = \sqrt{\sin^2(2\psi_V)\sigma^2(p_V^\infty) + 4(p_V^\infty)^2 \cos^2(2\psi_V)\sigma^2(\psi_V)} . \quad (3.24)$$

3.3.6 Selection of the lines of sight

The reddening ratio $E(B - V)^*/E(B - V)^\infty$ shown in Figure 3.4 represents the column density ratio between visible and sub-millimeter, and thus the fraction of ISM that is in front of each star. Significant disagreement between the two column density estimates, whether an effect of the medium beyond the star or an effect of different beams, would mean that the polarization data cannot be usefully compared, and this

would lead to incorrect estimates of the emission-to-extinction polarization ratio (Planck Collaboration Int. XXI, 2015).

First, the systematic presence of backgrounds beyond the stars could induce some deviations from orthogonality in the sub-millimeter and visible polarization directions (Planck Collaboration Int. XXI, 2015). Secondly, since the ISM not uniform, the estimates of the polarization ratio could be biased by the presence of a background whose properties are different from those of the foreground to the star (Planck Collaboration et al., 2020a). Therefore, I had to be cautious about including lines of sight with small reddening ratio values in my analysis, and I minimized the contribution of these uncertainties by excluding those lines of sight with an important background emission beyond the star.

I explicitly chose to retain only stars for which $E(B-V)^*/E(B-V)^\infty > 0.75$, setting the same arbitrary threshold as Planck Collaboration et al. (2020a), as a compromise for minimize the bias and to keep enough stars for statistical significance. The agreement of column densities appears to be a good indicator of consistency among between position angles as well, at least statistically, as will be shown in Subsection 3.4.1.

By making this cut, I eliminated 659 stars, thus building a final sample consisting of a total of 1,723 stars selected at high Galactic latitudes, which would be suitable for a polarization properties comparison in the diffuse ISM. The Galactic coordinates of my selected stars, located at high-Galactic latitudes ($b > 30^\circ$ and $b < -60^\circ$) are shown in Figure 3.5.

3.4 Polarized emission data

The *Planck* satellite has left a great legacy in terms of constraints on the properties of Galactic dust, thanks to the full-sky high-frequency coverage of its sub-millimetre emission. This knowledge can be confirmed and extended thanks to the addition of other sub-millimeter data, such as those of the Atacama Cosmology Telescope (ACT) experiment, which improve the resolution at small scales.

My intention is to present an updated quantitative validation of the correlation of polarized dust emission with starlight polarization in the diffuse ISM at high-Galactic latitudes, both with *Planck* data (in the analysis presented here), and with the new ACT data, looking at dust behavior at smaller scales.

I will publish my new estimates of the emission-to-extinction polarization ratio as first author in a forthcoming paper titled “New starlight polarization analysis with ACT and *Planck* data”, where I will also take advantage of the increased resolution and sensitivity of new ACT data to inspect the polarization ratio robustness.

In this analysis I found new estimates of the polarization ratio through a joint correlation of the Stokes parameters pair in emission, (Q, U) , with the Stokes parameters pair in extinction, (q_V, u_V) , at “dust channels” up to 143 GHz. In fact, even if the SNR is lower for the dust polarized emission at smaller frequencies than the preferential channel used to study this Galactic emission, 353 GHz, which is the highest-frequency

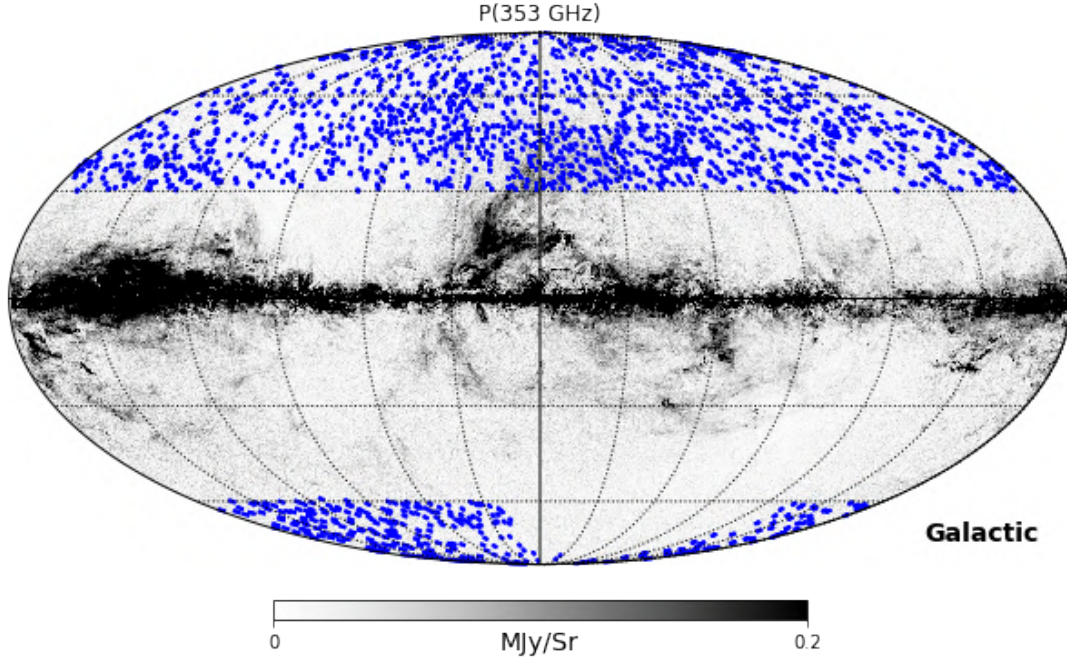


Figure 3.5: *Galactic lines of sight of my selected sample of 1,723 stars, in blue, at high-Galactic latitudes: $b > 30^\circ$ and $b < -60^\circ$. Each star is represented by an area of 0.25 square degrees for illustrative purpose. The background image is the 353 GHz polarized intensity P full-sky map of Planck 2020 release (PR4), in greys scale. The map has a pixel resolution of $6.9'$ ($N_{\text{side}} = 512$) for illustrative purpose, and it is shown in a Mollweide projection, in Galactic coordinates centred on the Galactic centre.*

polarization-sensitive channel of *Planck* (Ade et al., 2010; Planck Collaboration et al., 2014), I wanted to explore the robustness of the theoretical predictions on the comparison between polarized emission data and starlight polarization even at lower frequencies, where dust is still dominant.

To increase the SNR of the emission measurements on lines of sight to the target stars in the diffuse ISM, I decided to not to apply any Gaussian smoothing or downgrading effects to limit the noise in Q and U , but to use a different approach: the so-called photometric aperture method. It consists of taking a circular aperture with a specific radius centered on each star, and calculating the average of the emission and the corresponding noise.

The SNR of the original maps depends on the region studied; however, for simplicity, I adopted a common radius in all sky regions, and I explored the polarization ratio behavior using different choices of radius, each time deriving the polarization ratio value and its uncertainty by following these equations to estimate the Stokes parameters in emission and the relative errors:

$$Q_r = \frac{1}{n} \sum_{i=1}^n Q_i \quad (3.25)$$

$$U_r = \frac{1}{n} \sum_{i=1}^n U_i \quad (3.26)$$

$$\sigma(Q_r) = \frac{1}{n} \sqrt{\sum_{i=1}^n \sigma^2(Q_i)} \quad (3.27)$$

$$\sigma(U_r) = \frac{1}{n} \sqrt{\sum_{i=1}^n \sigma^2(U_i)} \quad (3.28)$$

where Q_i and U_i are the Stokes parameters values of each pixel, i , inside the aperture with radius r ; $\sigma^2(Q_i)$ and $\sigma^2(U_i)$ are the respective variances; finally, n is the number of pixel inside each aperture.

Figure 3.6 shows a visual representation of the photometric aperture method, with some radii of variable size around the star's position, on the 353 GHz Stokes Q 2020 *Planck* map with a pixel resolution of $1.7'$ (corresponding to the HEALPix parameter $N_{\text{side}}=2048$).

The averaging of the emission data can accentuate the beam difference with respect to the stellar probe since, in the visible, interstellar polarization and extinction arise from dust averaged over the angular diameter of the star, which is of the order of less than an arcminute, and so tiny compared to the sub-millimetre instrumental beam ([Planck Collaboration Int. XXI, 2015](#)). However, this approach represents a compromise between achieving higher SNR and maintaining high resolution.

I investigated the robustness of the polarization ratio with respect to the aperture radius, testing the behaviour of polarization ratio estimates with radius values ranging from $5'$ up to 1° . In fact, when considering radii up to 1° , I counted that more than one star fell inside the circular aperture for about 20% of the total stars sample. Going to larger radii, this type of contamination reached about 50%, preventing reliable estimates of the polarization ratio from being obtained.

In detail, I counted how many times more than one star fell inside the circular aperture each time, estimating the reciprocal distances between all possible pairs of stars, and establishing as “intruders” stars those characterized by a reciprocal distance equal to less than that of the aperture radius. With this procedure, I found that: only 4 stars (0.2%) were characterized by mutual distances of less than $5'$; only 12 stars (0.7%) were characterized by mutual distances of less than $10'$; only 35 stars (2.0%) were characterized

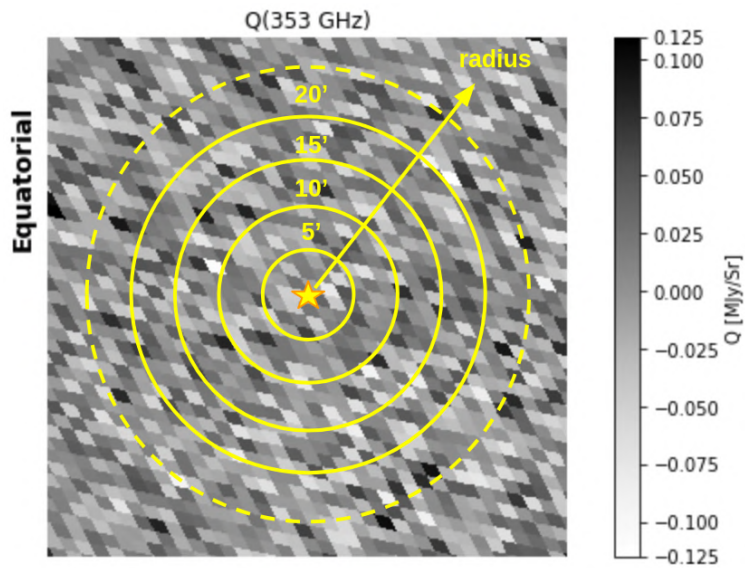


Figure 3.6: A visual representation of the photometric circular aperture method, with some radii varying in size around the star's position. The background map is the 353 GHz Stokes Q 2020 Planck map, with a pixel resolution of $1.7'$ (corresponding to the HEALPix parameter $N_{\text{side}}=2048$). The side of the map is approximately $\sim 1^\circ$. For illustrative purposes, the star is shown here with an angular diameter of $2.5'$, but it is usually smaller, down to half an arcminute.

by mutual distances of less than $20'$; 133 stars (7.7%) were characterized by mutual distances of less than $40'$; 386 stars (22.4%) were characterized by mutual distances of less than 1° ; and 857 stars (49.7%) were characterized by mutual distances of less than 1.3° , as shown in Figure 3.7.

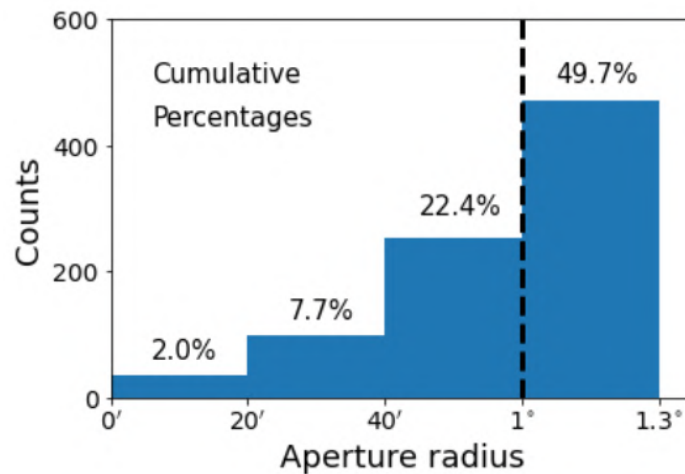


Figure 3.7: Counts of how many times more than one star fall inside each circular aperture characterized by a certain radius, up to 1.3° . The percentages shown are cumulative (up to the right end of the bin) and refer to the total sample of 1,723 stars.

3.4.1 Planck data

My analysis aims to expand the starlight polarization studies involving polarized thermal emission from Galactic dust at 353 GHz, carried out by [Planck Collaboration Int. XXI \(2015\)](#) for translucent lines of sight based on the 2015 data release (PR2, [Planck Collaboration et al., 2016](#)) and by [Planck Collaboration et al. \(2020a\)](#) with same diffuse ISM lines of sights based on the 2018 data release (PR3, [Planck Collaboration I et al., 2020](#)), in order to calculate the polarization ratio, R_P/p , going down to smaller frequencies.

I used the HFI full-sky maps from the *Planck* fourth public release (hereafter the Planck 2020 data release or PR4, [Planck Collaboration Int. LVII, 2020](#)), at 353 GHz, 217 GHz and 143 GHz frequency channels. In particular, I used the Stokes parameters maps, Q and U , in unit of K_{CMB} , and the noise covariance maps, σ_{QQ} and σ_{UU} , to estimate the statistical uncertainties at the position of each star, in unit of K_{CMB}^2 , both with a HEALPix N_{side} parameter of $N_{side} = 2048$ (corresponding to a pixel resolution of $1.7'$).

I converted both the Stokes parameters maps and the noise covariance maps into astrophysical units (MJy/sr) using the same conversion factors of [Planck Collaboration et al. \(2020c\)](#), for each frequency channel: $287.5 \text{ MJy/sr}/K_{CMB}$, $483.7 \text{ MJy/sr}/K_{CMB}$ and $371.7 \text{ MJy/sr}/K_{CMB}$, for the 353 GHz, 217 GHz and 143 GHz channels, respectively. The convention used for the Stokes parameters is to measure polarization angles from the direction of the Galactic north and positively towards Galactic west in accordance with the HEALPix convention used in cosmology⁹. However, as in [Planck Collaboration et al. \(2020a\)](#), I conformed the polarization angles to the IAU convention, being counted positively towards Galactic east, and so I computed them by simply changing the sign of Stokes U in the *Planck* data:

$$\psi = \frac{1}{2} \text{atan2}(-U, Q) \quad , \quad (3.29)$$

where the two-argument function $\text{atan2}(-U, Q)$ is used in place of $\text{atan}(-U/Q)$ to avoid the π -ambiguity.

In my analysis I decided not to exclude lines of sight significantly far from orthogonality. All distributions of the difference in orientation angles between the sub-millimetre and optical polarization data, $\Delta\psi_{S/V}$, peaked around the expected centering on 0° , because of the goodness of my stars sample selection. In fact, for example, the coherence found between the position angles is a good indicator, statistically, of the agreement of the column densities.

⁹See *Planck* Collaboration 2018, The Legacy Explanatory Supplement (ESA), <http://wiki.cosmos.esa.int/planck-legacy-archive>.

Figure 3.8 presents the histogram of $\Delta\psi_{S/V}$ for the 353 GHz channel, calculated in correspondence of the best aperture radius that I found to be valid for all three channels, equal to $14'$, as will be better explain in Section 3.5.

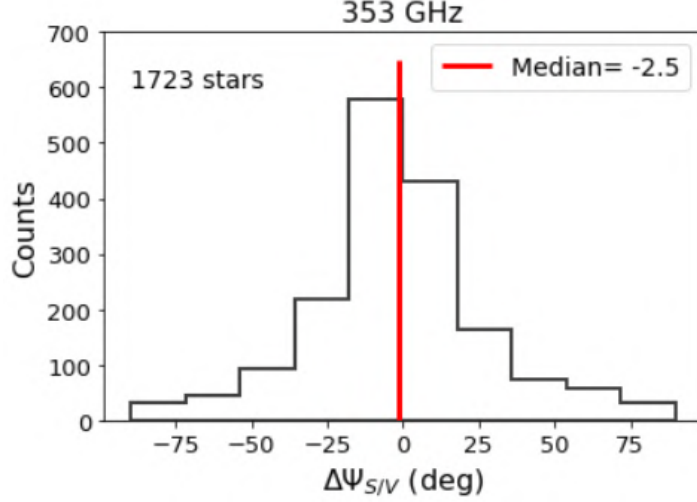


Figure 3.8: Histogram of the difference in polarization angles between *Planck*-derived angles and optical-polarization-derived angles, $\Delta\psi_{S/V}$, considering the 353 GHz *Planck* polarized emission data. The distribution is characterized by a median value equal to -2.5° , slightly different from the expected 0° due to systematic errors.

In this distribution of polarization angles between *Planck*-derived angles and optical-polarization-derived angles I found a median value of -2.5° , slightly different from the expected one of 0° due to systematic errors. However, it is lower than the value found by [Planck Collaboration et al. \(2020a\)](#), equal to -3.1° , with the same channel and similar amplitude of the stars sample (1,656 stars against 1,723 stars of my sample).

Before presenting the results, I anticipate that I had to built a sample of stars common to all *Planck* frequency channels, slightly smaller than the one identified in Section 3.3 consisting of 1,723 stars, as I had to eliminate some stars characterized by disproportionately large errors in the Stokes parameter in emission, which would have compromised the analysis and the polarization ratios estimates. Therefore, the results that will be shown in Section 3.5 for all three frequency channels (353, 217 and 143 GHz), refer to a sample consisting of 1,693 stars.

3.5 Results

Following the approach in both [Planck Collaboration Int. XXI \(2015\)](#) and [Planck Collaboration et al. \(2020a\)](#), I derived the emission-to-extinction polarization ratios, $R_{P/p}$, through a joint correlation of the Stokes parameters pair in emission (Q, U) with

the Stokes parameters pair in extinction (q_V^∞, u_V^∞), and this approach is both motivated and justified in Section 3.2.

I implemented the orthogonal distance regression method to fit the data, using a Python library already built in `scipy` (`scipy.odr`), and considering the uncertainties on both axes. I determined the value of the polarization ratio as the slope of the linear relation, and the relative uncertainty was derived in a standard way from the quality of the fit.

Considering the photometric circular aperture method explained in Section 3.4, I investigated the robustness of the polarization ratio with respect to the aperture radius, testing the behaviour of polarization ratio estimates with radii values ranging from $5'$ up to 1° , for all three channels, as explained in Section 3.4.

The trends of the polarization ratios with respect to the aperture radii are shown in Figures 3.9, 3.10 and 3.11 for the three channels at 353, 217 and 143 GHz, respectively.

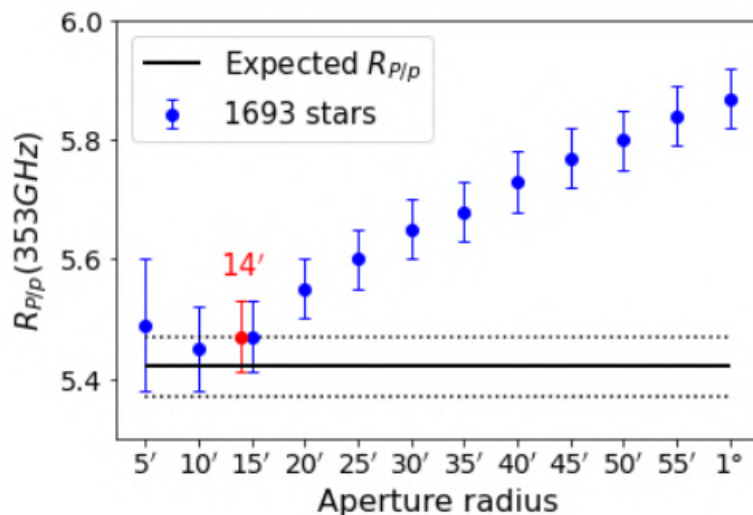


Figure 3.9: The trend of the emission-to-extinction polarization ratio with respect to the radius of the photometric circular aperture, between $5'$ and 1° , shown with discrete steps of $5'$, considering the polarized emission at 353 GHz. The best aperture radius found as the best compromise, considering these trends for all three frequency channels together, in terms of minimum of residuals with respect to the expected polarization ratios for each channel, is highlighted in red. It was obtained in correspondence of $14'$, at which I found a polarization ratio equal to $R_{P/p} = 5.47 \pm 0.06 \text{ MJy/sr}$ for the 353 GHz polarized emission, compatible with the result expected by the theory within 1σ , equal to $R_{P/p} = 5.42 \pm 0.05 \text{ MJy/sr}$.

I found the best aperture radius among those considered as the best compromise, considering the trends of the polarization ratios with respect to the aperture radius for all three frequency channels together, in terms of minimum of residuals with respect to the expected polarization ratios for each channel. This best radius for evaluating polarization ratio estimates was obtained at $14'$.

All the polarization ratios found in correspondence with this radius resulted compatible with those expected by the theory within 1σ , whose values were presented in Section 3.2, leading to new final estimates equal to:

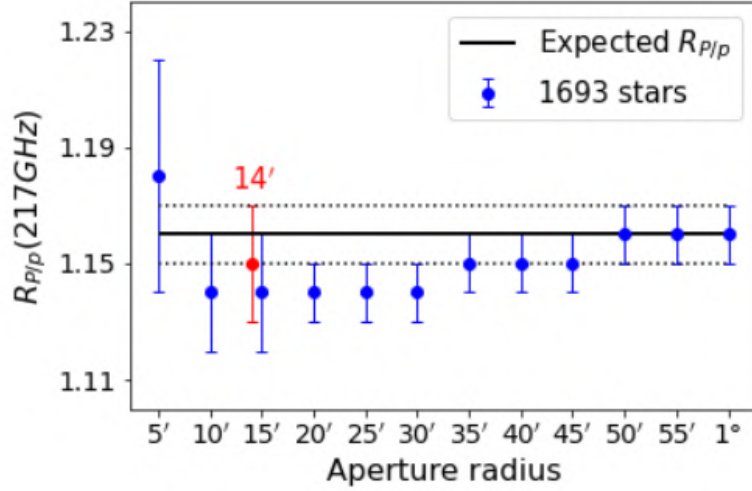


Figure 3.10: The trend of the emission-to-extinction polarization ratio with respect to the radius of the photometric circular aperture, between $5'$ and 1° , shown with discrete steps of $5'$, considering the polarized emission at 217 GHz. The best aperture radius found as the best compromise, considering these trends for all three frequency channels together, in terms of minimum of residuals with respect to the expected polarization ratios for each channel, is highlighted in red. It was obtained in correspondence of $14'$, at which I found a polarization ratio equal to $R_{P/p} = 1.15 \pm 0.02$ MJy/sr for the 217 GHz polarized emission, compatible with the result expected by the theory within 1σ , equal to $R_{P/p} = 1.16 \pm 0.01$ MJy/sr.

- $R_{P/p} = 5.47 \pm 0.06$ MJy/sr for the 353 GHz channel;
- $R_{P/p} = 1.15 \pm 0.02$ MJy/sr for the 217 GHz channel;
- $R_{P/p} = 0.294 \pm 0.010$ MJy/sr for the 143 GHz channel.

The final correlation plots between the Stokes polarization parameters in emission and in optical extinction, giving the new estimates of the emission-to-extinction polarization ratio I obtained, calculated with an aperture radius of $14'$, are shown in Figures 3.12, 3.13 and 3.14.

3.6 Conclusions

In the context of polarized dust characterization, I contributed to the research topic by presenting an updated quantitative validation of the correlation between starlight polarization and polarized dust emission in the diffuse ISM at high-Galactic latitude. I was motivated to examine this correlation since many of factors driving interstellar polarization in the visible, as the grain shape and alignment efficiency, and the magnetic field orientation, affect also the diffuse dust polarized emission in the sub-millimetre in similar ways, and they are hard to disentangle.

I performed a novel analysis to extend existing results of [Planck Collaboration et al. \(2020a\)](#) based on the PR3 *Planck* 353 GHz emission channel, using the last data release

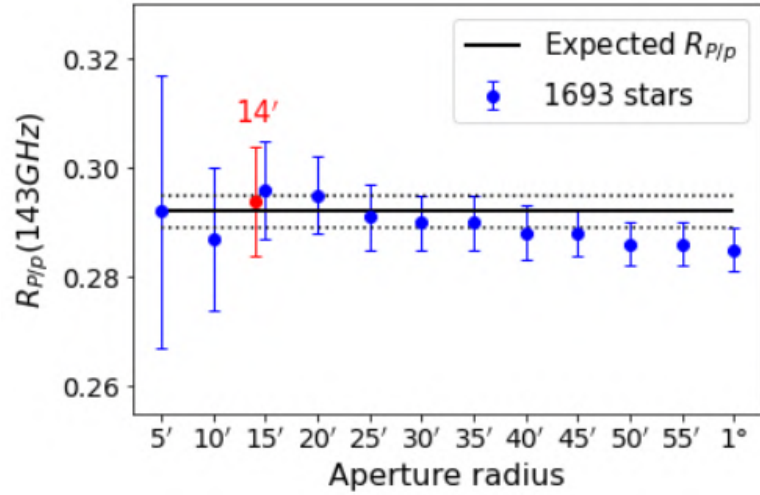


Figure 3.11: The trend of the emission-to-extinction polarization ratio with respect to the radius of the photometric circular aperture, between $5'$ and 1° , shown with discrete steps of $5'$, considering the polarized emission at 143 GHz. The best aperture radius found as the best compromise, considering these trends for all three frequency channels together, in terms of minimum of residuals with respect to the expected polarization ratios for each channel, is highlighted in red. It was obtained in correspondence of $14'$, at which I found a polarization ratio equal to $R_{P/p} = 0.294 \pm 0.010$ MJy/sr for the 143 GHz polarized emission, compatible with the result expected by the theory within 1σ , equal to $R_{P/p} = 0.292 \pm 0.003$ MJy/sr.

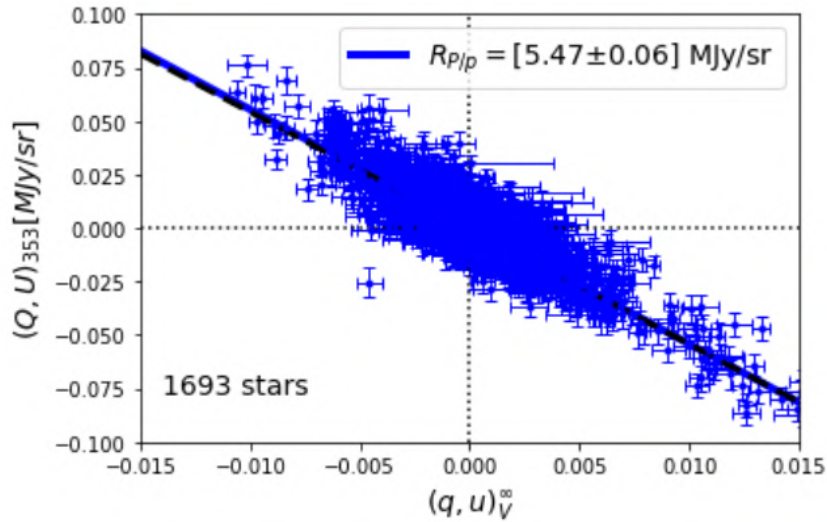


Figure 3.12: Correlation between Stokes polarization parameters in emission at 353 GHz, (Q, U) , and in optical extinction, $(q, u)_{V}^{\infty}$, which gives an estimate of emission-to-extinction polarization ratio equal to $R_{P/p} = [5.47 \pm 0.06]$ MJy/sr, with an aperture radius of $14'$. The expected value of $R_{P/p} = 5.42$ MJy/sr is shown as a dashed black line.

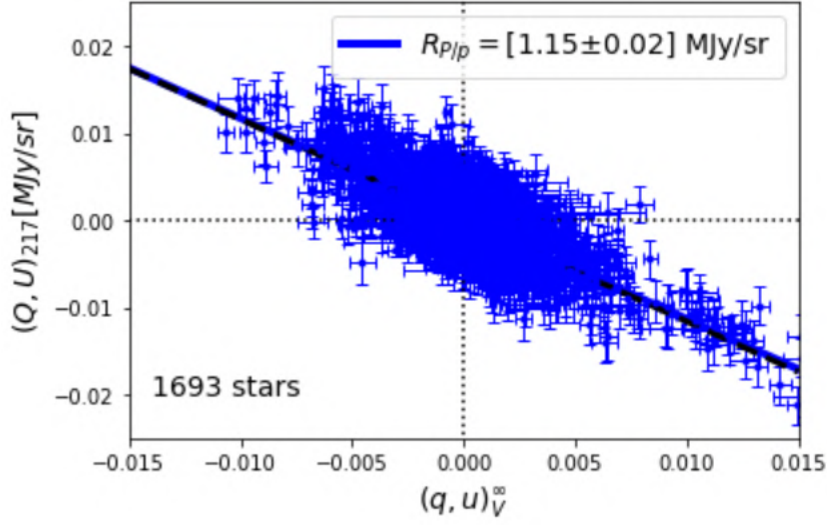


Figure 3.13: Correlation between Stokes polarization parameters in emission at 217 GHz, (Q, U) , and in optical extinction, (q_V^∞, u_V^∞) , which gives an estimate of emission-to-extinction polarization ratio equal to $R_{P/p} = [1.15 \pm 0.02] \text{ MJy/sr}$, with an aperture radius of $14'$. The expected value of $R_{P/p} = 1.16 \text{ MJy/sr}$ is shown as a dashed black line.

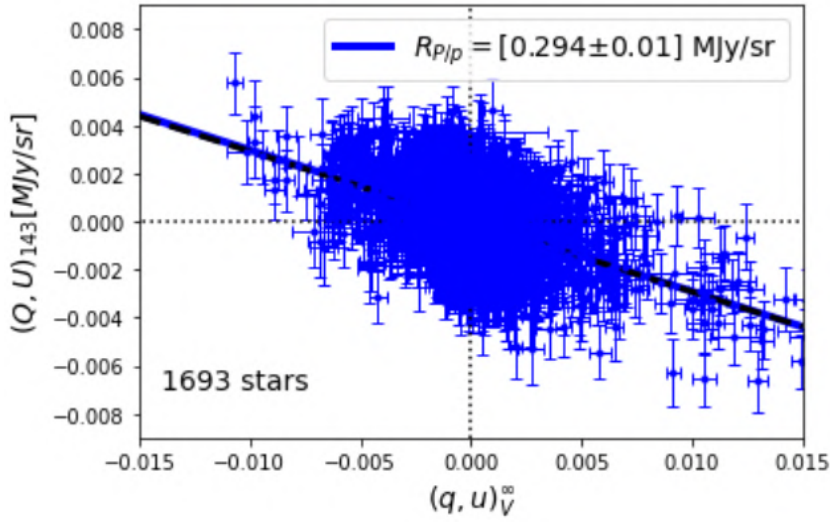


Figure 3.14: Correlation between Stokes polarization parameters in emission at 143 GHz, (Q, U) , and in optical extinction, (q_V^∞, u_V^∞) , which gives an estimate of emission-to-extinction polarization ratio equal to $R_{P/p} = [0.294 \pm 0.010] \text{ MJy/sr}$, with an aperture radius of $14'$. The expected value of $R_{P/p} = 0.292 \text{ MJy/sr}$ is shown as a dashed black line.

(PR4, [Planck Collaboration Int. LVII, 2020](#)) and going to smaller frequencies down to 143 GHz. The only value published in literature refers to the 353 GHz.

Even if the SNR is lower for dust polarized emission at smaller frequencies, I wanted to explore the robustness of the theoretical predictions on the comparison between polarized emission and starlight polarization data even at lower frequencies, where dust is still dominant.

I concentrated the analysis on high-Galactic latitudes and diffuse ISM lines of sights since more homogeneous properties might be expected, and for which the most comprehensive observational constraints on dust models are already available and exploited.

I obtained new original experimental estimates of the emission-to-extinction polarization ratio, a diagnostic involving dust emission and extinction for the aligned grains population, consistent with those predicted by dust models.

Using existing stellar catalogues of Berdyugin series (Berdyugin et al., 2001; Berdyugin & Teerikorpi, 2001; Berdyugin, A. & Teerikorpi, P., 2002; Berdyugin et al., 2004; Berdyugin, A. et al., 2014), Green et al. (2018) reddening estimates, and Gaia DR2 distances (Bailer-Jones et al., 2018), I built a stellar sample of 1693 stars. To increase the SNR of the emission measurements on lines of sight to the target stars in the diffuse ISM, and as a compromise between achieving higher SNR and maintaining high-resolution, I implemented the photometric aperture method, which allowed me to explore the polarization ratio behavior using different radius choices centered on each star.

The original maps SNR depends on the region being studied; however, I adopted a common radius in all sky regions, and I explored the polarization ratio behavior using different radius choices, deriving each time the mean polarization ratio value and its uncertainty.

In correspondence with minima of residuals with respect to the expected values, obtained in the function describing the trend of the polarization ratios with respect to the aperture radii, I found the optimal aperture radius at which compute the polarization ratios estimates equal to $14'$ for all three frequency channels considered: 353, 217 and 143 GHz. Then, I found new estimates of the emission-to-extinction polarization ratios through a joint correlation of the Stokes parameters pair in emission, (Q, U) , with the Stokes parameters pair in extinction, (q_V, u_V) , at the three frequency channels, being this approach both motivated and justified, since it has several advantages.

The new original estimates of the polarization emission-to-extinction ratios I found are:

- $R_{P/p} = [5.47 \pm 0.06]$ MJy/sr for the 353 GHz channel;
- $R_{P/p} = [1.15 \pm 0.02]$ MJy/sr for the 217 GHz channel;
- $R_{P/p} = [0.294 \pm 0.010]$ MJy/sr for the 143 GHz channel.

These new value I obtained can provide strong constraints for models of dust polarized emission, and further empirical validation of many of the common underlying assumptions of the models.

This project was designed in collaboration with the Galactic Science group of the Atacama Cosmology Telescope (ACT) collaboration, of I which I am a junior member.

ACT is a high-resolution ground-based telescope in the Chilean Desert, already active since 2007 and arrived at its latest data collection. My intention is also to take advantage of the increased resolution and sensitivity of new ACT data to inspect the robustness of the emission-to-extinction polarization ratio, observing dust behavior at smaller scales. I will publish all these results as first author in a paper in preparation titled “New starlight polarization analysis with ACT and *Planck* data”.

Chapter 4

Observational strategy simulations to map polarized Galactic dust emission as CMB foregrounds with the BLAST experiment

4.1 Introduction

The polarized thermal emission from interstellar dust in our Galaxy, which arises due to magnetic fields, dominates the polarized submillimeter sky above frequencies bigger than ~ 70 GHz, as was shown by *Planck* satellite ([Planck Collaboration X, 2016](#); [Planck Collaboration Int. XXII, 2015](#)). And not only is the strength of the polarized dust emission greater than previously thought, but also there are no “clean windows” for CMB observations where dust emission can be ignored ([Planck Collaboration Int. L, 2017](#)). Therefore, the characterization of dust as foreground is one of the most important requirements in cosmological questions, and in particular in subtracting this dust signal from polarized measurements to extract the very weak CMB *B*-mode signal caused by primordial gravitational waves, predicted by the cosmic inflationary theory.

In this scenario, multi-band measurements and a knowledge of the spectral properties of the phenomenon that produce dust foreground are required. In particular, it is necessary to have a thorough knowledge of the emission spectrum of the ISM dust, for which there are a variety of models, but not enough measurements to select which the different models best describes the observed trends.

And in addition to their cosmological goal, these efforts are also aimed to furnish sensitive new probes of the structure and physics of the Milky Way’s magnetic ISM.

Considering that the angular power spectrum of dust emission at CMB frequencies has a roughly power-law dependence which decreases with decreasing angular scale, the small scale features of the Galactic dust are often assumed to have a negligible effect on the CMB power spectrum at small scales. However, the exact behavior of the dust power spectrum on small scales is not known, and the presence or not of deviations from the power-law is uncertain (such as a steepening of the slope at higher multipoles [Caldwell et al., 2017](#)).

Current experiments work at frequencies that aren't high enough and typically have lower resolutions as well. They assume spectral patterns recognizable through multi-band measurements. However, the assumption that dust emission pattern is consistent with higher resolution observations has no experimental evidences at the moment.

Therefore, understanding the details of the foreground emission at small scales is crucial. And with the general aim of an adequate construction of polarized foreground removal templates to clean a CMB polarization map, it is necessary to take high-sensitivity sub-millimeter wavelengths maps where dust signal dominates, at several frequencies well above ~ 100 GHz.

In this context, a very important synergy in the constraining power of the extended spectral range on dust emission spectra, derives from the higher frequency balloon-borne experiments.

In intensity they will offer better constraints on SED fits to provide temperature and column density information in a variety of environments, from diffuse regions off the Galactic plane up to dense star forming regions. The increased spectral range allows for: more free parameters to be fitted in the dust SED and polarimetry fits; probes of the polarization spectral dependence on the environment; the ability to constrain multiple dust populations along the line of sight, and to examine the viability of more complex foreground models in diffuse environments, favored for CMB observations.

Balloons also offer a huge increase in sensitivity compared to ground based telescopes: ground-based observations at submillimeter wavelengths are affected by the fact that the atmosphere absorbs submillimeter light, and varies on large angular scales, and this limits ground experiments to observing in narrow wavelength bands, avoiding atmospheric emission lines, and restricts the observations to small angular scales. The ideal place to put a submillimeter telescope to solve problems caused by the Earth's atmosphere is in space, but a cheaper and faster alternative is to suspend it from a stratospheric balloon, which operate at more than 30 Km altitude. This allows observations to be done above 99.5% of the atmosphere in a near-space environment, unrestricted by atmospheric transmission, at a fraction of the cost of a satellite mission.

One of the most important balloon experiment is the Balloon-Borne Large Aperture Submillimeter Telescope (BLAST). It is a sub-orbital mapping experiment for characterizing the polarized submillimeter sky at high angular resolution, with a long history behind it that started in 2003, with a series of successively improved telescopes.

It was designed to study the role of magnetic fields in regulating star formation; and it is also uniquely suited to provide access to the most sensitive measurements of polarized Galactic dust emission to date of small regions of the diffuse ISM (degree scale), in areas relevant for CMB observations, by penetrating into the small scale structure of these regions. And so, for the next 10 years or so, BLAST should be crucial in address key understanding of interstellar dust.

To understand the work I have done and which will be described later, it is important to underline another relevant alternative for understanding dust foregrounds, and for predicting its emission.

Since from dust polarization measurements it is possible to obtain measurements of the Galactic magnetic field, as the latter showed a high degree of alignment with the structures of Galactic neutral hydrogen (HI), by mapping the HI emission line it is possible to probe the structure of the Cold Neutral Medium (CNM; [Martin et al., 2015](#)).

Moreover, the *Planck* dust data and the HI4PI survey ([HI4PI Collaboration, 2016](#)), in a joint analysis of full sky Galactic HI measurements with the GASS ([Kalberla & Haud, 2015](#)) and EBHIS ([Winkel et al., 2015](#)) surveys, indicated that most of the filamentary dust structures in the diffuse ISM are in the CNM phase ([Ghosh et al., 2017](#)).

This suggests that HI data trace the same structures that act as dust foregrounds, and so HI data can help to guide CMB observations.

My main role as a junior member of the BLAST collaboration was to give my contribution in the planning of the observational strategy, as memembr of the Science team: I identified some diffuse ISM fields to be observed in order to characterize the polarized dust emission as a CMB foreground, both for the BLAST-TNG (The Next-Generation) experiment and for his successor, the proposed BLAST Observatory.

During the work I benefited from the collaboration of other BLAST's members, mainly Susan E. Clark¹ and Laura M. Fissel², as will be detailed in the Chapter.

To reach this goal, the work I implemented and which will be described here, it is focused on developing an algorithm to identify the best diffuse dust regions of the sky (“patches”) with features similar to the ones of diffuse, low-intensity and highly-polarized dust regions, to observe for CMB foreground characterization. I considered a series of variables and constraints searching to find the optimal combination, such as: the target field visibility, the sky patch size, the observation time, and the instrument sensitivity and resolution.

This algorithm defined a metric, so as to allow the choice of sky regions on the basis of various criteria, shifting through all the possibilities within the target field visibility, which is variable within the launch window.

¹Assistant Professor at Department of Physics, Stanford University, CA, USA.

²Assistant Professor at Department of Physics, Engineering Physics & Astronomy, Queen's University, Kingston, ON, Canada.

This work of identification of diffuse ISM fields targets that the BLAST-TNG experiment was supposed to observe during the last launch campaign in January 2020, was developed during the first months of my PhD, November and December 2019. The sky target that I identified has been included in the flight plan of the experiment by the BLAST collaboration with high priority. Unfortunately, it was not possible to observe it due to the premature interruption of the mission, caused by an accidental damage. Therefore, the analysis I carried out was hindered by accident during BLAST-TNG deployment. This event suggests that the reason for the lack of published results is attributable to this accident of the experiment itself, totally independent of my work, which on the contrary has been used in more than one proposal sent to subsequent calls from NASA to repeat the BLAST experiment.

In fact, the set of simulations and selection methods I produced to identify the sky targets was considered a major work by the BLAST collaboration itself, so much so that they requested me to update the work to identify new sky targets for the successor of the BLAST experiment: BLAST Observatory (Lowe et al., 2020, currently being proposed to NASA). The two new diffuse ISM fields I identified, suitable for two different performance scenarios (both the one based on current telescope design and the one based on the mission top level requirements to meet all science objectives), were included in the observational strategy described in the proposal, and used to make theoretical predictions by the Science team, as will be better explained in detail in the Chapter. All the codes I developed for this purpose can be found in the BLAST github repository.

4.2 The Balloon-borne Large-Aperture Submillimeter Telescope experiments

The Balloon-Borne Large Aperture Submillimeter Telescope (BLAST) is a sub-orbital mapping experiment for characterizing the polarized IR/submillimeter sky at high angular resolution, and it was designed to study both the role of magnetic fields in shaping the structure and evolution of the ISM, and the role of magnetic fields in regulating star formation, by mapping polarized thermal emission from interstellar dust.

BLAST has a long history which begins in 2003, with a series of successively improved experiments, as it is summarized in Figure 4.1.

The first experiment, named BLAST, observed simultaneously in broadband (30%) spectral windows at three frequency channels (600, 857 and 1200 GHz, or, equivalently, 250, 350, and 500 μm). The optical designed was based on a 1.8 m diameter aluminum primary mirror, providing a diffraction-limited resolution of 30'' at 250 μm . It had a total of 266 NTE detectors cooled to a temperature of 300 mK. BLAST performed a test flight in 2003, and two scientifically productive Long-Duration Balloon (LDB) flights: a 100 hr flight from Kiruna (Sweden) to Victoria Island (northern Canada) in 2005; and a 250 hr circumpolar flight from McMurdo Station (Antarctica) in 2006 (Pascale et al., 2008).

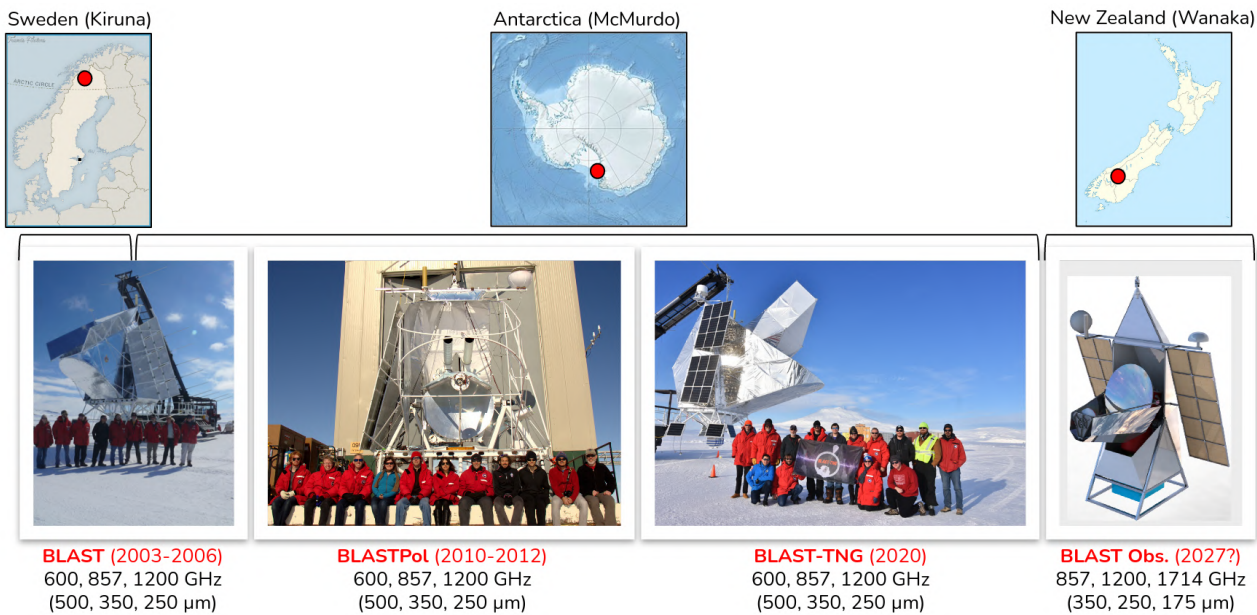


Figure 4.1: The Balloon-Borne Large Aperture Submillimeter Telescope (BLAST) timeline, with the series of successively improved experiments, with the launch location (on the top) and the frequency coverage (on the bottom): from BLAST in 2003, up to BLASTPol, BLAST-TNG, and the future proposed BLAST Observatory, which is designed to observe up to 1.7 THz. Credit for photos to: BLAST collaboration.

The second experiment was BLASTPol, which had the same characteristics as the first BLAST, but could also observe in polarization. The polarization sensitivity was achieved via the insertion of polarized grids in front of the detector arrays, and the polarization modulation was achieved via a stepped achromatic Half-Wave Plate (HWP). BLASTPol performed two LDB flights from McMurdo Station (Antarctica) in 2010 and 2012, which produced thousands of polarization vectors in several molecular cloud targets (Fissel et al., 2016).

Just for knowledge, regarding the one- versus two-component dust model debate, which provides for different spectral indices in total intensity versus polarization, observations from BLASTPol have found consistency between the dust SED in total intensity and polarization, with deviations not exceeding $\sim 10\%$ (Ashton et al., 2018). This seems to suggest a more likely single-component model, such as the “astrodust” one (Draine & Hensley, 2021).

The successor of BLASTPol was BLAST-TNG, which I will talk about in Subsection 4.2.1. It featured upgrades to nearly all major systems, including: the telescope, with a 2.5 m diameter aluminum primary mirror; 3,000 Microwave Kinetic Inductance Detectors (MKIDs) cooled to 280 mK; readout electronics; control and pointing systems. Unfortunately, BLAST-TNG performed just a very short flight of about ~ 15 hr, from McMurdo Station (Antarctica) in 2020, since the payload was damaged by falling debris during launch.

Finally, BLAST Observatory (Lowe et al., 2020), the proposed Super-Pressure Balloon-borne polarimeter for a future Ultra-Long Duration Balloon (ULDB) campaign from Wanaka (New Zealand) in 2028, which is designed to observe up to 1.7 THz with 9,000 MKID detectors cooled to a temperature of 100 mK. It will be described in the dedicated Subsection 4.2.2.

The BLAST experiment is an infrared polarimeter that measures the polarized Stokes parameters Q and U of the incoming sky light. The telescope is composed of a large primary mirror, a secondary mirror, and a series of re-imaging optics cooled down to 1 K in a liquid nitrogen-helium cryostat which hosts the focal plane (Galitzki et al., 2014). A series of dichroic filters direct and split light onto focal-plane arrays of bolometers, cooled below 300 mK, up to 100 mK. The use of dichroic filters allows BLASTs to observe simultaneously in three frequency bands. Unlike ground based telescopes it is not restricted to observe through narrow windows in the atmospheric transmission spectrum. Instead, BLASTs observe in three wide frequency bands ($\Delta f/f \approx 30\%$), which bracket the peak of 10–20 K thermal dust emission. Each detector array has a photo-lithographed linear polarizer, so a metal mesh polarizing grid, mounted in front of the feed-horn arrays for each bolometer detector array. The polarizing grid is patterned so that each adjacent detector samples only the vertical or horizontal component of the incoming radiation, in order to alternate the polarization component sampled by 90° from horn-to-horn and thus bolometer-to-bolometer along each row, since BLASTs scan primarily in azimuth so a source on the sky passes along a row of detectors. The rows are parallel to the nominal scan direction.

This alignment allows for sampling of either a Q or U Stokes parameter on a timescale that is much shorter compared to the array’s common mode $1/f$ noise, which has a f_{knee} at 0.035 mHz (Pascale et al., 2008) or higher. The sampling timescale of the Stokes parameters is ~ 0.125 s, which is determined by the detector separation (45 at 250 μm) and typical scan speed of the order of $\sim 0.5^\circ\text{s}^{-1}$. The field at the end of each feed-horn is approximately Gaussian, which results in very small leakage in polarization between adjacent pixels, estimated to be less than 0.07% (Galitzki et al., 2014).

A sapphire achromatic HWP was added to the optical configuration of BLASTPol and BLAST-TNG to provide additional polarization modulation (Moncelsi et al., 2013), while it was then eliminated for the BLAST Observatory proposal.

The BLAST’s detectors produce Time Ordered Data (TOD) which contains the signals acquired while the telescope scans the sky. This instrument is sensitive to the contrast of the sky signal from different directions, which translates into a time varying signal in the TOD thanks to the telescope scan strategy.

4.2.1 The BLAST-TNG experiment

The Next-Generation Balloon-borne Large Aperture Submillimeter Telescope (BLAST-TNG) was a submillimeter mapping experiment part of NASA’s Long Duration Balloon

(LDB) program, the successor to the BLASTPol and BLAST experiments. It was a particularly complex payload, with multiple subsystems that worked together to allow the observations.

With a long hold time cryogenic receiver, it was designed to observe for 28 days and make high-sensitivity maps, at sub-arcminute resolution, of the submillimeter polarized thermal emission from interstellar dust.

It was characterized by an high pixel count, and about ~ 3000 polarization sensitive Microwave Kinetic Inductance Detectors (MKIDs) operating simultaneously over 30% bandwidths centered at at 250, 350, and 500 μm (1.2 THz, 857 GHz, and 600 GHz, respectively). Each band was characterized by a diffraction limited resolution of 25", 35", and 50" respectively, making it capable of producing maps of diffuse ISM with higher fidelity than the 353 GHz *Planck* maps. In Table 4.1 are schematized the channels with their respective resolutions.

| Frequency (GHz) | Wavelength (μm) | Beam FWHM (") |
|--------------------|---------------------------------|------------------|
| 1200 | 250 | 25 |
| 857 | 350 | 35 |
| 600 | 500 | 50 |

Table 4.1: *The BLAST-TNG wavebands with their respective resolutions.*

With this experiment, the BLAST collaboration pioneered the concept of using a balloon mission as an “observatory”, whose observing time was also available to the scientific community.

During the 2019-2020 campaign, BLAST-TNG was launched from McMurdo Station in Antarctica during the southern summer, on January 6th 2020, as part of NASA’s LDB program. A photo of his payload his shown in Figure 4.2.

Unfortunately, during launch operations, the collar hit the payload³, and in particular one of the structural components, the spreader bar. The damage was not immediately spotted since this component was designed with a very high factor of safety. However, the carbon fiber structure slowly degraded until a catastrophic failure, which meant that it was no longer possible to point the telescope in azimuth, and therefore to make observations, after approximately 15 hours of flight. In Figure 4.3 is shown the flight path (Coppi et al., 2020).

Despite this unfortunate event and the short flight, every subsystem worked as expected: the team was able to get valuable data about the performance of the detectors and other subsystems that would prove their functionality on a balloon platform (Coppi et al., 2020; Lowe et al., 2020).

³Every launch has the intrinsic risk of the payload being hit by the collar, but statistics of previous launches show that the probability is very low.

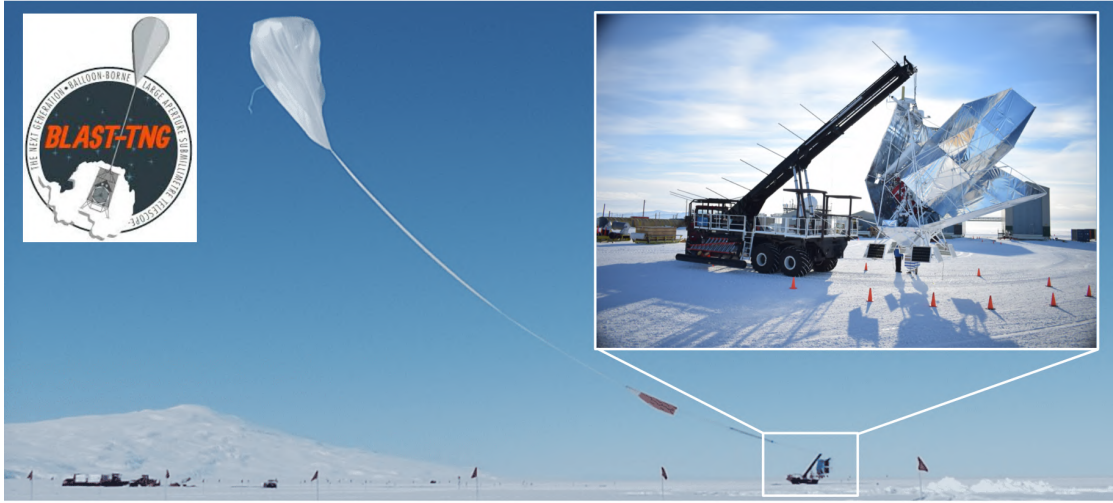


Figure 4.2: The BLAST-TNG payload from the Long Duration Balloon (LDB) facility at McMurdo Station (Antarctica) in January 2020, during the 2019-2020 campaign. Credit for photos to: BLAST collaboration.

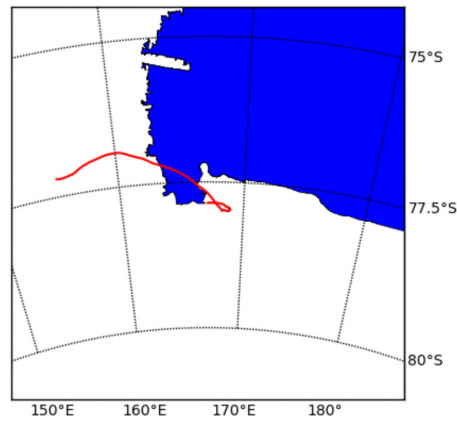


Figure 4.3: Flight path of the BLAST-TNG payload from the Antarctic LDB facility in January 2020, before the catastrophic failure after approximately 15 flight hours (Coppi et al., 2020).

I myself have also analyzed some of these data: in particular, about 5,000 star camera images, with the aim of reconstructing the post-flight pointing solution, as will be described in detail in Chapter 5. The star camera solutions I found are listed in Coppi et al. (2020).

4.2.2 The BLAST Observatory experiment

The Balloon-borne Large Aperture Sub-millimeter Telescope (BLAST) Observatory is a proposed Super-Pressure Balloon (SPB) experiment, and aims to continue the legacy left by BLAST-TNG.

It is a balloon-borne polarimeter designed for a future Ultra-Long Duration Balloon (ULDB) campaign, for a 5-year project, with the science flight midway through the last year. To maximize scientific output while staying within the stringent super-pressure weight envelope, BLAST will feature new 1.8 m off-axis optical system contained within a lightweight monocoque structure gondola (Lowe et al., 2020), which is shown in Figure 4.4.

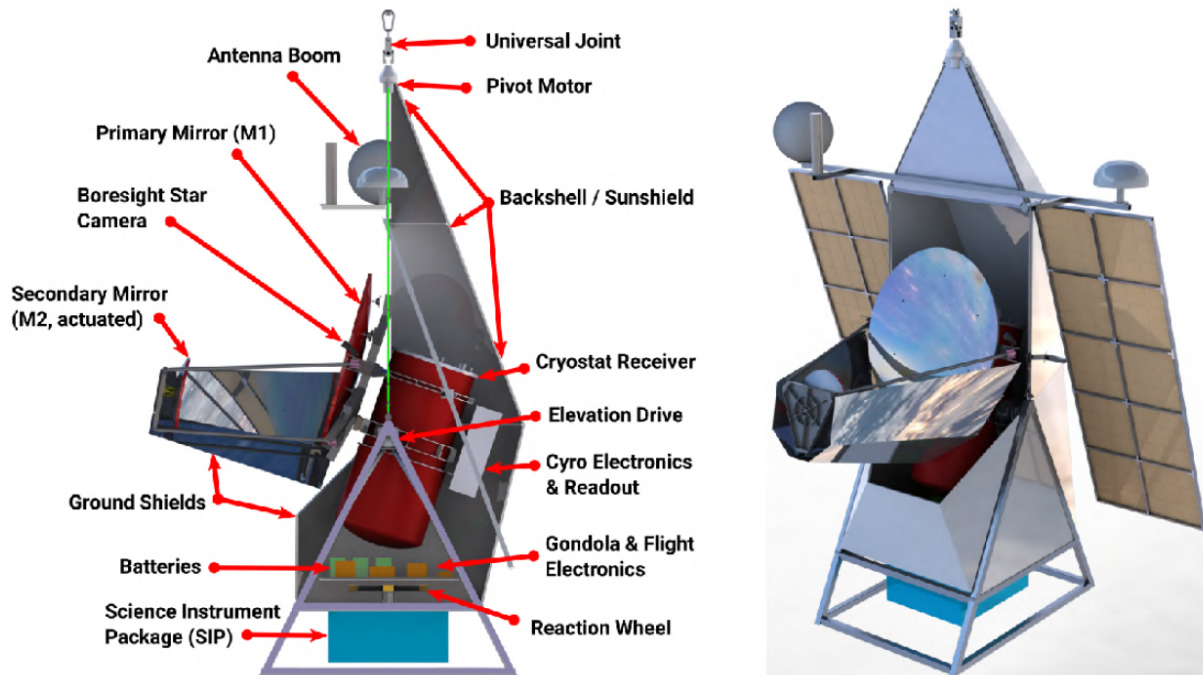


Figure 4.4: The BLAST Observatory gondola rendering. The outer-most dimensions are: $5.6\text{ m} \times 4.4\text{ m} \times 7.0\text{ m}$ ($W \times L \times H$). The height refers to the hook height, and the width includes the solar arrays. Suspension ropes are highlighted in green on the left side view (Lowe et al., 2020).

It will observe at three frequency channels simultaneously: 175 , 250 and $350\ \mu\text{m}$ (or, equivalently, 857 GHz , 1.2 and 1.7 THz), with a total of $8,274$ polarization-sensitive MKIDs detectors cooled to 100 mK . The $350\ \mu\text{m}$ band will be characterized by a diffraction limited resolution of $55''$, the $250\ \mu\text{m}$ band by a diffraction limited resolution of $39''$, while the higher frequency band at $175\ \mu\text{m}$ will be characterized by a diffraction limited resolution variable between $28''$ and $35''$, depending on the performance scenario considered, as I will describe better on the bottom of this Subsection.

Even the BLAST Observatory is conceived as an “observatory” available to the entire community, like its predecessor: 70% observation time will be dedicated to observations for BLAST scientific goals; the remaining 30% will be open to proposals from the wider astronomical community through a shared-risk program.

Previous flights utilized the circumpolar flight LDB campaigns (from Kiruna or McMurdo), providing access to the limited near-polar sky. But to achieve current scientific goals, such as to access to a statistically significant sample of star-forming regions, it requires larger sky coverage. In the BLAST Observatory experiment this is enabled by a mid-latitude flight from the Wanaka base, in New Zealand, offering increased access to the southern sky, with the possibility to reach a total of about 70% of the sky respect with the 15% reachable from Antarctica.

The BLAST Observatory experiment will map polarized thermal dust emission in large regions (tens of square degrees) both in Giant Molecular Clouds (GMC) and in diffuse ISM fields of the Milky Way, allowing to reach three main science goals. It will unveil the role of magnetic fields on all scales of star formation, from clouds, to filaments and dense core, looking also for correlations with cloud star formation efficiency. To reach this goal, it will quantify the magnetic field properties of these structures by mapping the polarized dust thermal emission of entire molecular cloud complexes at < 0.1 pc resolution, making the first statistical sample of high-resolution magnetic field maps. In addition, it will unveil the properties of Magneto-Hydro Dynamic (MHD) turbulence in the diffuse ISM, and it will understand the dominant mechanisms of energy dissipation, by constraining the polarized MHD power spectrum out to small angular scales ($\ell = 20,000$). Moreover, it will test models and dissipation mechanisms by high-resolution mapping the emission from the diffuse ISM.

Finally, the BLAST Observatory experiment will unveil the compositions and physical properties of interstellar dust grains in the ISM, by simultaneously measuring the polarized dust emission at three THz frequencies near the SED peak. It will be able to characterize the evolution of intrinsic dust properties from diffuse gas to cold cores, revealing the mechanical, chemical, and thermodynamic processes that shape grains. It will be also able to provide robust evidence to distinguish between competing dust models, since they predict systematic differences in polarization spectra for varied dust populations, particularly near the peak, as in shown in Figure 4.5 both for a diffuse ISM field and for a translucent cloud ($N_H \sim 1 \times 10^{21}$) named Pyxis⁴.

In my PhD thesis, I developed a work to identify diffuse ISM fields to observe. To explain all the main steps of the research algorithm I built, it is important to first explain two different performance scenarios predicted by the BLAST Observatory experiment, since in my analysis I considered both.

⁴The BLAST Observatory will also survey a *Planck*-selected highly polarized translucent cloud named Pyxis, which has an estimated distance of ~ 175 pc, and which is an ideal region for studying the transition from diffuse ISM to molecular gas.

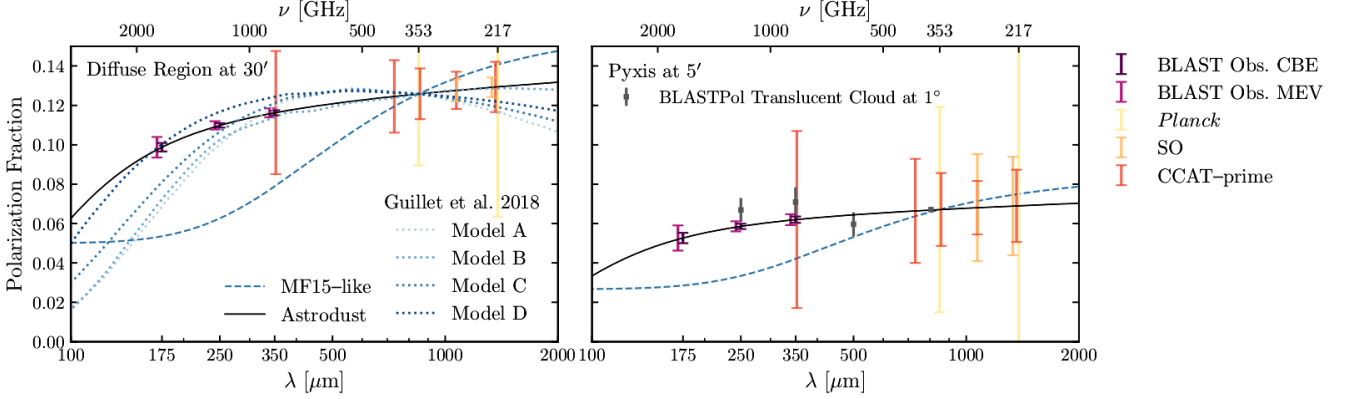


Figure 4.5: Models of the dust polarization fraction in a diffuse region at 30' resolution (left) and the Pyxis region at 5' resolution (right). The dark and light purple errorbars show the two BLAST Observatory forecasted performance scenarios (CBE and MEV). The suite of models presented are: the [Meisner & Finkbeiner \(2014\)](#) two-components fit to the Planck data; the post-Planck two-components models of [Guillet et al. \(2018\)](#); and the “astrodust” one-component model of [Draine & Hensley \(2021\)](#). BLAST Observatory complements the lower-frequency measurements of FYST/CCAT-prime and the Simons Observatory (LAT survey). On the right there are also BLASTPol/Planck measurements of the polarization fraction towards a diffuse cloud that has a much higher column density than Pyxis from [Ashton et al. \(2018\)](#). Credit to: Brandon S. Hensley.

Performance scenarios

The BLAST Collaboration decided to consider two different performance scenarios for the BLAST Observatory proposal: the Current Best Estimates (CBE) scenario, which refers to the projected performance based on current telescope design; and the Minimum Expected Value (MEV) scenario, which refers to the mission top level requirements to meet all the science objectives.

Both the CBE and MEV cases assume 80% detector yield. In addition, the MEV case assumes the following combined reductions in system performance, which to well over a factor of four contingency in effective integration time:

- the flight duration is 14 days instead of 31 days;
- the system sensitivity is degraded by a factor of 1.5;
- it provides nighttime only observations;
- the spatial resolution is 25% worse for the 175 μm band.

For the first 14 days of the flight, BLAST Observatory is designed to prioritize surveys needed to achieve the science objectives (it is designed to observe at least one diffuse field). For the remainder of the flight, the observing time will be divided roughly equally between shared-risk programs proposed by the astronomical community, and additional surveys for the CBE case (it is designed to observe two diffuse fields for the CBE case).

In Table 4.2 are schematized the main differences.

| | Days flight | Sensitivity | Observations | FWHM (175 μm) | Diffuse Field |
|-----|-------------|-------------|------------------|---------------------------|---------------|
| CBE | 31 | - | day & night time | - | #2 |
| MEV | 14 | 1.5x worse | night time | 25% worse | #1 |

Table 4.2: *Main differences between the two performance scenarios of the BLAST Observatory experiment: the Current Best Estimate (CBE) and the Minimum Expected Value (MEV).*

Finally, in Table 4.3 are schematized the BLAST Observatory channels with their respective resolutions, in the two performance scenarios (CBE and MEV):

| Frequency (GHz) | Wavelength (μm) | Beam FWHM (CBE) (") | Beam FWHM (MEV) (") |
|--------------------|---------------------------------|------------------------|------------------------|
| 1714 | 175 | 28 | 35 |
| 1200 | 250 | 39 | 39 |
| 857 | 350 | 55 | 55 |

Table 4.3: *The BLAST Observatory wavebands with their respective resolutions, in the two performance scenarios: the Current Best Estimate (CBE) and the Minimum Expected Value (MEV).*

4.3 Target field visibility

As a preliminary step for the polarized dust patch selection for CMB foreground purpose, on which the work I did is focused, it is necessary to consider which is the macro sky region that BLAST experiments are able to observe.

The visibility of BLAST experiments is determined by three main aspects: the sky above the launch site in the corresponding period (Antarctica during the austral summer for BLAST-TNG, and New Zealand during the austral fall for the BLAST Observatory); the geometry of the telescope payload; finally the Sun shields. The availability of targets and sky regions throughout the day depends instead of two factors: the launch date and the angle of the Sun.

Moreover, BLAST Observatory is designed to operate over a limited elevation range (20-60 degrees). In fact, if the elevation range is too low, you will get a lot of radiation from the ground; while if you look too high, you would be observing the balloon it self.

For a given day during the flight, a scheduling software (previously developed by some BLAST Collaboration members: Ed Chapin for BLAST, then modified by Tristan Matthews and discussed in his thesis (Matthews, 2013), and finally developed for BLASTPol by Laura M. Fissel⁵) calculates the number of hours each part of the sky is

⁵Assistant Professor at Department of Physics, Engineering Physics & Astronomy, Queen's University, Kingston, ON, Canada.

available for observation, and generates visibility plots. These indicate the approximate number of hours that each map pixel is visible in a 24-hour period, through concentric contours which, as they are more external, represent fewer visibility hours per day. These visibility calculations guide both the target selection and day-to-day observing plan throughout the flight.

4.3.1 The BLAST-TNG target field visibility

The analysis I carried out for the BLAST-TNG experiment in the selection of two diffuse dust fields to observe for CMB purposes, was done before the 2019/2020 campaign launch, scheduled for the austral summer in a time window of less than two months, starting from the late December 2019, at McMurdo Station latitude of -77.5° , approximately.

Not being able to accurately predict the launch date expected within the two months available and considering that the available observation area drifts about one degree per day towards the Galactic Center later in the flight, I decided to look for CMB fields valid even in case of delayed launch.

Therefore, I initially considered both the visibility plots of two representative dates, about one month apart from each other, for early and late launches: December 18, 2019 (shown in Figure 4.6) and January 21, 2020.

In the analysis I carried out to search for patch with characteristics similar to diffuse, low intensity dust regions, I decided to select targets which should be visible by the telescope for a minimum of 10 hours/day, trying to prioritize those available for 20 hours/day, to reduce conflicts and complications with scheduling.

Moreover, I also checked the overlap of BLAST-TNG target field visibility with current generation CMB telescopes, such as BICEP/Keck, PolarBear, SPTpol, ACTpol and SPIDER. Unfortunately, it was not possible to target a region with significant overlap with fields from other CMB experiments, as only a very small overlap area was found with the SPIDER experiment, close to the edge, at the December 18 launch date, intended to become thinner every next day, so not suitable for delayed flights.

4.3.2 The BLAST Observatory target field visibility

The analysis I carried out for the BLAST Observatory experiment focused on the selection of two diffuse dust fields to observe for CMB purposes, was done for the NASA proposal submitted in 2020. These sky targets then remained as a reference also for all subsequent proposals.

The observational strategy was planned to launch from the Wanaka Station, in New Zealand, for the 2028 campaign, even if the visibility should be applicable to any launch year. The Wanaka flight campaign is only once per year, typically in March or April, during the austral fall.

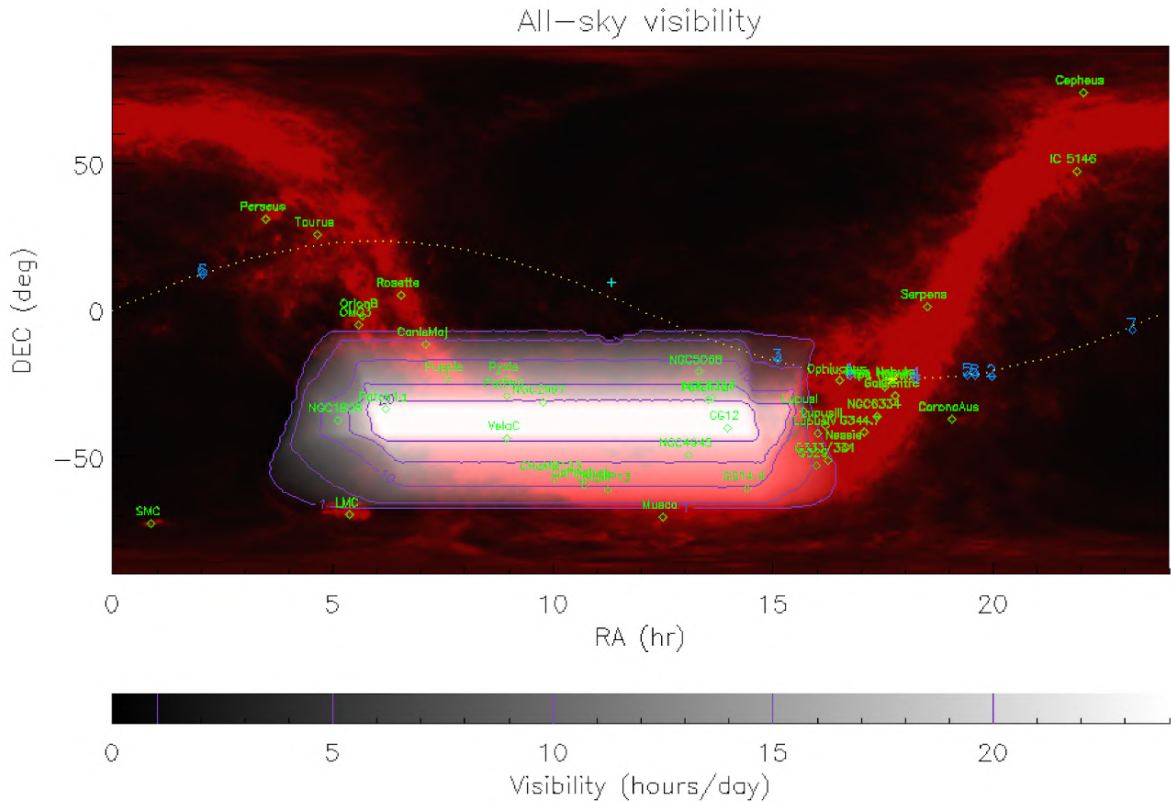


Figure 4.6: Sample visibility plot, at McMurdo Station latitude (-77.5°), for the launch date December 18, 2019, superimposed on an image of the Galaxy. Targets of interest are plotted as green boxes, and the path of the Sun throughout the day is shown in the yellow dotted line. The white shading and the purple contours represent the number of hours a region is available for observations; respectively, from the innermost to the outermost: 20, 15, 10, 5 and 1 hours. The map is represented in equatorial coordinates, Cartesian projection. The Galactic center is toward the right. Credit to: Laura M. Fissel.

A Super Pressure Balloon (SPB) launched from the mid-latitude Wanaka site provides access to the nighttime sky and more than five times the visible sky area under better thermal conditions than an Antarctic flight (where the previous BLASTs flew from), and so gives access to key science targets not available from Antarctica, to meet the BLAST Observatory science goals.

After a preliminary check on the Sun and Moon positions, the best representative launch date has been identified as March 15, 2026.

Not being able to accurately predict the launch date expected within the two months available, and considering that the available observation area drifts about one degree per day later in the flight, I decided to choose a patch that, starting from the considered launch date, could remain visible most of the time also in case of a delayed launch.

Moreover, given the latitude of Wanaka equal to -44.7° , and considering the latitude range based on previous mid-latitude flights, from -29° up to -65.5° (the balloon could

drift in latitude over this range), in my analysis I considered the visibility plots of four representative latitudes, even slightly higher or lower than the Wanaka one: -40° , -44.7° (shown in Figure 4.7), -50° and -55° .

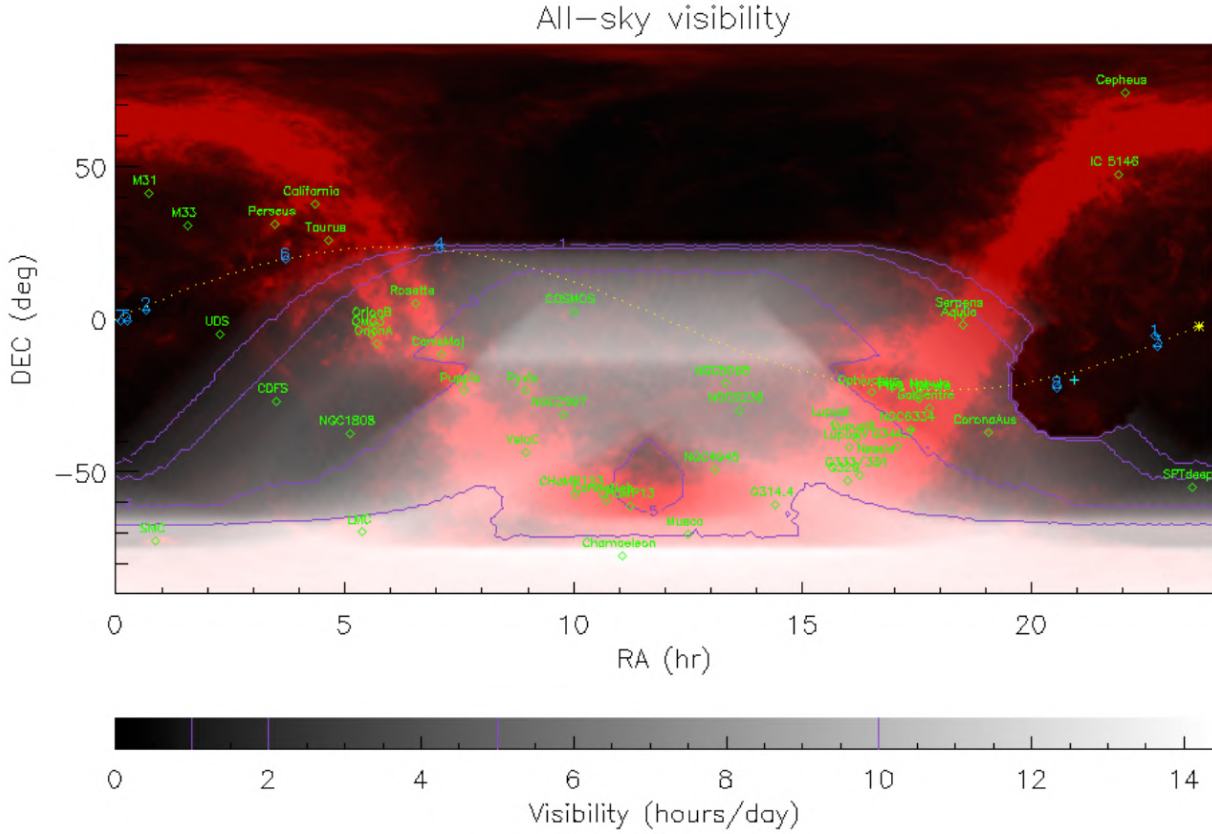


Figure 4.7: Sample visibility plot, at Wanaka Station latitude (-44.7°), for the launch date March 15, 2026, superimposed on an image of the Galaxy. Targets of interest are plotted as green boxes, and the path of the Sun throughout the day is shown in the yellow dotted line. The white shading and the purple contours represent the number of hours a region is available for observations; respectively, from the innermost to the outermost: 20, 15, 10, 5 and 1 hours. The map is represented in equatorial coordinates, Cartesian projection. The Galactic center is toward the right. Credit to: Laura M. Fissel.

In this analysis carried out for the BLAST Observatory experiment, I analyzed target field visibility available at least 5 hours/day, trying to prioritize those available for 10 hours/day, so that they were available for observation during most of the flight. In fact, the collaboration planned to observe each diffuse ISM target field for a total of 40/48 hours integration time, as will be described in Subsection 4.4.2, so the target field need to be available for many hours per day.

The legacy polarization surveys addressing the BLAST collaboration key science objectives overlap with observations of next-generation CMB polarization experiments, among them the Simons Observatory.

Therefore, the BLAST Observatory’s strategy of observing diffuse ISM regions was planned to overlap with surveys targeted by current and next-generation CMB experiments, with the aim of complementing information on the polarized dust emission at different wavelengths to remove the foreground contamination.

I calculated the overlap in coverage between BLAST Observatory and some CMB experiments: from the ground I considered the Small-Aperture Telescope (SAT) of the Simons Observatory experiment and the BICEP/Keck experiment; and SPIDER as balloon experiment.

In Figure 4.8 it is possible to see how I modeled the problem, taking for example in consideration the BLAST Observatory target field visibility at latitude= -44.7° , with both 5 hours/day and 10 hours/day contours, and the target field visibility of the considered CMB experiments.

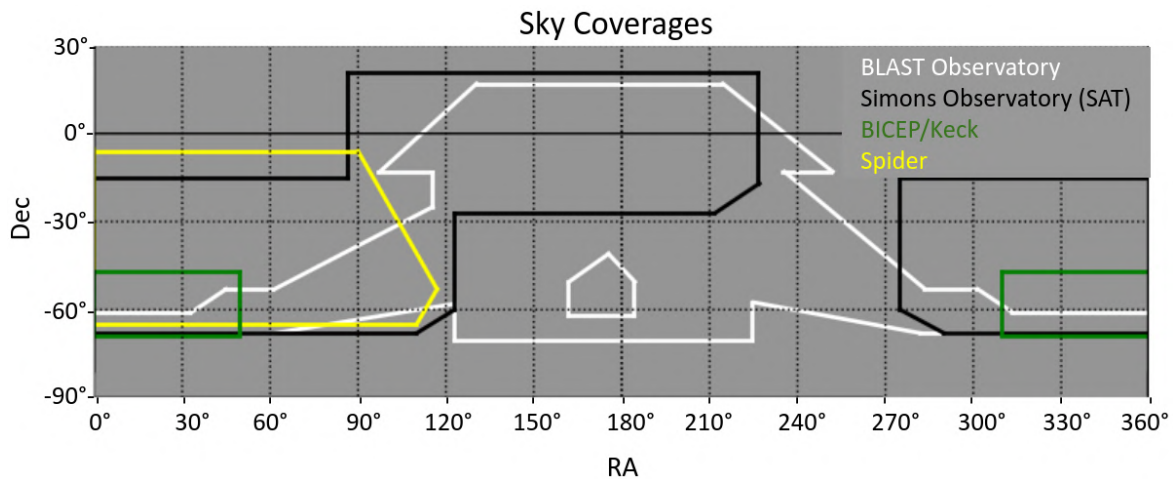


Figure 4.8: Target field visibility contours for the BLAST Observatory experiment (in white), both 5 hours/day and 10 hours/day, considering a launch from the Wanaka Station at a latitude of -44.7° , in the date March 15, 2026. The sky coverages of other CMB experiments are also shown: the Simons Observatory, with the survey of the Small-Aperture Telescope (SAT, in black); the BICEP/Keck experiment (in green), and the SPIDER experiment (in yellow). The map is represented in equatorial coordinates, Cartesian projection. The Galactic center is toward the right.

It is easy to see how well BLAST Observatory overlaps with these surveys. For example, at this latitude (-44.7°), it covers: about $\sim 40\%$ of the BICEP/Keck experiment survey; about $\sim 30\%$ of the SPIDER experiment survey; and about $\sim 55\%$ of the Simons Observatory SAT experiment survey. The contours have been geometrically delimited by making a minimal approximation, in order to narrow the search field of sky patches in the intersection areas.

4.4 Observational strategy

Being aspects related to the observational strategy I implemented, it is important to remember that *Planck* data revealed that the degree of polarization varies widely over the sky: most regions of the sky are characterized by a polarization fraction more than 5%, while polarization greater than 15% is less common, though some areas are polarized up to 25% (Planck Collaboration Int. XIX, 2015).

Moreover, dust with high polarization fractions tend to occur in low density, more diffuse regions (Planck Collaboration Int. XXII, 2015) (a trend observed also in the region around the Vela C molecular cloud by BLASTPol (Fissel et al. 2016)). Higher density regions, including the Galactic plane, on the contrary, tend to have lower polarization fractions due the effect of depolarization along the line of sight; and it was observed a general decrease in the dust polarization fraction with increasing column density above $N_H \sim 1 \times 10^{21} \text{ cm}^{-2}$ and in particular a sharp drop above $N_H \sim 1.5 \times 10^{22} \text{ cm}^{-2}$ (Planck Collaboration Int. XIX, 2015).

In order to optimize the flight time of BLAST experiments, and to reach the goal of target a diffuse polarized patch for the CMB foreground characterization, I established five selection criteria:

1. Selected regions should be highly polarized, as regions typically targeted for CMB observations. I established a 10% threshold for the polarization fraction as a compromise between the selection of a strongly polarized region, and the availability of regions characterized by an high level of polarization fraction⁶, so: $p_\lambda \geq 10\%$, for each waveband λ considered.
2. Selected regions should reside at high Galactic latitude to probe a diffuse ISM region off the Galactic plane, so to avoid denser areas characterized by less homogeneous properties. I established a 10° threshold for the Galactic latitude as a compromise between the distance from the Galactic plane and the availability of regions to match all criteria simultaneously, so: $|b| \geq 10^\circ$, preferring regions at even higher latitudes.
3. Each target region must have features for which we expect to detect polarized power with high SNR. I established a minimum threshold for the SNR equal to 5, as a compromise between a high enough SNR and the availability of regions to match all criteria simultaneously, so: $SNR \geq 5$.
4. Target regions should be no smaller than $2^\circ \times 2^\circ$ to minimize the amount of time spent during scan turnarounds (azimuth speed reversals of the telescope).
5. Selected regions should probe diffuse dust emission. Since there is a point where the linear relationship between the reddening, $E(B - V)$, and the HI column

⁶Choosing, for example, a 15% threshold for the polarization fraction would have significantly reduced the number of candidate regions, and would not have made it possible for all criteria to occur simultaneously.

density, $N(HI)$, breaks down, to be able to consider a patch “diffuse” in the CNM, in the sense of having little to no molecular hydrogen, it must be characterized by an HI column density smaller than this breaking point, roughly 10^{20} cm^{-2} . I established this latter value of the neutral hydrogen column density as threshold in my selection, so: $N(HI) < 4 \cdot 10^{20} \text{ cm}^{-2}$. Moreover, since HI data trace the same structures that act as dust foregrounds (as it is explained in Section 4.1), and so the HI data can help to guide the CMB observations, I established to select regions characterized by known HI features to correlate with the dust polarization.

It is important to note that, as diffuse fields to observe, I considered both square and rectangular sky patches. However, the best observational strategy found involved square patches, both for the BLAST-TNG and for the BLAST Observatory experiments, also for reasons that concerned the azimuth speed reversals of the telescope. Only results of the analysis referring to square-shaped patches are reported here.

4.4.1 The BLAST-TNG observational strategy

To satisfy the fourth observational requirement, after the assumption of an observation time of 48 hours, I decided to choose a scenario which involves a scan for a $5^\circ \times 5^\circ$ patch, with an area of 25 deg^2 , whose size represents the best optimization for the scientific purpose. This scenario is schematized in Table 4.4.

| | Patch Size [deg] | Patch Area [deg ²] | Obs. Time [hrs] |
|-------------------|---------------------|-----------------------------------|--------------------|
| Diffuse ISM Field | 5 | 25 | 48 |

Table 4.4: *Observational scenario of the BLAST-TNG experiment for one dust diffuse ISM field to observe for CMB purpose.*

4.4.2 The BLAST Observatory observational strategy

The BLAST Observatory experiment considers larger patch sizes than the BLAST-TNG experiment, because it was designed to have a higher sensitivity, involving a scan for a $10^\circ \times 10^\circ$ patch, with an area of 100 deg^2 .

Since the BLAST Observatory proposal considers two different performance scenarios, as was described in Subsection 4.2.2, the Current Best Estimates (CBE) and the Minimum Expected Value (MEV), the observational scenarios diversify accordingly. Regarding the CBE case, its scenario considers observing both diffuse ISM fields for an observation time equal to 48 hours each, as is schematized in Table 4.5. While, regarding the MEV case, its scenario considers observing just one diffuse ISM field for a smaller observation time equal to 40 hours, as is schematized in Table 4.6.

| | Patch Size [deg] | Patch Area [deg ²] | Obs. Time [hrs] |
|---------------------|---------------------|-----------------------------------|--------------------|
| Diffuse ISM Field 1 | 10 | 100 | 48 |
| Diffuse ISM Field 2 | 10 | 100 | 48 |

Table 4.5: *Observational scenario of the BLAST Observatory experiment in the Current Best Estimates (CBE) case, for the two dust diffuse ISM fields to observe for CMB purpose.*

| | Patch Size [deg] | Patch Area [deg ²] | Obs. Time [hrs] |
|---------------------|---------------------|-----------------------------------|--------------------|
| Diffuse ISM Field 1 | 10 | 100 | 40 |
| Diffuse ISM Field 2 | 0 | 0 | 0 |

Table 4.6: *Observational scenario of the BLAST Observatory experiment in the Minimum Expected Value (MEV) case, for the two dust diffuse ISM fields to observe for CMB purpose.*

4.5 Sensitivity

To establish which is the best sky area to observe, after having chosen the observational strategy, and beyond the evaluation of the intrinsic characteristics of the area, it is necessary to establish to what extent the telescope is able to detect a certain signal. This property is encoded by the SNR quantity, and it can be evaluated for any observed quantity, once the instrument sensitivity has been calculated.

Before going into details, it is fair to underline that the information presented in this Section are the result of the joint effort of various members of the BLAST Collaboration: Giles Novak⁷, Laura M. Fissel⁸, Joy Didier, Ian Lowe⁹ and Gabriele Coppi¹⁰.

I started from the calculation of the sensitivity of a single beam (in units of MJy/sr), that means the noise in the map from a single beam accounting for all N_d detectors stared at the same beam sized area on the sky and operating at 30% bandwidth, N_f , with the given beam FWHM and beam diffraction-limited solid angle (Ω_B), integrated over a scanning time (t_{beam}):

$$S_{beam} = N_f \frac{1}{\sqrt{t_{beam}}} \quad (4.1)$$

Note that the sensitivity per beam inversely depends on the integration time, since the SNR in the map improves integrating for longer periods of time.

⁷Professor at Department of Physics and Astronomy, Northwestern University, IL, USA.

⁸Assistant Professor at Department of Physics, Engineering Physics & Astronomy, Queen's University, Kingston, ON, Canada.

⁹Postdoctoral Research Associate at Department of Astronomy and Steward Observatory, University of Arizona, AZ, USA.

¹⁰Marie-Curie Fellow Researcher at Department of Physics, University of Milano-Bicocca, Italy.

The integration time is typically stated for the integration over a full map of some angular size (t_{map}), which we can relate to the integration time per beam-size pixel (t_{beam}) using the ratio of the map size (A_{map}) to the beam solid angle:

$$t_{beam} = t_{map} \times \frac{\Omega_B}{A_{map}} \quad . \quad (4.2)$$

By combining the Equations (4.1) and (4.2), we can obtain the sensitivity in a beam-size pixel:

$$S_{beam} = N_f \sqrt{\frac{A_{map}}{\Omega_B}} \frac{1}{\sqrt{t_{map}}} \quad (4.3)$$

The SNR of the maps can also be improved by smoothing them using a larger pixel size, and this can be done smoothing the pixel size from the diffraction limited solid angle to a large area (A_{pix}). This operation gives a sensitivity of:

$$S_{pix} = S_{beam} \sqrt{\frac{\Omega_B}{A_{pix}}} = N_f \sqrt{\frac{A_{map}}{A_{pix}}} \frac{1}{\sqrt{t_{map}}} \quad (4.4)$$

The map resolution is less important than the map depth for the CMB foreground study and, in the need to choose patches of size $5^\circ \times 5^\circ$ or $10^\circ \times 10^\circ$ for cosmological purposes, despite this it has a negative effect on the sensitivity (other factors being equal), degrading the resolution to some arcminutes is sufficient to keep a sufficiently high SNR.

4.5.1 The BLAST-TNG sensitivity

To search the best polarized diffuse patch to observe with BLAST-TNG experiment, I carried out sky simulations with a resolution of $27.5'$ (HEALPix Nside=128) in order to obtain an higher SNR. In fact, although it is much worse than that which characterizes the instrument, this not particularly high resolution made it possible to reduce the computational cost and the time required to carry out simulations¹¹.

Therefore, for the sensitivity calculation, I considered these main parameters:

- A scan time of: $t_{map} = 48$ hours
- A map area of: $A_{map} = 5^\circ \times 5^\circ$ square degrees
- A pixel area of: $A_{pix} = 27.5' \times 27.5'$ square arcminutes (0.21 square degrees)

¹¹The choice of the resolution for sky simulations was driven by a question of timing: this type of project, started in November 2019 in conjunction with the start of my PhD, had to produce results within two months, for the BLAST-TNG campaign launch scheduled for late December 2019/early January 2020 (BLAST-TNG then flew on 6 January 2020).

This parameters combination was chosen after having evaluated a series of different possibilities, such as: using $2^\circ \times 2^\circ$ patch (the size threshold established by fourth criterion in Section 4.4), or an higher map resolution, up to $2'$. However, to achieve SNRs high enough to reach the scientific goals, inside the BLAST-TNG sky coverage, and considering to choose patches far away from the Galactic plane, this combination was found to be the best optimization.

Finally, I calculated the pixel sensitivities in polarization for each wavelengths channels ($S_{pix}(P)$), using estimates of the polarized map noises per beam ($N_f(P)$). I also calculated the pixel sensitivities in total intensity for each frequency channels, using the Equation:

$$S_{pix}(I) = \frac{0.9 \cdot S_{pix}(P)}{\sqrt{2}} \quad , \quad (4.5)$$

where 0.9 is the polarimetric efficiency.

All these estimates are shown in Table 4.7, which then allowed to estimate the expected SNR in the simulated maps described in Section 4.6.

| Frequency (GHz) | Wavelength (μm) | $N_f(P)$ (MJy/sr $\cdot \sqrt{s}$) | $S_{pix}(P)$ (MJy/sr) | $S_{pix}(I)$ (MJy/sr) |
|--------------------|---------------------------------|--|--------------------------|--------------------------|
| 1200 | 250 | 3.86E-01 | 1.01E-02 | 6.44E-03 |
| 860 | 350 | 2.87E-01 | 7.54E-03 | 4.80E-03 |
| 600 | 500 | 1.55E-01 | 4.06E-03 | 2.59E-03 |

Table 4.7: *In the third column are shown the values of the polarized map noise from a single beam accounting for detectors operating at 30% bandwidth ($N_f(P)$) for each BLAST-TNG frequency channels. This noise is based on BLAST-Pol measured noise in flight, and scaled to account for differences in mirror size and number of detectors. It is a realistic/pessimist estimate using 85% of detectors working. In the fourth and fifth columns, there are the values of the pixel sensitivity in polarization and total intensity ($S_{pix}(P)$ and $S_{pix}(I)$), respectively, for each BLAST-TNG frequency channels, considering an observation time of 48 hours, a resolution of $27.5'$, and a patch size of $5^\circ \times 5^\circ$.*

4.5.2 The BLAST Observatory sensitivity

To search the best diffuse polarized patch to observe with the BLAST Observatory proposal, I carried out sky simulations with a resolution of $13.7'$ (HEALPix Nside=256) in order to obtain an higher SNR. In fact, although it is much worse than that which characterizes the instrument, this resolution made it possible to reduce the computational cost and the time required to carry out simulations.

In this case, however, having a less restrictive timing, I used a better resolution, of a factor of 2, than the one used for simulations developed for the BLAST-TNG patch selection.

Therefore, for the sensitivity calculation, I considered these main parameters:

- A scan time of: $t_{map} = 48$ hours (CBE) and $t_{map} = 40$ hours (MEV)
- A map area of: $A_{map} = 10^\circ \times 10^\circ$ square degrees
- A pixel area of: $A_{pix} = 13.7' \times 13.7'$ square arcminutes (0.05 square degrees)

Also in this case, this parameters combination (which respects the patch size threshold established by the fourth criterion in Section 4.4) was chosen after having evaluated a series of different possibilities, but it was found to be the best optimization.

Finally, I calculated the pixel sensitivities in polarization for each frequency channels ($S_{pix}(P)$), using estimates of the polarized map noises per beam ($N_f(P)$), and considering the two performance scenarios CBE (Current Best Estimates) and MEV (Minimum Expected Value). I also calculated the pixel sensitivities in total intensity for each frequency channels using Equation 4.5.1.

All these estimates are shown in Tables 4.8 and 4.9, which then allowed to estimate the expected SNR in the simulated maps described in Section 4.6.

| Frequency (GHz) | Wavelength (μm) | $N_f(P)$ (MEV) (MJy/sr $\cdot \sqrt{s}$) | $S_{pix}(P)$ (MEV) (MJy/sr) | $S_{pix}(I)$ (MEV) (MJy/sr) |
|-----------------|------------------------------|---|-----------------------------|-----------------------------|
| 1714 | 175 | 1.77E-00 | 3.01E-02 | 1.91E-02 |
| 1200 | 250 | 4.32E-01 | 8.38E-03 | 5.33E-03 |
| 860 | 350 | 1.77E-01 | 4.81E-03 | 3.06E-03 |

Table 4.8: *In the third column are shown the values of the polarized map noise from a single beam accounting for detectors operating at 30% bandwidth ($N_f(P)$) for each BLAST Observatory frequency channels, considering the MEV performance scenario. In the fourth and fifth columns, are shown the values of the pixel sensitivity in polarization and total intensity ($S_{pix}(P)$ and $S_{pix}(I)$), respectively, for each BLAST Observatory frequency channels, considering a resolution of $13.7'$, a patch size of $10^\circ \times 10^\circ$, and an observation time of 40 hours (MEV scenario).*

| Frequency (GHz) | Wavelength (μm) | $N_f(P)$ (CBE) (MJy/sr $\cdot \sqrt{s}$) | $S_{pix}(P)$ (CBE) (MJy/sr) | $S_{pix}(I)$ (CBE) (MJy/sr) |
|-----------------|------------------------------|---|-----------------------------|-----------------------------|
| 1714 | 175 | 1.28E-00 | 1.45E-02 | 9.20E-03 |
| 1200 | 250 | 3.31E-01 | 5.35E-03 | 3.41E-03 |
| 860 | 350 | 1.42E-01 | 3.21E-03 | 2.04E-03 |

Table 4.9: *In the third column are shown the values of the polarized map noise from a single beam accounting for detectors operating at 30% bandwidth ($N_f(P)$) for each BLAST Observatory frequency channels, considering the CBE performance scenario. In the fourth and fifth columns, are shown the values of the pixel sensitivity in polarization and total intensity ($S_{pix}(P)$ and $S_{pix}(I)$), respectively, for each BLAST Observatory frequency channels considering a resolution of $13.7'$, a patch size of $10^\circ \times 10^\circ$, and an observation time of 48 hours (CBE scenario).*

4.6 Foreground simulations

The algorithm that I built with the aim of choosing the best diffuse patch to observe for CMB foreground purpose, it is the extension and the development of the code originally written by a BLAST Collaboration member, Nathan P. Lourie¹² (Lourie, 2018). The code is based on the PySM sky model software (Thorne et al., 2017), and at first level, at each of the three BLAST bands, compute sky maps of dust emission, showing the total intensity, the polarized intensity and the polarization fraction: I_λ , P_λ and p_λ , respectively. These last two quantities have already been defined in Equations 1.1 and 1.2.

It should be emphasized that the maps produced here are smoothed to the resolution that I adopted in the observational strategy of each BLAST experiment, as described in Section 4.5: 27.5' for BLAST-TNG, corresponding to an HEALPix Nside parameter used by the PySM software equal to Nside=128; and 13.7' for the BLAST Observatory, corresponding to Nside=256.

In Figure 4.9 are shown the polarization fraction maps inside the target field visibility of the BLAST Observatory experiment (5 and 10 hours/day contours), and of the BLAST-TNG experiment (10 and 20 hours/day contours), at their respective representative launch dates, locations and latitudes: December 18, 2019 and January 21, 2020 at McMurdo Station (Antarctica), latitude -77.5° , for the BLAST-TNG experiment; March 15, 2026 at Wanaka Station (New Zealand), latitude -44.7° , for the BLAST Observatory experiment (see Section 4.3 for more details).

In reality, although for the intended purpose it is of fundamental importance to choose highly polarized sky regions, the BLAST experiment is not able to measure the absolute degree of polarization, being sensitive only to relative measurements, not measuring the zero level of either total intensity or polarization.

Therefore, it is necessary to plan observations based not on polarized intensity but on contrast in the polarized power. To account for this in simulations, I subtracted off the mean value of Q_λ and U_λ from each prospective patch ($\langle Q_\lambda \rangle$ and $\langle U_\lambda \rangle$), to calculate the polarization power contrast defined as:

$$P_{c,\lambda} = \sqrt{(Q_\lambda - \langle Q_\lambda \rangle)^2 + (U_\lambda - \langle U_\lambda \rangle)^2} \quad . \quad (4.6)$$

After having produced smoothed maps and defined the polarized quantities of interest (the polarization fraction and the polarized contrast), it was necessary to quantify the instrument's sensitivity to these same quantities, i.e. evaluate their SNR for each pixel.

As regards the SNR of the polarization power contrast at each wavelength λ , I just divided the polarization power contrast, $P_{c,\lambda}$, by the smoothed pixel sensitivity in polarization, $S_{pix,\lambda}(P)$, calculated in the previous Section 4.5, obtaining:

¹²Research Scientist, MIT Kavli Institute for Astrophysics and Space Research, Massachusetts Institute of Technology, Cambridge, MA, USA.

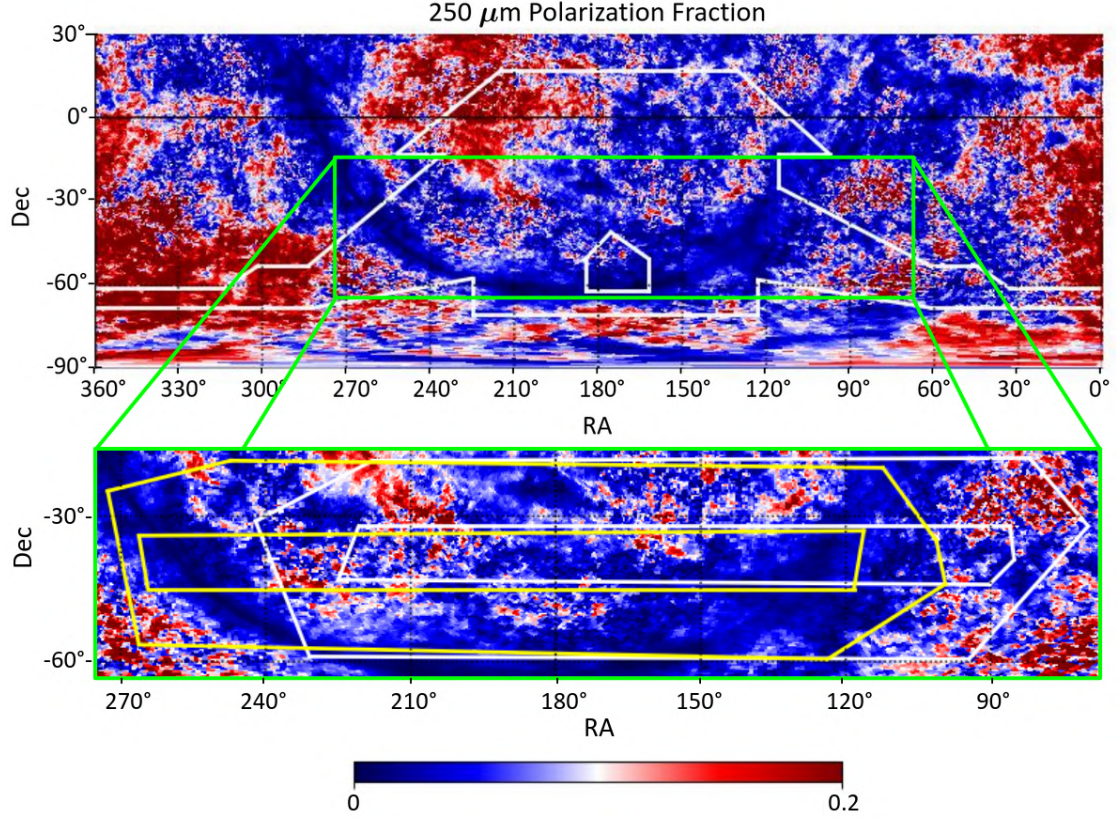


Figure 4.9: Polarization fraction sky maps in the geometrically modeled target field visibility, both of BLAST Observatory (top) and BLAST-TNG (bottom), at the same 250 μm channel and at the same map resolution 27.5' (HEALPix $N_{\text{side}}=128$), for comparison purposes. Regarding the BLAST-TNG target field visibility, are represented both early and late launch dates, corresponding to December 18, 2019 (white contours), and January 21, 2020 (yellow contours), both from McMurdo Station (Antarctica) at a latitude of -77.5° . For each of the BLAST-TNG contours, the outer one corresponds to an area available 10 hours/day, and the second smaller internal one corresponds to an area available 20 hours/day. Regarding the BLAST Observatory field, it correspond to the launch date March 15, 2026 from the Wanaka Station (New Zealand) at a latitude of -44.7° , and it corresponds to an area available 5 and 10 hours/day (on the bottom). The red regions are representative of a polarization fraction higher than 10%. The maps are represented in equatorial coordinates, Cartesian projection. The Galactic center is toward the left.

$$SNR(P_{c,\lambda}) = \frac{P_{c,\lambda}}{S_{pix,\lambda}} \quad (4.7)$$

As regards the SNR of the polarization fraction, however, it was first necessary to estimate the value of the uncertainty associated with the polarization fraction. In fact, in addition to the polarized intensity, it also depends on the total intensity. Thus, propagating both the polarized intensity sensitivity, $S_{pix,\lambda}(P)$, and the total intensity sensitivity, $S_{pix,\lambda}(I)$, I defined the uncertainty associated with the polarization fraction as:

$$\sigma(p_\lambda) = |p_\lambda| \sqrt{\left(\frac{S_{pix,\lambda}(P)}{P_\lambda}\right)^2 + \left(\frac{S_{pix,\lambda}(I)}{I_\lambda}\right)^2}, \quad (4.8)$$

where I assumed that the polarized intensity and the total intensity were independent, thus a null covariance term. Through a preliminary study, I verified the robustness of this approximation, verifying that it did not significantly affect the final value, also testing the maximum and minimum values of the covariance term.

Therefore, the SNR of the polarization fraction at each wavelength λ was defined as:

$$SNR(p_\lambda) = \frac{p_\lambda}{\sigma(p_\lambda)} \quad (4.9)$$

On the basis of first and third dust patch selection criteria, listed in Section 4.4, these simulations therefore highlighted two useful planning tools for CMB foreground observations:

1. A first step, based on polarization fraction maps, with the intent to identify regions of possible interest.
2. A second passage, based on SNR maps, with the intent of identifying regions of possible interest based on the characteristics of the BLAST experiments, mainly sensitivity, resolution, and observational strategy.

In this preliminary analysis phase, I used these maps to visually identify the regions that might be suitable for the chosen observational scenarios. I considered as suitable the areas characterized by a high value of both the polarization fraction, the SNR of the polarization fraction, and the SNR of the polarization power contrast (at least $SNR \geq 5$, according to the third selection criterion listed in Section 4.4) for both BLAST-TNG and BLAST Observatory observational strategy.

4.7 Quality factors

Although it was possible to zoom into various parts of the map, selecting the patches that appeared most suitable, this approach is subject to bias. For this reason, with the aim of developing a selection method based on a more quantitative than qualitative basis, I have developed an algorithm in order to setting up a systematic research of the sky areas characterized by the best possible values of the quantities argued in the previous Section 4.6: the polarization fraction, defined in Equation 1.2; the SNR of the polarization fraction, defined in Equation 4.9; and the SNR of the polarization power contrast, defined in Equation 4.7, for both BLAST-TNG and BLAST Observatory experiments.

From a hint by my supervisor Federico Nati¹³, another member of the BLAST Collaboration, I then defined three evaluation parameters, which I called “Quality Factors”.

¹³Assistant Professor at Department of Physics, University of Milano-Bicocca, Italy.

They are reference scalar values for each patch, defined as the average values of the three quantities described above, of all the pixels (of number n) within a certain patch, in detail:

- The Quality Factor for the polarization fraction, at each wavelength λ :

$$QF(p_\lambda) = \sum_{i=0}^n \frac{p_\lambda(i)}{n} \quad (4.10)$$

- The Quality Factor for the SNR of the polarization fraction, at each wavelength λ :

$$QF(SNR_{p_\lambda}) = \sum_{i=0}^n \frac{SNR_{p_\lambda}(i)}{n} \quad (4.11)$$

- The Quality Factor for the SNR of the polarization power contrast, at each wavelength:

$$QF(SNR_{P_{c,\lambda}}) = \sum_{i=0}^n \frac{SNR_{P_{c,\lambda}}(i)}{n} \quad (4.12)$$

The name ‘‘Quality Factors’’ refers to the purpose they have to provide the ‘‘goodness’’ of the patches, based on the representative value of the quantities of interest within the sky patch. In a very simple and intuitive way: the higher these values are, the better the patch is.

Thanks to these factors, it is thus possible to clearly and easily meet the thresholds of the first and third sky patch selection criteria listed in Section 4.4. By evaluating the Quality Factors for each patch, it is immediate to understand if the minimum thresholds required by the criteria are met: $QF(p_\lambda) > 10\%$, $QF(SNR_{p_\lambda}) \geq 5$ and $QF(SNR_{P_{c,\lambda}}) \geq 5$, for each waveband λ considered.

Figure 4.10, for example, shows a visual representation of the meaning of the first Quality Factor for two only slightly different sky patches, very close to each other and almost completely overlapping: the average values of the two polarization fraction maps at $250 \mu\text{m}$ within patches, respectively, are scalar values that quantify that one patch is better than the other in terms of high polarization fraction level ($QF(p_{250}) = 16.6\%$ vs $QF(p_{250}) = 14.4\%$).

I set up the code to scan the target field visibility of BLAST experiments, considering both early and later launch dates one month apart in the case of BLAST-TNG experiment, and $5^\circ \times 5^\circ$ patches, and the range of latitudes for the BLAST Observatory experiment, and $10^\circ \times 10^\circ$ patches, as described in Sections 4.3 and 4.4. The aim of the systematic research was to find the patches characterized by the best combinations of Quality Factors considered simultaneously, in terms of the highest possible values.

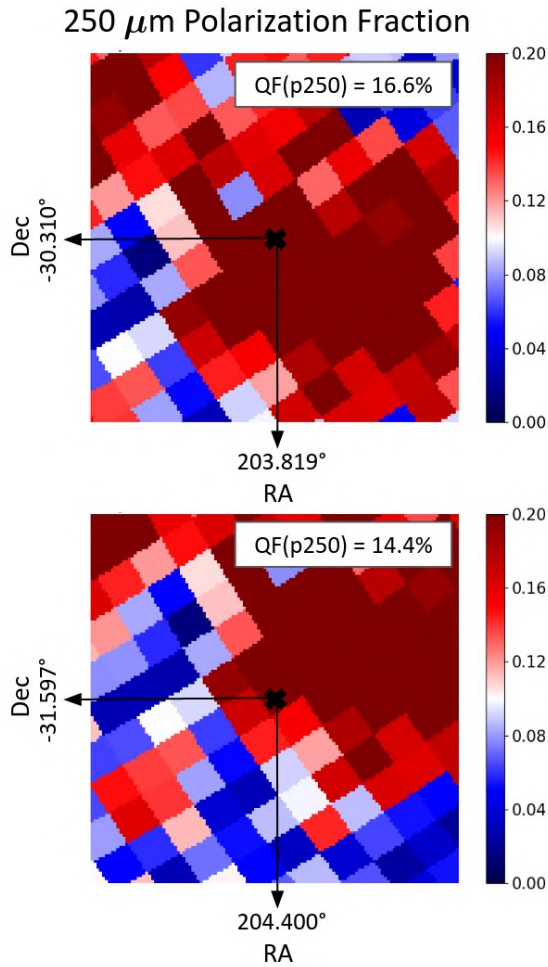


Figure 4.10: Polarization fraction maps at 250 μm , with a resolution of 27.5' ($N_{\text{side}}=128$), within two $5^\circ \times 5^\circ$ sky patches very close to each other and almost completely overlapping. On the label is shown the corresponding average value, i.e. the Quality Factor, equal to 16.6% and 14.4%, respectively. Considering the divergent colour scale (0-20%), it is easy to understand which patch is better in terms of high polarization fraction level.

However, considering the two BLAST experiments, I implemented a slightly different framework for finding the best targets.

For the BLAST-TNG experiment, I scanned the entire visibility area by shifting the center of each patch by 0.1° , both in longitude and in latitude, considering a total of hundreds of thousands of possible patches, and calculating for each the Quality Factors values, so taking into account all the minimal variations of the maps. This systematic research took into consideration the shift of about one degree per day that the visibility area makes with no certainty of the launch date, and excluded areas at risk too close to the edge.

At the end of this preliminary analysis, I selected two patches, shown in Figure 4.11: one patch (the yellow one) is characterized by the best polarization fraction Quality Factor and by the best SNR of the polarization fraction Quality Factor; the other patch (the orange one) is characterized by the best SNR of the polarized contrast Quality Factor. These patches almost entirely overlap ($\sim 70\%$) as the criteria with which they were selected (the Quality Factors) are not mutually independent, as all three are based on the polarized intensity, and two of these on the characteristics of the instrument. Then, I checked the areas with better constraints on the polarized SED (see Section 4.8), and finally I looked for the best compromise considering the HI column density values, as it is described in Subsection 4.9.1.

For the BLAST Observatory experiment, first I identified areas of interest in the target field visibility, considering the intersection with some current and next-generation CMB experiments (see Section 4.3.2 and Figure 4.7); then I looked for the best compromise considering the HI column density values; and finally I searched for the best patches implementing the Quality Factors method, and checking the accuracy on the polarized SED constraints (see Section 4.8), as will be described in Subsection 4.9.2.

4.8 Constraints on the polarized SED

After all simulations carried out based on the observational strategies and on the Quality Factors definitions, I explored another way to approach the patch selection, based on polarized SED constraints extracted from any patch on the simulated maps already described. The purpose was to determine how well a flat polarization spectrum can be measured for a given polarization fraction SNR measurement, in each band considered, and in each patch. To do this, I made changes and developed a Python code originally written by a BLAST Collaboration member, Laura M. Fissel¹⁴.

Setting a more general reasoning, I implemented a systematic search on the target field visibility of BLAST experiments, excluding the regions closest to the Galactic plane more than 10° , in order to verify if the region providing the best constraint on the polarized SED coincided with the location of patches selected using the Quality Factors method.

To create polarization spectra simulations for each patch, the code made use of 2,000 Monte Carlo simulations to generate polarization fraction noise realizations, at each band considered. In each patch, it assumed a flat polarization spectrum, taking as reference the polarization fraction value at $350\mu\text{m}$, and in particular its average value, i.e. the respective Quality Factor, $QF(p_{350})$. The SNR of the polarization fraction values for all three channels, and for each considered patch, were also used in the code.

¹⁴Assistant Professor at Department of Physics, Engineering Physics & Astronomy, Queen’s University, Kingston, ON, Canada.

Even in this case, I considered its average value, i.e. the respective Quality Factor, $QF(SNR_{p_{350}})$.

Considering that a different noise realization was added to each simulation, the slopes derived from each linear fit to each set of simulated polarization spectra did not manifest as exactly zero. A least squares polynomial fit was used using the Python function `polyfit` of the python library `numpy`. The slope was then normalized by the range in frequency, and so expressed in terms of percentage change in the polarization fraction respect to the frequency range of BLAST experiments bands. The statistic of the slope of the polarization spectrum, in each patch, was then calculated, considering both the Median Absolute Deviation (MAD) and the Standard Deviation (SD) to measure slope uncertainty. The width of the slope values of the polarization spectrum was then taken as a reference to evaluate the percentage level expected to constrain the polarization fraction.

These uncertainties have been taken as a reference to give an idea of how well it is possible to constrain the polarization spectrum for the specified SNR of each band, and for this reason my simulations have been set up to look for patches characterized by the smallest slope MAD value and by the smallest slope SD value, with the aim of obtaining those in which the flat polarization spectrum would be best constrained.

However, considering how these simulations were built (due to noise realizations from the Monte Carlo simulations), the smallest slope MAD value and the smallest slope SD value tended to vary slightly each time a simulation was run, and the coordinates that identify the best patch also tended to vary slightly, both in longitude and in latitude.

As regards the BLAST-TNG experiment, it was found that, considering all patches analyzed inside the target field visibility, the lower slope values, MAD and SD, tended to be around 2.2% and 3.3%, respectively, in a specific area shown in Figure 4.11. This gave us the information that, within the target field visibility of BLAST-TNG experiment, we could expect to constrain the polarization fraction with high accuracy, up to an approximate level of 2-3%.

Therefore, this simulation provided evidence that the area in which the polarized SED appears best constrained, overlaps patches selected using the Quality Factors method. This important result constitutes a significant and independent confirmation of the confidence with which the patches deriving from the algorithm I built can be considered excellent candidates for the intended scientific purpose.

The characteristics of the affected area and the patches involved will be explored in Subsection 4.9.1, where the last important selection criterion is applied before reaching the final results shown in Subsection 4.10.1. Here the characteristics of some proposed patches are shown as the best compromise between the Quality Factors values and the HI column density, and the MAD and SD values of the polarized SED slope (in the range 3.0 – 5.1%) are shown.

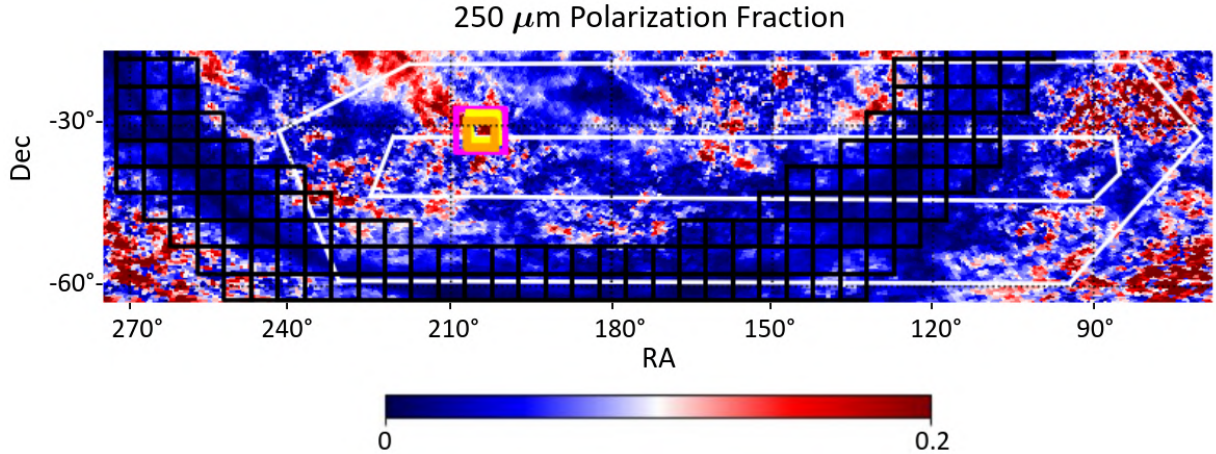


Figure 4.11: Polarization fraction sky map at 250 μm on the BLAST-TNG target field visibility. The black patches are close to the Galactic plane more than 10° , and they have been excluded from my research. The two $5^\circ \times 5^\circ$ patches highlighted in yellow (Patch 1a) and orange (Patch 1b) represent the best ones obtained from the preliminary simulations based on the Quality Factors selection method. These patches almost entirely overlap ($\sim 70\%$) as the criteria with which they were selected (the Quality Factors) are not mutually independent, as all three are based on the polarized intensity, and two of these on the characteristics of the instrument. The magenta rectangular patch identifies the area on the map where the polarized SED slope is constrain with the better accuracy (2-3%). It easy to see that the area in which the polarized SED appears best constrained overlaps the two best patches selected using the Quality Factors method.

As regards the BLAST Observatory experiment, it was found that, considering all patches analyzed inside its target field visibility, the lower polarized SED slope values, MAD and SD, tended to be around 0.8% and 1.2% for the CBE scenario, respectively, and around 1.3% and 1.9% for the MEV scenario, respectively. In Subsection 4.10.2, the characteristics of some proposed patches are shown as the best compromise between the Quality Factors values and the HI column density, and the respective MAD and SD values of the polarized SED slope for both scenarios, CBE (in the range 0.8 – 2.5%), and MEV (in the range 1.3 – 4.0%) are shown.

Being the BLAST Observatory target field visibility bigger than the one of the BLAST-TNG experiment, and having been able to extend the search for the best patches to more sky areas, the best patches found for the BLAST Observatory experiment have lower, and therefore better, minimum values of MAD and SD polarized SED slope values.

4.9 HI column density maps

In the light of these preliminary results obtained, it is now necessary to consider the final selection criterion, among those listed in Section 4.4, for the optimized dust targets selection. It concerns the need to link the patch selection with the emission, density and structure of the neutral hydrogen (HI).

Theory suggests that HI data trace the same structures that act as dust foreground, and therefore represent an important alternative for predicting dust emission (Martin et al., 2015; Ghosh et al., 2017).

As regards the part of the selection criterion which refers to HI filaments, they are needed in order to correlate them with the dust polarization. Indeed, most of the filamentary dust structures in the diffuse ISM are actually in the CNM phase Ghosh et al. (2017), and the CNM structure can be probed by mapping the HI emission line. It was showed a high degree of alignment between the HI structures and the magnetic field inferred from dust polarization Martin et al. (2015).

As regards the part of the selection criterion which refers to a diffuse dust emission field, to be able to consider a patch “diffuse” in the CNM, in the sense of having little to no molecular hydrogen, it must be characterized by an HI column density $N(HI) < 4 \times 10^{20} \text{cm}^{-2}$. This value is roughly the point where the linear relationship between the reddening, $E(B - V)$, and the HI column density, $N(HI)$, breaks down (Savage et al., 1977; Liszt, 2014; Lenz et al., 2017).

At this point, I implemented slightly different strategies for the two BLAST experiments.

4.9.1 The BLAST-TNG selection strategy

In order to further evaluate the interstellar environment towards the two best patches identified as best candidate within the 10 hour BLAST-TNG target field visibility, shown in Figure 4.11, I focused the analysis in a preliminary area, which includes the environment around the patches.

With the aim of combining the analysis resulting from previous simulations and a new analysis based on HI maps, I initially started from two maps concerning the HI column density, created by a BLAST Collaboration member, Susan E. Clark¹⁵. She used data from the HI4PI survey (HI4PI Collaboration, 2016), with an angular resolution of $16.1'$ and a sensitivity of 43 mK, based on data from the first coverage of the Effelsberg-Bonn HI Survey (EBHIS; Winkel et al., 2015) and from the third revision of the Galactic All-Sky Survey (GASS; Kalberla & Haud, 2015)¹⁶. These maps had a metric linked to the amplitudes of the $5^\circ \times 5^\circ$ patches, and were designed to perform a check on the two candidate patches obtained from previous simulations. They were based, respectively: on the median value of the HI column density inside $5^\circ \times 5^\circ$ patches, and on the fraction of the $5^\circ \times 5^\circ$ patches that have a HI column density small than $4 \times 10^{20} \text{cm}^{-2}$, both shown in Figure 4.12.

In these HI column density maps, it is possible to observe how the candidate patches obtained from the previous simulations were unfortunately not fully optimized.

¹⁵Assistant Professor at Department of Physics, Stanford University, CA, USA.

¹⁶HI4PI datasets are available at the CDS via <http://cdsarc.u-strasbg.fr/viz-bin/qcat?J/A+A/594/A116>.

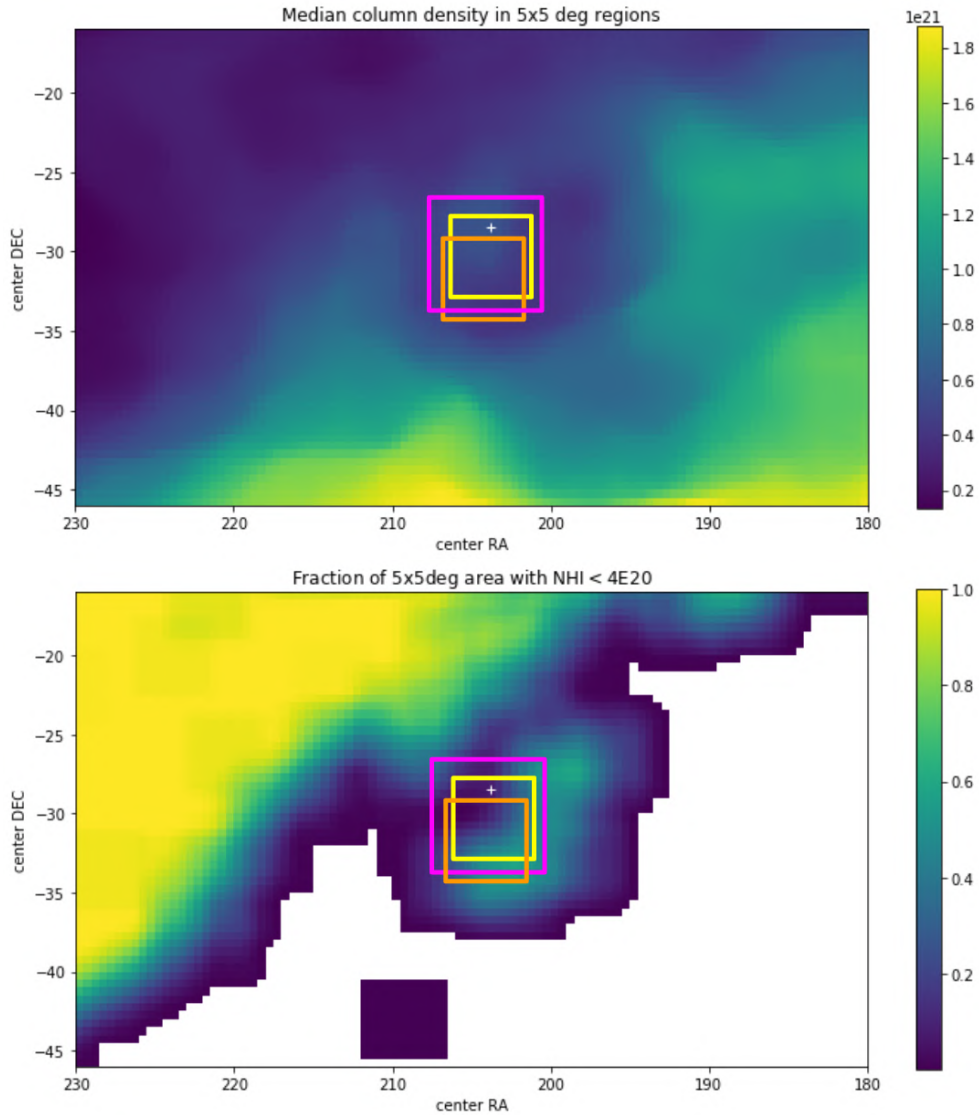


Figure 4.12: On the top: map of the median HI column density in regions $5^\circ \times 5^\circ$ degrees wide. On the bottom: map of the fraction of the regions $5^\circ \times 5^\circ$ degrees wide where the HI column density is lower than the established threshold of $4 \times 10^{20} \text{ cm}^{-2}$, and the white colour represent a fraction equal to zero. The axes indicate the center of each $5^\circ \times 5^\circ$ patch in (RA, DEC) expressed in decimal degrees. The two $5^\circ \times 5^\circ$ patches obtained from selection method based on Quality Factors are highlighted in yellow (Patch 1a) and orange (Patch 1b). The magenta rectangular patch identifies the area on the map where the polarized SED slope is constraint with the best accuracy (2-3%). Credit for background maps to: Susan E. Clark.

In fact, in correspondence with the two candidate patches, the HI column density shows an area of median values around $6 - 7 \times 10^{20} \text{ cm}^{-2}$, higher than the desired ones. Moreover, in correspondence with the same area, there is a very low fraction (less than 20%) of regions $5^\circ \times 5^\circ$ degrees wide where the column density is less than $4 \times 10^{20} \text{ cm}^{-2}$.

I examined the possibility of shifting attention to other maps areas showing a low median HI column density values, or a corresponding high fraction of regions $5^\circ \times 5^\circ$ degrees wide where the HI column density is lower than the established threshold. However, the values of the Quality Factors of the polarization fraction, the SNR of the polarization fraction and the SNR of the polarized power contrast, were not all simultaneously high enough from the simulations.

I therefore chose to proceed with the selection of the final patches by strictly moving around the area of the two patches obtained from previous analysis, with the intention of choosing the one which more than any other optimized all the Quality Factors, the accuracy on the polarized SED constraint, and the fraction of the HI column density less than $4 \times 10^{20} \text{cm}^{-2}$ within the patches.

4.9.2 The BLAST Observatory selection strategy

For the BLAST Observatory, I decided to use a slightly different strategy for dust targets search. To avoid the after-the-fact optimization process applied for the BLAST-TNG strategy, I went back to the stage of the algorithm where areas of interest were identified in the target field visibility. The areas of interest were those of intersection with some current and next-generation CMB experiments (the Simons Observatory, with the survey of the Small-Aperture Telescope (SAT); the BICEP/Keck experiment; and the SPIDER experiment), as shown in Figure 4.8 in correspondence with one of the latitudes considered, equal to -44.7° .

Then, in these areas of interest, I immediately looked at the HI column density. As was done for the BLAST-TNG analysis, I used data from the HI4PI survey (HI4PI Collaboration, 2016), with an angular resolution of $16.1'$ and a sensitivity of 43 mK, based on data from the first coverage of the Effelsberg-Bonn HI Survey (EBHIS; Winkel et al., 2015) and from the third revision of the Galactic All-Sky Survey (GASS; Kalberla & Haud, 2015)¹⁷.

Figure 4.13 shows the final search areas in the BLAST Observatory target field visibility for a latitude of -44.7° , where it is possible to see the HI column density map superimposed.

Only at that point, in areas with adequate column density values, I searched for the best patches implementing the Quality Factors method and checking the accuracy on the polarized SED constraint.

¹⁷HI4PI datasets are only available at the CDS via <http://cdsarc.u-strasbg.fr/viz-bin/qcat?J/A+A/594/A116>.

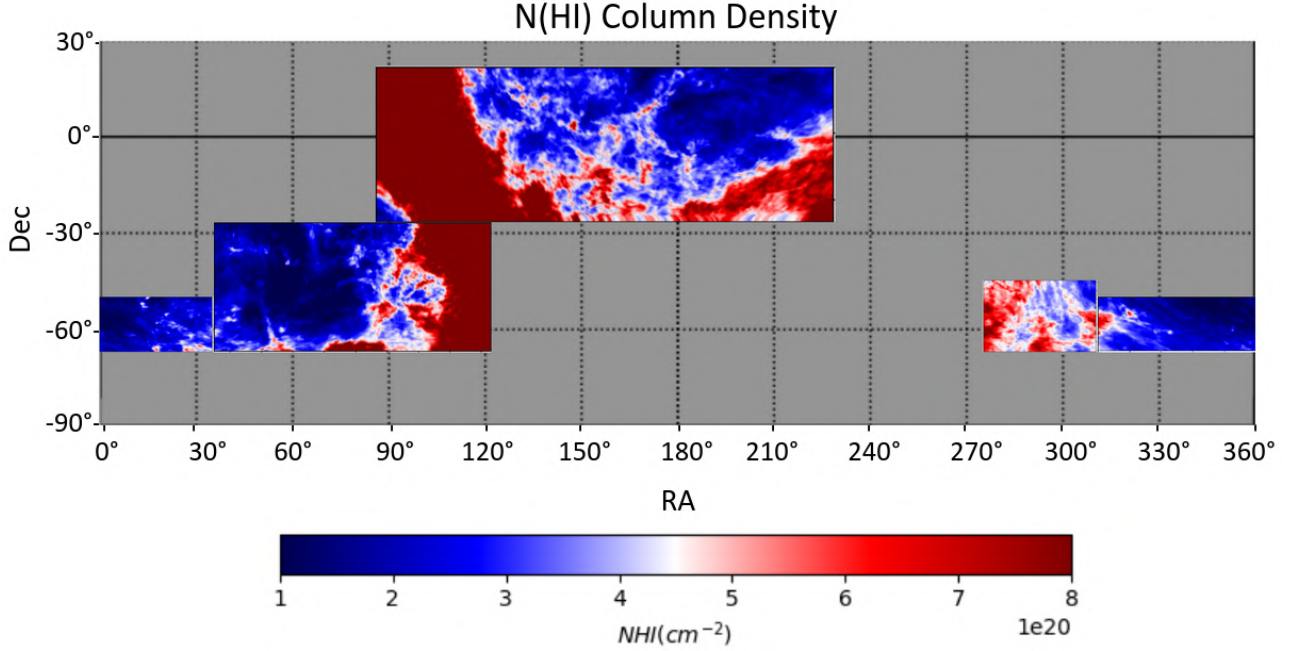


Figure 4.13: HI column density map superimposed on the search areas on the BLAST Observatory target field visibility, considering a launch from the Wanaka Station at a latitude of -44.7° , on March 15, 2026. The areas of interest are those of intersection with some current- and next-generation CMB experiments: the SAT Simons Observatory, BICEP/Keck and SPIDER. The map is represented in equatorial coordinates, Cartesian projection. The Galactic center is toward the right. The blue areas are those that satisfy the selection criterion ($N(\text{HI}) < 4 \times 10^{20} \text{ cm}^{-2}$).

4.10 Results

4.10.1 The BLAST-TNG diffuse ISM field selection

I performed the final analysis for the BLAST-TNG diffuse ISM fields selection, after a series of tests around the two best patches I identified by the preliminary simulations based on the Quality Factors method (Patch 1a and Patch 1b), defined in Section 4.7, and I selected the best four alternatives, with represent the best compromise not only considering the Quality Factors, but also the median value of the HI column density.

I called these four alternatives as “Proposal 1”, “Proposal 2”, “Proposal 3” and “Proposal 4”, and their positions with respect to Patch 1a and Patch 1b are highlighted in Figure 4.14, while their coordinates are listed in Table 4.10. Table 4.11 also specifies, quantitatively, how much the area of each new “Proposal” patch overlaps with the area of the best candidate patches based on the Quality Factors (Patch 1a and Patch 1b) and with the area in which the polarization fraction is best constrained. In Table 4.12, are listed other characteristics, such as: the MAD (Median Absolute Deviation) and SD (Standard Deviation) values of the slope of the polarization spectrum, which indicate how accurately the polarized SED is constrained in the patches; and the fraction of the

patches $5^\circ \times 5^\circ$ which have a HI column density less than $4 \times 10^{20} \text{cm}^{-2}$. Moreover, all the Quality Factors of “Proposal” patches, for each frequency channel, are summarized in Table 4.13.

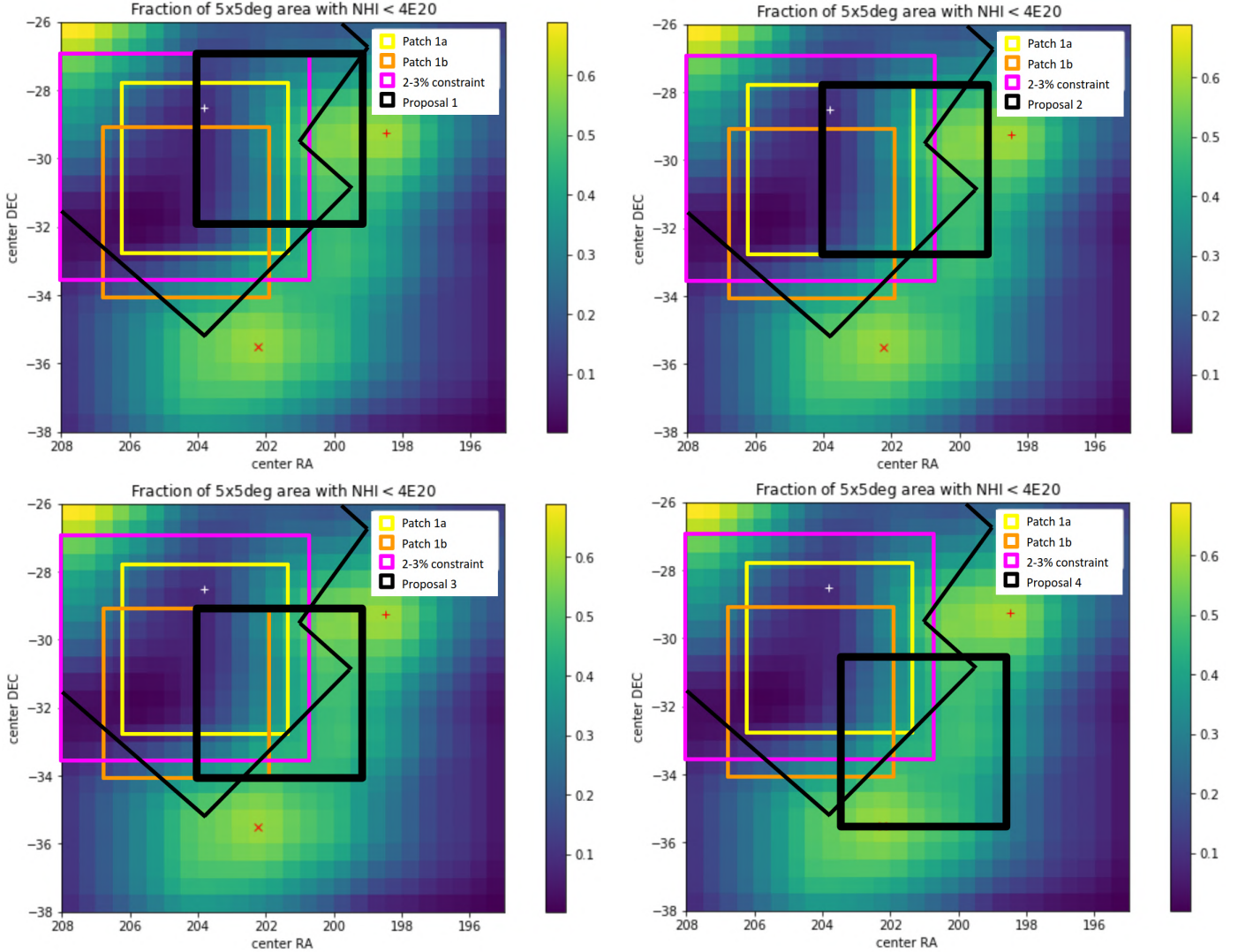


Figure 4.14: The maps indicate the location of each proposed patch in the final analysis (thick black line). The first row shows the “Proposal 1” and the “Proposal 2”, from left to right; while the second row shows the “Proposal 3” and the “Proposal 4”, always from left to right. The maps show the fraction of the regions $5^\circ \times 5^\circ$ degrees wide where the HI column density is lower than the established threshold of $4 \times 10^{20} \text{cm}^{-2}$. The axes indicate the equatorial coordinates (RA, DEC), expressed in decimal degrees. The two $5^\circ \times 5^\circ$ candidate patches from previous simulations are highlighted in yellow (Patch 1a) and orange (Patch 1b). The magenta rectangular patch identifies the area on the map where the polarization spectrum is constrained with the best accuracy (2-3%). The thin black line identifies the approximate limit to which the Quality Factors defined in Section 4.7 remain simultaneously high. Credit for background maps to: Susan E. Clark.

| Map Target | RA (J2000) | Dec (J2000) | Area (deg^2) | t_{obs} (hrs) |
|------------|-------------------|----------------------|---------------------|--------------------|
| Proposal 1 | $13^h26^m24.00^s$ | $-29^\circ27'00.0''$ | 25 | 48 |
| Proposal 2 | $13^h26^m24.00^s$ | $-30^\circ18'36.0''$ | 25 | 48 |
| Proposal 3 | $13^h26^m24.00^s$ | $-31^\circ35'49.2''$ | 25 | 48 |
| Proposal 4 | $13^h24^m20.63^s$ | $-33^\circ01'19.2''$ | 25 | 48 |

Table 4.10: *The centers coordinates of the new “Proposal” patches derived from the final analysis, with some properties, as the area and the observation time. The system in which the coordinates are expressed is the equatorial one.*

| Map Target | Patch 1a | Patch 1b | PF Better Constraint |
|------------|----------|----------|----------------------|
| Proposal 1 | 45.5% | 27.0% | 67.5% |
| Proposal 2 | 55.0% | 34.0% | 67.5% |
| Proposal 3 | 41.0% | 45.0% | 61.0% |
| Proposal 4 | 20.0% | 21.0% | 34.5% |

Table 4.11: *It is specified, in percentages, how much the area of each new “Proposal” patch overlaps with the area of the best candidate patches, previously identified by Quality Factors (Patch 1a and Patch 1b), and with the area where the Polarization Fraction (PF) is best constrained.*

| Map Target | MAD-SD(p_λ) | $N(HI) < 4E20$ |
|------------|-----------------------|----------------|
| Proposal 1 | 3.0%-4.5% | 55.6% |
| Proposal 2 | 3.0%-4.3% | 48.9% |
| Proposal 3 | 3.0%-4.2% | 38.9% |
| Proposal 4 | 3.5%-5.1% | 39.0% |

Table 4.12: *Some characteristics of the new “Proposal” patches, such as: the Median Absolute Deviation (MAD) and the Standard Deviation (SD) values of the slope of the respective polarization spectrum, which are expressed in terms of fractional change of the polarization fraction respect to the frequency range of BLAST-TNG bands; and the fraction of the $5^\circ \times 5^\circ$ patches that have a HI column density, $N(HI)$, minor of $4 \times 10^{20} cm^{-2}$.*

To conclude the analysis, a check was performed in each of these patches to verify the presence of complicated HI structures. This verification indicated the presence of CNM filaments, and therefore all the “Proposal” patches appeared more or less coherently filamentary in the HI.

Therefore, considering all the results and all the factors that guided my sky patch selection for the study of CMB dust foregrounds, it can be observed that all my “Proposal” patches are characterized by the following outlines:

| Map Target | Wavelength (μm) | $QF(p_\lambda)$ | $QF(SNR_{p_\lambda})$ | $QF(SNR_{P_{c,\lambda}})$ |
|------------|------------------------|-----------------|-----------------------|---------------------------|
| Proposal 1 | 250 | 12.4% | 42.1 | 28.8 |
| | 350 | 12.4% | 28.2 | 19.2 |
| | 500 | 12.3% | 21.0 | 14.3 |

| Map Target | Wavelength (μm) | $QF(p_\lambda)$ | $QF(SNR_{p_\lambda})$ | $QF(SNR_{P_{c,\lambda}})$ |
|------------|------------------------|-----------------|-----------------------|---------------------------|
| Proposal 2 | 250 | 13.3% | 43.5 | 27.9 |
| | 350 | 13.3% | 28.9 | 18.5 |
| | 500 | 13.2% | 21.5 | 13.8 |

| Map Target | Wavelength (μm) | $QF(p_\lambda)$ | $QF(SNR_{p_\lambda})$ | $QF(SNR_{P_{c,\lambda}})$ |
|------------|------------------------|-----------------|-----------------------|---------------------------|
| Proposal 3 | 250 | 13.2% | 41.6 | 27.4 |
| | 350 | 13.2% | 27.6 | 18.2 |
| | 500 | 13.2% | 20.5 | 13.5 |

| Map Target | Wavelength (μm) | $QF(p_\lambda)$ | $QF(SNR_{p_\lambda})$ | $QF(SNR_{P_{c,\lambda}})$ |
|------------|------------------------|-----------------|-----------------------|---------------------------|
| Proposal 4 | 250 | 10.9% | 42.0 | 30.0 |
| | 350 | 10.9% | 28.0 | 19.7 |
| | 500 | 10.9% | 20.8 | 14.5 |

Table 4.13: *The Quality Factors of the new “Proposal” patches ($QF(p_\lambda)$, $QF(SNR_{p_\lambda})$ and $QF(SNR_{P_{c,\lambda}})$) are shown, for the three observation channels of BLAST-TNG.*

- They can be observed more than 10 hours per day, according to the scheduler.
- Over most of the map of “Proposal” patches we should be able to constrain the polarization spectral slope with an accuracy of about 3.5% or 5.0%, considering the MAD and SD, respectively (the constraint is slightly better in “Proposal 2” and in “Proposal 3”).
- They have, on average, an high polarization fraction, which varies by less than two percentage point, equal to 11% – 13%; and an equivalently very high polarization fraction SNR, variable from about 20 – 21 up to 42 – 43 (the polarization fraction is slightly better in “Proposal 2” and in “Proposal 3”, while the polarization fraction SNR is slightly better in “Proposal 2”).
- They have on average a high SNR of the polarized power contrast, variable from about 13 – 15 up to 27 – 30 (it is slightly better in “Proposal 4”).

These listed results, all extremely comparable, led to the choice of the best patch on the basis of the only value that substantially changes, which is the fractional value of the patch characterized by HI column density values below the threshold of $4 \times 10^{20} cm^{-2}$. The latter, equal to 55.6% for “Proposal 1”, provided proof that this patch truly samples the diffuse ISM, thus making it the best candidate, followed closely by “Proposal 2”.

To conclude, the two best diffuse dust patches that I have identified, “Proposal 1” and “Proposal 2”, almost entirely overlapping, with characteristics suitable for carrying out studies of dust as a CMB foreground, were both considered as valid targets to observe in the flight plan of the 2019/2020 campaign of the BLAST-TNG experiment. In the end the BLAST collaboration selected “Proposal 1” as target to observe, having a slightly higher position in the final ranking.

4.10.2 The BLAST Observatory diffuse ISM fields selection

The final analysis for the BLAST Observatory diffuse ISM fields selection focused on the implementation of the “Quality Factors” selection method on the narrow target field visibility corresponding to the intersection areas with current and next-generation CMB experiments (the Simons Observatory, with the survey of the Small-Aperture Telescope (SAT-SO); the BICEP/Keck experiment; and the SPIDER experiment), characterized by adequate HI column density values ($N(HI) < 4 \times 10^{20} \text{ cm}^{-2}$).

But since in my analysis, to have a wider range of options, I considered the visibility plots of four different latitudes, even slightly higher or lower than the flight location of Wanaka in New Zealand (-40° , -44.7° , -50° and -55°), I had to look for a compromise between this extensive range of target field visibility at multiple latitudes, and the objective of observing a sky area that was superimposable with one or more of listed CMB experiments.

In addition, since the BLAST Observatory proposal considers two different performance scenarios, as was described in Subsection 4.2.2, the Current Best Estimates (CBE), which refers to the projected performance based on current telescope design, and the Minimum Expected Value (MEV), which refers to the mission top level requirements to meet all the science objectives, the “Quality Factors” related to the instrument performance, i.e. the SNR of the polarization fraction and the SNR of the polarized contrast, were evaluated for both scenarios, as well as the slope constraint of the polarized spectrum.

Therefore, I followed the principle of finding the best compromise considering all these aspects together: the Quality Factors, taking into account both the CBE and MEV scenarios; the median value of the HI column density; the target visibility from multiple latitudes; and the overlap with the current and next-generation CMB experiments.

I found five best candidates, called as “Proposal 1”, “Proposal 2”, “Proposal 3”, “Proposal 4” and “Proposal 5”, all overlapping with the SAT-SO survey, and the respective sky positions are highlighted in Figure 4.15. In particular, the “Proposal 1”, the “Proposal 2” and the “Proposal 3” are visible at all latitudes taken into consideration for 5 hours/day, and in addition the “Proposal 3” also overlaps with the SPIDER experiment field; the “Proposal 4” and the “Proposal 5” are visible only at two latitudes: -50° , where half of the patches are visible for 5 hours/day and the other half for 10 hours/day; and at latitude -55° , visible for 10 hours/day. These latest patches also overlaps with the BICEP/Keck experiment field. All these characteristics related to the observational strategy are summarized in Table 4.14. The “Proposal” patches coordinates are listed in the Table 4.15.

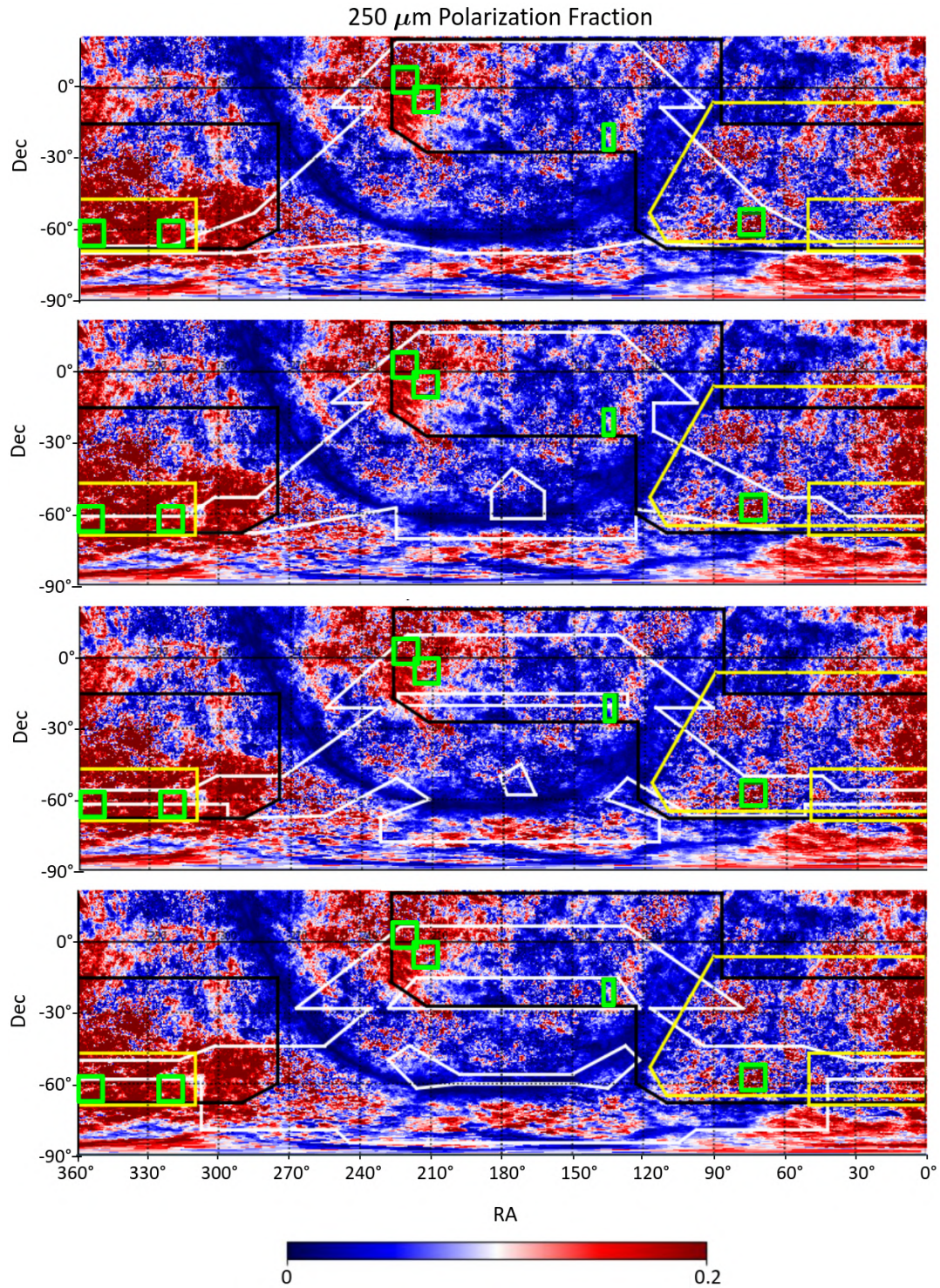


Figure 4.15: Polarization fraction sky maps at 250 μm , in the geometrically modeled target field visibility for the BLAST Observatory experiment (white contours) considering a launch from the Wanaka Station (New Zealand) on March 15, 2026, at a latitude equal to -40° , -44.7° , -50° and -55° , from the top to the bottom. The external white contours corresponds to an area available 5 hours/day, the most internal 10 hours/day (on the bottom). The target field visibility of the considered CMB experiments are also represented: the SO-SAT survey (black contours); the BICEP/Keck survey (yellow rectangular contours); and the SPIDER survey (yellow irregular contour on the right). The maps indicate the location of each proposed patch in the final analysis (green squares), showing their visibility latitudes and the CMB experiment overlapping. The translucent cloud Pyxis is also indicated (green rectangle $5^\circ \times 10^\circ$). The red regions are representative of a polarization fraction higher than 10%. The maps are represented in equatorial coordinates, Cartesian projection. The Galactic center is toward the left.

| Map Target | Latitude visibility (deg) | Daily visibility (hours/day) | CMB experiment overlap |
|------------|---------------------------|--|------------------------|
| Proposal 1 | -40, -44.7, -50, -55 | 5 | SO-SAT |
| Proposal 2 | -40, -44.7, -50, -55 | 5 | SO-SAT |
| Proposal 3 | -40, -44.7, -50, -55 | 5 | SO-SAT, SPIDER |
| Proposal 4 | -50, -55 | $(\frac{1}{2})10$ $(\frac{1}{2})5$ or 10 | SO-SAT, BICEP/Keck |
| Proposal 5 | -50, -55 | $(\frac{1}{2})10$ $(\frac{1}{2})5$ or 10 | SO-SAT, BICEP/Keck |

Table 4.14: *Some observational strategy characteristics of the “Proposal” patches: the target field visibility latitudes; the hours/day they are visible; and the CMB experiments with which they overlap. “Proposal 4” and “Proposal 5” are visible for 10 hours/day at latitude -55° while, at latitude -50° , half of the area is visible for 5 hours/day and the other half for 10 hours/day.*

| Map Target | RA (J2000) | Dec (J2000) | Area (deg^2) | t_{obs} (CBE) (hrs) | t_{obs} (MEV) (hrs) |
|------------|---------------------|------------------------|------------------|-----------------------|-----------------------|
| Proposal 1 | $14^h 12^m 00.00^s$ | $-5^\circ 00' 00.0''$ | 100 | 48 | 40 |
| Proposal 2 | $14^h 44^m 00.00^s$ | $3^\circ 00' 00.0''$ | 100 | 48 | 40 |
| Proposal 3 | $4^h 56^m 12.00^s$ | $-57^\circ 46' 40.8''$ | 100 | 48 | 40 |
| Proposal 4 | $21^h 20^m 00.00^s$ | $-62^\circ 00' 00.0''$ | 100 | 48 | 40 |
| Proposal 5 | $23^h 40^m 00.00^s$ | $-62^\circ 00' 00.0''$ | 100 | 48 | 40 |

Table 4.15: *The centers coordinates of the “Proposal” patches derived from the final analysis. The system in which the coordinates are expressed is the equatorial one. The two different observation times related to the two performance scenarios, CBE (Current Best Estimates) and MEV (Minimum Expected Value), are indicated.*

In Table 4.16 are listed some characteristics, such as: the MAD (Median Absolute Deviation) and SD (Standard Deviation) values of the polarization spectrum slope, which indicate how accurately the polarization fraction is constrained in the patches; the fraction of the patches $10^\circ \times 10^\circ$ which have a HI column density less than $4 \times 10^{20} cm^{-2}$; and the mean HI column density value in the patches. Moreover, all the Quality Factors of “Proposal” patches, for each frequency channel, are summarized in Table 4.17. To conclude the analysis, a check was performed in each of these patches to verify the presence of coherently filamentary HI structures.

Therefore, considering all the results I obtained, and all the factors that guided my sky patch selection for the study of CMB dust foregrounds, it can be observed that all my “Proposal” patches are characterized by the following outlines:

- Over most of the map of “Proposal” patches I should be able to constrain the polarization spectral slope with an accuracy: minor of 1.7% in the CBE case and minor of 2.7% in the MEV case, considering the MAD value; minor of 2.5% in

| Map Target | MAD-SD(p_λ) (CBE) | MAD-SD(p_λ) (MEV) | $N(HI) < 4E20$ | $\langle N(HI) \rangle$ (cm^{-2}) |
|------------|--------------------------------|--------------------------------|----------------|--|
| Proposal 1 | 1.0%-1.5% | 1.7%-2.4% | 75.7% | 3.32E20 |
| Proposal 2 | 0.8%-1.2% | 1.3%-1.9% | 87.6% | 3.04E20 |
| Proposal 3 | 1.5%-2.3% | 2.5%-3.6% | 100% | 1.57E20 |
| Proposal 4 | 1%-1.5% | 1.6%-2.3% | 86.5% | 3.23E20 |
| Proposal 5 | 1.7%-2.5% | 2.7%-4.0% | 100% | 1.83E20 |

Table 4.16: *Some characteristics of the “Proposal” patches, such as: the Median Absolute Deviation (MAD) and the Standard Deviation (SD) values of the slope of the respective polarization spectrum, which are expressed in terms of fractional change of the polarization fraction respect to the frequency range of BLAST Observatory bands; the fraction of the $10^\circ \times 10^\circ$ patches that have a HI column density, $N(HI)$, minor of $4 \times 10^{20} cm^{-2}$; and the mean value of the HI column density inside the patch.*

the CBE case and minor of 4.0% in the MEV case, considering the SD value (the constraint is slightly better in “Proposal 2”).

- They have, on average, an high polarization fraction variable between 14% and 21%; and an equivalently very high polarization fraction SNR, variable from about 26 up to 88 in the CBE case, and from about 16 up to 56 in the MEV case (both the polarization fraction and the polarization fraction SNR are slightly better in “Proposal 2”).
- They have on average a high SNR of the polarized power contrast, variable from about 13 up to 43 in the CBE case, and from about 8 up to 28 in the MEV case (it is slightly better in “Proposal 3”).
- They have on average a very low value of the HI column density, from about $1.6 \times 10^{20} cm^{-2}$ up to $3.3 \times 10^{20} cm^{-2}$, well below the threshold listed in the selection criteria (see Section 4.4), and a very big value of the fraction of the $10^\circ \times 10^\circ$ patches that have a HI column density, minor of the threshold, from about 76% up to 100% (these values are better in “Proposal 3” and in “Proposal 5”).

In Figures from 4.16 to 4.25 there are the “identity cards” of all “Proposal” patches I identified, where you can see how they appear in each of the properties considered so far: the polarization fraction (approximately constant in all channels), and the HI column density; the SNR of the polarization fraction and the SNR of the polarized contrast, for each frequency channel, and for both the considered performance scenarios, the Current Best Estimates (CBE) and the Minimum Expected Value (MEV).

These diffuse dust patches that I have identified, with characteristics suitable for carrying out a dust study as CMB foreground, have been used to make other theoretical predictions presented in NASA proposal, including the demonstration that, thanks to

| Map Target | Wavelength (μm) | $QF(p_\lambda)$ | $QF(SNR_{p_\lambda})$ (CBE) | $QF(SNR_{p_\lambda})$ (MEV) | $QF(SNR_{P_{c,\lambda}})$ (CBE) | $QF(SNR_{P_{c,\lambda}})$ (MEV) |
|------------|---------------------------|-----------------|--------------------------------|--------------------------------|------------------------------------|------------------------------------|
| Proposal 1 | 175 | 14.4% | 40.7 | 24.4 | 19.1 | 11.5 |
| | 250 | 14.4% | 70.0 | 44.7 | 33.5 | 21.4 |
| | 350 | 14.4% | 58.7 | 39.2 | 28.5 | 19.1 |

| Map Target | Wavelength (μm) | $QF(p_\lambda)$ | $QF(SNR_{p_\lambda})$ (CBE) | $QF(SNR_{p_\lambda})$ (MEV) | $QF(SNR_{P_{c,\lambda}})$ (CBE) | $QF(SNR_{P_{c,\lambda}})$ (MEV) |
|------------|---------------------------|-----------------|--------------------------------|--------------------------------|------------------------------------|------------------------------------|
| Proposal 2 | 175 | 21.4% | 52.3 | 31.5 | 20.9 | 12.6 |
| | 250 | 21.4% | 87.8 | 56.1 | 36.0 | 23.0 |
| | 350 | 21.4% | 72.4 | 48.3 | 30.4 | 20.3 |

| Map Target | Wavelength (μm) | $QF(p_\lambda)$ | $QF(SNR_{p_\lambda})$ (CBE) | $QF(SNR_{p_\lambda})$ (MEV) | $QF(SNR_{P_{c,\lambda}})$ (CBE) | $QF(SNR_{P_{c,\lambda}})$ (MEV) |
|------------|---------------------------|-----------------|--------------------------------|--------------------------------|------------------------------------|------------------------------------|
| Proposal 3 | 175 | 19.7% | 28.8 | 17.3 | 28.6 | 17.2 |
| | 250 | 19.7% | 43.6 | 27.9 | 43.3 | 27.7 |
| | 350 | 19.7% | 33.7 | 22.5 | 33.4 | 22.3 |

| Map Target | Wavelength (μm) | $QF(p_\lambda)$ | $QF(SNR_{p_\lambda})$ (CBE) | $QF(SNR_{p_\lambda})$ (MEV) | $QF(SNR_{P_{c,\lambda}})$ (CBE) | $QF(SNR_{P_{c,\lambda}})$ (MEV) |
|------------|---------------------------|-----------------|--------------------------------|--------------------------------|------------------------------------|------------------------------------|
| Proposal 4 | 175 | 17.4% | 43.5 | 26.2 | 13.9 | 8.4 |
| | 250 | 17.4% | 71.2 | 45.5 | 22.1 | 14.1 |
| | 350 | 17.4% | 57.7 | 38.5 | 17.7 | 11.8 |

| Map Target | Wavelength (μm) | $QF(p_\lambda)$ | $QF(SNR_{p_\lambda})$ (CBE) | $QF(SNR_{p_\lambda})$ (MEV) | $QF(SNR_{P_{c,\lambda}})$ (CBE) | $QF(SNR_{P_{c,\lambda}})$ (MEV) |
|------------|---------------------------|-----------------|--------------------------------|--------------------------------|------------------------------------|------------------------------------|
| Proposal 5 | 175 | 20.2% | 26.1 | 15.7 | 12.9 | 7.7 |
| | 250 | 20.2% | 41.1 | 26.2 | 20.3 | 13.0 |
| | 350 | 20.2% | 32.5 | 21.7 | 16.1 | 10.7 |

Table 4.17: *The Quality Factors of the “Proposal” patches resulting from the final analysis are shown, for the three observation channels of BLAST Observatory: the polarization fraction Quality Factor ($QF(p_\lambda)$); the polarization fraction SNR Quality Factor ($QF(SNR_{p_\lambda})$), considering the Current Best Estimates (CBE) and the Minimum Expected Value (MEV) performance scenarios; and the polarized contrast SNR Quality Factor ($QF(SNR_{P_{c,\lambda}})$), also in this case considering both the CBE and the MEV scenarios.*

the observation of one of these patches, it will be possible to distinguish one- versus two-component dust model (see discussion in Subsection 1.2.3), as presented in Figure 4.5. To conclude, as regards the BLAST Observatory proposal, BLAST collaboration planned to observe a patch that overlaps with the Simons Observatory SAT field from all latitudes (most likely the “Proposal 2” I identified), and a diffuse field that will also overlap with the BICEP/Keck experiment (most likely the “Proposal 5” I identified).

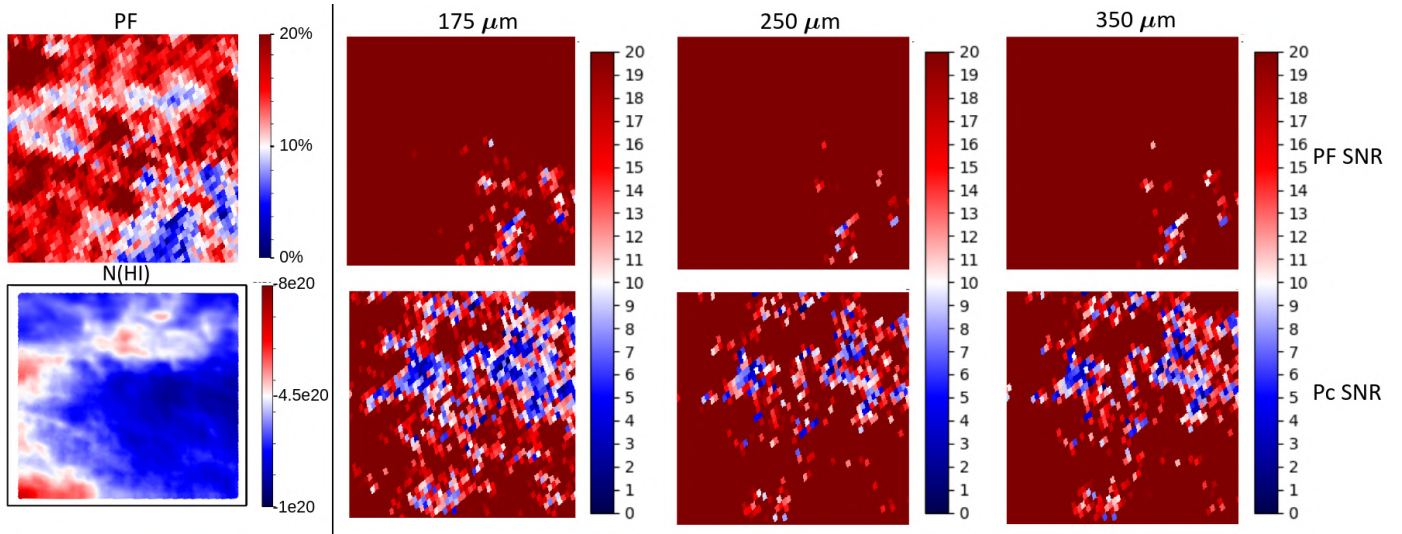


Figure 4.16: The "identity card" of the $10^\circ \times 10^\circ$ "Proposal 1" patch I identified. In the first column there are the polarization fraction (top), where the red colour corresponds to values higher than 10%, and the HI column density in unit of cm^{-2} (bottom), where the blue colour correspond to values smaller than the threshold $4 \times 10^{20} \text{cm}^{-2}$. In the first row there are the polarization fraction SNRs maps for each channel (175 μm , 250 μm and 350 μm), and in the second row the polarized contrast SNRs maps for each channel, where the red colour corresponds to a SNR > 10 . The the Current Best Estimates (CBE) scenario is considered.

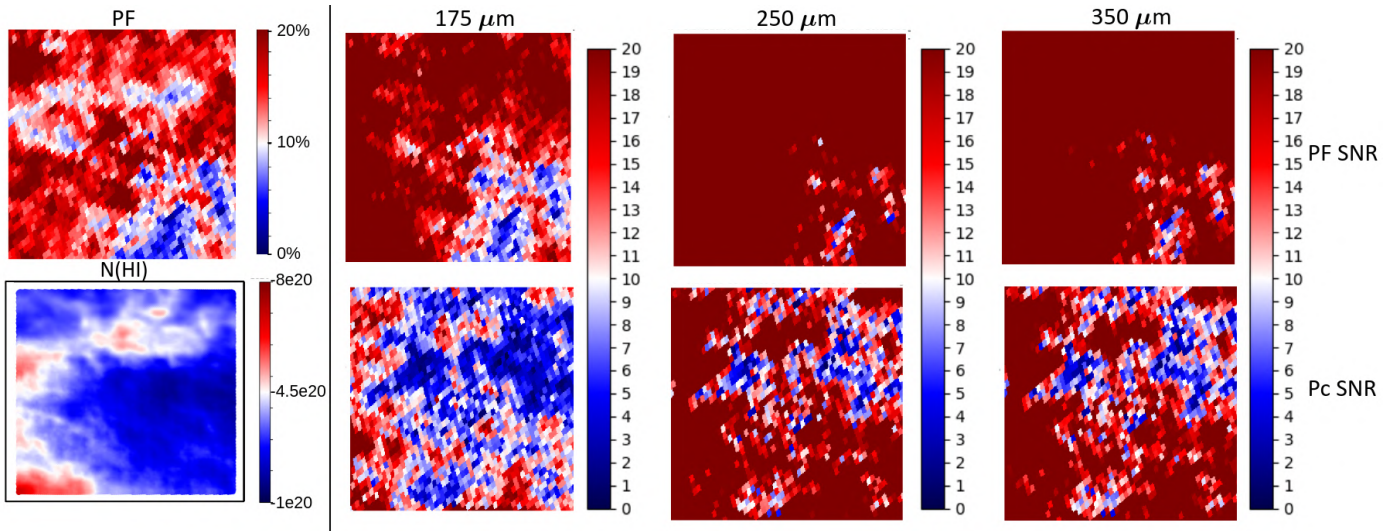


Figure 4.17: The "identity card" of the $10^\circ \times 10^\circ$ "Proposal 1" patch I identified, considering the Minimum Expected Value (MEV) scenario. For further details see caption of Figure 4.16 (the first column is repeated identically, as they are values independent of the chosen scenario).

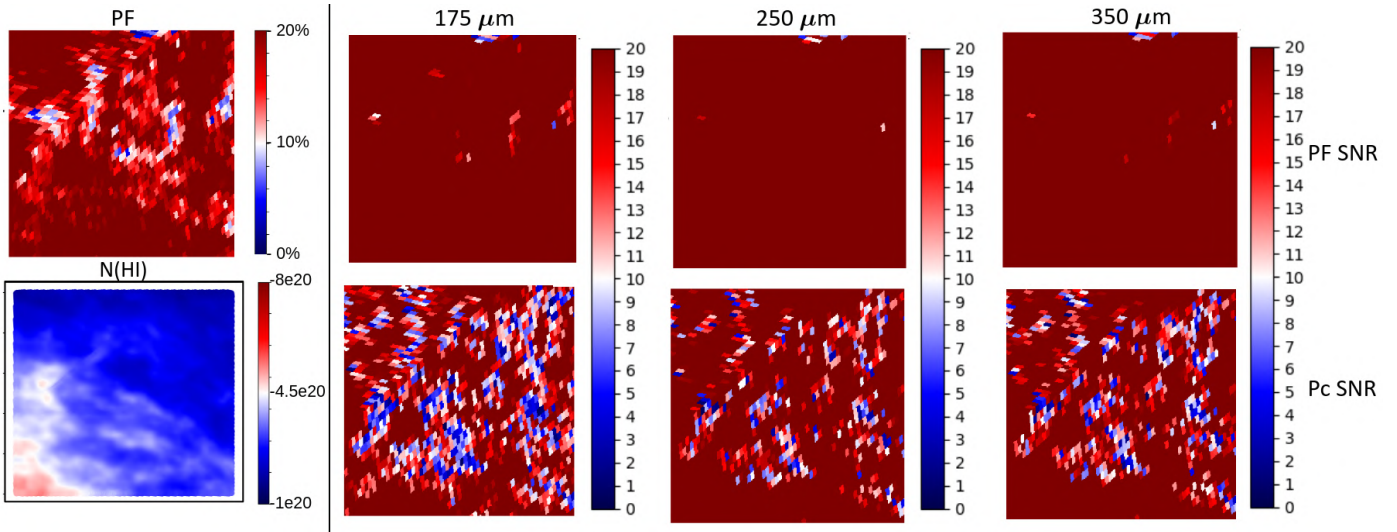


Figure 4.18: The "identity card" of the $10^\circ \times 10^\circ$ "Proposal 2" patch I identified. In the first column there are the polarization fraction (top), where the red colour corresponds to values higher than 10%, and the HI column density in unit of cm^{-2} (bottom), where the blue colour correspond to values smaller than the threshold $4 \times 10^{20} \text{cm}^{-2}$. In the first row there are the polarization fraction SNRs maps for each channel (175 μm , 250 μm and 350 μm), and in the second row the polarized contrast SNRs maps for each channel, where the red colour corresponds to a SNR > 10. The the Current Best Estimates (CBE) scenario is considered.

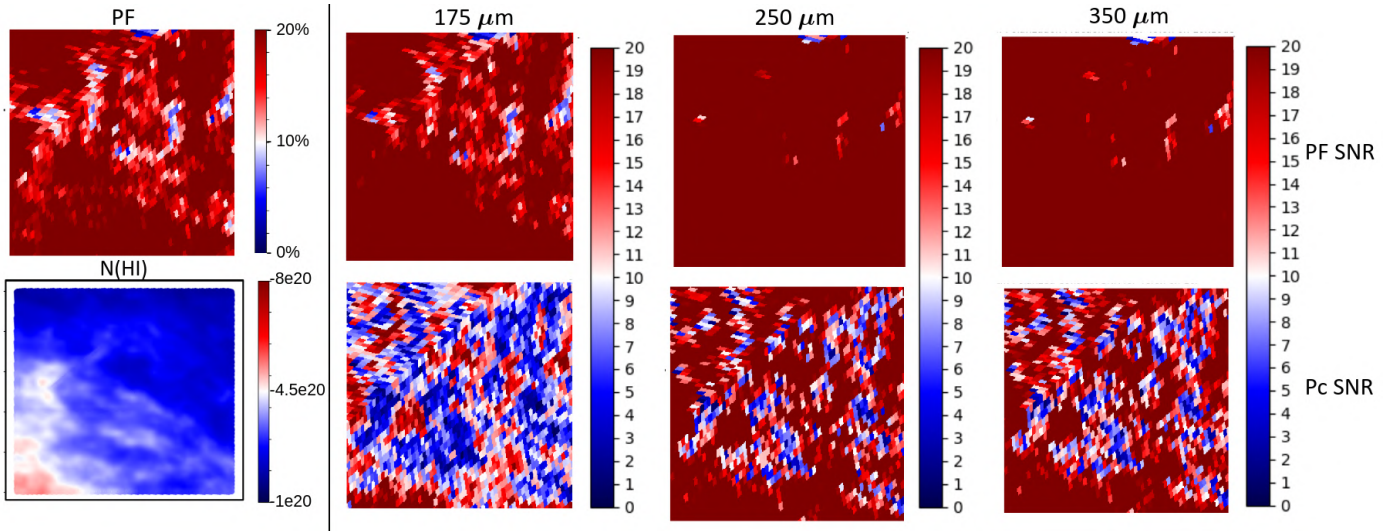


Figure 4.19: The "identity card" of the $10^\circ \times 10^\circ$ "Proposal 2" patch I identified, considering the Minimum Expected Value (MEV) scenario. For further details see caption of the Figure 4.18 (the first column is repeated identically, as they are values independent of the chosen scenario).

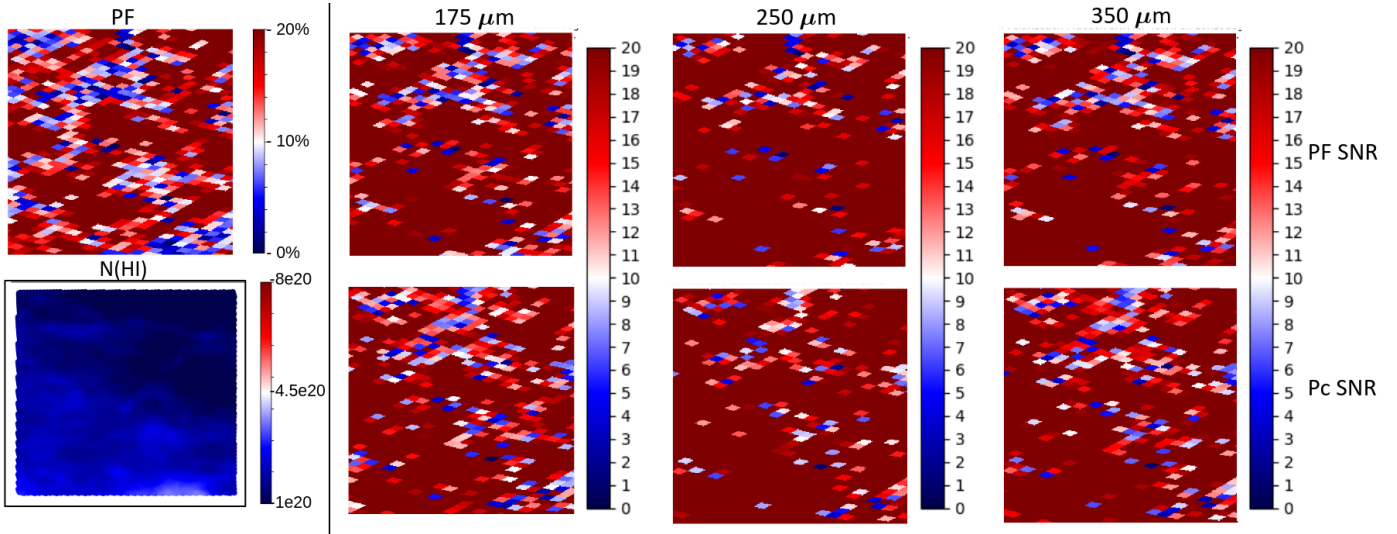


Figure 4.20: The "identity card" of the $10^\circ \times 10^\circ$ "Proposal 3" patch I identified. In the first column there are the polarization fraction (top), where the red colour corresponds to values higher than 10%, and the HI column density in unit of cm^{-2} (bottom), where the blue colour correspond to values smaller than the threshold $4 \times 10^{20} \text{cm}^{-2}$. In the first row there are the polarization fraction SNRs maps for each channel (175 μm , 250 μm and 350 μm), and in the second row the polarized contrast SNRs maps for each channel, where the red colour corresponds to a SNR > 10. The the Current Best Estimates (CBE) scenario is considered.

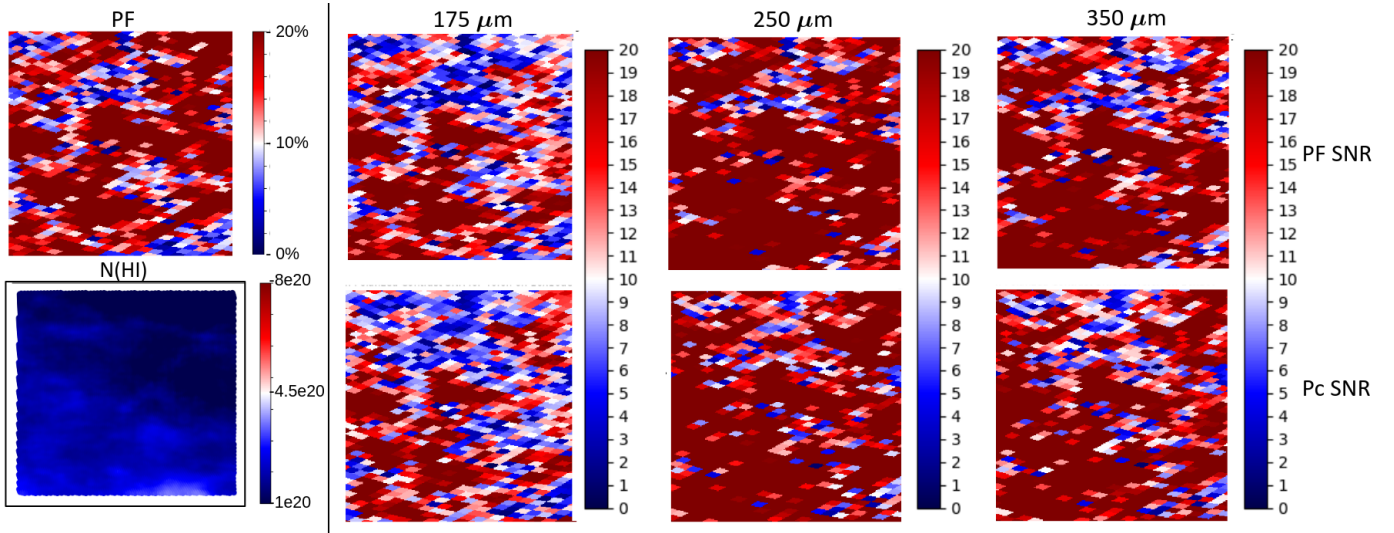


Figure 4.21: The "identity card" of the $10^\circ \times 10^\circ$ "Proposal 3" patch I identified, considering the Minimum Expected Value (MEV) scenario. For further details see caption of the Figure 4.20 (the first column is repeated identically, as they are values independent of the chosen scenario).

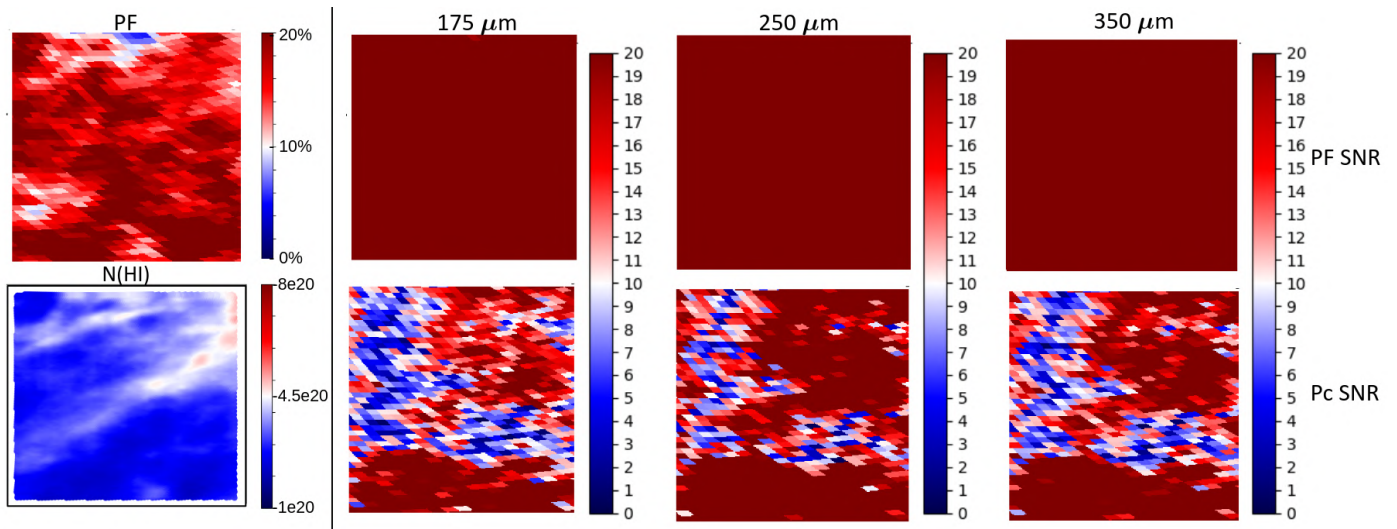


Figure 4.22: The "identity card" of the $10^\circ \times 10^\circ$ "Proposal 4" patch I identified. In the first column there are the polarization fraction (top), where the red colour corresponds to values higher than 10%, and the HI column density in unit of cm^{-2} (bottom), where the blue colour correspond to values smaller than the threshold $4 \times 10^{20} \text{cm}^{-2}$. In the first row there are the polarization fraction SNRs maps for each channel (175 μm , 250 μm and 350 μm), and in the second row the polarized contrast SNRs maps for each channel, where the red colour corresponds to a SNR > 10. The the Current Best Estimates (CBE) scenario is considered.

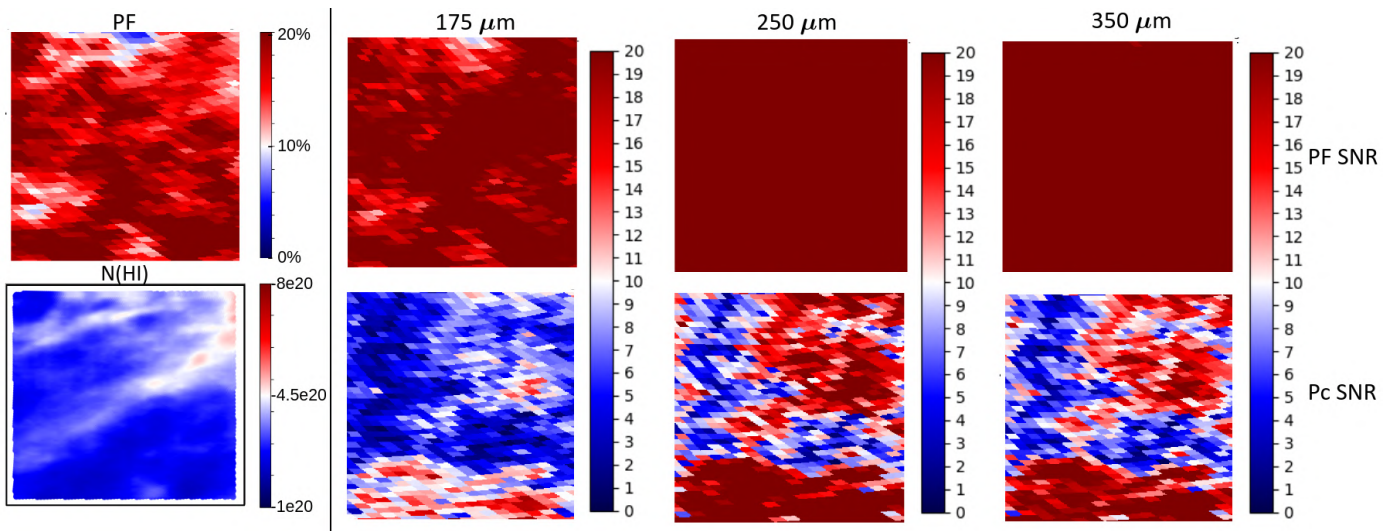


Figure 4.23: The "identity card" of the $10^\circ \times 10^\circ$ "Proposal 4" patch I identified, considering the Minimum Expected Value (MEV) scenario. For further details see caption of the Figure 4.22 (the first column is repeated identically, as they are values independent of the chosen scenario).

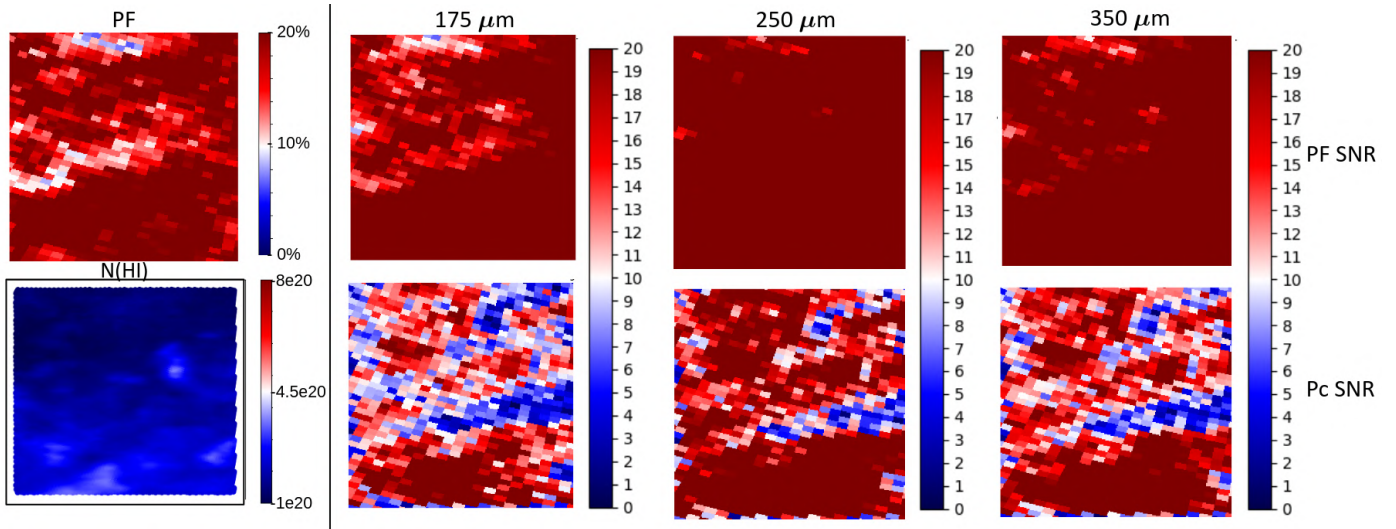


Figure 4.24: The "identity card" of the $10^\circ \times 10^\circ$ "Proposal 5" patch I identified. In the first column there are the polarization fraction (top), where the red colour corresponds to values higher than 10%, and the HI column density in unit of cm^{-2} (bottom), where the blue colour correspond to values smaller than the threshold $4 \times 10^{20} \text{cm}^{-2}$. In the first row there are the polarization fraction SNRs maps for each channel (175 μm , 250 μm and 350 μm), and in the second row the polarized contrast SNRs maps for each channel, where the red colour corresponds to a $\text{SNR} > 10$. The the Current Best Estimates (CBE) scenario is considered.

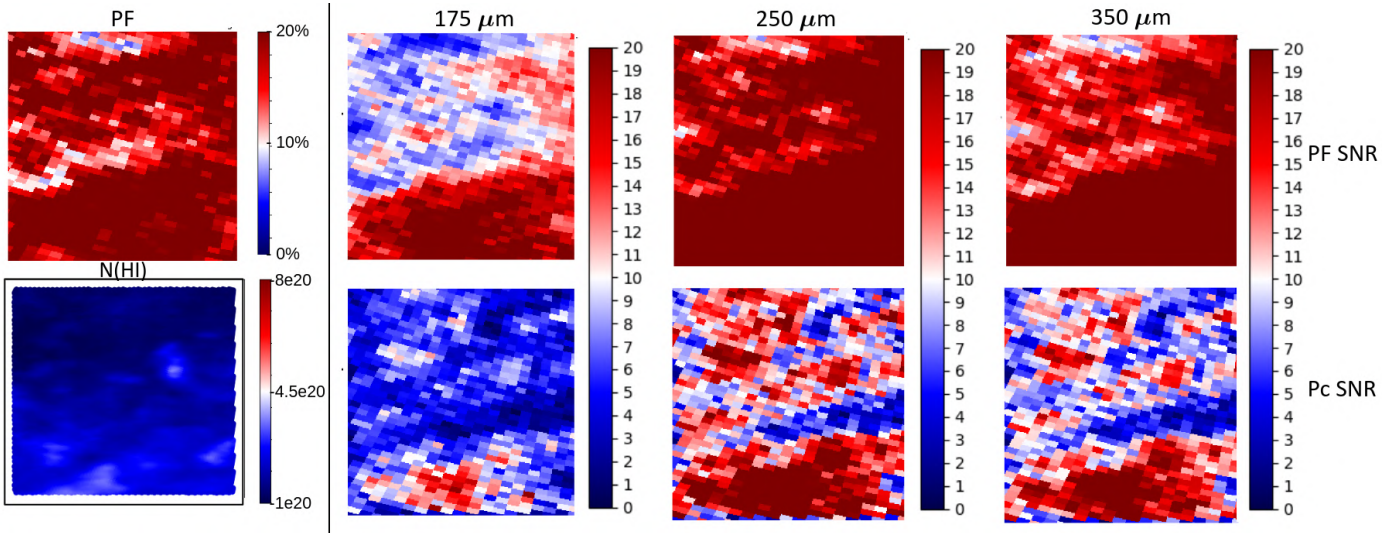


Figure 4.25: The "identity card" of the $10^\circ \times 10^\circ$ "Proposal 5" patch I identified, considering the Minimum Expected Value (MEV) scenario. For further details see caption of the Figure 4.24 (the first column is repeated identically, as they are values independent of the chosen scenario).

4.11 Conclusions

The BLAST experiment boasts a long series of experiments starting since 2003, as BLAST-TNG (The Next Generation) launched from Antarctica during last campaign in January 2020, up to the NASA proposal BLAST Observatory, its successor, which is expected to launch in 2028 from New Zealand.

BLAST will produce the most sensitive measurements of polarized Galactic dust emission to date in small regions of diffuse ISM (tens of square degree), in areas relevant for CMB observation. This will help to characterize dust properties, such as polarization, temperature and emissivity, and how they vary both with frequency and spatially, from the scale of arcminutes up to that of degrees. In fact, making up for *Planck*'s lack of observational polarization data at small angular scales, BLAST Observatory will reveal previously unresolved small-scale structures, setting a new upper limit on the resolution of foreground dust in these dark, diffuse ISM regions, thus making current simulations less limited. Therefore, it will be able to verify the consistency of the polarized signals to vary of the view's direction changes within the beam typical of CMB observation polarimeters, and the validity of this consistency will provide experimental support for components separation methods.

By penetrating into the small scale structure of these regions, it will be capable of explore and constrain correlations between diffuse dust emission and HI structures and HI column density in the Cold Neutral Medium (CNM) phase of the ISM, and in general to trace Galactic magnetic field structure, also in compact objects such as molecular clouds, providing a complementary study of magnetic field morphology.

All this information is also fundamental for the design and planning of current and next-generation CMB experiments, and in this sense BLAST will play a crucial role.

In the context of the observational strategy definition for an IR polarimetry balloon experiment, collaborating with the Science team of the BLAST collaboration, I contributed to the topic by planning the observation strategy for BLAST-TNG and the BLAST Observatory experiments: I identified some diffuse ISM fields to be observed in order to characterize the polarized dust emission as a CMB foreground.

My work has shed some light on a very important tool for selecting a diffuse dust region for in-flight observation. In this analysis both the observation requirements, the dust emission simulations, based on the PySM models and then extrapolated to higher frequencies, and finally the HI data, were combined together, obtaining quantitative comparisons. I developed a series of selection criteria, among which one based on a metric defined by three new parameters called "Quality Factors", which are scalar values defined as the average values of the polarization fraction, the signal-to-noise ratio (SNR) of the polarization fraction, and the SNR of the polarization power contrast of all the pixels within a certain patch.

For the BLAST-TNG observational strategy, I identified one $5^\circ \times 5^\circ$ best diffuse dust patch, visible for 10 hours/day, characterized by a high average value of the polarization fraction (12.4%), and high average SNR values of both the polarization fraction and the polarized contrast, with a minimum value of 14. About $\sim 56\%$ of the patch is characterized by a HI column density value, $N(HI)$, smaller than the threshold $4 \times 10^{20} \text{ cm}^{-2}$. This patch that I identified has been selected by BLAST collaboration as target to be observed with high priority in the flight plan 2019/2020 campaign of the experiment. Unfortunately, it was not possible to observe it due to the premature interruption of the mission, caused by an accidental damage. Therefore, the analysis I carried out was hindered by accident during BLAST-TNG deployment. This event suggests that the reason for the lack of published results is attributable to this accident of the experiment itself, totally independent of my work.

For the NASA proposed BLAST Observatory, I identified two $10^\circ \times 10^\circ$ ISM fields to be observed, suitable for two different performance scenarios, CBE and MEV (the one based on current telescope design and the one based on the mission top level requirements to meet all science objectives, respectively), one which overlaps with the Simons Observatory SAT field, and one which also overlaps with the BICEP/Keck experiment:

- The first patch identified, visible for 5 hours/day, is characterized by a very high average value of the polarization fraction (21.4%), and high average SNR values of both the polarization fraction and the polarized contrast, with a minimum value of 13 in the MEV scenario. About $\sim 76\%$ of the patch is characterized by a HI column density value, $N(HI)$, smaller than the threshold $4 \times 10^{20} \text{ cm}^{-2}$, with an average value of $N(HI) = 3.32 \times 10^{20} \text{ cm}^{-2}$.
- The second patch identified, visible for 5 hours/day for half of the area and 10 hours/day for the other half, is characterized by a very high average value of the polarization fraction (20.2%), and high average SNR values of both the polarization fraction and the polarized contrast, with a minimum value of 8 in the MEV scenario. The $\sim 100\%$ of the patch is characterized by a HI column density value, $N(HI)$, smaller than the threshold $4 \times 10^{20} \text{ cm}^{-2}$, with an average value of $N(HI) = 1.83 \times 10^{20} \text{ cm}^{-2}$.

Both patches have been used to make theoretical predictions by the Science team presented in the NASA proposal, including the demonstration that, thanks to the observation of one of these patches, it will be possible to distinguish one- versus two-component dust model.

In general, this analysis provides a systematic procedure that can also be applied to other datasets, and it is also intended to be a small part of a systematic program necessary to study polarized emissions from our Galaxy.

Chapter 5

Post-flight performance analysis of the BLAST-TNG star cameras pointing system

5.1 Introduction

This chapter is about the attitude data analysis of the BLAST-TNG experiment, described in Subsection 4.2.1, during the 15 hours flight from McMurdo (Antarctica) in January 2020, corresponding to the last campaign.

My work focused on the post-flight analysis of the star cameras images, and in particular on the search for images astrometric calibration, that is the pointing, scale, and orientation.

Star cameras pointing solutions are of fundamental importance for characterizing BLAST-TNG, and without these pointing solutions the BLAST-TNG collaboration would not have been able to characterize the performance of the instrument, by testing the accuracy of the pointing system.

To calculate a pointing solution for a balloon borne telescope is very challenging, for example more than for a ground based telescope, and the importance of star cameras lies in the fact that they are the most-accurate sensors for the telescope's pointing, and the only sensor that can provide a post-flight pointing solution with the required accuracy to make maps from raw data that over-sample the angular resolution of the telescope. Therefore, my work was crucial to making possible any sort of maps from BLAST-TNG data.

I found all the astrometric solutions through the more stable version of the `astrometry.net` service (Lang et al., 2010). Furthermore, due to the contaminant presence in the images of numerous Polar Mesospheric Clouds (PMCs), typical of the polar altitude at which the balloon flew, which lead to the inability to solve most images, I carried out a work of advanced images filtering, collaborating with three BLAST members: James

Aguirre¹, James Park, a graduate student at Queen’s University, and Ian Lowe². I implemented a custom algorithm to clean all the PMCs-contaminated images, and I was able to increase the number of post-flight star camera solutions, compared to solutions found without the use of filtering techniques, by a factor of more than 4. This results I found is mentioned in Coppi et al. (2020).

5.2 The pointing system

BLAST-TNG was a scan-mode telescope, pointing to the elevation and azimuth axes. It generally scanned quickly in azimuth ($0.1\text{ }^\circ\text{s}^{-1}$ - $0.2\text{ }^\circ\text{s}^{-1}$), and slowly stepping elevation. To control the attitude of the telescope, BLAST-TNG used three motors, which are described in Subsection 5.2.1. However, the motors were only a part of the global pointing system: during each scan, to reconstruct the position and determine the attitude, BLAST-TNG combined multiple pointing sensors, each taking advantage of different strengths, which are described in Subsection 5.2.2 (Coppi et al., 2020).

A payload scheme indicating the motors and some pointing sensors is shown in Figure 5.1.

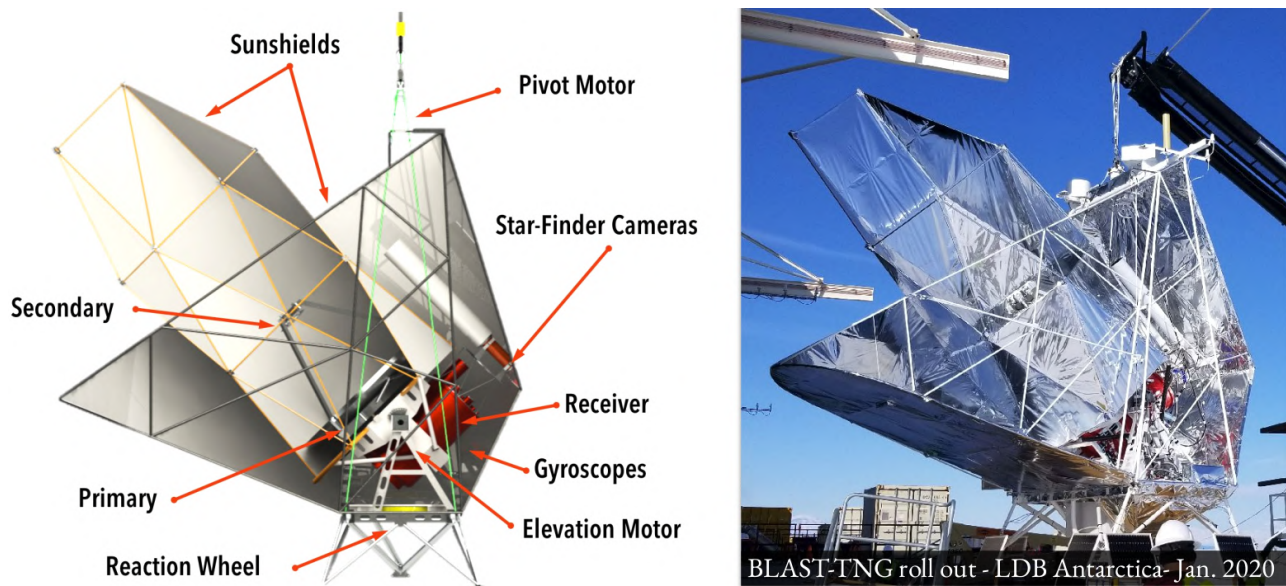


Figure 5.1: On the left there is a scheme of the BLAST-TNG payload where pointing motors (pivot, reaction wheel and elevation motor) and some pointing sensors (gyroscopes and star cameras) are shown. On the right there is a photo of the fully assembled payload in Antarctica, just before the launch opportunity on January 6th 2020. Credit to: Javier Romualdez.

¹Associate Professor at Department of Physics and Astronomy, University of Pennsylvania, Philadelphia, PA, USA.

²Postdoctoral Research Associate at Department of Astronomy and Steward Observatory, University of Arizona, AZ, USA

5.2.1 The pointing motors

- the elevation drive;
- the pivot;
- the reaction wheel.

By controlling the elevation scan speed, the elevation drive motor took care of changing the telescope’s elevation while, by controlling the azimuth scan speed, the pivot and the reaction wheel motors worked together to control the telescope’s movement in azimuth (Coppi et al., 2020).

5.2.2 The pointing sensors

There are two goals that the pointing sensors are designed to achieve. First, the in-flight pointing needs to be accurate enough to ensure that the detector array observes the desired targets. Second, the post-flight reconstructed pointing solution must be accurate enough to make a map that over-samples the beam of the telescope.

The BLAST-TNG attitude determination system consisted of a combination of multiple sensors that can be divided into three categories:

- high-accuracy (“fine”) pointing sensors;
- low-accuracy (“coarse”) pointing sensors;
- two 3-axis rate gyroscopes.

The solutions from the high- and low-accuracy pointing sensors were weighted according to their accuracies, and combined together into a pointing solution at each time. The time-dependent pointing solution was then created by combining also data coming from the gyroscopes, which measure the angular velocity, allowing us to integrate between pointing sensor solutions (Coppi et al., 2020).

Pointing reconstruction uses an algorithm based on a similar multiplicative extended Kalman filter technique (Markley, 2003) used by WMAP (Harman, 2005), which has been modified (Pittelkau, 2001) to allow for the evaluation of the star camera and gyroscope alignment parameters. The offsets between the star cameras and the sub-millimeter telescope are measured by repeated observations of pointing calibrators throughout the flight. Post flight absolute pointing accuracy using this system is typically $< 2''$, and random pointing errors were found to be $< 3''$ rms (Pascale et al., 2008; Marsden et al., 2008).

General insights into the performance of various pointing sensors and the resulting pointing solution can be explored in Natalie Gandilo’s thesis (Gandilo, 2015).

High-accuracy pointing sensors

The high-accuracy pointing sensors were:

- one high resolution elevation encoder;
- two identical optical star cameras.

The elevation encoder was the only elevation sensor, apart from the star cameras, and throughout the scan it was read-out continuously. The elevation encoder was especially important for locking the inner frame, as it provided a direct measurement of the inner frame elevation relative to the outer frame, which was the relevant measurement for matching the lock-pin to the holes on the inner frame.

The two identical star cameras, named XSC0 and XSC1, were two 1.45 megapixel CCDs with a 100 mm f/2L lens and a $2.5^\circ \times 2^\circ$ Field of View (FoV), and were mounted parallel to the boresight of the telescope, in the inner frame.

They were triggered to take exposures during scan turnarounds in azimuth, where the angular velocity of the telescope is at its minimum, to avoid streaking the stars in the images for the typical integration time. Depending on the scan speed and on the region's size to scan, this kind of strategy allowed to take images every 10 – 20 seconds approximately, so with a rate of $0.05 - 1 \text{ Hz}$ (Coppi et al., 2020). Star cameras could return a solution approximately every $\sim 1 - 2$ seconds, if stationary and pointed at a bright star field.

The optical star cameras measure directly celestial coordinates (RA and Dec) through detection of stars centroid, and so measurements of their positions on the sky; then these positions are compared to star catalogues. This process is based on a blob-finding algorithm to detect bright sources in the image, which then compare the angular distances between the identified blobs in the image and an already built database of angular distances between stars. The RA and Dec coordinates of the image centre are then calculated using a least-squares fit of the celestial angular distances from the image centre to each star and the distances in the frame in tangent plane coordinates.

This kind of algorithm was implemented in an in-flight software, called STARS (Chapman et al., 2014, see Section 5.3), and in a service named `astrometry.net` I used to solve post-flight images, described in detail in Subsection 5.4.1.

Although star cameras only measure celestial coordinates directly, and do not measure elevation, knowing the telescope's location and the local sidereal time, it is possible to convert celestial coordinates into telescope coordinates, thus azimuth and elevation. Actually, star cameras are the most accurate elevation sensor. In fact the elevation encoder, while precise, could not accurately measure the elevation of the telescope because it measures the elevation relative to the gondola, which is pendulating with respect to the ground.

A picture of the BLAST-TNG star cameras is shown in Figure 5.2, and the properties of each star camera are summarized in Table 5.1.



Figure 5.2: A picture of the BLAST-TNG experiment star cameras, named XSC0 and XSC1. Credit to: BLAST collaboration.

| | |
|-------------------------|---|
| Pixels | 1392 x 1040 |
| Pixel Size | 6.45 μm x 6.45 μm |
| Peak Quantum Efficiency | 60% |
| Dynamic Range | 14 bit |
| Well Depth | 16000 e^- |
| Read Noise | 6.5 e^- |
| Pixel FOV | 7'' |
| Camera FOV | 2.5° x 2° |
| Lens Diameter | 100 mm |
| Lens F/# | 2 |
| Lens Optical Efficiency | 0.8 |
| Filter Cut-off | 600 nm |

Table 5.1: BLAST-TNG star camera properties (Coppi et al., 2020).

In Figure 5.3 is shown an example of how appear a star camera image in CCD coordinates, where the longest axis it is composed of 1,392 pixels, while the shortest of 1,040 pixels, and each pixel has a Field of View (FoV) of $\sim 7''$.

In Section 5.3 I will discuss the in-flight behavior and functioning of star cameras, and in Section 5.4 will be described all the work I did during my PhD on post-flight images reconstruction for the search for astrometric solutions, in order to obtain high-accuracy pointing solutions.

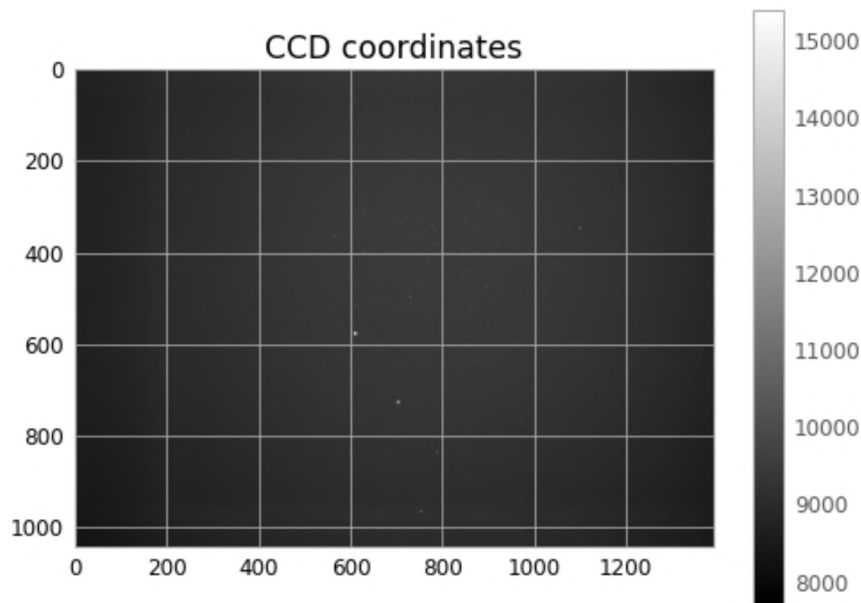


Figure 5.3: *How a star camera image looks like in CCD coordinates, where the longest axis it is composed of 1,392 pixels, while the shortest of 1,040 pixels, and each pixel has a Field of View (FoV) of $\sim 7''$. In this image, 102 pixels have counts greater than 10,000, appear brighter, and represent stars (two stars are clearly visible at the bottom center); while about 1.45 million pixels have counts less than 10,000 and represent the dark background.*

Star cameras are the only sensor capable of providing a post-flight pointing solution with the required accuracy to create maps from raw data that over-sample the telescope’s angular resolution.

Therefore, my post-flight work was crucial to making possible any sort of maps from BLAST-TNG data, and for characterizing the instrument performance, by testing the accuracy of the pointing system.

Low-accuracy pointing sensors

The low-accuracy pointing sensors were:

- one differential GPS (“dGPS”);
- six Pinhole Sun Sensors (PSS);
- two magnetometers;
- two inclinometers.

These “coarse” pointing sensors served two purposes: the first was to provide rough pointing solutions when the star cameras were unable to get solutions, due to a lack of visibility or in the event that the planets (which are not present in the catalogues used by star cameras) entered in the field of view; and the second was to correct for

long-timescale drifts in the gyroscope signal (Coppi et al., 2020).

The differential GPS was provided by CSBF and was used as an azimuth sensor, which has a precision of about 0.2° when compared with the in-flight star camera solutions. The pinhole sun sensors used Hamamatsu S5991-01 Position Sensitive Diodes (PSDs). When the spot of light from the $200\ \mu\text{m}$ pinhole light struck the PSD, a charge proportional to the light’s intensity was generated. When the voltage is biased, current flowed to the four electrodes at the corners of the active area, and the relative magnitudes of these currents could be used to determine the spot location (Coppi et al., 2020). Initial results from the pinhole sun sensors analysis from the January 2020 BLAST-TNG flight showed a pointing precision of 0.2° (Williams, 2021).

AS regard the magnetometers, to minimize the effect of magnetic fields induced by current in this components, they were mounted as far as possible from any active components, so on the sun shields. Their aim is provided information about the azimuth, as as with the rest of the “coarse” sensors. However, since to get the azimuth solution they measure the horizontal component of the Earth magnetic field, but close to the geomagnetic pole the magnetic field has almost only a vertical component and a very weak horizontal component, their use in a polar flight is particularly challenging (Coppi et al., 2020).

Finally, there were also two capacitive inclinometers, and they played a central role in reconstructing the event that caused the end of the BLAST-TNG flight in January 2020. They found that the outer frame of the gondola pitched forward by 4° during this event, confirming results found by the star cameras elevation solutions and the elevation encoder (Coppi et al., 2020).

Some properties of both low- and high-accuracy sensors are summarized in Table 5.2.

| Sensor | Location | Rate(Hz) | Accuracy($^\circ$) |
|---------------------|-------------|----------|----------------------|
| Elevation Encoder | Outer Frame | 100 | <0.01 |
| Star Cameras | Inner Frame | 0.05-0.1 | <0.001 |
| DGPS | Outer Frame | 5 | 0.2 |
| Pinhole Sun Sensors | Outer Frame | 5 | 0.2 |
| Magnetometers | Outer Frame | 100 | 5 |
| Inclinometers | Both Frames | 5 | 0.1 |

Table 5.2: *Low- and high-accuracy pointing sensors properties (Coppi et al., 2020).*

Gyroscopes

The gyroscopes (KVH Industries) measure the angular velocity, allowing to integrate between pointing sensor solutions. They presented a low frequency noise component, that manifested as a slowly varying DC offset between the true and measured angular velocities. To estimate the DC offset, the velocity measured by gyroscopes was compared to the true velocity reported by each “coarse” pointing sensor (Coppi et al., 2020).

5.3 In-flight star cameras performance

To solve for a pointing solution, on each image the in-flight star cameras ran STARS (Chapman et al., 2014), a “lost in space” algorithm which does not take into account any prior pointing information, and therefore the search is conducted over the entire sky.

During the BLAST-TNG January 2020 flight, the star cameras performed well and worked as expected, achieving the required accuracy and a good pointing stability of the system, less than $10''$. For example, over ten representative minutes, the pointing was stable to $2.4''$ in azimuth and to $7.1''$ in elevation, as shown in Figure 5.4.

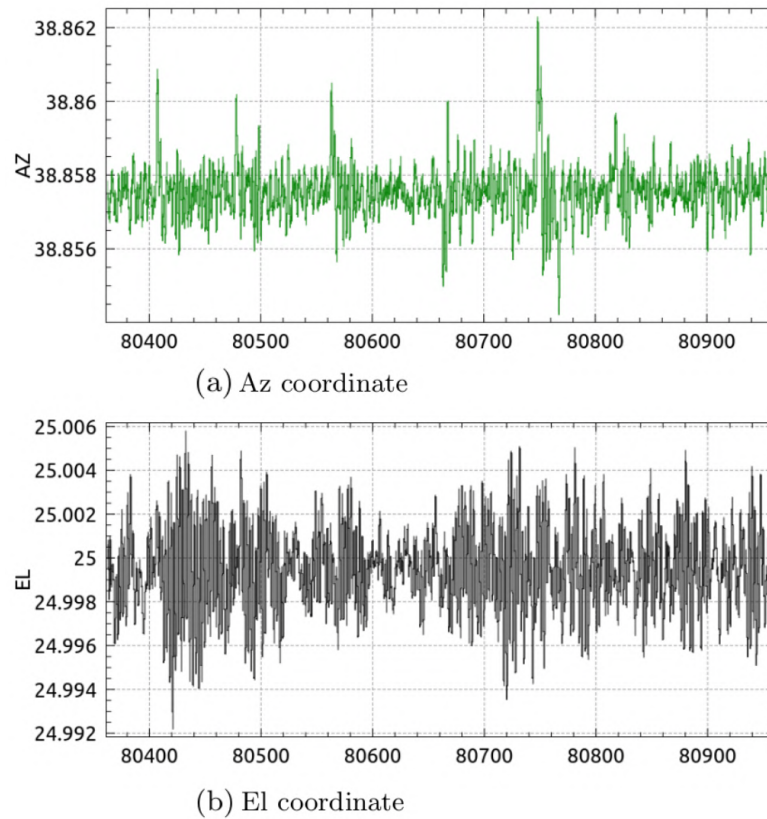


Figure 5.4: Example of azimuth (top) and elevation (bottom) pointing stability of BLAST-TNG January 2020 flight, during a period of ten minutes. The pointing was stable to $2.4''$ in azimuth and to $7.1''$ in elevation, how the standard deviations in azimuth and elevation over this time period describe. The x-axes are expressed in seconds, while the y-axes in degrees. Credit to: Ian Lowe.

Unfortunately, star cameras were not always been able to solve for an in-flight pointing solution due to the presence of Polar Mesospheric Clouds (PMCs), described in Subsection 5.3.1.

PMCs impacted the quality of star camera images which made it harder to obtain accurate pointing solutions, and this led to the inability to solve most images and to provide the sky position, obtaining only few (exactly 593) in-flight solutions during about 15 hours flight. A representative plot is shown in Figure 5.5.

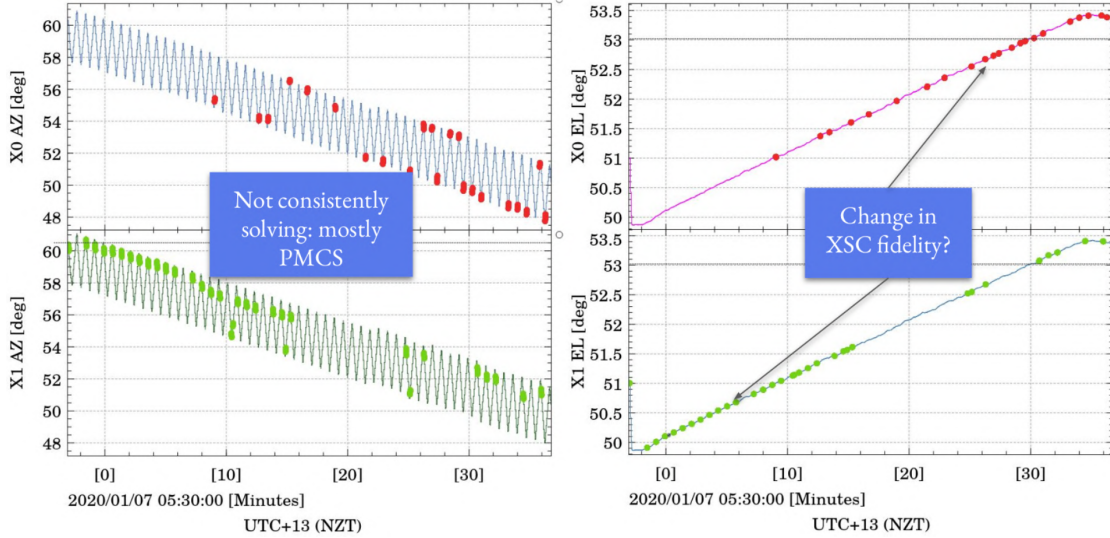


Figure 5.5: The in-flight star cameras pointing performance during a raster scan: XSC0 above (red) and XSC1 below (light green). The solutions coverage in azimuth (left) and elevation (right) is very partial, mainly due to the presence of Polar Mesospheric Clouds (PMCs). Credit to: Javier Romualdez.

5.3.1 Polar mesospheric clouds

A lot of BLAST-TNG star cameras images displayed numerous strange features (e.g. streaks, ripples), and similar features were observed also in star camera images of other balloon experiments, as EBEX (the E and B Experiment), which was also in stratosphere above Antarctica at the same time as BLASTPol, and SPIDER, even if just in a small fraction of raw images ($< 10\%$). The presence of these features interfered with the star camera's ability to identify stars, since large portions of the features would instead be identified as blobs by the solver software. The structures seen in these images are consistent with Polar Mesospheric Clouds.

These clouds are typical of the polar altitude at which the balloon flew (just under 40Km), and they are more commonly observed at high latitudes (above 70° to 75°). PMCs are composed of a diffuse layer of water ice crystals in the mesosphere, and increase in occurrence during the polar summer, when the temperature in the mesosphere is coldest. It is believed that PMCs occurrence is increasing, possibly due to climate change, or an increase in space traffic. In support of this thesis, it is reported that they were not observed in star camera images during the Antarctic flight of BLAST, in 2006, or during the Antarctic flight of BLASTPol, in 2010.

PMCs were strongly present in BLAST-TNG star camera images in correspondence of 280 – 320 sun azimuth range, while at 220 there was a drop off in brightness at which they were no longer visible.

In general, they reflected sunlight with a strong angular dependence causing different levels of image coverage. In fact, as can be seen in Figure 5.6, there was a large variation in light intensity from PMCs in star camera images, ranging from no obstruction of stars (and no issues solving for a pointing solution) up through complete obstruction.

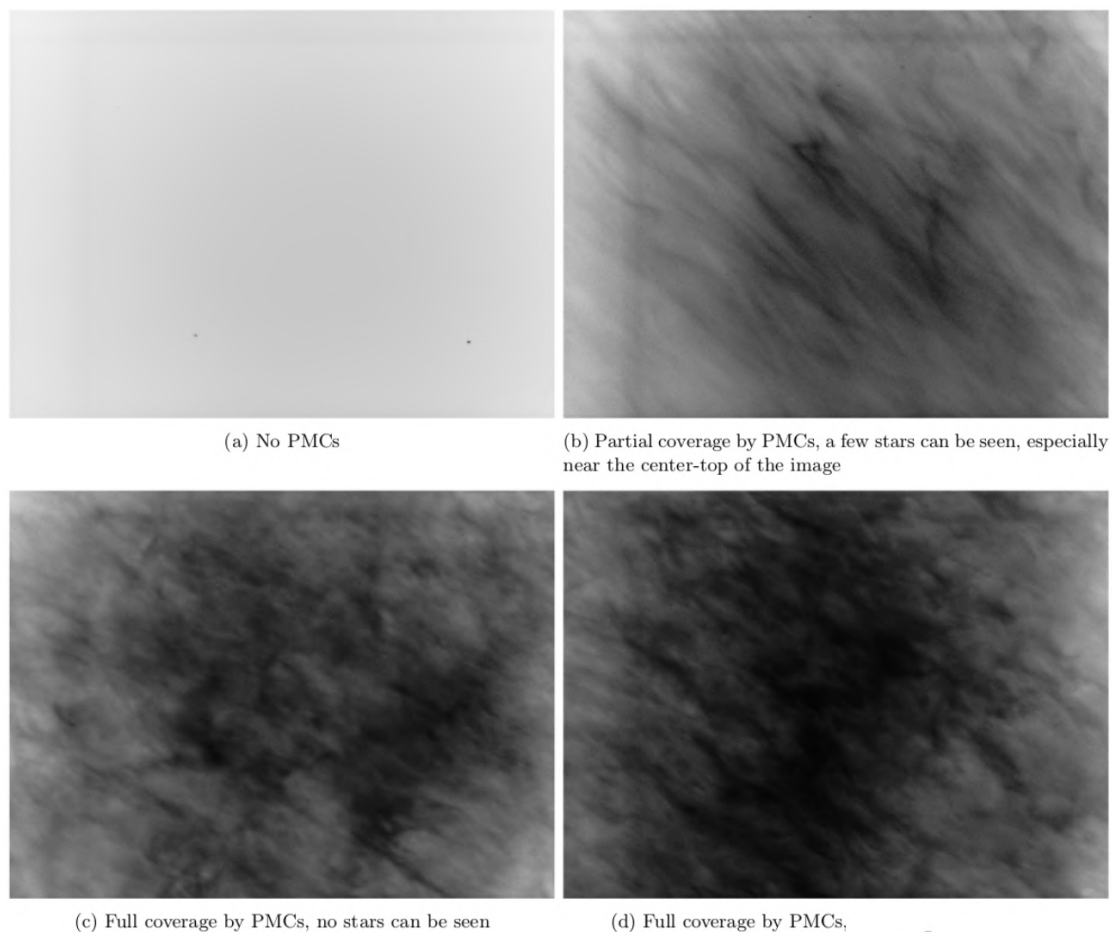


Figure 5.6: *BLAST-TNG star camera images from the 2019-2020 campaign, showing Polar Mesospheric Clouds (PMCs) with various brightness, ranging from no obstruction of stars (and no issues solving for a pointing solution) up through complete obstruction. All images have an inverted scale, with bright pixels represented by black, and dark pixels represented by white. Credit to: Ian Lowe.*

Due to the brightness and frequency of these clouds in star camera images, to ensure that stars could still be identified for the reconstruction of a post-flight pointing solution, I devised a solution: I wrote an algorithm based on advanced filtering techniques to sub-

tract the clouds from all PMC-contaminated images, obtaining just sky background with stars and some residuals, and then I ran the “cleaned” images with the `astrometry.net` service. This analysis is described in Section 5.4.

As for the BLAST-TNG experiment, it was not possible to implement the algorithm I wrote even in flight, due to the low computational power available (Coppi et al., 2020). However, thinking to forthcoming balloon-borne experiments, it is possible to elaborate strategies for the mitigation of this effect, improving the accuracy of the telescopes pointing and so of experiments performance. For example, to find in-flight pointing solutions, both the filtering techniques algorithm I wrote for the post-flight analysis and a clouds brightness track using daily images from the AIM (Aeronomy of Ice in the Mesosphere) satellite³, could be used jointly.

A further study of the general scientific topic of the PMCs goes beyond the purposes of this thesis, being not pertinent except in relation to their presence as a disturbance in the BLAST-TNG star cameras images analyzed, reported in detail in the thesis as a self-consistent work.

5.4 Post-flight star cameras analysis

With the aim of increasing the number of solved star camera images, and so the number of successfully recovered pointing solutions, I carried out a post-flight images analysis.

I analyzed 5,161 images, starting with the image obtained at what was considered the beginning of the flight, 9:50 pm New Zealand Time (NZT) on January 6 2020, up to the end of the flight, and to the last image obtained for each star camera: 09:23 am (NZT) on January 7 2020 for the XSC0 star camera, and 11:02 am (NZT), on the same day, for the XSC1 star camera. The XSC0 star camera stopped reporting data approximately one hour and 40 minutes earlier than the XSC1 star camera. Therefore, I thoroughly analyzed a total of 2,493 images of the XSC0 star camera, obtained during about 12 hours of flight, and a total of 2,668 images of the XSC1 star camera, obtained during about 13 hours of flight, as summarized in Table 5.3.

The software I used for the post-flight astrometric solution calculation is not the same used in-flight (STARS), but it is always a “lost in space” algorithm, which does not take into account any pointing information from the previous solutions. The software is named `astrometry.net` (Lang et al., 2010), whose characteristics and functioning are described in Subsection 5.4.1.

³<http://lasp.colorado.edu/aim/browse-images.php>.

| Star Camera | Number of Images | First Image (NZT) | Last Image (NZT) |
|-------------|------------------|-------------------------|--------------------------|
| XSC0 | 2,493 | Jan 6 2020 - 9:50:12 pm | Jan 7 2020 - 09:23:28 am |
| XSC1 | 2,668 | Jan 6 2020 - 9:50:12 pm | Jan 7 2020 - 11:02:52 am |
| Total | 5,161 | Jan 6 2020 - 9:50:12 pm | Jan 7 2020 - 11:02:52 am |

Table 5.3: *Some information of the star cameras images of the BLAST-TNG January 2020 flight, which I analyzed post-flight, referred to the XSC0 star camera (first line) and to the XSC1 star camera (second line). A total of 2,493 images of the XSC0 star camera, obtained during about 12 hours of flight, and a total of 2,668 images of the XSC1 star camera, obtained during about 13 hours of flight, were analyzed. Times refer to the New Zealand Time (NZT). The XSC0 star camera stopped reporting data about one hour and 40 minutes earlier than the XSC1 star camera.*

5.4.1 Astrometry.net: an astrometric calibration service

Astrometry.net⁴ (Lang et al., 2010) is an astrometric calibration service capable of obtaining correct and standards-compliant astrometric meta-data for every astronomical image, as well as lists of known objects within the Field of View (FoV). It is a robust software that makes the sky searchable, and it takes as input an astronomical image and tell where on the sky it came from, returning as output the astrometric calibration or World Coordinate System (WCS) information, a standards-based description of the transformation between image coordinates and sky coordinates: the determination of imaging pointing, orientation, and scale (Lang et al., 2010).

The system is based on the “blind astrometric calibration”, also known as “lost in space” problem, in which nothing is known: neither any previous information beyond the data, nor even the image scale. Therefore, not requiring a first guess, and working only with the information in the image pixels alone, this is a fully-automated and reliable system: the calibration meta-data and related error estimates are derived from the images themselves, and not from some unknown and undocumented external sources (Lang et al., 2010).

The orientation of the camera can be determined by the identification of the stars that are visible. A source detection is performed in the input image, and sets of four or five stars, named asterisms, are geometrically hashed and used as geometric features to compare to pre-indexed hashes. Then, a set of hypotheses from sparse matches about the astrometric calibration is generated. A next step performs detailed quantitative testing of the hypotheses, and it is accepted as true only if it passes a Bayesian decision theory test against a null hypothesis (Lang et al., 2010).

To solve new images, the search starts by building a set of indexes from a catalogue of stars in the sky, which are particular “features” for any sky view. These features are the relative positions of nearby quadruples of stars (named “quads” or “skymarks”), using a coordinate system defined by the most widely separated pair.

⁴<http://astrometry.net/>.

These are then used to assist in locating the new images, finding which views on the sky exhibit certain combinations of “quads”. And by intersecting the various lists of candidates which each feature generates, it is possible to identify the correct match. The “quads” are characterized by some properties, being:

- invariant to scale;
- invariant to rotation;
- invariant to translation;
- robust to small positional noise.

There may be the additional problem of “distractor” and “dropout” stars: query images may contain some extra stars that are not in the index catalogue, and some catalogue stars may be missing from the image, respectively.

Finally, the software solve the images blindly through image-solving programs, searching for the best-fit WCS solution.

These programs work by looking at sources in the images, starting with the brightest. They search for all “skymarks” that can be built from the N brightest stars before considering star $N + 1$. When using several index files, it can be much faster to search for many “skymarks” in one index file before switching to the next one. This flag allows to control when the solver switches between index files. It also allows to control how much effort the solver puts in before giving up: by default, it looks at all the sources in the image, and usually times out before this finishes (Lang et al., 2010).

Index files

There are three options for using the `astrometry.net` service, and images can be calibrated, respectively:

- on the flickr photo-sharing site;
- through a user-friendly web service;
- by a downloadable software package.

In my analysis, I chose this third option as it is the most stable version, downloading the source and building the software on my local Linux, starting from one of the most important steps that is to grab some index files.

The index files are used by `astrometry.net` to solve images, and are built from an astrometric reference catalogue such as USNO-B 1.0, 2MASS or TYCHO-2, designed for uniformity of coverage and redundancy (Lang et al., 2010):

- USNO-B 1.0: is an all-sky catalogue compiled from scans of old Schmidt plates, and contains about 10^9 objects, both stars and galaxies;
- 2MASS: is a catalogue with over $300 \cdot 10^6$ observed objects, including minor planets of the Solar System, brown dwarfs, low-mass stars, nebulae, star clusters and galaxies;
- TYCHO-2: is a tiny subset of $2.5 \cdot 10^6$ brightest stars.

Each index file is designed to solve images within a narrow range of scales.

For wide-angle images, there are index files called the “4100-series”.

Instead, the set of indices I used are part of the “4200-series”. In particular, in this series, the files are named like `index-42XX.fits` or `index-42XX-YY.fits`, where `XX` is the “scale” and `YY` is the HEALPix number. In fact, the code includes a simple but powerful HEALPix implementation: the medium-sized index files are split into 12 HEALPix tiles, each one covers 1/12th of the sky; and the small-sized ones are split into 48 HEALPixes.

If the user grabs extra index files, the solver will run more slowly (even if the results should be the same), so I downloaded index files whose “skymarks” are from 10% to 100% of the sizes of the images I wanted to solve: considering that the Field Of View (FOV) of each star camera image was $2.5^\circ \times 2^\circ$, I used 137 index files that contained “skymarks” of size from 0.1° up to 2.5° or, equivalently, from $6'$ up to $150'$, as shown in Figure 5.7.

Solving program and output files

As image-solving program I chose `solve-field`, that is the main high-level command-line user interface, and processes FITS images too. The `solve-field` program takes the input files, does source extraction on them to produce a FITS BINTABLE of source positions, named `xylist`, then takes the information that I can supplied about the fields on the command-line.

For speed up of solving, as tip, I assumed known pixel scale adding to the command line `--scale-units arcsecperpix --scale-low 6.000 --scale-high 7.000`: knowing in fact that the star camera FoV was equal to $2.5^\circ \times 2^\circ$, and knowing that the CCD had dimensions of $1,392 \times 1,040$ in pixels, it was possible to trace the FoV of each pixel in arcseconds, equal to $6.5\text{--}7''$ approximately, thus obtaining that the pixel scale was therefore between 6 and 7 arcseconds, as written in the command line. Adding the scale of the image, `solve-field` program uses this to decide which index files to try to use to solve the image. Therefore, it adds FITS headers to the `xylist` FITS BINTABLE, encoding the information that I added in the command line, calling this new file `augmented xylist`, using the filename suffix `.axy`.

Finally, `solve-field` then calls the “backend” program, passing it the `axy` file. This program reads a configuration file that describes where to find index files, whether to load

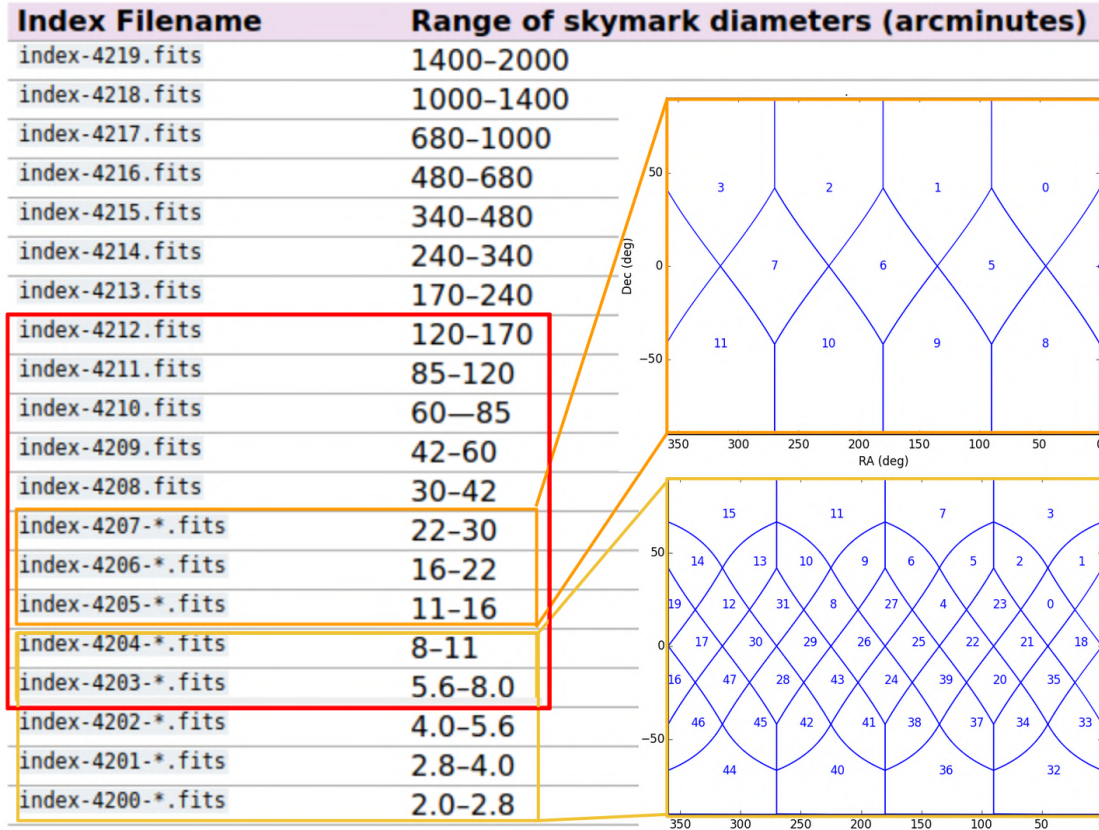


Figure 5.7: Index files of the “4200-series” used by *astrometry.net* service to blindly solve the images. The red box indicates the indexes (from 4203 to 4212) used by me in the post-flight star camera images analysis of the BLAST-TNG 2019-2020 campaign. Names with an asterisk indicate medium- (orange, top) or small- (yellow, bottom) sized index files splitted into different pixellizations, equal to 12 or 48 HEALPixes, respectively. I used 36 (= 12 × 3) medium-sized index files, 96 (= 48 × 2) small-sized index files, and 5 other index files, for a total of 137 index files. Source: <http://astrometry.net/doc/readme.html>.

all the index files at once or run them one at a time, and how long to spend on each field.

The output files that are produced are the following, where <base>, in my analysis, indicated the name of star camera image showing the date and the time (NZT) of acquisition:

- <base>-indx.xy1s: a FITS BINTABLE with the pixel locations of stars from the index;
- <base>.axy: a FITS BINTABLE of the sources extracted from the image;
- <base>.rd1s: a FITS BINTABLE with the RA and Dec coordinates of the extracted sources;

- `<base>.match`: a FITS BINTABLE describing the “quad” match that solved the image;
- `<base>.solved`: it exists if the field is solved;
- `<base>.wcs`: a FITS WCS header for the solution;
- `<base>.new`: a new FITS file containing the WCS header.

In addition to output files, `astrometry.net` also produces output plots.

Output plots and results

The output plots produced by `astrometry.net` are the following, where `<base>` also here indicates the name of the star camera images I analyzed, showing the date and the time (NZT) of acquisition:

- `<base>.ngc.png`: an annotation of the image;
- `<base>-objs.png`: a plot of the sources (stars) extracted from the image;
- `<base>-indx.png`: sources (red), plus stars from the index files (green), plus the “skymark” (“quad”) used to solve the image.

As example, the `astrometry.net` output plots produced by the analysis of a single image, one of the XSC0 star camera without Polar Mesospheric Clouds (PMCs) contamination, are shown in Figure 5.8.

Before to describe the filtering techniques applied to the PMCs contaminated images, in Subsection 5.4.2, it should be emphasized that the pointing solutions I obtained for each image consisted of:

- the field center celestial coordinates, RA and Dec, both in degrees, with an accuracy of one millionth of a degree, and in the formats H:M:S and D:M:S respectively, with an accuracy of 0.001 s;
- the field rotation angle, in degrees, with an accuracy of 0.001 degrees;
- the image size (FoV) in degrees by degrees, with an accuracy of $1 \cdot 10^{-5}$ degrees on each side.

Finally, I implemented the code I wrote for this analysis by parallelizing the software execution and distributing the input data over four processes, with the aim of optimizing the image analysis time. This parallelization was implemented at the script level by collaborating with James Park, a graduate student of Queen’s University.

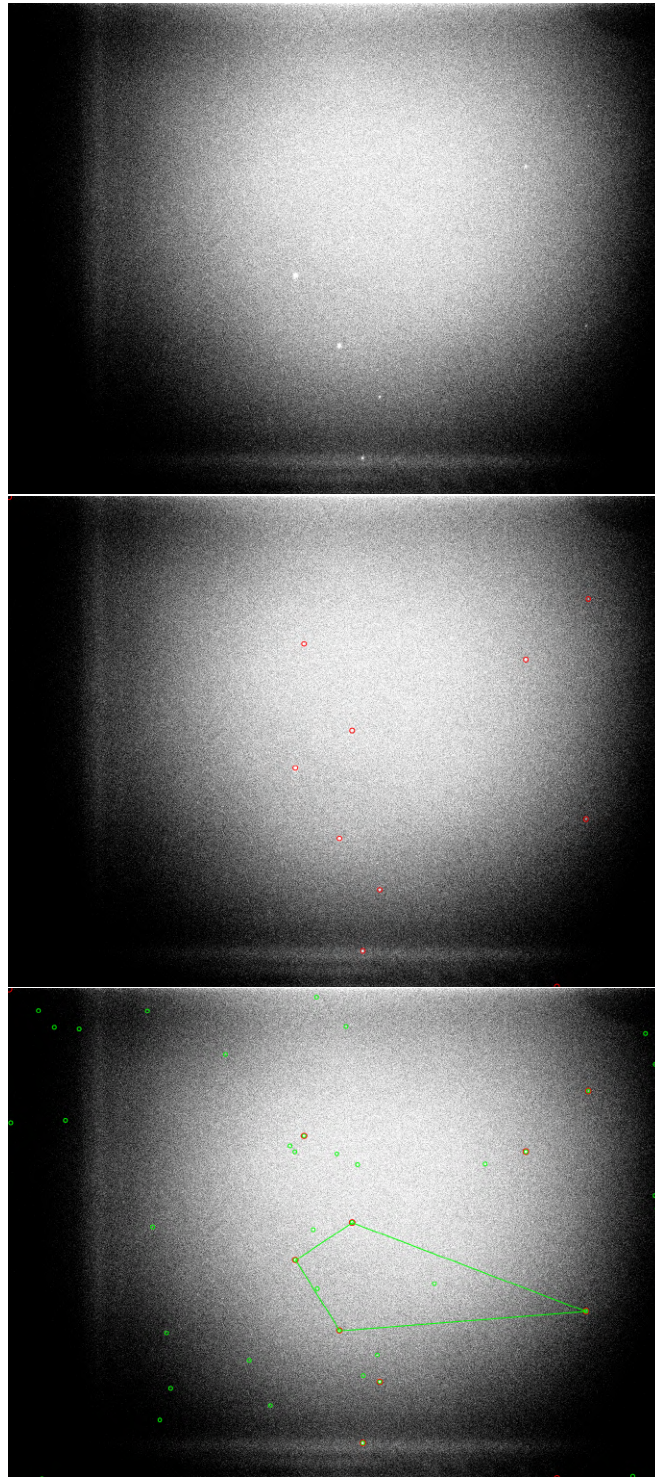


Figure 5.8: Three types of output plots produced by the *astrometry.net* service after the search I did for the astrometric solution of a star camera image. At the top, there is an annotation of the image (`<base>.ngc.png`); at the center, there is a plot of the sources (stars, in red) extracted from the image (`<base>-objs.png`); at the bottom, there are both sources (in red), stars from the index files (in green), and “Skymark” (“quad”) used to solve the image (`<base>-indx.png`).

5.4.2 Filtering techniques

With the aim to recover other solutions, since the presence of Polar Mesospheric Clouds (PMCs) caused the search for the pointing solution to fail, I cleaned up the images contaminated by PMCs (a total of 4,828), before returning them to `astrometry.net`. I implemented a custom algorithm I originally wrote for solutions search, with advanced filtering techniques to subtract the PMCs' effects, collaborating with James Aguirre⁵, which gave me some tips on filtering. This algorithm is based to the consecutive application and fine-tuning of some main filtering techniques, described here:

1. The **flat field reduction**: it is a standard calibration technique used to improve quality in digital imaging, and it consists in canceling the effects of image artifacts caused by variations in the pixel-to-pixel sensitivity of the detector, and by distortions in the optical path.

I applied the flat field reduction technique by dividing each PMC-contaminated image with the flat field taken for the respective star camera (XSC0 or XSC1), and then by subtracting the average value of this new image.

An alternative to this step, which I used in some images, was to flatten the image by removing low order polynomials of degree equal to 3.

2. The removal of the **pixels outliers**: I calculated a robust standard deviation (σ) using the Median Absolute Deviation (MAD) of the flatten image (from Phase 1.), and I therefore established a threshold equal to 6σ . This threshold has been changed in case of non-solved image, proceeding by trial and error, and it was used to define the image outliers: the pixels outside the range established by the threshold. To create the flatten image with no outliers, I replaced the pixel outliers with the value of the median of the flatten image neighboring pixels at the pixel outliers.
3. The application of a **low-pass filter** to the flatten image (with or without outliers) using a Gaussian filter, and in detail a σ equal to 5. Here it was the possibility to change the sigma value in case of non-solved image, proceeding by trial and error. I subtracted the low-pass filter from the image, and I applied the Gaussian filter to this new image again, using in this case a lower sigma value, typically equal to 3. Also at this point, it was the possibility to change the sigma value in case of non-solved image, proceeding by trial and error.
4. The use of a **threshold** in the plot to make the star candidates more obvious, with the possibility to change the limits in case of non-solved image, proceeding by trial and error.

As example, in Figure 5.9 are shown the effects of major filtering techniques applied to a PMC-contaminated image.

⁵Associate Professor at Department of Physics and Astronomy, University of Pennsylvania, Philadelphia, PA, USA.

The original image shows a very high number of counts in all pixels, from a minimum of $\sim 11,000$ up to $\sim 14,000$. As first step, I applied a three order polynomials removal, which left an image with zero mean, as this type of filtering accomplishes much of what a “window” would do. Basically, this first phase lets to eliminate big large-scale features out of the image. Then, as second step, I low-pass filtered with a Gaussian filter using $\sigma = 5$, subtract that from the image, and then I Gaussian filtered again using $\sigma = 2$. Finally, I changed limits in the plot to make the star candidates more obvious.

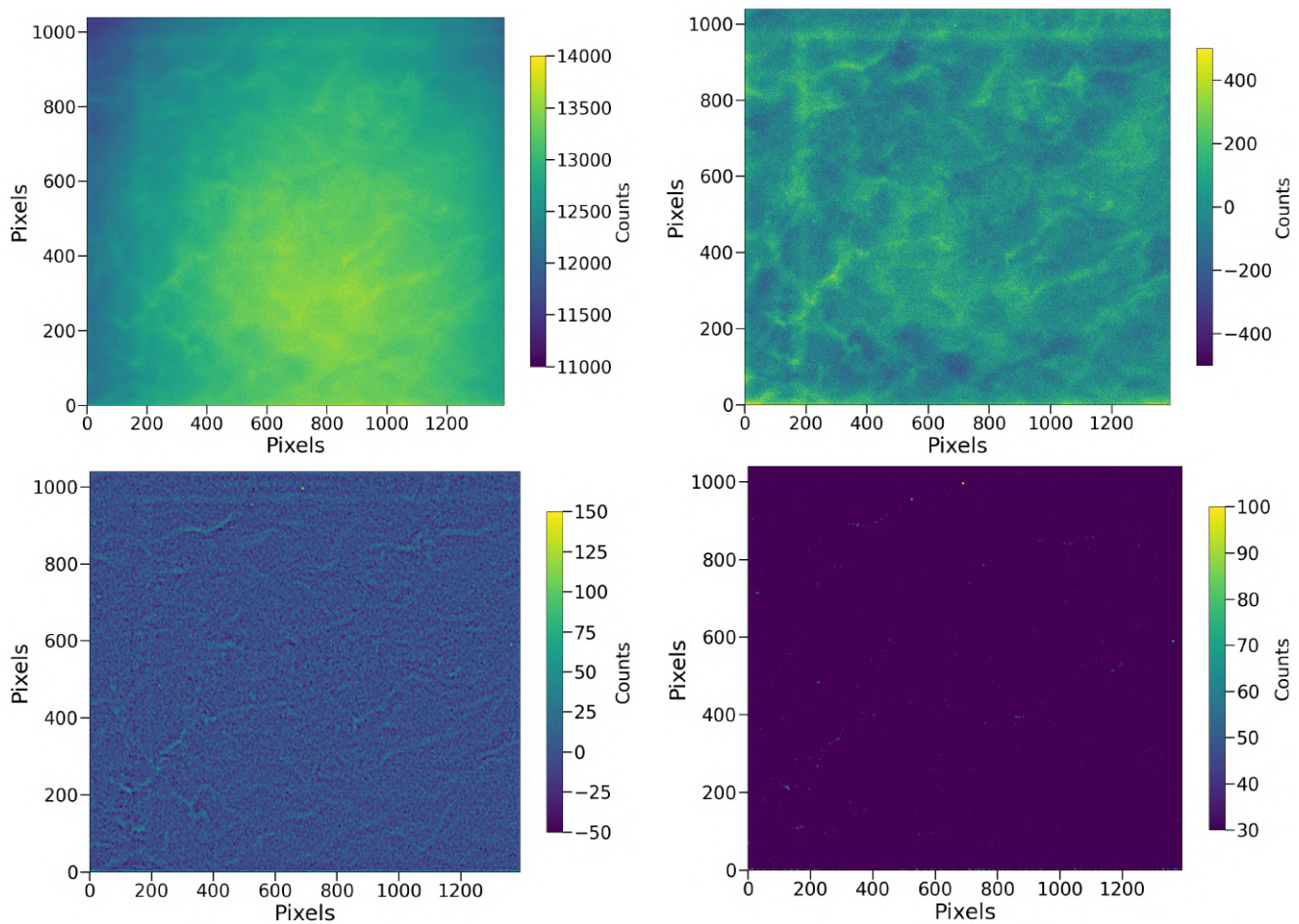


Figure 5.9: *The consecutive application of main filtering techniques to an image contaminated by the presence of a Polar Molecular Cloud, on the top left. The effect of flatten the image by removing low order polynomials of degree equal to 3 (phase 1) is shown on the top right; then, the effect of Gaussian low-pass filtering at the bottom left (phase 3); finally, at the bottom right, the use of a different limits in the plot to make the star candidates more obvious (phase 4), of which the two most evident are visible in the upper center of the image.*

Dependence of solutions on filtering techniques

During the star camera images post-flight analysis I carried out, and in particular during the cleaning phase of the Polar Mesospheric Clouds (PMCs) from the contaminated images using the filtering techniques just described, I carried out a preliminary study. The aim was to understand how much the choice of these techniques which very often they were fine-tuned and refined image by image, affected the accuracy of the astrometric solution resulting from the `astrometry.net` service.

To perform this kind of control, I filtered a number of images several times, with some variations of the filtering techniques, such as different flat field reductions, and also different sigma choices for the Gaussian filters, setting values even much lower than those normally used to clean the images, for a total of ten different methods given by the combinations of the chosen variations. I also decided to deliberately use an improper flat field, related to the other star camera instead of to the star camera with which the image was obtained, to see the effect on the final accuracy.

I then analyzed the standard deviations of the values distributions obtained for the astrometric solutions of each image, i.e. the coordinates of the field center, the image Field of View (FoV), and the image rotation angle, finally obtaining an agreement of reference values.

In general, this preliminary study demonstrated that the coordinates of the image center that the software returns are stable with respect to the choice of filtering techniques used to clean up the PMC-contaminated images, and in particular I obtained variations to the order of the third decimal digit (thousandth of a degree), therefore a standard deviation value for both Right Ascension (RA) and Declination (Dec) lower than 0.001° : $\sigma(RA) < 0.001^\circ$ and $\sigma(Dec) < 0.001^\circ$.

The same stability was also shown by the FoV, since I obtained the same order of variation also for this image property, of the order of the third decimal place (thousandth of a degree) for each side: $\sigma(FoV) < 0.001^\circ$.

On the contrary, the field rotation angle proved to be the least stable and the most dependent on the choices of filtering techniques, with a variation of the order of the first decimal place (tenth of a degree): in fact, I got a greater value for the standard deviation equal to $\sigma(\theta) \sim 0.1^\circ$.

Since this higher standard deviation in the rotation angle was also dependent on the use of incompletely correct filtering techniques that I had deliberately chosen to test, such as an improper flat field, and the use of a too low sigma in the Gaussian filter ($\sigma = 1$), eliminating the results due to these incorrect methods the standard deviation of the rotation angle has been reduced by an order of magnitude, resulting in a better accuracy: $\sigma(\theta) < 0.01^\circ$.

Finally, as last consideration, by testing various filtering techniques on the same image, the indication of the correct value of the rotation angle always resulted from the statistical mode rather than from the mean or median value.

5.4.3 Estimation of stars number in anti-sun images

As a final piece of the post-flight analysis that I have carried out, I tried to understand how many stars the cameras could see per image, even without the severe scattered light from the sun. Answering this type of question is in fact of fundamental importance for the next generation of star cameras which has to be developed.

In order to obtain an estimate of the number of stars that can likely be get per exposure, it was necessary to figure out the background scattered light level that is seen at float.

I pointed out to a handful of images that were mostly anti-Sun, for which I was able to get solutions, and with identifiable stars to get the background levels. In detail, I selected 32 images for each star camera, some of which were original without the application of any filtering technique, 7 for the XSC0 star camera and 15 for the XSC1 star camera, and some which I cleaned from PMCs through filtering techniques, 25 for the XSC0 star camera and 17 for the XSC1 star camera.

The selected images were relative to the same instant of time up to order of seconds, from 06:26:41 NZT up to 06:54:53 NZT on January 7, 2020.

To select images in anti-Sun position, I taken the position of the sun in terms of horizontal coordinates at the same instant of time of images (AltSun and AzSun, directly from dirfiles). Then, I calculated the horizontal coordinates of the star camera images from the equatorial coordinates obtained from the `astrometry.net` service, using as position the values provided directly by the dirfiles. Finally, I chose the images that were near the anti-sun azimuth ($Az_{sun} \pm 180^\circ$) for less than 10° : from 3.3° up to 8.7° for the XSC0 star camera, thus taking images with an azimuth variable from 301.733° to 312.170° ; and from 4.8° up to 10.2° for the XSC1 star camera, thus taking images with an azimuth variable from 303.240° to 313.631° .

Finally, the background was computed as numbers of photons per second on pixel (background=photons/second/pixel). In general, these solved images showed a low number of stars, variable between 6 and 16 for the XSC0 star camera, and between 6 and 24 for the XSC1 star camera.

5.4.4 Results

The star camera images were subjected to the post-flight analysis, and I ran them with the `astrometry.net` service in two phases:

1. during the first phase all “original” images were runned by the software, trying to solve them whether or not there are Polar Mesospheric Clouds (PMCs);
2. during the second phase, all PMCs contaminated images have been subjected to advanced filtering techniques which, in many cases, made it possible to subtract PMCs, obtaining just the sky background with stars and some residuals. The “cleaned” images were then run with the `astrometry.net` service.

Through phase one, I obtained a number of post-flight solutions equal to 96 for the XSC0 star camera, i.e. only about 4% of the XSC0 images, and a number of 237 for the XSC1 star camera, i.e. only about 9% of the XSC1 images. Therefore, through this phase, I obtained only 333 total solutions, equal to about 6.5% of the total star camera images analyzed post-flight, as summarized in Table 5.4.

| Star Camera | Number of Images Solved (1° Phase) | % |
|-------------|------------------------------------|------|
| XSC0 | 96 | 4% |
| XSC1 | 237 | 9% |
| Total | 333 | 6.5% |

Table 5.4: *Number of not filtered post-flight star cameras images solved with the `astrometry.net` service, considering the XSC0 star camera (first line), the XSC1 star camera (second line) and both together (third line). The percentages refer to the XSC0 images (2,493), to the XSC1 images (2,668), and to the total number of stellar images analyzed (5,161), respectively.*

Phase two was intended to recover other post-flight pointing solutions and obtain them for as many images as possible. To do this, I used advanced filtering techniques, described in Subsection 5.4.2. The filtering techniques applied to all PMCs contaminated images allowed to significantly increase the number of successfully recovered pointing solutions: I obtained 795 post-flight solutions for the XSC0 star camera and 855 for the XSC1 star camera, i.e. about 33% and 35% of the PMCs contaminated images, respectively. Therefore, through this second phase, another 1,650 total solutions were obtained, i.e. about 34% of the filtered star camera images analyzed post-flight, as summarized in Table 5.5.

| Star Camera | Number of Images Solved (2° Phase) | % |
|-------------|------------------------------------|-----|
| XSC0 | 795 | 33% |
| XSC1 | 855 | 35% |
| Total | 1,650 | 34% |

Table 5.5: *Number of filtered post-flight star cameras images solved with the `astrometry.net` service, considering the XSC0 star camera (first line), the XSC1 star camera (second line) and both together (third line). The percentages refer to the XSC0 PMCs contaminated images (2,397), to the XSC1 PMCs contaminated images (2,431), and to the total number of PMCs contaminated stellar images (4,828), respectively.*

Considering both solutions obtained from the “original” and filtered images (first and second phase), I have therefore obtained: 891 post-flight solutions for the XSC0 star camera and 1,092 solutions for the XSC1 star camera, i.e. about 36% and 41% of their images, respectively. Therefore, I obtained a total of 1,983 solutions, equal to about 38% of the total star camera images analyzed post-flight, as summarized in Table 5.6.

| Star Camera | Number of Images Solved ($1^\circ+2^\circ$ Phase) | % |
|-------------|--|-----|
| XSC0 | 891 | 36% |
| XSC1 | 1,092 | 41% |
| Total | 1,983 | 38% |

Table 5.6: Number of post-flight star camera images solved with the *astrometry.net* service: considering the XSC0 star camera (first line), the XSC1 star camera (second line) and both together (third line). The percentages refer to the XSC0 images (2,493), to the XSC1 images (2,668), and to the total number of stellar images analyzed (5,161), respectively.

The post-flight solutions I found are not uniformly distributed over the flight duration, and considering the timeline as a reference, there are more than 100 solutions found for the XSC0 star camera and not for the XSC1 one, and on the contrary more than 300 solutions found for the XSC1 star camera and not for the other one, as can be seen approximately in the scheme in Figure 5.10.

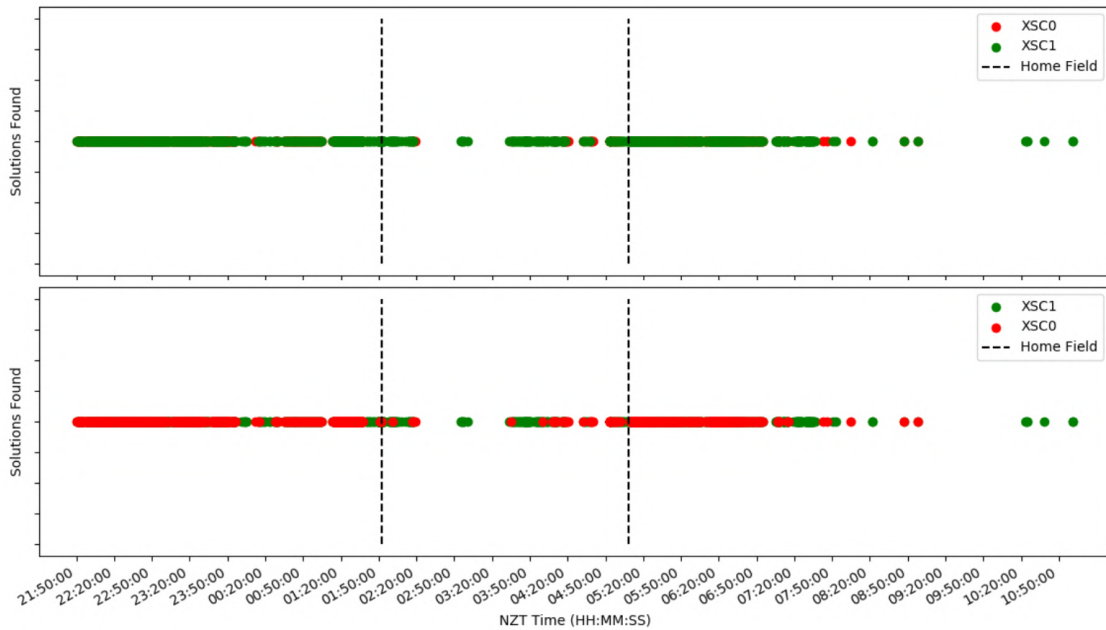


Figure 5.10: Timeline (NZT) showing the BLAST-TNG post-flight solutions I found for the star camera images, during the 2019-2020 campaign flight, January 6 and 7, 2020, both without and with filtering techniques applied. The solutions found for the XSC0 star camera are shown in red (featured in the second line), while those relating to the XSC1 star camera are shown in green (featured in the first line). The time span in which the telescope observed the Home field, a reference field for the observational strategy, is highlighted by black dashed lines: here a small number of solutions were found, equal to 38 for the XSC0 star camera and to 143 for the XSC1 star camera (out of 700 total images).

The final comparison between the number of star camera solutions solved in- and post-flight, thanks also to the use of filtering techniques, shows how much this posterior work I did was of fundamental importance in the reconstruction of a high-accuracy pointing solution for the entire length of the flight, as shown in Table 5.7.

| Type of Solution | Number of Images Solved |
|------------------------------|-------------------------|
| In-flight | 593 |
| Post-flight (no filtering) | 333 |
| Post-flight (with filtering) | 1,650 |

Table 5.7: *Number of in- and post-flight star cameras images solved (without and with filtering techniques applied), using STARS for the in flight analysis, and astrometry.net for the post flight analysis, respectively.*

Being the star cameras the only sensor that can provide a post-flight pointing solution with the required accuracy to make maps from raw data that over-sample the angular resolution of the telescope, my work was crucial to making possible any sort of maps from BLAST-TNG data.

Moreover, the star cameras pointing solutions I found are of fundamental importance for characterizing the performance of the instrument, by testing the accuracy of the pointing system, and they are also mentioned in Coppi et al. (2020).

One of the most important results of the January 2020 Antarctic flight of BLAST-TNG, obtained thanks to this search for star camera solutions I did, was the observation of the Galactic HII region RCW 92B. These data were used by the BLAST collaboration as valuable test data to characterize the performance of detectors and optics. In Figure 5.11 is shown the plot of the cut across this double-peaked HII region.

5.5 Conclusions

The BLAST program has already shown the importance of the study of the sub-millimeter sky from a balloon platform with great scientific results (Fissel et al., 2016; Soler et al., 2017; Fissel et al., 2019). Unfortunately, the 15 hours flight from McMurdo (Antarctica) in January 2020 of the BLAST-TNG experiment, corresponding to the last campaign, was not be able to provide the expected scientific outcome. However, it provided invaluable information from a technology point of view.

First of all, it was demonstrated that every subsystem worked as expected, including the high-accuracy pointing sensors, i.e. the star cameras, which achieved the required accuracy and a good pointing stability of the system, less than $10''$.

When BLAST had problems during flight, e.g. due to the presence of Polar Mesospheric Clouds (PMCs) which contaminated the star cameras images making harder to obtain accurate in-flight pointing solutions and leading to the inability to solve most images, the BLAST collaboration was able to fix these issues after the flight.

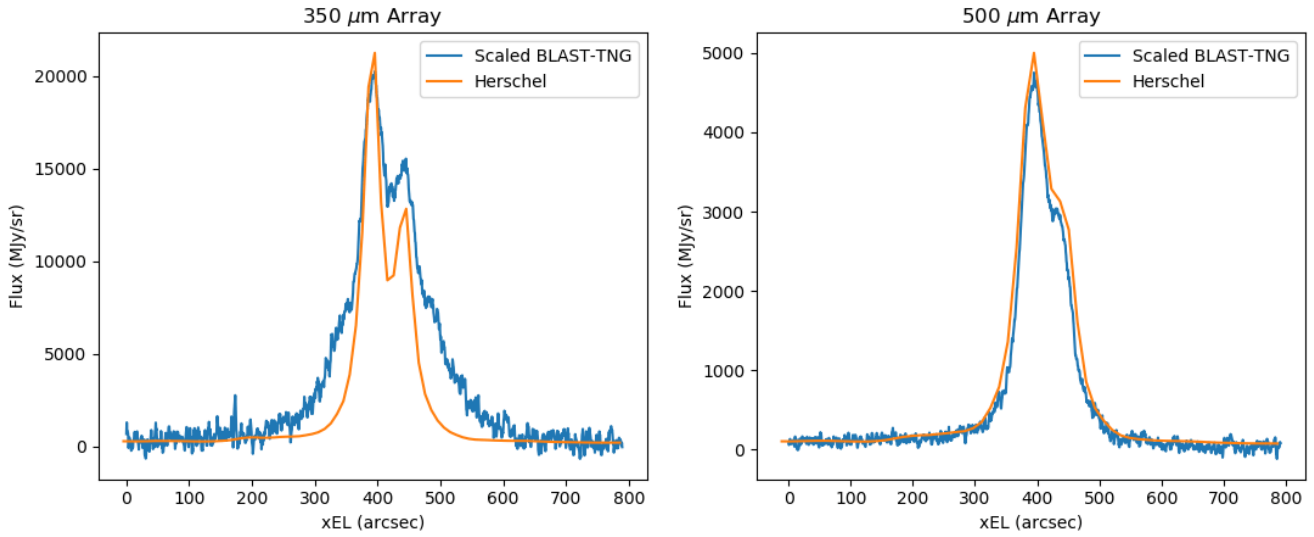


Figure 5.11: *The plot of the cut across the double-peaked Galactic HII, RCW 92B. On the left panel there are initial results at 350 μm , while on the right panel at 500 μm . In each case, in blue is shown the signal collected by just one MKID during a single sweep. In orange, is shown the corresponding profile of the target from maps made by ESA’s SPIRE/Herschel instrument. The BLAST-TNG sweeps shown here each correspond to two seconds of data. Source: <https://sites.northwestern.edu/blast/2020/11/19/blast-tng-initial-results-for-hii-region-rcw-92b/>.*

During my PhD I analyzed attitude data related to the star cameras pointing system from the ~ 15 hours 2020 science flight of the BLAST-TNG experiment. I carried out a post-flight analysis of 5,161 star camera images, searching for astrometric calibration, that is the pointing, scale, and orientation, with the aim of significantly increase the number of successfully recovered solved images.

Being the most part of images contaminated by the presence of Polar Mesospheric Clouds (PMCs), which lead to the inability to solve most images, I implemented a custom algorithm based on advanced filtering techniques to clean all the PMCs-contaminated images. I was able to obtain a total of 1,983 new post-flight star camera solutions, $\sim 38\%$ of the total star camera images analyzed post-flight, recovering 1,650 solutions compared to only 333 found without the use of filtering techniques, and so increasing the number of original post-flight star camera solutions by a factor larger than 4.

This results I found is mentioned in Coppi et al. (2020).

Moreover, I also carried out a preliminary study to understand how much the choice of the filtering techniques, which very often was fine-tuned and refined image by image, affected the accuracy of the astrometric solution resulting from the `astrometry.net` service, which I used to obtain the pointing solution.

In general, this preliminary study demonstrated that the coordinates of the image center that the software returns and of the image Field of View (FoV) are stable with respect

to the choice of filtering techniques, since I obtained a standard deviation value for both Right Ascension (RA), Declination (Dec) and FoV lower than 0.001° : $\sigma(RA) < 0.001^\circ$, $\sigma(Dec) < 0.001^\circ$ and $\sigma(FoV) < 0.001^\circ$.

On the contrary, the field rotation angle proved to be the least stable and the most dependent on the choices of filtering techniques, and I got a greater value for the standard deviation equal to $\sigma(\theta) < 0.01^\circ$.

Finally, as last piece of the post-flight analysis I carried out, with the BLAST team I tried to understand how many stars the star cameras could see per image, even without the severe scattered light from the sun, in the context of the next generation of star cameras which has to be developed.

To do this, I selected 32 star cameras images for each star camera in anti-Sun position, for which I was able to find a solution, obtaining both the background scattered light level that is seen at float, and an estimate of the number of stars that can be get per exposure, which proved to vary from a minimum of 6 to a maximum of 24.

To conclude, the importance of this work lies in the fact that it is crucial both for testing the accuracy of the pointing system and understanding the performance of the instrument. Moreover, this work is fundamental for reconstructing the post-flight pointing solution with the required accuracy to make maps from BLAST-TNG raw data that over-sample the angular resolution of the telescope.

Chapter 6

Conclusions

My PhD project developed around the subject of Galactic polarized foregrounds, synchrotron and dust thermal emissions, which dominate the sky at complementary frequencies. My intent was to characterize them at several levels, also focusing on their role of contaminants for CMB B -modes measurements. In order to obtain pure CMB measurements, it is necessary a deep understanding of their distinct emission mechanisms.

I focused on the polarized foregrounds modeling, and I contributed to the research topic by forecasting new constraints on spectral models parameters for current and upcoming polarized microwave experiments, among which the Simons Observatory (SO), which is poised to address many questions in Galactic astrophysics in addition to its principal cosmological goals.

As the leader¹ of the power spectrum analysis of multi-frequency Galactic emission, I co-authored the SO Galactic Science paper (Hensley et al., 2022), and all the codes I developed for this purpose can be found in the SO github repository available to the collaboration members.

I quantified the effect of the addition of SO data to existing measurements in test models of polarized Galactic emission. I found new improved constraints on all spectral parameters, demonstrating that SO will allow to elaborate models beyond what has sufficed for the lower sensitivity observations of WMAP and *Planck*. I focused primarily on B -modes, both for the importance of accurate foreground modeling for B -mode science, as well as the fact that a BB analysis is less sensitive to treatment of the CMB component itself, and my framework aims to measure astrophysical parameters only.

The main results I found are summarized here:

1. Regarding the energetic of synchrotron emission, at low frequencies (up to 39 GHz), and in the multipole range $70 < \ell < 300$, the additional sensitivity of upcoming data from both the lowest-frequency SO bands and C-BASS will constrain the presence of curvature in the Galactic synchrotron SED, improving by a factor of

¹A supplement describing author contributions to this paper can be found at https://simonsobservatory.org/wp-content/uploads/2022/02/SO_GS_Contributions.pdf

two level compared to constraints that employ S-PASS, WMAP, and *Planck* data alone.

Furthermore, I demonstrated that the sensitivity of the SO data at comparatively high radio frequencies can break the degeneracy between the synchrotron amplitude A_s and the spectral index β_s , sharpening constraints on the level of synchrotron emission (see Subsection 2.7.1).

2. Regarding the composition of interstellar dust, at higher frequencies (up to 353 GHz), and in the multipole range $70 < \ell < 600$, the polarization sensitivity of SO will reveal the nature of interstellar dust, enabling detailed tests of one- versus two-component models by constraining the frequency spectrum of polarized dust emission, and in particular the value of the dust spectral index in polarization β_d , with an improvement of a factor of two level relative to current constraints. Achieving the forecasted sensitivity of $\sigma(\beta_d) < 0.01$ will definitively establish whether the two current, distinct, best determinations of $\beta_d = 1.48$ (measured in total intensity with much smaller uncertainty) and $\beta_d = 1.53 \pm 0.02$ (measured in polarization) published in (Planck Collaboration et al., 2020b), actually correspond to two distinct grain populations, thus testing one-component dust models, which predict nearly identical β_d for both (see Subsection 2.7.2).
3. Finally, regarding the nature of the observed spatial correlation between dust and synchrotron emission, SO’s multi-frequency view of Galactic magnetic fields probing both dust and synchrotron emission will help unravel the field structure in different ISM phases and in different regions of the Galaxy to understand how they correlate with each other as well as the distinct properties of each. I have shown that SO, in combination with other microwave and radio polarimetry up to 353 GHz, and in the multipole range $70 < \ell < 600$, will measure the correlation coefficient between polarized dust and synchrotron emission with double the precision available compared to current data (see Subsection 2.7.3).

More broadly, my quantitative forecasts on astrophysical parameters will serve as a roadmap for Galactic science with other microwave polarization experiments, to expand their scientific scope via Milky Way astrophysics, as the analysis of the CMB is moving towards “Stage 4”. In fact, the next generation of CMB survey data, in addition to probing cosmology, will provide rich information on the physics of Galactic processes and sources of emission, and will join SO in pushing the boundaries of Galactic polarization science. For example, the science case I detailed in Chapter 2 is directly applicable to the future ground-based experiment CMB-S4 (Abazajian et al., 2019), or it can be extended to all-sky data with proposed satellite experiments like LiteBIRD (Montier et al., 2020) and PICO (Hanany et al., 2019).

I propose a final summary of some possible future extensions of this work:

1. Combining the framework presented here with that detailed in Simons Observatory Collaboration (2019), to measure jointly both cosmological and astrophysical parameters.

2. Applying a more sophisticated approach of the present study, considering a more detailed study of spatial variability property of frequency spectral indices. There are in fact two possibilities: by separately analyzing different sub-regions of the sky, or by map-level modeling of the SEDs.
3. A potential Galactic science objective using SO data is to search for frequency decorrelation in dust and synchrotron emission, including it in both simulated maps and parametric fits.

I then focused on the polarized foregrounds characterization, and I contributed to the research topic by presenting an updated quantitative validation of the correlation between starlight polarization and polarized dust emission in the diffuse ISM at high-Galactic latitude, being a powerful probe to disentangle several effects measurable at both frequency ranges, since both dust emission and extinction are affected by the grain shape, the grain alignment efficiency and the magnetic field orientation.

I performed a novel analysis to extend existing results of [Planck Collaboration et al. \(2020a\)](#) based on the PR3 *Planck* 353 GHz emission channel, using the last data release (PR4, [Planck Collaboration Int. LVII, 2020](#)) and going to smaller frequencies down to 143 GHz. The only value published in literature refers to the 353 GHz. Even if the SNR is lower for dust polarized emission at smaller frequencies, I wanted to explore the robustness of the theoretical predictions on the comparison between polarized emission and starlight polarization data even at lower frequencies, where dust is still dominant. I concentrated the analysis on high-Galactic latitudes and diffuse ISM lines of sights since more homogeneous properties might be expected, and for which the most comprehensive observational constraints on dust models are already available and exploited.

I obtained new original experimental estimates of the emission-to-extinction polarization ratio, a diagnostic involving dust emission and extinction for the aligned grains population, consistent with those predicted by dust models.

Using existing stellar catalogues of Berdyugin series ([Berdyugin et al., 2001](#); [Berdyugin & Teerikorpi, 2001](#); [Berdyugin, A. & Teerikorpi, P., 2002](#); [Berdyugin et al., 2004](#); [Berdyugin, A. et al., 2014](#)), [Green et al. \(2018\)](#) reddening estimates, and Gaia DR2 distances ([Bailer-Jones et al., 2018](#)), I built a stellar sample of 1693 stars. To increase the SNR of the emission measurements on lines of sight to the target stars in the diffuse ISM, and as a compromise between achieving higher SNR and maintaining high-resolution, I implemented the photometric aperture method, which allowed me to explore the polarization ratio behavior using different radius choices centered on each star.

The original maps SNR depends on the region being studied; however, I adopted a common radius in all sky regions, and I explored the polarization ratio behavior using different radius choices, deriving each time the mean polarization ratio value and its uncertainty. In correspondence with minima of residuals with respect to the expected values, obtained in the function describing the trend of the polarization ratios with respect to the aperture radii, I found the optimal aperture radius at which compute the polarization ratios estimates equal to 14' for all three frequency channels considered.

I found new estimates of the emission-to-extinction polarization ratios through a joint correlation of the Stokes parameters pair in emission, (Q, U) , with the Stokes parameters pair in extinction, (q_V, u_V) , at the three frequency channels, 353, 217 and 143 GHz, being this approach both motivated and justified, since it has several advantages.

The new original estimates of the polarization emission-to-extinction ratios I found are:

- $R_{P/p} = [5.47 \pm 0.06]$ MJy/sr for the 353 GHz channel;
- $R_{P/p} = [1.15 \pm 0.02]$ MJy/sr for the 217 GHz channel;
- $R_{P/p} = [0.294 \pm 0.010]$ MJy/sr for the 143 GHz channel.

These new value I obtained can provide strong constraints for models of dust polarized emission, and further empirical validation of many of the common underlying assumptions of the models.

This work was designed in collaboration with the Atacama Cosmology Telescope (ACT) Galactic science working group, being a junior member of the ACT collaboration. The results I showed here represent the first results of a larger project: my intention is to take advantage of the increased resolution and sensitivity of new ACT data to inspect the robustness of the emission-to-extinction polarization ratio, observing dust behavior at smaller scales. I will publish all these results as first author in a paper in preparation titled “New starlight polarization analysis with ACT and *Planck* data”.

I also worked on the planning of the observational strategy for the infrared polarimeter BLAST-TNG (The Ballon-borne Large Aperture Submillimeter Telescope), launched from Antarctica in January 2020, and its successor, the NASA proposal BLAST Observatory (Lowe et al., 2020), which is expected to launch in 2028 from New Zealand.

I developed and implemented an algorithm to identify optimal diffuse ISM fields to be observed in order to characterize the polarized dust emission, and suitable for CMB foreground characterization: I look for square sky patches with features similar to the ones of diffuse, low-intensity and highly-polarized dust regions.

I took into account different possible launch dates and the instrument sensitivity and resolution, trying a range of patch sizes and required observational time to find the optimal combination. I developed a series of selection criteria, among which one based on a metric defined by three new parameters called “Quality Factors”, which are scalar values defined as the average values within a certain patch of three simulated quantities: the polarization fraction, the signal-to-noise ratio (SNR) of the polarization fraction, and the SNR of the polarization power contrast. I considered also HI column density maps from HI4PI survey (HI4PI Collaboration, 2016) to be able to consider a patch “diffuse” in the CNM, in the sense of having little to no molecular hydrogen ($N(HI) < 4 \times 10^{20} \text{ cm}^{-2}$). Finally, I found constraints on the polarized dust SED inside selected ISM targets.

The results I obtained in planning the observational strategy are the following:

- For the BLAST-TNG experiment, I identified one $5^\circ \times 5^\circ$ best diffuse dust patch, visible for 10 hours/day, which has been selected as target to be observed in the

flight plan of the BLAST-TNG 2019/2020 campaign.

Unfortunately, it was not possible to observe it due to the premature interruption of the mission, caused by an accidental damage (see Subsection 4.10.1).

- For the BLAST Observatory, I identified two $10^\circ \times 10^\circ$ best ISM fields to be observed, visible for 5-10 hours/day, suitable for two different performance scenarios (both the one based on current telescope design and the one based on the mission top level requirements to meet all science objectives): one which overlaps with the Simons Observatory SAT field, and one which also overlaps with the BICEP/Keck experiment.

Both have been used to make theoretical predictions by the Science team presented in the NASA proposal, including the demonstration that, thanks to the observation of one of these patches, it will be possible to distinguish one- versus two-component dust model (see Subsection 4.10.2).

In general, this analysis provides a systematic procedure that can also be applied to other datasets. All the codes I developed for this purpose can be found in the BLAST github repository.

Finally, I analyzed data from the ~ 15 hours 2020 science flight of the BLAST-TNG experiment. In particular, I worked on the telescope's attitude control system, by analyzing star camera images. Star camera provide the crucial information for reconstructing the post-flight pointing solution with the required accuracy to make sky maps from BLAST-TNG raw data that over-sample the angular resolution of the telescope.

I wrote a code to process 5,161 star camera images, searching for images astrometric calibration, like pointing, scale, and boresight rotation. This resulted into a very challenging task, as most of the images were contaminated by the presence of Polar Mesospheric Clouds (PMCs), typical of the polar altitude at which the balloon flew, leading to the inability to find solutions. I mitigated such problem by implementing a custom algorithm based on advanced filtering techniques to clean all the PMCs-contaminated images.

I was able to obtain a total of 1,983 new post-flight star camera solutions, $\sim 38\%$ of the total star camera images analyzed post-flight, recovering 1,650 solutions compared to only 333 found without the use of filtering techniques, and so managing to increase the number of original post-flight star camera solutions by a factor larger than 4.

My results were useful for testing the accuracy of the pointing system and understanding the performance of the instrument, and they were published in Coppi et al. (2020).

I also carried out a preliminary study to understand how much the choice of the filtering techniques, which very often was fine-tuned and refined image by image, affected the accuracy of the astrometric solution resulting from the `astrometry.net` service, which I used to obtain the pointing solution. In general, this preliminary study demonstrated that the coordinates of the image center and the image Field of View (FoV) that the software returns are stable with respect to the choice of filtering techniques, while the field rotation angle proved to be the least stable and the most dependent on these choices.

I also tried to understand how many stars the star cameras could see per image, even without the severe scattered light from the sun, in the context of the next generation of star cameras which has to be developed, and a very preliminary estimate of the number of stars that can be get per exposure, which proved to vary from a minimum of 6 to a maximum of 24.

As a final note, I am happy to report that the international working groups specialized in Galactic Science with which I collaborated over the past three years, recognize the presented results as a robust brick on the knowledge of the research topic of Galactic polarized foregrounds.

Bibliography

- Abazajian, K., Addison, G., Adshead, P., et al. 2019, CMB-S4 Science Case, Reference Design, and Project Plan, arXiv, doi: [10.48550/ARXIV.1907.04473](https://doi.org/10.48550/ARXIV.1907.04473)
- Abazajian, K., Addison, G. E., Adshead, P., et al. 2022, *The Astrophysical Journal*, 926, 54, doi: [10.3847/1538-4357/ac1596](https://doi.org/10.3847/1538-4357/ac1596)
- Abazajian, K. N., Adshead, P., Ahmed, Z., et al. 2016, CMB-S4 Science Book, First Edition, arXiv, doi: [10.48550/ARXIV.1610.02743](https://doi.org/10.48550/ARXIV.1610.02743)
- Adachi, S., Faúndez, M. A. O. A., Arnold, K., et al. 2020, *The Astrophysical Journal*, 904, 65, doi: [10.3847/1538-4357/abbacd](https://doi.org/10.3847/1538-4357/abbacd)
- Adamson, A. J., Whittet, D. C. B., Chrysostomou, A., et al. 1999, *ApJ*, 512, 224, doi: [10.1086/306766](https://doi.org/10.1086/306766)
- Ade, P., Aghanim, N., Ahmed, Z., et al. 2015, *Physical Review Letters*, 114, doi: [10.1103/physrevlett.114.101301](https://doi.org/10.1103/physrevlett.114.101301)
- Ade, P. A. R., Savini, G., Sudiwala, R., et al. 2010, *A & A*, 520, A11, doi: [10.1051/0004-6361/200913039](https://doi.org/10.1051/0004-6361/200913039)
- Ade, P. A. R., Aikin, R. W., Amiri, M., et al. 2014a, *The Astrophysical Journal*, 792, 62, doi: [10.1088/0004-637X/792/1/62](https://doi.org/10.1088/0004-637X/792/1/62)
- Ade, P. A. R., Ahmed, Z., Aikin, R. W., et al. 2016, *Phys. Rev. Lett.*, 116, 031302, doi: [10.1103/PhysRevLett.116.031302](https://doi.org/10.1103/PhysRevLett.116.031302)
- Ade, T. P. C. P. A. R., Akiba, Y., Anthony, A. E., et al. 2014b, *The Astrophysical Journal*, 794, 171, doi: [10.1088/0004-637X/794/2/171](https://doi.org/10.1088/0004-637X/794/2/171)
- Aiola, S., Calabrese, E., Maurin, L., et al. 2020, *Journal of Cosmology and Astroparticle Physics*, 2020, 047, doi: [10.1088/1475-7516/2020/12/047](https://doi.org/10.1088/1475-7516/2020/12/047)
- Ali, A. M., Adachi, S., Arnold, K., et al. 2020, *Journal of Low Temperature Physics*, 200, 461, doi: [10.1007/s10909-020-02430-5](https://doi.org/10.1007/s10909-020-02430-5)
- Alonso, D., Sanchez, J., Slosar, A., & LSST Dark Energy Science Collaboration. 2019, *MNRAS*, 484, 4127, doi: [10.1093/mnras/stz093](https://doi.org/10.1093/mnras/stz093)

- Alves, M. I. R., Boulanger, F., Ferrière, K., & Montier, L. 2018, *A & A*, 611, L5, doi: [10.1051/0004-6361/20183263710.48550/arXiv.1803.05251](https://doi.org/10.1051/0004-6361/20183263710.48550/arXiv.1803.05251)
- Andersson, B. G., Lazarian, A., & Vaillancourt, J. E. 2015, *ARAA*, 53, 501, doi: [10.1146/annurev-astro-082214-122414](https://doi.org/10.1146/annurev-astro-082214-122414)
- Appenzeller, I. 1968, *ApJ*, 151, 907, doi: [10.1086/149492](https://doi.org/10.1086/149492)
- Asano, R., Takeuchi, T., Hirashita, H., & Inoue, A. 2012, *Earth, Planets, and Space*, 65, doi: [10.5047/eps.2012.04.014](https://doi.org/10.5047/eps.2012.04.014)
- Ashton, P. C., Ade, P. A. R., Angilè, F. E., et al. 2018, *ApJ*, 857, 10, doi: [10.3847/1538-4357/aab3ca](https://doi.org/10.3847/1538-4357/aab3ca)
- Astropy Collaboration, Price-Whelan, A. M., Lim, P. L., et al. 2022, *ApJ*, 935, 167, doi: [10.3847/1538-4357/ac7c74](https://doi.org/10.3847/1538-4357/ac7c74)
- Bailer-Jones, C. A. L., Rybizki, J., Foesneau, M., Mantelet, G., & Andrae, R. 2018, *ApJ*, 156, 58, doi: [10.3847/1538-3881/aacb21](https://doi.org/10.3847/1538-3881/aacb21)
- Bailer-Jones C.A.L., Rybizki J., F. M. M. G. A. R. 2018, Distances to 1.33 billion stars in Gaia DR2, Version 05-Mar-2020 (last modified), Centre de Donnees astronomique de Strasbourg (CDS)
- Balkenhol, L., Dutcher, D., Ade, P. A. R., et al. 2021, *Phys. Rev. D*, 104, 083509, doi: [10.1103/PhysRevD.104.083509](https://doi.org/10.1103/PhysRevD.104.083509)
- Barron, D., Chinone, Y., Kusaka, A., et al. 2018, *Journal of Cosmology and Astroparticle Physics*, 2018, 009, doi: [10.1088/1475-7516/2018/02/009](https://doi.org/10.1088/1475-7516/2018/02/009)
- Baumann, D., Jackson, M. G., Adshead, P., et al. 2009, in *American Institute of Physics Conference Series*, Vol. 1141, *CMB Polarization Workshop: Theory and Foregrounds: CMBPol Mission Concept Study*, ed. S. Dodelson, D. Baumann, A. Cooray, J. Dunkley, A. Fraisse, M. G. Jackson, A. Kogut, L. Krauss, M. Zaldarriaga, & K. Smith, 10–120, doi: [10.1063/1.3160885](https://doi.org/10.1063/1.3160885)
- Bennett, C. L., Larson, D., Weiland, J. L., et al. 2013, *The Astrophysical Journal Supplement Series*, 208, 20, doi: [10.1088/0067-0049/208/2/20](https://doi.org/10.1088/0067-0049/208/2/20)
- Benoît, A., Ade, P., Amblard, A., et al. 2004, *A & A*, 424, 571, doi: [10.1051/0004-6361:20040042](https://doi.org/10.1051/0004-6361:20040042)
- Berdyugin, A., Piirola, V., & Teerikorpi, P. 2004, *A&A*, 424, 873, doi: [10.1051/0004-6361:20040308](https://doi.org/10.1051/0004-6361:20040308)
- Berdyugin, A., & Teerikorpi, P. 2001, *A & A*, 368, 635, doi: [10.1051/0004-6361:20010202-1](https://doi.org/10.1051/0004-6361:20010202-1)

- Berdyugin, A., Teerikorpi, P., Haikala, L., et al. 2001, *A & A*, 372, 276, doi: [10.1051/0004-6361:20010328](https://doi.org/10.1051/0004-6361:20010328)
- Berdyugin, A., Piirola, V., & Teerikorpi, P. 2014, *A&A*, 561, A24, doi: [10.1051/0004-6361/201322604](https://doi.org/10.1051/0004-6361/201322604)
- Berdyugin, A., & Teerikorpi, P. 2002, *A&A*, 384, 1050, doi: [10.1051/0004-6361:20020069](https://doi.org/10.1051/0004-6361:20020069)
- Berdyugin A., T. P. 2002, Interstellar polarization. VI., Version 10-Jan-2018 (last modified), Centre de Donnees astronomique de Strasbourg (CDS), doi: <https://doi.org/10.26093/cds/vizier.33841050>
- Berdyugin A., Piirola V., T. P. 2013, Polarization at high galactic latitude, Version 12-Oct-2017 (last modified), Centre de Donnees astronomique de Strasbourg (CDS), doi: <https://doi.org/10.26093/cds/vizier.35610024>
- Berdyugin A.V., Teerikorpi P., H. L. H. M. K. J. M. T. 2001, Polarization catalogue for NGP area, Version 08-Feb-2013 (last modified), Centre de Donnees astronomique de Strasbourg (CDS), doi: <https://doi.org/10.26093/cds/vizier.33720276>
- Bernard, J. P., Ade, P., André, Y., et al. 2016, *Experimental Astronomy*, 42, 199, doi: [10.1007/s10686-016-9506-1](https://doi.org/10.1007/s10686-016-9506-1)
- Bernstein, R. A., Freedman, W. L., & Madore, B. F. 2002, *ApJ*, 571, 107, doi: [10.1086/339424](https://doi.org/10.1086/339424)
- BICEP2 Collaboration, Keck Array Collaboration, Ade, P. A. R., et al. 2018, , 121, 221301, doi: [10.1103/PhysRevLett.121.221301](https://doi.org/10.1103/PhysRevLett.121.221301)
- BICEP/Keck Collaboration, SPTpol Collaboration, Ade, P. A. R., et al. 2021, *Physical Review Letters*, 103, 022004, doi: [10.1103/PhysRevD.103.022004](https://doi.org/10.1103/PhysRevD.103.022004)
- Bierman, E. M., Matsumura, T., Dowell, C. D., et al. 2011, *ApJ*, 741, 81, doi: [10.1088/0004-637X/741/2/81](https://doi.org/10.1088/0004-637X/741/2/81)
- Cabral, B., & Leedom, L. C. 1993, *Proceedings of the 20th annual conference on Computer graphics and interactive techniques*
- Caldwell, R. R., Hirata, C., & Kamionkowski, M. 2017, *The Astrophysical Journal*, 839, 91, doi: [10.3847/1538-4357/aa679c](https://doi.org/10.3847/1538-4357/aa679c)
- Carretti, E., Haverkorn, M., Staveley-Smith, L., et al. 2019, *Monthly Notices of the Royal Astronomical Society*, 489, 2330, doi: [10.1093/mnras/stz806](https://doi.org/10.1093/mnras/stz806)
- Cepeda-Arroita, R., Harper, S. E., Dickinson, C., et al. 2021, *Monthly Notices of the Royal Astronomical Society*, 503, 2927, doi: [10.1093/mnras/stab583](https://doi.org/10.1093/mnras/stab583)

- Chapman, D., Didier, J., Hanany, S., et al. 2014, in SPIE Proceedings, ed. G. Chiozzi & N. M. Radziwill (SPIE), doi: [10.1117/12.2057181](https://doi.org/10.1117/12.2057181)
- Chiar, J. E., Adamson, A. J., Whittet, D. C. B., et al. 2006, *ApJ*, 651, 268, doi: [10.1086/507462](https://doi.org/10.1086/507462)
- Choi, S. K., & Page, L. A. 2015, *Journal of Cosmology and Astroparticle Physics*, 2015, 020, doi: [10.1088/1475-7516/2015/12/020](https://doi.org/10.1088/1475-7516/2015/12/020)
- Choi, S. K., Austermann, J., Basu, K., et al. 2020, *Journal of Low Temperature Physics*, 199, 1089, doi: [10.1007/s10909-020-02428-z](https://doi.org/10.1007/s10909-020-02428-z)
- Clark, S. E., & Hensley, B. S. 2019, *The Astrophysical Journal*, 887, 136, doi: [10.3847/1538-4357/ab5803](https://doi.org/10.3847/1538-4357/ab5803)
- Clarke, T. J., Copeland, E. J., & Moss, A. 2020, *Journal of Cosmology and Astroparticle Physics*, 2020, 002, doi: [10.1088/1475-7516/2020/10/002](https://doi.org/10.1088/1475-7516/2020/10/002)
- Collaboration, Q., Bischoff, C., Brizius, A., et al. 2011, *The Astrophysical Journal*, 741, 111, doi: [10.1088/0004-637X/741/2/111](https://doi.org/10.1088/0004-637X/741/2/111)
- Collaboration, Q., Araujo, D., Bischoff, C., et al. 2012, *The Astrophysical Journal*, 760, 145, doi: [10.1088/0004-637X/760/2/145](https://doi.org/10.1088/0004-637X/760/2/145)
- Collaboration, T. P., Ade, P. A. R., Aguilar, M., et al. 2017, *The Astrophysical Journal*, 848, 121, doi: [10.3847/1538-4357/aa8e9f](https://doi.org/10.3847/1538-4357/aa8e9f)
- Compiègne, M., Verstraete, L., Jones, A., et al. 2011, *A & A*, 525, A103, doi: [10.1051/0004-6361/201015292](https://doi.org/10.1051/0004-6361/201015292)
- Coppi, G., Ade, P. A., Ashton, P. C., et al. 2020, in *Ground-based and Airborne Telescopes VIII*, ed. H. K. Marshall, J. Spyromilio, & T. Usuda (SPIE), doi: [10.1117/12.2560849](https://doi.org/10.1117/12.2560849)
- Crawford, T. M., Chown, R., Holder, G. P., et al. 2016, *The Astrophysical Journal Supplement Series*, 227, 23, doi: [10.3847/1538-4365/227/2/23](https://doi.org/10.3847/1538-4365/227/2/23)
- Crill, B. P., Ade, P. A. R., Battistelli, E. S., et al. 2008, in *Space Telescopes and Instrumentation 2008: Optical, Infrared, and Millimeter*, ed. J. M. O. Jr., M. W. M. de Graauw, & H. A. MacEwen, Vol. 7010, International Society for Optics and Photonics (SPIE), 70102P, doi: [10.1117/12.787446](https://doi.org/10.1117/12.787446)
- Davis, Leverett, J., & Greenstein, J. L. 1951, *ApJ*, 114, 206, doi: [10.1086/145464](https://doi.org/10.1086/145464)
- Davis, L., & Greenstein, J. L. 1949, *Phys. Rev.*, 75, 1605, doi: [10.1103/PhysRev.75.1605](https://doi.org/10.1103/PhysRev.75.1605)
- Dickinson, C., Eriksen, H. K., Banday, A. J., et al. 2009, *The Astrophysical Journal*, 705, 1607, doi: [10.1088/0004-637X/705/2/1607](https://doi.org/10.1088/0004-637X/705/2/1607)

- Dickinson, C., Ali-Haïmoud, Y., Barr, A., et al. 2018, , 80, 1, doi: [10.1016/j.newar.2018.02.00110.48550/arXiv.1802.08073](https://doi.org/10.1016/j.newar.2018.02.00110.48550/arXiv.1802.08073)
- Didier, J. 2017, Unpublished report wrote for the BLAST Collaboration.
- Dolginov, A. Z. 1990, in Galactic and Intergalactic Magnetic Fields, ed. R. Beck, P. P. Kronberg, & R. Wielebinski, Vol. 140, 242
- Draine, B. T. 2003, ARAA, 41, 241, doi: [10.1146/annurev.astro.41.011802.094840](https://doi.org/10.1146/annurev.astro.41.011802.094840)
- Draine, B. T., & Fraisse, A. A. 2009, ApJ, 696, 1, doi: [10.1088/0004-637X/696/1/1](https://doi.org/10.1088/0004-637X/696/1/1)
- Draine, B. T., & Hensley, B. S. 2021, ApJ, 909, 94, doi: [10.3847/1538-4357/abd6c6](https://doi.org/10.3847/1538-4357/abd6c6)
- Draine, B. T., & Hensley, B. S. 2021, The Astrophysical Journal, 919, 65, doi: [10.3847/1538-4357/ac0050](https://doi.org/10.3847/1538-4357/ac0050)
- Draine, B. T., & Lazarian, A. 1998, ApJL, 494, L19, doi: [10.1086/31116710.48550/arXiv.astro-ph/9710152](https://doi.org/10.1086/31116710.48550/arXiv.astro-ph/9710152)
- Draine, B. T., & Lee, H. M. 1984, ApJ, 285, 89, doi: [10.1086/162480](https://doi.org/10.1086/162480)
- Draine, B. T., & Li, A. 2007, ApJ, 657, 810, doi: [10.1086/511055](https://doi.org/10.1086/511055)
- Dunkley, J., Spergel, D. N., Komatsu, E., et al. 2009, The Astrophysical Journal, 701, 1804, doi: [10.1088/0004-637X/701/2/1804](https://doi.org/10.1088/0004-637X/701/2/1804)
- Dunkley, J., Calabrese, E., Sievers, J., et al. 2013, Journal of Cosmology and Astroparticle Physics, 2013, 025, doi: [10.1088/1475-7516/2013/07/025](https://doi.org/10.1088/1475-7516/2013/07/025)
- Dutcher, D., Balkenhol, L., Ade, P. A. R., et al. 2021, Phys. Rev. D, 104, 022003, doi: [10.1103/PhysRevD.104.022003](https://doi.org/10.1103/PhysRevD.104.022003)
- Dwek, E., Arendt, R. G., Fixsen, D. J., et al. 1997, The Astrophysical Journal, 475, 565, doi: [10.1086/303568](https://doi.org/10.1086/303568)
- Essinger-Hileman, T., Ade, P. A., Baildon, T., et al. 2020, in American Astronomical Society Meeting Abstracts, Vol. 236, American Astronomical Society Meeting Abstracts 36, 244.01
- Ferrière, K. 2009, A&A, 505, 1183, doi: [10.1051/0004-6361/200912617](https://doi.org/10.1051/0004-6361/200912617)
- Ferrière, K. 2015, Journal of Physics: Conference Series, 577, 012008, doi: [10.1088/1742-6596/577/1/012008](https://doi.org/10.1088/1742-6596/577/1/012008)
- Finkbeiner, D. P., Davis, M., & Schlegel, D. J. 1999, The Astrophysical Journal, 524, 867, doi: [10.1086/307852](https://doi.org/10.1086/307852)
- Fissel, L. M., & Lowe, I. 2017, Unpublished report wrote for the BLAST Collaboration.

- Fissel, L. M., Ade, P. A. R., Angilè, F. E., et al. 2016, *The Astrophysical Journal*, 824, 134, doi: [10.3847/0004-637X/824/2/134](https://doi.org/10.3847/0004-637X/824/2/134)
- Fissel, L. M., Ade, P. A. R., Angilè, F. E., et al. 2019, *The Astrophysical Journal*, 878, 110, doi: [10.3847/1538-4357/ab1eb0](https://doi.org/10.3847/1538-4357/ab1eb0)
- Fitzpatrick, E. L. 1999, *Publications of the Astronomical Society of the Pacific*, 111, 63, doi: [10.1086/316293](https://doi.org/10.1086/316293)
- Fixsen, D. J., Bennett, C. L., & Mather, J. C. 1999, *The Astrophysical Journal*, 526, 207, doi: [10.1086/307962](https://doi.org/10.1086/307962)
- Fonnesbeck, C., Patil, A., Huard, D., & Salvatier, J. 2015, *PyMC: Bayesian Stochastic Modelling in Python*. <http://ascl.net/1506.005>
- Fuskeland, U., Andersen, K. J., Aurlen, R., et al. 2021, *Astronomy & Astrophysics*, 646, A69, doi: [10.1051/0004-6361/202037629](https://doi.org/10.1051/0004-6361/202037629)
- Gaia Collaboration, Prusti, T., de Bruijne, J. H. J., et al. 2016, *A & A*, 595, A1, doi: [10.1051/0004-6361/201629272](https://doi.org/10.1051/0004-6361/201629272)
- Galitzki, N., Ade, P. A. R., Angilè, F. E., et al. 2014, in *Ground-based and Airborne Telescopes V*, ed. L. M. Stepp, R. Gilmozzi, & H. J. Hall, Vol. 9145, International Society for Optics and Photonics (SPIE), 91450R, doi: [10.1117/12.2054759](https://doi.org/10.1117/12.2054759)
- Gandilo, N. 2015, Phd dissertation, University of Toronto.
- Gavilan, L., Lemaire, J. L., & Vidali, G. 2012, *Monthly Notices of the Royal Astronomical Society*, 424, 2961, doi: [10.1111/j.1365-2966.2012.21463.x](https://doi.org/10.1111/j.1365-2966.2012.21463.x)
- Ghosh, T., Boulanger, F., Martin, P. G., et al. 2017, *Astronomy & Astrophysics*, 601, A71, doi: [10.1051/0004-6361/201629829](https://doi.org/10.1051/0004-6361/201629829)
- Gold, B., Odegard, N., Weiland, J. L., et al. 2011, *The Astrophysical Journal Supplement Series*, 192, 15, doi: [10.1088/0067-0049/192/2/15](https://doi.org/10.1088/0067-0049/192/2/15)
- Gorski, K. M., Hivon, E., Banday, A. J., et al. 2005, *The Astrophysical Journal*, 622, 759, doi: [10.1086/427976](https://doi.org/10.1086/427976)
- Green, G. M. 2018, *Journal of Open Source Software*, 3, 695, doi: [10.21105/joss.00695](https://doi.org/10.21105/joss.00695)
- Green, G. M., Schlafly, E. F., Finkbeiner, D., et al. 2018, *MNRAS*, 478, 651, doi: [10.1093/mnr/sty1008](https://doi.org/10.1093/mnr/sty1008)
- Guan, Y., Clark, S. E., Hensley, B. S., et al. 2021, *The Astrophysical Journal*, 920, 6, doi: [10.3847/1538-4357/ac133f](https://doi.org/10.3847/1538-4357/ac133f)
- Gudmundsson, J. E., Gallardo, P. A., Puddu, R., et al. 2021, *Appl. Opt.*, 60, 823, doi: [10.1364/AO.411533](https://doi.org/10.1364/AO.411533)

- Guillet, V., Fanciullo, L., Verstraete, L., et al. 2018, *A & A*, 610, A16, doi: [10.1051/0004-6361/201630271](https://doi.org/10.1051/0004-6361/201630271)
- Hall, J. S. 1949, *Science*, 109, 166, doi: [10.1126/science.109.2825.166](https://doi.org/10.1126/science.109.2825.166)
- Hanany, S., Alvarez, M., Artis, E., et al. 2019, PICO: Probe of Inflation and Cosmic Origins. <https://arxiv.org/abs/1902.10541>
- Hanany, S., Alvarez, M., Artis, E., et al. 2019, arXiv e-prints, arXiv:1902.10541. <https://arxiv.org/abs/1902.10541>
- Harman, R. R. 2005, Tech. rep., Flight Mechanics Symposium; Greenbelt, MD. [oai:casi.ntrs.nasa.gov:20060002447](https://ntrs.nasa.gov/casi.ntrs.nasa.gov/20060002447)
- Hazumi, M., Ade, P. A., Adler, A., et al. 2020, in *Space Telescopes and Instrumentation 2020: Optical, Infrared, and Millimeter Wave*, ed. M. Lystrup, N. Batalha, E. C. Tong, N. Siegler, & M. D. Perrin (SPIE), doi: [10.1117/12.2563050](https://doi.org/10.1117/12.2563050)
- Hensley, B. S., & Draine, B. T. 2020, *ApJ*, 895, 38, doi: [10.3847/1538-4357/ab8cc3](https://doi.org/10.3847/1538-4357/ab8cc3)
- Hensley, B. S., & Draine, B. T. 2021, *The Astrophysical Journal*, 906, 73, doi: [10.3847/1538-4357/abc8f1](https://doi.org/10.3847/1538-4357/abc8f1)
- Hensley, B. S., Clark, S. E., Fanfani, V., et al. 2022, *The Astrophysical Journal*, 929, 166, doi: [10.3847/1538-4357/ac5e36](https://doi.org/10.3847/1538-4357/ac5e36)
- HI4PI Collaboration. 2016, *Astronomy & Astrophysics*, 594, A116, doi: [10.1051/0004-6361/201629178](https://doi.org/10.1051/0004-6361/201629178)
- Hildebrand, R. H., Dotson, J. L., Dowell, C. D., Schleuning, D. A., & Vaillancourt, J. E. 1999, *ApJ*, 516, 834, doi: [10.1086/307142](https://doi.org/10.1086/307142)
- Hiltner, W. A. 1949, *Science*, 109, 165, doi: [10.1126/science.109.2825.165](https://doi.org/10.1126/science.109.2825.165)
- Hoang, T., & Lazarian, A. 2016, *ApJ*, 831, 159, doi: [10.3847/0004-637X/831/2/159](https://doi.org/10.3847/0004-637X/831/2/159)
- Hollenbach, D., & McKee, C. F. 1979, *ApJS*, 41, 555, doi: [10.1086/190631](https://doi.org/10.1086/190631)
- Hunter, J. D. 2007, *Computing in Science and Engineering*, 9, 90, doi: [10.1109/MCSE.2007.55](https://doi.org/10.1109/MCSE.2007.55)
- Jansson, R., & Farrar, G. R. 2012, *The Astrophysical Journal*, 757, 14, doi: [10.1088/0004-637X/757/1/14](https://doi.org/10.1088/0004-637X/757/1/14)
- Jones, A. P., Fanciullo, L., Köhler, M., et al. 2013, *A & A*, 558, A62, doi: [10.1051/0004-6361/201321686](https://doi.org/10.1051/0004-6361/201321686)
- Jones, A. P., Köhler, M., Ysard, N., Bocchio, M., & Verstraete, L. 2017, *A & A*, 602, A46, doi: [10.1051/0004-6361/201630225](https://doi.org/10.1051/0004-6361/201630225)

- Jones, M. E., Taylor, A. C., Aich, M., et al. 2018, MNRAS, 480, 3224, doi: [10.1093/mnras/sty1956](https://doi.org/10.1093/mnras/sty1956)
- Kalberla, P. M. W., & Haud, U. 2015, Astronomy & Astrophysics, 578, A78, doi: [10.1051/0004-6361/201525859](https://doi.org/10.1051/0004-6361/201525859)
- Kamionkowski, M., Kosowsky, A., & Stebbins, A. 1997, Physical Review Letters, 78, 2058, doi: [10.1103/physrevlett.78.2058](https://doi.org/10.1103/physrevlett.78.2058)
- Kamionkowski, M., & Kovetz, E. D. 2016, Annual Review of Astronomy and Astrophysics, 54, 227, doi: [10.1146/annurev-astro-081915-023433](https://doi.org/10.1146/annurev-astro-081915-023433)
- Kim, S.-H., & Martin, P. G. 1995, ApJ, 444, 293, doi: [10.1086/175604](https://doi.org/10.1086/175604)
- Kinney, W. H. 1998, Physical Review D, 58, doi: [10.1103/physrevd.58.123506](https://doi.org/10.1103/physrevd.58.123506)
- Knox, L. 1995, Phys. Rev. D, 52, 4307, doi: [10.1103/PhysRevD.52.4307](https://doi.org/10.1103/PhysRevD.52.4307)
- Kogut, A. 2012, The Astrophysical Journal, 753, 110, doi: [10.1088/0004-637X/753/2/110](https://doi.org/10.1088/0004-637X/753/2/110)
- Kogut, A., Banday, A. J., Bennett, C. L., et al. 1996, ApJ, 460, 1, doi: [10.1086/176947](https://doi.org/10.1086/176947)
- Kogut, A., Chluba, J., Fixsen, D. J., Meyer, S., & Spergel, D. 2016, in Society of Photo-Optical Instrumentation Engineers (SPIE) Conference Series, Vol. 9904, Space Telescopes and Instrumentation 2016: Optical, Infrared, and Millimeter Wave, ed. H. A. MacEwen, G. G. Fazio, M. Lystrup, N. Batalha, N. Siegler, & E. C. Tong, 99040W, doi: [10.1117/12.2231090](https://doi.org/10.1117/12.2231090)
- Kogut, A., Dunkley, J., Bennett, C. L., et al. 2007, ApJ, 665, 355, doi: [10.1086/519754](https://doi.org/10.1086/519754)
- Krachmalnicoff, N., Baccigalupi, C., Aumont, J., Bersanelli, M., & Mennella, A. 2016, Astronomy & Astrophysics, 588, A65, doi: [10.1051/0004-6361/201527678](https://doi.org/10.1051/0004-6361/201527678)
- Krachmalnicoff, N., Carretti, E., Baccigalupi, C., et al. 2018, A & A, 618, A166, doi: [10.1051/0004-6361/201832768](https://doi.org/10.1051/0004-6361/201832768)
- Kusaka, A., Appel, J., Essinger-Hileman, T., et al. 2018, Journal of Cosmology and Astroparticle Physics, 2018, 005, doi: [10.1088/1475-7516/2018/09/005](https://doi.org/10.1088/1475-7516/2018/09/005)
- Lamarre, J. M., Puget, J. L., Ade, P. A. R., et al. 2010, A & A, 520, A9, doi: [10.1051/0004-6361/200912975](https://doi.org/10.1051/0004-6361/200912975)
- Lang, D., Hogg, D. W., Mierle, K., Blanton, M., & Roweis, S. 2010, The Astronomical Journal, 139, 1782, doi: [10.1088/0004-6256/139/5/1782](https://doi.org/10.1088/0004-6256/139/5/1782)
- Lawson, K. D., Mayer, C. J., Osborne, J. L., & Parkinson, M. L. 1987, Monthly Notices of the Royal Astronomical Society, 225, 307, doi: [10.1093/mnras/225.2.307](https://doi.org/10.1093/mnras/225.2.307)

- Lazarian, A., & Hoang, T. 2019, *The Astrophysical Journal*, 883, 122, doi: [10.3847/1538-4357/ab3d39](https://doi.org/10.3847/1538-4357/ab3d39)
- Leitch, E. M., Readhead, A. C. S., Pearson, T. J., & Myers, S. T. 1997, *The Astrophysical Journal*, 486, L23, doi: [10.1086/310823](https://doi.org/10.1086/310823)
- Lenz, D., Hensley, B. S., & Doré, O. 2017, *ApJ*, 846, 38, doi: [10.3847/1538-4357/aa84af](https://doi.org/10.3847/1538-4357/aa84af)
- Lewis, A., Challinor, A., & Lasenby, A. 2000, *ApJ*, 538, 473, doi: [10.1086/309179](https://doi.org/10.1086/309179)
- Lisenfeld, U., & Voelk, H. J. 1999, On the radio spectral index of galaxies, arXiv, doi: [10.48550/ARXIV.ASTRO-PH/9912232](https://doi.org/10.48550/ARXIV.ASTRO-PH/9912232)
- Liszt, H. 2014, *ApJ*, 780, 10, doi: [10.1088/0004-637X/780/1/10](https://doi.org/10.1088/0004-637X/780/1/10)
- Louis, T., Grace, E., Hasselfield, M., et al. 2017, *Journal of Cosmology and Astroparticle Physics*, 2017, 031, doi: [10.1088/1475-7516/2017/06/031](https://doi.org/10.1088/1475-7516/2017/06/031)
- Lourie, N. P. 2018, Phd dissertation, University of Pennsylvania.
- Lowe, I., Coppi, G., Ade, P. A. R., et al. 2020, in *Society of Photo-Optical Instrumentation Engineers (SPIE) Conference Series*, Vol. 11445, *Society of Photo-Optical Instrumentation Engineers (SPIE) Conference Series*, 114457A, doi: [10.1117/12.2576146](https://doi.org/10.1117/12.2576146)
- Lowe, I. N., Ade, P., Ashton, P., et al. 2020, in *Millimeter, Submillimeter, and Far-Infrared Detectors and Instrumentation for Astronomy X*, ed. J. Zmuidzinas & J.-R. Gao (SPIE), doi: [10.1117/12.2560854](https://doi.org/10.1117/12.2560854)
- Markley, L. 2003, *Journal of Guidance Control and Dynamics - J GUID CONTROL DYNAM*, 26, 311, doi: [10.2514/2.5048](https://doi.org/10.2514/2.5048)
- Marsden, G., Ade, P. A. R., Benton, S., et al. 2008, in *Millimeter and Submillimeter Detectors and Instrumentation for Astronomy IV*, ed. W. D. Duncan, W. S. Holland, S. Withington, & J. Zmuidzinas (SPIE), doi: [10.1117/12.788413](https://doi.org/10.1117/12.788413)
- Martin, P. G., Blagrove, K. P. M., Lockman, F. J., et al. 2015, *The Astrophysical Journal*, 809, 153, doi: [10.1088/0004-637X/809/2/153](https://doi.org/10.1088/0004-637X/809/2/153)
- Martin, P. G., Clayton, G. C., & Wolff, M. J. 1999, *ApJ*, 510, 905, doi: [10.1086/306613](https://doi.org/10.1086/306613)
- Martin, P. G., Adamson, A. J., Whittet, D. C. B., et al. 1992, *ApJ*, 392, 691, doi: [10.1086/171470](https://doi.org/10.1086/171470)
- Martin, P. G., Roy, A., Bontemps, S., et al. 2012, *ApJ*, 751, 28, doi: [10.1088/0004-637X/751/1/28](https://doi.org/10.1088/0004-637X/751/1/28)
- Mathis, J. S., Rumpl, W., & Nordsieck, K. H. 1977, *ApJ*, 217, 425, doi: [10.1086/155591](https://doi.org/10.1086/155591)
- Matthews, T. G. 2013, Phd dissertation, Northwestern University.

- Mayne, N. J., Baraffe, I., Acreman, D. M., et al. 2014, *A & A*, 561, A1, doi: [10.1051/0004-6361/201322174](https://doi.org/10.1051/0004-6361/201322174)
- Meinert, C., de Marcellus, P., Le Sergeant dHendecourt, L., et al. 2011, *Physics of Life Reviews*, 8, 307, doi: <https://doi.org/10.1016/j.plrev.2011.08.005>
- Meisner, A. M., & Finkbeiner, D. P. 2014, *The Astrophysical Journal*, 798, 88, doi: [10.1088/0004-637X/798/2/88](https://doi.org/10.1088/0004-637X/798/2/88)
- Moncelsi, L., Ade, P. A. R., Angilè, F. E., et al. 2013, *Monthly Notices of the Royal Astronomical Society*, 437, 2772, doi: [10.1093/mnras/stt2090](https://doi.org/10.1093/mnras/stt2090)
- Montier, L., Mot, B., de Bernardis, P., et al. 2020, in *Society of Photo-Optical Instrumentation Engineers (SPIE) Conference Series*, Vol. 11443, *Society of Photo-Optical Instrumentation Engineers (SPIE) Conference Series*, 114432G, doi: [10.1117/12.2562243](https://doi.org/10.1117/12.2562243)
- Naess, S., Aiola, S., Austermann, J. E., et al. 2020, *Journal of Cosmology and Astroparticle Physics*, 2020, 046, doi: [10.1088/1475-7516/2020/12/046](https://doi.org/10.1088/1475-7516/2020/12/046)
- Næss, S. K., & Louis, T. 2013, *Journal of Cosmology and Astroparticle Physics*, 2013, 001, doi: [10.1088/1475-7516/2013/09/001](https://doi.org/10.1088/1475-7516/2013/09/001)
- Nikolov, Y. 2022, *New Astronomy*, 97, 101859, doi: <https://doi.org/10.1016/j.newast.2022.101859>
- Ochsenbein, F., Bauer, P., & Marcout, J. 2000, *Astron. Astrophys. Suppl. Ser.*, 143, 23, doi: [10.1051/aas:2000169](https://doi.org/10.1051/aas:2000169)
- Page, L., Hinshaw, G., Komatsu, E., et al. 2007, *The Astrophysical Journal Supplement Series*, 170, 335, doi: [10.1086/513699](https://doi.org/10.1086/513699)
- Paine, S. 2018, *The am atmospheric model, 10.0*, Zenodo, doi: [10.5281/zenodo.1193771](https://doi.org/10.5281/zenodo.1193771)
- Pardo, J., Cernicharo, J., & Serabyn, E. 2001, *IEEE Transactions on Antennas and Propagation*, 49, 1683, doi: [10.1109/8.982447](https://doi.org/10.1109/8.982447)
- Pascale, E., Ade, P. A. R., Bock, J. J., et al. 2008, *The Astrophysical Journal*, 681, 400, doi: [10.1086/588541](https://doi.org/10.1086/588541)
- Pelgrims, V., Clark, S. E., Hensley, B. S., et al. 2021, *Astronomy & Astrophysics*, 647, A16, doi: [10.1051/0004-6361/202040218](https://doi.org/10.1051/0004-6361/202040218)
- Pittelkau, M. E. 2001, *Journal of Guidance Control and Dynamics - J GUID CONTROL DYNAM*, 24, 1187, doi: [10.2514/2.4834](https://doi.org/10.2514/2.4834)
- Planck Collaboration, Ade, P. A. R., Aghanim, N., et al. 2014, *A&A*, 571, A1, doi: [10.1051/0004-6361/201321529](https://doi.org/10.1051/0004-6361/201321529)

- Planck Collaboration, Adam, R., Ade, P. A. R., et al. 2016, *A & A*, 594, A1, doi: [10.1051/0004-6361/201527101](https://doi.org/10.1051/0004-6361/201527101)
- Planck Collaboration, Aghanim, N., Akrami, Y., et al. 2020a, *A & A*, 641, A12, doi: [10.1051/0004-6361/201833885](https://doi.org/10.1051/0004-6361/201833885)
- Planck Collaboration, Akrami, Y., Ashdown, M., et al. 2020b, *A & A*, 641, A11, doi: [10.1051/0004-6361/201832618](https://doi.org/10.1051/0004-6361/201832618)
- Planck Collaboration, Aghanim, N., Akrami, Y., et al. 2020c, *A & A*, 641, A3, doi: [10.1051/0004-6361/201832909](https://doi.org/10.1051/0004-6361/201832909)
- Planck Collaboration I. 2011, *A & A*, 536, A1, doi: [10.1051/0004-6361/201116464](https://doi.org/10.1051/0004-6361/201116464)
- Planck Collaboration I, Aghanim, N., Akrami, Y., et al. 2020, *A&A*, 641, A1, doi: [10.1051/0004-6361/201833880](https://doi.org/10.1051/0004-6361/201833880)
- Planck Collaboration Int. L. 2017, *Astronomy & Astrophysics*, 599, A51, doi: [10.1051/0004-6361/201629164](https://doi.org/10.1051/0004-6361/201629164)
- Planck Collaboration Int. LVII. 2020, *A&A*, 643, A42, doi: [10.1051/0004-6361/202038073](https://doi.org/10.1051/0004-6361/202038073)
- Planck Collaboration Int. XIX. 2015, *A & A*, 576, A104, doi: [10.1051/0004-6361/201424082](https://doi.org/10.1051/0004-6361/201424082)
- Planck Collaboration Int. XLII. 2016, *A & A*, 596, A103, doi: [10.1051/0004-6361/201528033](https://doi.org/10.1051/0004-6361/201528033)
- Planck Collaboration Int. XV. 2014, *A & A*, 565, A103, doi: [10.1051/0004-6361/201322612](https://doi.org/10.1051/0004-6361/201322612)
- Planck Collaboration Int. XX. 2015, *A & A*, 576, A105, doi: [10.1051/0004-6361/201424086](https://doi.org/10.1051/0004-6361/201424086)
- Planck Collaboration Int. XXI. 2015, *A & A*, 576, A106, doi: [10.1051/0004-6361/201424087](https://doi.org/10.1051/0004-6361/201424087)
- Planck Collaboration Int. XXII. 2015, *A & A*, 576, A107, doi: [10.1051/0004-6361/201424088](https://doi.org/10.1051/0004-6361/201424088)
- Planck Collaboration Int. XXX. 2016, *A&A*, 586, A133, doi: [10.1051/0004-6361/201425034](https://doi.org/10.1051/0004-6361/201425034)
- Planck Collaboration Int. XXXV. 2016, *A & A*, 586, A138, doi: [10.1051/0004-6361/201525896](https://doi.org/10.1051/0004-6361/201525896)
- Planck Collaboration IV. 2020, 641, A4, doi: [10.1051/0004-6361/201833881](https://doi.org/10.1051/0004-6361/201833881)
- Planck Collaboration VI. 2020, *A & A*, 641, A6, doi: [10.1051/0004-6361/201833910](https://doi.org/10.1051/0004-6361/201833910)

- Planck Collaboration X. 2016, *Astronomy & Astrophysics*, 594, A10, doi: [10.1051/0004-6361/201525967](https://doi.org/10.1051/0004-6361/201525967)
- Planck Collaboration XI. 2014, *A & A*, 571, A11, doi: [10.1051/0004-6361/201323195](https://doi.org/10.1051/0004-6361/201323195)
- Planck Collaboration XII. 2014, *A&A*, 571, A12, doi: [10.1051/0004-6361/201321580](https://doi.org/10.1051/0004-6361/201321580)
- Planck Collaboration XVI. 2014, *A & A*, 571, A16, doi: [10.1051/0004-6361/201321591](https://doi.org/10.1051/0004-6361/201321591)
- Planck Collaboration XVII. 2011, *A & A*, 536, A17, doi: [10.1051/0004-6361/201116473](https://doi.org/10.1051/0004-6361/201116473)
- Planck Collaboration XXV. 2016, *A & A*, 594, A25, doi: [10.1051/0004-6361/201526803](https://doi.org/10.1051/0004-6361/201526803)
- Planck Collaboration XXVIII. 2016, *A & A*, 594, A28, doi: [10.1051/0004-6361/201525819](https://doi.org/10.1051/0004-6361/201525819)
- Plaszczynski, S., Montier, L., Levrier, F., & Tristram, M. 2014, *MNRAS*, 439, 4048, doi: [10.1093/mnras/stu270](https://doi.org/10.1093/mnras/stu270)
- Potapov, A., Theulé, P., Jäger, C., & Henning, T. 2019, *The Astrophysical Journal Letters*, 878, L20, doi: [10.3847/2041-8213/ab2538](https://doi.org/10.3847/2041-8213/ab2538)
- Presta, G., Ade, P. A. R., Battistelli, E. S., et al. 2020, in *Journal of Physics Conference Series*, Vol. 1548, *Journal of Physics Conference Series*, 012018, doi: [10.1088/1742-6596/1548/1/012018](https://doi.org/10.1088/1742-6596/1548/1/012018)
- Prime Collaboration, Aravena, M., Austermann, J. E., et al. 2021, *CCAT-prime Collaboration: Science Goals and Forecasts with Prime-Cam on the Fred Young Submillimeter Telescope*, arXiv, doi: [10.48550/ARXIV.2107.10364](https://doi.org/10.48550/ARXIV.2107.10364)
- Quinn, J. L. 2012, *A & A*, 538, A65, doi: [10.1051/0004-6361/201015785](https://doi.org/10.1051/0004-6361/201015785)
- Remazeilles, M., Delabrouille, J., & Cardoso, J.-F. 2011, *MNRAS*, 418, 467, doi: [10.1111/j.1365-2966.2011.19497.x](https://doi.org/10.1111/j.1365-2966.2011.19497.x)
- Roy, A., Martin, P. G., Polychroni, D., et al. 2013, *ApJ*, 763, 55, doi: [10.1088/0004-637X/763/1/55](https://doi.org/10.1088/0004-637X/763/1/55)
- Savage, B. D., Bohlin, R. C., Drake, J. F., & Budich, W. 1977, *ApJ*, 216, 291, doi: [10.1086/155471](https://doi.org/10.1086/155471)
- Schlafly, E. F., & Finkbeiner, D. P. 2011, *ApJ*, 737, 103, doi: [10.1088/0004-637X/737/2/103](https://doi.org/10.1088/0004-637X/737/2/103)
- Schlafly, E. F., Meisner, A. M., Stutz, A. M., et al. 2016, *ApJ*, 821, 78, doi: [10.3847/0004-637X/821/2/78](https://doi.org/10.3847/0004-637X/821/2/78)
- Schlegel, D. J., Finkbeiner, D. P., & Davis, M. 1998, *ApJ*, 500, 525, doi: [10.1086/305772](https://doi.org/10.1086/305772)

- Seljak, U., & Zaldarriaga, M. 1997, *Physical Review Letters*, 78, 2054, doi: [10.1103/physrevlett.78.2054](https://doi.org/10.1103/physrevlett.78.2054)
- Serkowski, K., Mathewson, D. S., & Ford, V. L. 1975, *ApJ*, 196, 261, doi: [10.1086/153410](https://doi.org/10.1086/153410)
- Shaw, E. C., Ade, P., Akers, S., et al. 2020, in *Millimeter, Submillimeter, and Far-Infrared Detectors and Instrumentation for Astronomy X*, ed. J. Zmuidzinas & J.-R. Gao (SPIE), doi: [10.1117/12.2562941](https://doi.org/10.1117/12.2562941)
- Siebenmorgen, R., Voshchinnikov, N. V., & Bagnulo, S. 2014, *A & A*, 561, A82, doi: [10.1051/0004-6361/201321716](https://doi.org/10.1051/0004-6361/201321716)
- Siebenmorgen, R., Voshchinnikov, N. V., & Bagnulo, S. 2014, *A&A*, 561, A82, doi: [10.1051/0004-6361/201321716](https://doi.org/10.1051/0004-6361/201321716)
- Simmons, J. F. L., & Stewart, B. G. 1985, *A & A*, 142, 100
- Simons Observatory Collaboration. 2019, *Journal of Cosmology and Astroparticle Physics*, 2019, 056, doi: [10.1088/1475-7516/2019/02/056](https://doi.org/10.1088/1475-7516/2019/02/056)
- Skalidis, R., & Pelgrims, V. 2019, *A & A*, 631, L11, doi: [10.1051/0004-6361/20193654710.48550/arXiv.1908.08706](https://doi.org/10.1051/0004-6361/20193654710.48550/arXiv.1908.08706)
- Soler, J. D., Ade, P. A. R., Angilè, F. E., et al. 2017, *Astronomy & Astrophysics*, 603, A64, doi: [10.1051/0004-6361/201730608](https://doi.org/10.1051/0004-6361/201730608)
- Stein, W. 1966, *ApJ*, 144, 318, doi: [10.1086/148606](https://doi.org/10.1086/148606)
- Stephens, I. W., Looney, L. W., Dowell, C. D., Vaillancourt, J. E., & Tassis, K. 2011, *ApJ*, 728, 99, doi: [10.1088/0004-637X/728/2/99](https://doi.org/10.1088/0004-637X/728/2/99)
- Stevens, J., Goeckner-Wald, N., Keskitalo, R., et al. 2018, in *Millimeter, Submillimeter, and Far-Infrared Detectors and Instrumentation for Astronomy IX*, ed. J. Zmuidzinas & J.-R. Gao, *Proceedings of SPIE - The International Society for Optical Engineering* (United States: SPIE), doi: [10.1117/12.2313898](https://doi.org/10.1117/12.2313898)
- Sutin, B. M., Alvarez, M., Battaglia, N., et al. 2018, in *Society of Photo-Optical Instrumentation Engineers (SPIE) Conference Series*, Vol. 10698, *Space Telescopes and Instrumentation 2018: Optical, Infrared, and Millimeter Wave*, ed. M. Lystrup, H. A. MacEwen, G. G. Fazio, N. Batalha, N. Siegler, & E. C. Tong, 106984F, doi: [10.1117/12.2311326](https://doi.org/10.1117/12.2311326)
- Svalheim, T. L., Andersen, K. J., Aurlen, R., et al. 2020, *BeyondPlanck XV. Polarized foreground emission between 30 and 70 GHz*, arXiv, doi: [10.48550/ARXIV.2011.08503](https://doi.org/10.48550/ARXIV.2011.08503)
- Takakura, S., Aguilar, M., Akiba, Y., et al. 2017, *Journal of Cosmology and Astroparticle Physics*, 2017, 008, doi: [10.1088/1475-7516/2017/05/008](https://doi.org/10.1088/1475-7516/2017/05/008)

- Tegmark, M., Eisenstein, D. J., Hu, W., & de Oliveira-Costa, A. 2000, *The Astrophysical Journal*, 530, 133, doi: [10.1086/308348](https://doi.org/10.1086/308348)
- Thorne, B., Dunkley, J., Alonso, D., & Næss, S. 2017, *Monthly Notices of the Royal Astronomical Society*, 469, 2821, doi: [10.1093/mnras/stx949](https://doi.org/10.1093/mnras/stx949)
- Unger, M., & Farrar, G. R. 2017, in *International Cosmic Ray Conference*, Vol. 301, 35th International Cosmic Ray Conference (ICRC2017), 558. <https://arxiv.org/abs/1707.02339>
- Vaillancourt, J. E., Dowell, C. D., Hildebrand, R. H., et al. 2008, *ApJL*, 679, L25, doi: [10.1086/589152](https://doi.org/10.1086/589152)
- van der Walt, S., Colbert, S. C., & Varoquaux, G. 2011, *Computing in Science and Engineering*, 13, 22, doi: [10.1109/MCSE.2011.37](https://doi.org/10.1109/MCSE.2011.37)
- Virtanen, P., Gommers, R., Oliphant, T. E., et al. 2020, *Nature Methods*, 17, 261, doi: [10.1038/s41592-019-0686-2](https://doi.org/10.1038/s41592-019-0686-2)
- Wakelam, V., Bron, E., Cazaux, S., et al. 2017, *Molecular Astrophysics*, 9, 1, doi: <https://doi.org/10.1016/j.molap.2017.11.001>
- Wardle, J. F. C., & Kronberg, P. P. 1974, *ApJ*, 194, 249, doi: [10.1086/153240](https://doi.org/10.1086/153240)
- Whittet, D. C. B., Martin, P. G., Hough, J. H., et al. 1992, *ApJ*, 386, 562, doi: [10.1086/171039](https://doi.org/10.1086/171039)
- Williams, P. A. 2021, PhD thesis. <https://www.proquest.com/dissertations-theses/mapping-galactic-clouds-with-balloon-borne-large/docview/2616963445/se-2>
- Winkel, B., Kerp, J., Flöer, L., et al. 2015, *Astronomy & Astrophysics*, 585, A41, doi: [10.1051/0004-6361/201527007](https://doi.org/10.1051/0004-6361/201527007)
- Xu, Z., Adachi, S., Ade, P., et al. 2021, *Research Notes of the AAS*, 5, 100, doi: [10.3847/2515-5172/abf9ab](https://doi.org/10.3847/2515-5172/abf9ab)
- Zaldarriaga, M. 2001, *Physical review D: Particles and fields*, 64, doi: [10.1103/PhysRevD.64.103001](https://doi.org/10.1103/PhysRevD.64.103001)
- Zaldarriaga, M., Spergel, D. N., & Seljak, U. 1997, *The Astrophysical Journal*, 488, 1, doi: [10.1086/304692](https://doi.org/10.1086/304692)
- Zonca, A., Singer, L., Lenz, D., et al. 2019, *Journal of Open Source Software*, 4, 1298, doi: [10.21105/joss.01298](https://doi.org/10.21105/joss.01298)
- Zonca, A., Thorne, B., Krachmalnicoff, N., & Borrill, J. 2021, *Journal of Open Source Software*, 6, 3783, doi: [10.21105/joss.03783](https://doi.org/10.21105/joss.03783)
- Zubko, V., Dwek, E., & Arendt, R. G. 2004, *ApJS*, 152, 211, doi: [10.1086/382351](https://doi.org/10.1086/382351)